Komplexe Halogenidometallate der Gruppe 15 - Struktur, Eigenschaften und neue Funktionalität

Kumulative Dissertationsschrift

zur Erlangung des akademischen Grades eines
Doktors der Naturwissenschaften
(Dr. rer. nat.)

dem
Fachbereich Chemie der Philipps-Universität Marburg
(Hochschulkennziffer 1180)
vorgelegt von

Natalie Dehnhardt, M. Sc.
aus Rotenburg an der Fulda

Marburg 2020

Erstgutachterin:	Dr. Johanna Heine
Zweitgutachterin:	Prof. Dr. Stefanie Dehnen
Einreichungstermin:	06.08.2020
Promotionsverfahren eröffnet:	18.08.2020
Disputationstermin:	16.09.2020

Lizenzierung

Meiner Familie gewidmet.

Kinder, in ihrer Einfalt, fragen immer und immer: Warum?
Der Verständige tut das nicht mehr - denn jedes Warum,
das weiß der längst, ist nur der Zipfel eines Fadens,
der in den dicken Knäuel der Unendlichkeit ausläuft,
mit dem keiner recht fertig wird,
er mag wickeln und haspeln - so viel er nur will.
Wilhelm Busch

Erklärung

Ich erkläre, dass eine Promotion noch an keiner anderen Hochschule als der Philipps-Universität Marburg, Fachbereich Chemie, versucht wurde. Weiterhin versichere ich, dass ich meine vorgelegte Dissertation:

„Komplexe Halogenidometallate der Gruppe 15 - Struktur, Eigenschaften und neue Funktionalität“

selbst und ohne fremde Hilfe verfasst, nicht andere als die in ihr angegebenen Quellen oder Hilfsmittel benutzt, alle vollständig oder sinngemäß übernommenen Zitate als solche gekennzeichnet, sowie die Dissertation in der vorliegenden oder einer ähnlichen Form noch bei keiner anderen in- oder ausländischen Hochschule anlässlich eines Promotionsgesuchs oder zu anderen Prüfungszwecken eingereicht habe.

Marburg, den 06.08.2020

Natalie Dehnhardt

Die vorliegende Arbeit entstand in der Zeit von August 2018 bis August 2020 unter der Leitung von Dr. Johanna Heine am Fachbereich Chemie der Philipps-Universität Marburg.

Inhaltsverzeichnis

Abbildungsverzeichnis

Tabellenverzeichnis

Abkürzungsverzeichnis

AE2T	5,5′-diylbis(aminoethyl)-[2,2′-bithiophene]
aq.	wässrig
BA	Butylammonium
Bipy	Bipyridin
Bz	Benzylgruppe
Cp	Cyclopentadienyl
DFT	Dichtefunktionaltheorie
DTA/TG	Differenz-Thermoanalyse/Thermogravimetrie
EDX	Energiedispersive Röntgenspektroskopie
Et	Ethylgruppe
Im	Imidazol
IR	Infrarotspektroskopie
LED	*engl.* Light Emitting Diode, lichtemittierende Diode
Me	Methylgruppe
nBu	n-Butylgruppe
pEDA	*engl.* periodic energy decomposition analysis
PL	Photolumineszenzspektroskopie
PPh_4	Tetraphenylphosphonium
PXRD	*engl.* Powder X-ray Diffraction, Röntgenbeugung an Pulvern
Py	Pyridin
SCXRD	*engl.* Single Crystal X-ray Diffraction, Röntgenbeugung an Einkristallen
SHG	*engl.* Second Harmonic Generation, Frequenzverdopplung
UV	ultraviolett
Vis	visuell, sichtbar
VSEPR	*engl.* Valence Shell Electron Pair Repulsion Valenzschalen-Elektronenpaar-Abstoßung

Einleitung 1

Im Rahmen dieser Arbeit beschäftigte ich mich mit der Synthese neuer Halogenidometallate der Elemente Antimon und Bismut. Obwohl die Substanzklasse schon seit langem bekannt ist, sind ihre Verbindungen besonders im Bezug auf die Strukturvielfalt, Synthesemethoden und Eigenschaften noch relativ unerforscht. In den letzten Jahren hat sie zunehmend an Bedeutung gewonnen, auch vor dem Hintergrund des rasant wachsenden Forschungsfeldes der Perowskit-Solarzellen. Diese stellen eine neue Anwendung für Halogenidometallate der schweren Hauptgruppenelemente dar, stehen aber auf Grund des in ihnen verwendeten Bleis in der Kritik. Im folgenden Kapitel soll deshalb zunächst auf Gruppe 14 Halogenidometallate und deren Eignung als Absorptionsmaterial in Perowskitsolarzellen, sowie weitere Anwendungen schwerer Hauptgruppenelementverbindungen eingegangen werden. Hierbei wird eine Differenzierung von Perowskiten, perowskit-verwandten Strukturen und Halogenidometallaten vorgenommen. Anschließend wird der aktuelle Forschungsstand auf dem Gebiet der Gruppe 15 Halogenidometallate näher erläutert.

1.1. Halogenidometallate in Perowskit-Solarzellen

Die Solartechnik ist eine vielversprechende Methode, um eine kostengünstige und umweltfreundliche Energieversorgung zu gewährleisten. Derzeit verwendete Solarzellen basieren zu 85 % auf kristallinem Silizium und erreichen einen Wirkungsgrad über 27 %. Ein Nachteil der siliziumbasierten Solartechnik ist jedoch ihre teure und aufwendige Produktion, sodass ein dringender Bedarf für neue Lichtabsorptionsmaterialen mit geringeren Produktionskosten und einer einfacheren Synthesemethode besteht.[1]

Ein schnell wachsender Bereich der Photovoltaikforschung sind Solarzellen auf Basis von Hybrid-Perowskitverbindungen. Bezeichnend für den Erfolg der Verbindungsklasse ist die rasante Steigerung ihrer Effizienz in Solarzellmodulen.[2] *Miyasaka* und Mitarbeiter setzten 2009 die Verbindung $(CH_3NH_3)PbI_3$, welche eine Struktur des Perowskittyps aufweist, in Solarzellen ein und beobachteten einen Wirkungsgrad von 3,8 %.[3] Bereits drei Jahre später konnte erstmals eine zweistellige Effizienz von 10,9 % erreicht werden.[4] Eingeleitet durch diesen Erfolg begann ein wissenschaftliches Wettrennen um die Effizienz bleibasierter Perowskitsolarzellen, welches die Effizienz innerhalb von einem Jahrzehnt auf bemerkenswerte 25,2 % steigerte.[2] Perowskitsolarzellen erreichen somit einen ähnlichen

Effizienzbereich wie siliziumbasierte Solarzellen, bieten aber den Vorteil einer einfacheren Synthese nahe Raumtemperatur in Lösung und damit verbundenen geringeren Produktionskosten.[5] Im Folgenden soll zunächst auf die zu Grunde liegende Chemie, den aktuellen Forschungsstand sowie auf Probleme der Materialklasse eingegangen werden.

1.1.1. Halogenidoplumbate mit Perowskitstruktur

Historisches

Bei Perowskiten handelt es sich um eine Materialklasse der Zusammensetzung ABX_3, wobei mit dem Begriff Perowskit klassischerweise $CaTiO_3$ in Verbindung gebracht wird. Entdeckt wurde die Verbindung bereits 1839 von *Rose*, der sie von seinem russischen Kollegen *Kämmerer* zugeschickt bekommen, und auf dessen Wunsch nach dem russischen Mineralogen *Perovskiy* benannte.[6] Oxidische Perowskite können in einer Vielzahl von Bauteilen zum Einsatz kommen, wie etwa in Ferroelektrika oder Piezoelektrika, weisen aber im Gegensatz zu ihren verwandten Halogenidverbindungen nur schlechte Halbleitereigenschaften auf.[7]

Wells berichtete bereits 1893 über halogenidbasierte Perowskite der Zusammensetzung $CsPbX_3$ in denen Chlorid-, Bromid- oder Iodidatome die X-Position im Kristallgitter besetzen.[8] Neben rein anorganischen Perowskiten können auch organisch-anorganische Hybridverbindungen synthetisiert werden, bei denen das einwertige Kation der A-Position durch ein sterisch wenig anspruchsvolles organisches Kation ersetzt wird. *Weber* berichtete 1978 erstmals über die Verbindung $(CH_3NH_3)PbI_3$, die auch in der Perowskitsolarzelle von *Miyasaka* verwendet wurde.[9] Durch röntgenografische Untersuchungen konnte *Weber* zeigen, dass sie im Gegensatz zu den rein anorganischen Verbindungen $CsPbX_3$, deren Struktur 1957 von *Møller* aufgeklärt wurde, bereits bei Raumtemperatur in der kubischen Perowskitstrutkur kristallisiert.[9,10]

Perowskite, perowskitverwandte Strukturen und Halogenidometallate

Im kubischen Perowskit ABX_3 treten zwei verschiedene Kationen auf. Die A-Kationen bilden zusammen mit den X-Atomen eine kubisch dichteste Packung, wobei die A-Kationen von 12 X-Atomen kuboktaedrisch umgeben sind. Die B-Kationen besetzen $\frac{1}{4}$ der Oktaederlücken im Kristallgitter. Daraus resultiert ein Gitter aus allseits eckenverknüpften $\{BX_6\}$-Oktaedern, wie es auch im ReO_3-Typ zu finden ist.[11] Ausschlaggebend dafür, dass diese Struktur angenommen werden kann ist das A-Kation, was sich in der kuboktaedrischen Lücke befindet.

Der *Goldschmidt*'sche Toleranzfaktor τ korreliert die Ionenradien der vorliegenden Anionen und Kationen mit dem Auftreten der Perowskitstruktur. Beispiele für Strukturtypen die für unterschiedliche Werte von τ erhalten werden sind in Abbildung 1.1 dargestellt.

$$\tau = \frac{r_A + r_X}{\sqrt{2}(r_B + r_X)} \tag{1.1}$$

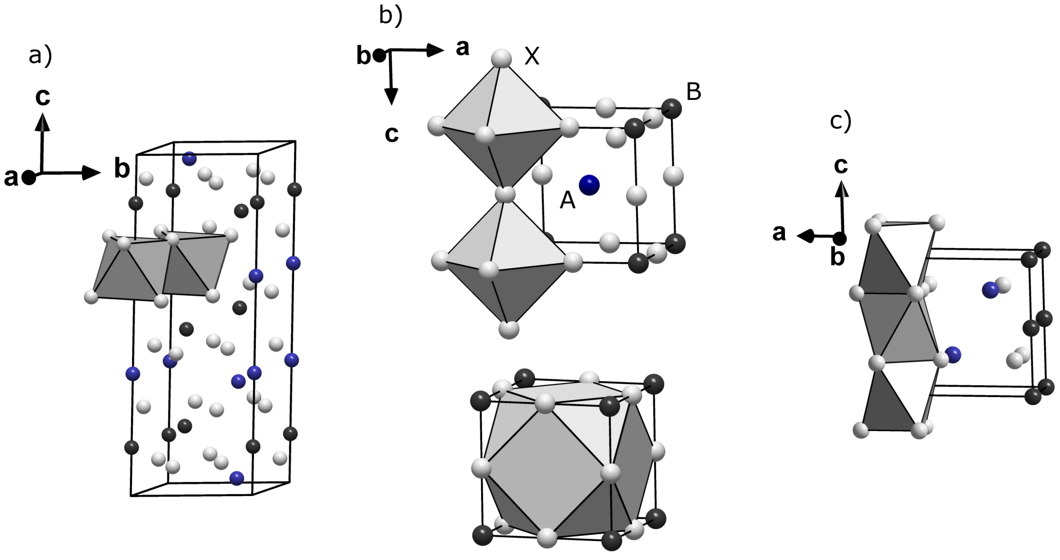

τ < 0,8
Ilemnit

0,8 < τ < 1
Perowskit,
kubisch

τ > 1
Perowskit,
hexagonal

Abbildung 1.1: Ausschnitte aus den Kristallstrukturen verschiedener ABX_3-Strukturtypen, A-Atome sind blau, B-Atome schwarz und X-Atome grau dargestellt. a) Ilmenit $FeTiO_3$[12] mit kantenverknüpften Koordinationspolyedern b) Kubischer Perowskit $SrTiO_3$[13] mit oktaedrischer Koordinationssphäre am B- und kuboktaedrischer Koordinationssphäre am A-Atom c) Hexagonaler Perowskit $BaNiO_3$[14] mit flächenverknüpften Koordinationspolyedern.

Wird für τ ein Wert zwischen 0,8 und 1 erhalten liegt die kubische Perowskitstruktur vor, wobei diese nur für einen Wert von $0{,}89 < \tau > 1$ unverzerrt auftritt. Für $\tau < 0{,}8$ kann keine Perowskitstruktur mehr erhalten werden und es kommt zum Auftreten des Ilmenit-Typs. Das selbe gilt für $\tau > 1$, was zum Auftreten der hexagonalen Stapelvariante des Perowskits führt.[11] Gemäß Formel 1.1 wird für $CsPbI_3$ ein Wert von $\tau = 0{,}85$ erhalten. Dieser befindet sich im unteren Bereich des τ-Wertes für den eine kubische Perowskitstruktur erwartet werden würde. Entsprechend kristallisiert die Verbindung bevorzugt in der von *Møller* beschriebenen orthorhombisch verzerrten Modifikation der kubischen Perowskitstruktur.[10] Für die Hybridverbindung $(CH_3NH_3)PbI_3$ wird ein Wert von $\tau = 0{,}91$ erhalten, welcher im guten Einklang mit der kubischen Perowskitstruktur steht, in welcher die Verbindung kristallisiert. Jedoch sind diese Werte mit Vorsicht zu genießen, da der Toleranzfaktor davon abhängt, welche Ionenradien eingesetzt werden, und besonders die Radien für organische Kationen fehleranfällig sind.[7]

Auf Grund der Prominenz der Bleihalogenidperowskite kam es in den letzten Jahren zu einer übermäßigen Benutzung des Begriffs „Perowskit“.[15] Halogenidometallate, die keine strukturelle Verwandschaft mit der Perowskitstruktur aufweisen, werden auf Grund ihrer hervorragenden optoelektronischen Eigenschaften, die an $(CH_3NH_3)PbI_3$ erinnern, als „perovskite-like“[16] oder „perovskitoid“[17] bezeichnet. Um der missbräuchlichen Benutzung des Begriffs „Perowskit“ entgegenzukommen, soll im folgenden Abschnitt auf einige Strukturmotive von halogenidbasierten Perowskiten sowie von Halogenidometallaten die keine Perowskitstruktur aufweisen, eingegangen werden.[1]

In der Literatur ist klar definiert, welche Merkmale eine Verbindung aufweisen muss, um als Perowskit bezeichnet werden zu können. Dazu gehören ein A:B:X-Verhältnis von 1:1:3, eine oktaedrische Koordination der B-Kationen sowie die Verknüpfung der $\{BX_6\}$-Oktaeder zu einem allseits eckenverknüpften 3D-Netzwerk.[18] Neben der klassischen kubischen Perowskitstruktur gibt es noch weitere Strukturmotive, die diese Voraussetzungen erfüllen. Da die ideale kubische Perowskitstruktur nur für wenige Verbindungen auftritt, wie im Aristotyp $SrTiO_3$, sind hier zuerst verzerrte Perowskistrukturen zu nennen, die im orthorhombischen oder tetragonalen Kristallsystem kristallisieren. Die $\{BX_6\}$-Oktaeder weisen hier dieselbe Verknüpfung wie im idealen kubischen Perowskit auf, sind aber auf Grund der abweichenden Ionenradien von A, B und X-Ionen zueinander verkippt. Eine solche Verzerrung kann auch für $(CH_3NH_3)PbI_3$ und in sehr geringem Maße sogar für den ursprünglichen Perowskit $CaTiO_3$ gefunden werden. Zwei Beispiele sind in Abbildung 1.2 a) und b) dargestellt.

Als nächstes ist die Klasse der Elpasolithe zu nennen, deren Verbindungen in einer Überstruktur des kubischen Perowskits kristallisieren. Wie im Aristotyp K_2NaAlF_6 werden hier die B-Kationen durch zwei heterovalente Kationen ersetzt, die feste kristallographische Positionen besetzen. Ein Beispiel ist in Abbildung 1.2 c) dargestellt. Damit sind die Elpasolithe von „gemischten Perowskiten“ abzuheben, in denen homovalente Kationen dotiert werden, deren kristallographische Position nicht eindeutig ist.

Zuletzt sind Perowskite mit geordneten Leerstellen zu nennen, in denen die B-Kationen teilweise fehlen, beziehungsweise ihre Positionen durch Leerstellen besetzt sind. In diesen Verbindungen wird die B-Position im Kristallgitter durch ein Kation anderer Valenz ersetzt, wodurch zum Ladungsausgleich eine Leerstelle an anderer Position auftreten muss. Beispiele sind Verbindungen der Zusammensetzung $A_2B[V]X_6$ in denen B ein vierwertiges Kation wie Sn^{4+} oder Pd^{4+} sein kann und V für eine unbesetzte B-Position, also eine Leerstelle, steht. Da für jedes Kation formal eine Leerstelle erzeugt wird ist eine Eckenverknüpfung der $\{BX_6\}$-Oktaeder nicht mehr gegeben. Ein Beispiel ist in Abbildung 1.2 d) dargestellt. Auch dreiwertige Kationen wie Sb^{3+} und Bi^{3+} können Perowskite mit geordneten Leerstellen bilden. Hier ist die Verbindung $Cs_3Sb_2I_9$ zu nennen, in der die B-Position im Verhältnis 2:1 von Sb^{3+}-Kationen und Leerstellen besetzt sind, was zu einer $A_3B_2[V]X_9$-Stöchiometrie führt. Die Leerstellen liegen hierbei in der [111]-Ebene, wodurch 2D-Schichten aus $\{BX_6\}$-Oktaedern erhalten werden.[15] Ein Ausschnitt aus der

---

[1] Da das Strukturmotiv des hexagonalen Perowskits für die weiteren Ausführungen nicht relevant ist, bezieht sich die Bezeichnung „Perowskit“ in den folgenden Kapiteln stets auf die kubische Perowskitstruktur sowie von ihr abgeleitete Strukturmotive.

Kristallstruktur ist in Abbildung 1.2 e) zu sehen.

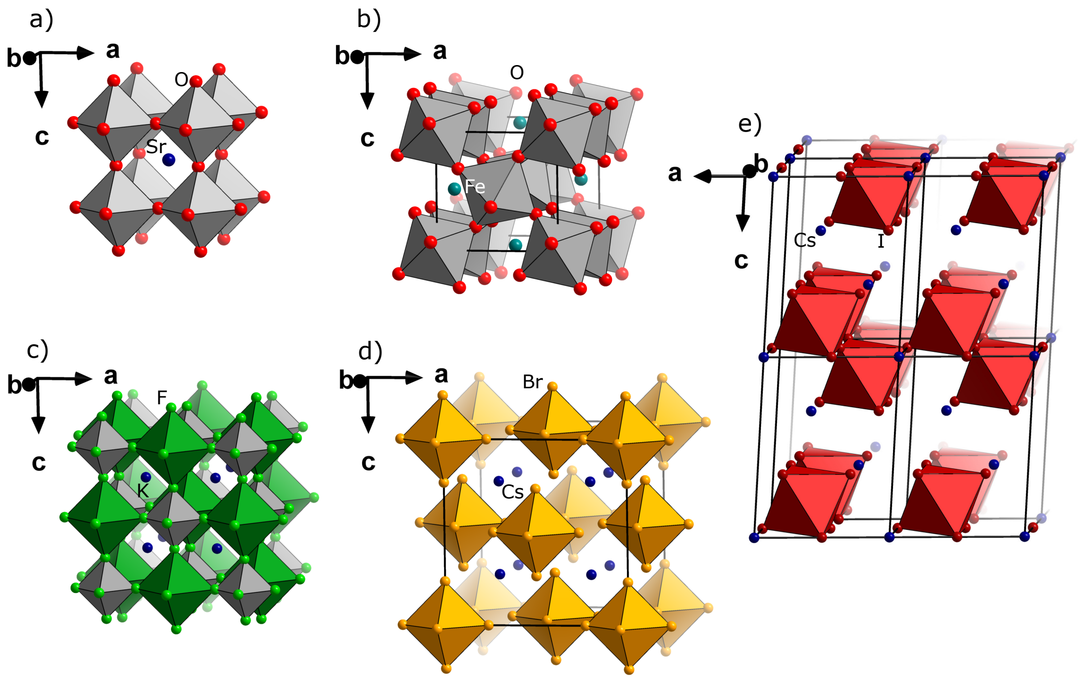

Abbildung 1.2: Ausschnitte aus den Kristallstrukturen verschiedener Perowskite. a) Kubischer Perowskit $SrTiO_3$,[13] b) orthorhombisch verzerrter Perowskit $FeGdO_3$,[19] c) Elpasolith $KNaAlF_6$,[20] d) Perowskit mit geordneten Leerstellen Cs_2PdBr_6,[21] e) Perowskit mit geordneten Leerstellen $Cs_3Sb_2I_9$.[22]

Während die bisher beschriebenen Strukturmotive als Perwoskite bezeichnet werden können, gibt es noch einige weitere interessante Strukturmotive, die auch auf eckenverknüpften $\{BX_6\}$-Oktaedern beruhen, allerdings die anderen Bedingungen der Perowskitstruktur nicht erfüllen. Da diese Motive vom kubischen Perowskit abgeleitet werden können, werden sie im Folgenden als perowskitverwandten Strukturen bezeichnet. Für rein anorganische Verbindungen sind hier *Ruddlesden-Popper*- und *Dion-Jacobson*-Phasen zu nennen.[18] Verbindungen dieser Phasen weisen Schichten aus allseits eckenverknüpften Oktaedern auf, wie sie im kubischen Perowskit auftreten. Zwischen den Schichten befinden sich mono- oder divalente Kationen, im Fall von *Dion-Jacobson*-Phasen eins, bei den *Ruddlesden-Popper*-Phasen zwei Kationen. Dadurch sind sie von Perowskiten mit Leerstellen wie $Cs_3Sb_2I_9$ zu unterscheiden, da zwischen den Schichten in *Dion-Jacobson*- und *Ruddlesden-Popper*-Phasen keine Leerstellen auftreten. Auch die Koordination und damit die Anordnung der Schichten zueinander ist ausschlaggebend. In *Dion-Jacobson*-Phasen ist das A-Kation kubisch von acht X-Atomen umgeben, wodurch eine parallele Anordnung der Schichten erhalten wird.[23,24] In *Ruddlesden-Popper*-Phasen sind die Kationen quadratisch anti-prismatisch überkappt umgeben, wodurch eine gestaffelte Anordnung der Schichten erhalten wird.[25] Für Hybrid-Verbindungen ist die Einteilung in *Ruddlesden-Popper*- und *Dion-Jacobson*-Phasen nicht mehr eindeutig gegeben, da sich die organischen Kationen im Gegensatz zu anorganischen Kationen anders in den Zwischenräumen zwischen den anorganischen Schichten anordnen. So wird ein organisches Kation, wie zum Beispiel ein Diammoniumkation, seine positiv geladenen Kopfgruppen immer in Richtung der negativ geladenen X-Ionen anordnen. Hierdurch kommt es auch mit nur einem Kation, was für eine *Dion-Jacobson*-Phase sprechen würde, zu einer gestaffelten Anordnung, wie sie für *Ruddlesden-Popper*-Phasen erwartet wird.[18] Bespiele für eine *Dion-Jacobson*- und eine *Ruddlesden-Popper*-Phase sind in Abbildung 1.3 zu sehen.

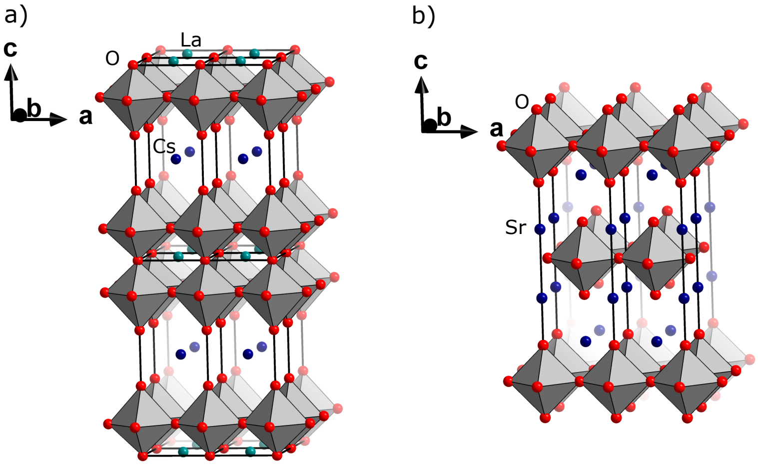

Abbildung 1.3: Ausschnitte aus den Kristallstrukturen der a) *Dion-Jacobson*-Phase $CsLaNbO_7$[26] mit paralleler Anordnung der $LaNbO_7$-Schichten und b) *Ruddlesden-Popper*-Phase Sr_2RuO_4[27] mit gestaffelter Anordnung der RuO_4-Schichten.

Trotzdem können auch Hybridverbindungen strukturell vom Perowskit abgeleitet werden. Hierfür stellte *Mitzi* ein Kozept zu dimensionalen Reduzierung von Hyprid-Perowskiten vor, welches in Abbildung 1.4 verdeutlicht wird. Hierbei wird die 3D-Perowskitstruktur durch Schnitte entlang verschiedener Ebenen in 2D-Ausschnitte zerteilt. Je nachdem entlang welcher Raumrichtung und nach wie vielen Schichten n geschnitten wird, können Strukturmotive unterschiedlicher Dimensionalität erhalten werden. Wird senkrecht zur <100>-Richtung geschnitten werden Schichtstrukturen unterschiedlicher Dicken erhalten. Bei den Verbindungen der <110>-Familie können für 1D-Stränge für $n = 1$ erhalten werden, oder schichtartige Strukturen für $n > 1$. Wenn senkrecht zur <111>-Richtung geschnitten wird, können schließlich isolierte $\{BX_6\}$-Oktaeder für $n = 1$ oder Schichtstrukturen für $n > 1$ erhalten werden. In allen Fällen werden die einzelnen Ausschnitte aus der Perowskitstruktur durch typischerweise größere organische Kationen voneinander getrennt.[28] Sprachlich findet man häufig, besonders für niederdimensionale Strukturen wie die <111> Struktur für $n = 1$ Bezeichnungen wie 0D-Perowskit. Diese Bezeichnungen sind irreführend, da eine Perowskitstruktur, wie zuvor erläutert, dreidimensional ist.[18] Von daher werden Verbindungen, die nach dem hier vorgestellten Prinzip erhalten werden, im Folgenden als Halogenidometallate bezeichnet. Das Konzept wird in Abbildung 1.4 verdeutlicht.

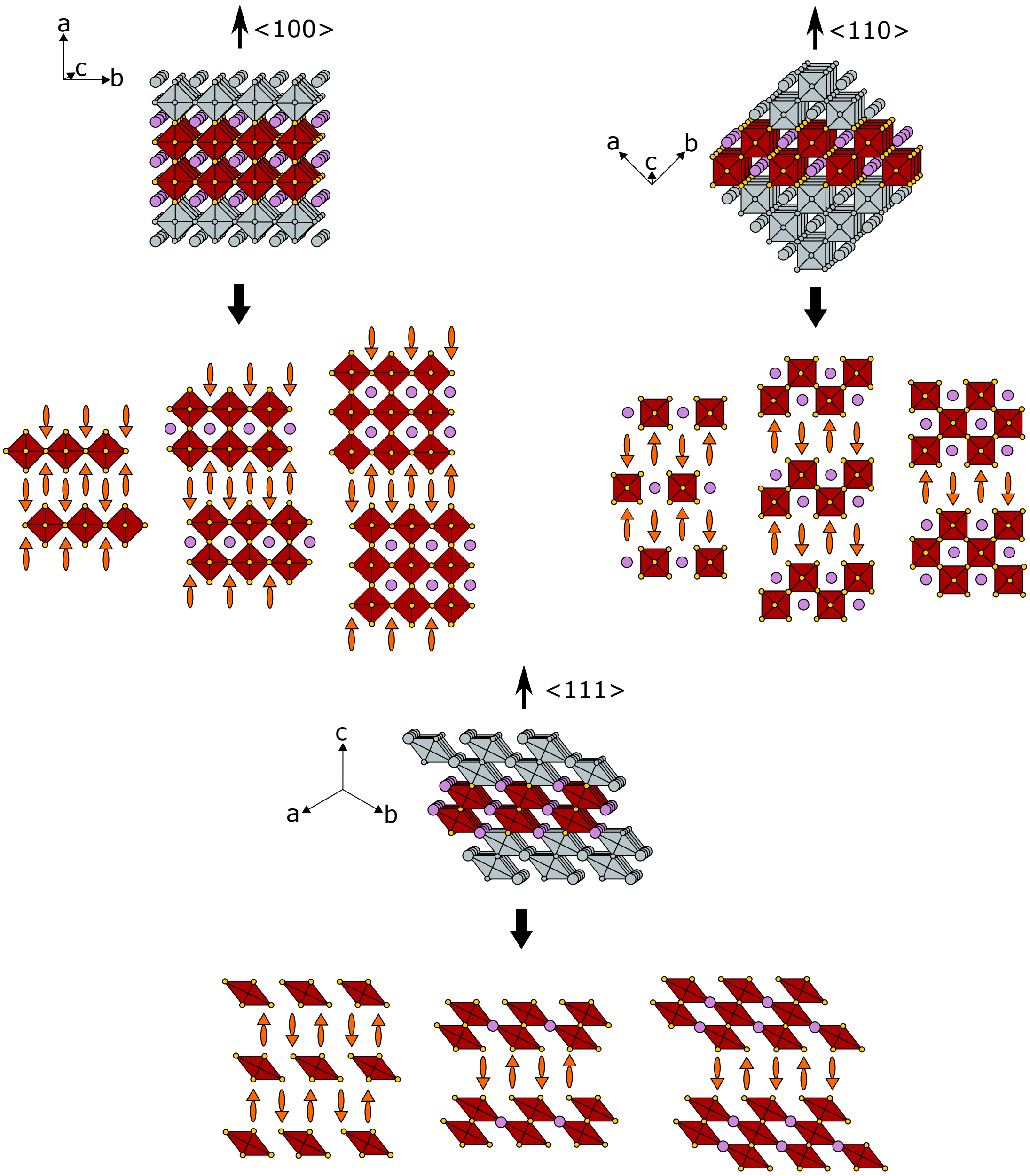

Abbildung 1.4: Dimensionale Reduktion der kubischen Perowskitstruktur durch Schnitte senkrecht zu den kristallographischen Raumrichtungen <100>, <110> und <111>. Oktaedrische Koordinationspolyeder sind rot, anorganische Kationen violett, organische Kationen orange dargestellt. Abbildung inspiriert durch [28].

1.1.2. Eigenschaften halogenidbasierter Perowskite

Perowskite und ihre verwandten Strukturen können eine Reihe von interessanten Eigenschaften aufweisen. Besonders die halogenidbasierten Verbindungen zeigen hervorragende Halbleitereigenschaften wie eine direkte Bandlücke, hohe Absoprtionskoeffizienten und eine hohe Defekttoleranz. Die Struktur des Perwoskits und seiner verwandten Strukturen bieten viele Möglichkeiten für Variationen. So können neben den Halogeniden auf der X-Position eine Reihe von Übergangs- und Hauptgruppenmetallen die B-Position besetzen. Neben anorganischen Kationen wie Alkali- und Erdalkalimetallkationen können auch eine Reihe von organischen Kationen in die Kristallstruktur integriert werden. Hierdurch wird die Klasse der Hybrid-Halogenidometallate erschlossen. Im Folgenden soll anhand von $(CH_3NH_3)PbI_3$ auf die Vorteile dieser Verbindungsklasse eingegangen werden, bevor optoelektronische Eigenschaften sowie Stabilität und Toxizität diskutiert werden.[29]

Organisch-anorganische Hybridmaterialien

Als Hybridmaterial im Allgemeinen werden Verbindungen oder Materialien bezeichnet, die sich aus unterschiedlichen Komponenten zusammensetzen und deren nützliche Eigenschaften in einem neuen Material miteinander kombinieren. Einfache makroskopische Beispiele, in denen anorganische und organische Komponenten kombiniert werden sind sowohl in der Natur zu finden, z.B. im Zahnschmelz oder in Knochen, aber auch im Alltag. So ist z.B. Wandfarbe als Dispersion von anorganischen Pigmenten in organischen Lösungsmitteln ein Hybridmaterial im weiteren Sinne.[28,30]

Ist die Rede von Hybridmaterialien im chemischen Sinne, sind hiermit meist ionische Verbindungen gemeint, die ein organisches Kation mit einem anorganischen Anion kombinieren. Eigenschaften von anorganischen Verbindungen sind unter anderem eine hohe thermische Stabilität, sowie Magnetismus und eine hohe thermische Leitfähigkeit, während organische Verbindungen interessante optische Eigenschaften wie Photochromie, Lumineszenz oder nicht-lineare Optik zeigen können. Durch Kombination beider Verbindungsklassen in ionischen Hybridmetallaten können neue Materialien mit einer größeren Funktionalität zielgerichtet dargestellt werden.[31] Während in Hybrid-Perowskiten bislang nur einfache organische Kationen wie Methylammonium oder Formamidinium eingesetzt wurden, da größere Kationen mit einer zusätzlichen Funktionalität nicht mehr im Einklang mit dem *Goldschmidt*'schen Toleranzfaktor wären, eröffnet sich jenseits der Perowskitstruktur ein ganzes Feld von potentiellen neuen Materialien. Als Beispiel sind hier die Untersuchungen von *Guo* und Mitarbeitern zu nennen, die ein Chloridobismutat mit Methylviologenkationen als Gegenion darstellen konnten, welches ausgeprägte Photochromie von gelb zu schwarz nach Bestrahlung mit UV-Licht zeigt.[32,33] Hierbei kommt die Photochromie durch einen Charge-Transfer-Übergang von den Bismutatomen der $[Bi_2Cl_8]^{2-}_{\infty}$-Anionen auf das Methylviologen-Dikation zustande, welches zum Methylviologenradikalkation reduziert wird.

Optoelektronische Eigenschaften

Damit ein Material als Lichtabsorptionsschicht in Solarzellen eingesetzt werden kann, muss es bestimmte Voraussetzungen erfüllen. Ausschlaggebend ist hierbei, dass die Verbindung im passenden Wellenlängenbereich des elektromagnetischen Spektrums absorbiert und eine passende Bandlücke besitzt, da diese den Wirkungsgrad der Solarzellmodule wesentlich beeinflusst. Als Richtwert kann hier der von *Shockley* und *Queiser* postulierte Bereich zwischen 1,10 eV und 1,55 eV angenommen werden, für den eine maximale Effizienz erwartet wird.[34] Neben einer passenden Bandlücke ist auch der Absorptionskoeffizient entscheidend, da auch schlechte Absorber mit passenden Bandlücken nur wenig Effizienz erzielen. Hohe Absorptionskoeffizienten werden meist von Verbindungen mit direkter Bandlücke erzielt, weshalb diese Verbindungen bevorzugt sind.[35]

Für die für ein Iodidoplumbat ungewöhnlich kleine Bandlücke von 1,55 eV für $(CH_3NH_3)PbI_3$ lassen sich mehrere Ursachen finden. Die Verbindung kristallisiert in der kubischen Raumgruppe $Pm\bar{3}m$. *Yan* und Mitarbeiter konnten zeigen, dass die damit einhergehende hohe Symmetrie einen hohen Absorptionskoeffizienten und damit verbunden die ungewöhnlichen optoelektronischen Eigenschaften begünstigt. Die direkte Bandlücke kommt durch einen Übergang vom Valenz- ins Leitungsband zustande, wobei das Valenzband von I(5p) und Pb(6s) Orbitalen aufgebaut wird, während das Leitungsband von Pb(6p) Orbitalen dominiert wird.[36] Die $6s^2$-Elektronenkonfiguration des Pb^{2+}-Kations ist hierbei entscheidend. Starke antibindende Wechselwirkungen zwischen Pb(s)-I(p)-Zuständen und schwache Wechselwirkungen zwischen Pb(p)- und I(p)-Zuständen sowie der ionische Charakter der Verbindungen tragen zur geringen Anfälligkeit der Kristallstruktur für Defekte bei.[36] Durch die antibindenden Wechselwirkungen in der Nähe des Valenzbandmaximums treten Defekte eher in Nähe der Bandkanten auf. Dadurch tragen sie zur Langlebigkeit der angeregten elektronsichen Zustände und der getrennten Ladungsträger bei, da sie im Gegensatz zu tiefen Defekten nicht als Rekombinationszentrum dienen können.[35]

Des Weiteren bietet die Perowskitstruktur eine ungewöhnlich hohe Flexibilität, um durch unterschiedliche Elementkombination diese Eigenschaften zu verändern. So konnten *Mora-Sero* und Mitarbeiter durch schrittweise Dotierung von Bromid in $(CH_3NH_3)PbI_3$ die Absorptionskante zwischen 1,57 eV und 2,27 eV für steigenden Bromidgehalt variieren.[37]

Die Möglichkeit Verbindungen zu synthetisieren, die einen breiten Bereich des elektromagnetischen Spektrums abdecken können, macht halbleitende Metallate der schweren Hauptgruppenelemente auch für weitere Anwendungen interessant. Möglich sind Anwendungen in Lasern oder Feldeffekttransistoren, die von der Möglichkeit die Bandlücke durch Substitution des Hauptgruppenmetalls oder des Halogenids einzustellen, profitieren. *Zhu* und Mitarbeiter setzten $(CH_3NH_3)PbI_3$ erfolgreich als Lasermedium ein.[38] *Wu* und Mitarbeiter konnten ein ternäres Bromidobismutat, $[C_8H_9NH_3]_4[BiAgBr_8]$, als Feldeffektransistor-Material einsetzen.[39] Iodidoplumbate können starke Photolumineszenz zeigen, sodass eine Anwendung in LED's (light emitting diodes) möglich ist, wie *Bodnarchuk* und Mitarbeiter zusammenfassten.[40] Aufgrund der hohen Ordnungszahl, der guten Stabilität und der hohen Dichte können sowohl Blei- als auch Bismutverbindungen mit Perowskitstruktur in Detektoren für Röntgenstrahlung verwendet werden, wie *Huang* und *Tang* zeigen konnten. [41,42] Da eine Untersuchung aller Anwendungsgebiete den Rahmen dieser Arbeit überschreiten würde, wird der Fokus der folgenden Auslegungen auf einer Anwendung in der Photovoltaiktechnik liegen.

Stabilität und Toxizität

Trotz ihrer hervorragenden optoelektronischen Eigenschaften stehen der Kommerzialisierung von Blei-Perowskitsolarzellen auf Basis von $(CH_3NH_3)PbI_3$ zwei entscheidende Punkte entgegen. Der erste ist die Stabilität der Verbindungen. $(CH_3NH_3)PbI_3$ ist instabil gegenüber Feuchtigkeit, Licht und Wärme.[43] Auch wenn die Verbindung zu lange unter Luftatmosphäre gelagert wird, kommt es zu einer Zersetzung in Blei(II)iodid, Methylamin, Iod und Wasser, eingeleitet durch einen Elektronentransfer vom angeregten Bleiperowskit auf molekularen Sauerstoff auf der Oberfläche.[44] Die Empfindlichkeit gegenüber Wasser und Sauerstoff könnte durch eine Ummantelung der Module mit einer Schutzhülle umgangen werden. Ein wesentlich größeres Problem stellt allerdings die Empfindlichkeit gegenüber Licht und die geringe thermische Stabilität der Verbindung und im besonderen der organischen $(CH_3NH_3)^+$-Kationen dar, da ein Erhitzen der Zellen während ihrer Anwendung nicht vermieden werden kann.[7]

Ein weiterer kritischer Punkt ist die Verwendung von Blei, dessen Toxizität nicht zu vernachlässigen ist. Die Weltgesundheitsorganisation listet Blei als eine der zehn giftigsten Chemikalien für Mensch und Umwelt.[45] Blei schädigt das zentrale Nervensystem und kann dadurch zu Entwicklungsstörungen, neurologischen Schäden und Unfruchtbarkeit führen, weswegen es aus Farben, Benzin und Wasserleitungen zum großen Teil verbannt wurde.[46]

Cahen und Mitarbeiter simulierten ein Szenario in dem Regen auf Blei-Perowskitsolarzellen fällt, die ein beschädigtes *encasing* haben, um zu untersuchen wie viel Blei(II)iodid tatsächlich aus den Zellen herausgewaschen wird. Die Ergebnisse zeigten, dass die Menge vergleichbar gering ist, verglichen mit dem natürlichen Vorkommen von Blei im Erdboden. Vor dem Hintergrund der Toxizität und der Verbannung vieler bleihaltiger Materialien und Geräte aus dem Alltag sollte eine erneute kommerzielle Anwendung von Bleiverbindungen allerdings sorgfältig geprüft werden.[47] Nachdem gezeigt werden konnte, dass Perowskitsolarzellen sich mit der verbreiteten siliziumbasierten Technik messen können, rücken nun Umweltaspekte in den Vordergrund, die die Suche nach Verbindungen mit einer geringeren Toxizität als $(CH_3NH_3)PbI_3$ essenziell machen.[48]

1.1.3. Substitutionsmöglichkeiten für Pb^{2+}

Homovalente Substitution

Für die Substitution von Blei in Perowskitsolarzellen gibt es verschiedene Wege. Eine Reihe von Tetrelen, Erdalkali- und Übergangsmetallen bilden stabile zweiwertige Kationen, und eigenen sich somit für eine homovalente Substitution von Blei. Damit die Perowskitstruktur adaptiert werden kann, müssen allerdings einige Voraussetzungen erfüllt sein, wie etwa die Kriterien des *Goldschmidt*'schen Toleranzfaktors, sowie dass die Elementkationen von den Halogenidatomen oktaedrisch koordiniert werden können. Entscheidend hierfür ist unter anderem ein dem Pb^{2+}-Kation ähnlicher Ionenradius.
Vor dem Hintergrund einer potentiellen Anwendung in der Solartechnik rücken noch weitere Aspekte in den Fokus, wie etwa die Stabilität der Oxidationsstufe +2, eine ns^2-Elektronenkonfiguration, eine ausreichend niedrige Bandlücke und die Toxizität der Verbindungen.[49] Am naheliegendsten ist daher eine Substitution durch andere Gruppe 14 Elemente, wie Germanium oder Zinn.[50] *Snaith* und Mitarbeiter fertigten Solarzellmodule auf Basis der $(CH_3NH_3)PbI_3$ analogen Zinnverbindung $(CH_3NH_3)SnI_3$, welche eine Effizienz von 6,4% erreichten.[50] Für $(CH_3NH_3)SnI_3$ wurde eine Bandlücke von 1,2 eV ermittelt, welche 0,35 eV kleiner als die der analogen Bleiverbindung ist.[51] *Kanatzidis* und Mitarbeiter konnten des Weiteren zeigen, dass sich die optische Bandlücke in Verbindungen des Typs $(CH_3NH_3)SnI_{3-x}Br_x$ durch schrittweise Änderung des Bromidgehaltes einstellen lässt. Für x=0 konnten sie eine Effizienz von 5,23% ermitteln, die etwas unter dem von *Snaith* erhaltenen Wert liegt.[52] Auf Grund der Labilität der Oxidationsstufe +2 des Zinns zeigten beide Module allerdings nur eine geringe Stabilität an Luft und Licht, was eine Anwendung für die Solartechnik erschwert.
Eine Verbesserung der Stabilität kann durch Verringerung der Ausdehnung der Perowskitstruktur erreicht werden, wie *Yang* und Mitarbeiter schon für die Verbindung $(C_4H_9NH_3)_2PbBr_4$ zeigen konnten.[53] Die Arbeitsgruppe um *Kanatzidis* berichtete über eine Reihe von Hybrid-Iodidostannaten, die eine *Ruddlesden-Popper* Struktur aufweisen. Die Verbindungen der allgemeinen Zusammensetzung $(CH_3(CH_2)_3NH_3)_2(CH_3NH_3)_{n-1}Sn_nI_{3n+1}$ weisen besonders für n=4 in gefertigten Solarzellemodulen eine deutlich gesteigerte Stabilität im Vergleich zu $(CH_3NH_3)SnI_3$ auf.[54]

Heterovalente Substitution

Eine weitere Möglichkeit zur Substitution von Blei in umweltfreundlicher Solartechnik ist die heterovalente Substitution mit Metallkationen anderer Valenzen.[49] Hier sind besonders Halogenidverbindungen des Bismuts in den Fokus gerückt, da Bi^{3+}-Verbindungen nicht nur ausgesprochen stabil sind, sondern auch eine $6s^2$-Elektronenkonfiguration und einen ähnlichen Ionenradius wie Pb^{2+} bei geringer Toxizität aufweisen. Eine direkte Substitution unter Beibehaltung der Perowskitstruktur ist auf Grund der unterschiedlichen

Valenzen von Pb^{2+} und Bi^{3+} hierbei nicht möglich. Resultierende Verbindungen kristallisieren mit molekularen oder eindimensionalen Anionen, oder als Defekt-Perowskite mit Leerstellen in der Gitterstruktur. Beispielhaft dafür stehen Verbindungen der Klasse $A_3Bi_2I_9$ ($A = K^+$, Rb^+, NH_4^+, Cs^+, $CH_3NH_3^+$). Die Verbindungen können mit zwei Anionenmotiven kristallisieren. Mit den kleineren Kationen K^+, Rb^+ und NH_4^+ werden Verbindungen mit schichtartigem Anion erhalten. Die Schichten bestehen aus eckenverknüpften $\{BiI_6\}$-Oktaedern, die eine zick-zack Schicht ausbilden. Die Struktur entspricht der des in Abbildung 1.2 e) dargestellten Perowskits mit Leerstellen, $Cs_3Sb_2I_9$, in dem die M^{3+}-Atome jeder dritten Oktaederschicht entlang der kristllographischen <111>-Richtung entfernt wurden.[22,55] Mit den größeren Kationen Cs^+ und $CH_3NH_3^+$ werden Verbindungen erhalten, welche im $Cs_3Cr_2Cl_9$-Typ kristallisieren.[56] Im Gegensatz zum oben beschriebenen Perowksit mit Leerstellen liegen hier keine ecken- sondern flächenverknüpfte Koordinationspolyeder vor, sodass isolierte $[Bi_2I_9]^{3-}$-Einheiten zu finden sind. Die Verbindungen sind auf Grund ihrer hohen Stabilität an Luft vielversprechend, zeigten in photovoltaischen Bauelementen aber nur eine Effizienz von maximal 1-3 %.[56,57,58] Dieser geringe Wert kann auf eine zu geringe Exzitonen-Dynamik und eine zu große Bandlücke zwischen 1,9 eV und 2,2 eV zurückgeführt werden.[57,59]

Diese beiden Faktoren können beeinflusst werden, indem man die anionische Struktur ausdehnt. Für Verbindungen mit netzwerkartigen Anionen werden auf Grund des ausgedehnteren Systems niedrigere Bandlücken und größere Exzitonen-Dynamiken erwartet.[7] Eine Möglichkeit anionische Netzwerke auf Basis von Bismut und Antimon zu erhalten, ist eine Erweiterung hin zu Verbindungen mit ternären Anionen, in dem man formal zwei Pb^{2+}-Kationen durch ein trivalentes und ein monovalentes Kation ersetzt. Einige Beispiele sind in Abbildung 1.5 dargestellt.

Cheetham und Mitarbeitern gelang die Darstellung des Elpasoliths $[CH_3NH_3]_2[AgBiBr_6]$ (Abb. 1.5 a)).[60] Die Verbindung weist eine indirekte Bandlücke von 2.0 eV auf, welche 0,2 eV kleiner als die der analogen Brom-Blei-Verbindung $[CH_3NH_3][PbBr_3]$ ist.[64] In photovoltaischen Bauelementen konnte die Verbindung jedoch nur Effizienzen von 1-3 % erreichen, wobei ihr größtes Hindernis die zu große Bandlücke ist.[65]

Karunadasa und Mitarbeiter konnten unter Verwendung von Butylammoniumkationen verschiedene Bromidobismutate erhalten, deren Anionen Ausschnitte aus der Elpasolithstruktur mit unterschiedlicher Schichtdicke darstellen. Quantenchemische Rechnungen ergaben, dass die indirekte Bandlücke des Elpasoliths $Cs_2AgBiBr_6$ durch dimensionale Reduktion der anorganischen Einheit auf Monolagen-Dicke, wie in $[BA]_4[BiAgBr_8]$ (Abb. 1.5 c)) zu einer direkten Bandlücke übergeht.[61]

Dieses Ergebnis motivierte die weitere Erforschung von Halogenidobismutaten mit Schichtstruktur. Neben der Ausdehnung des Anions hat auch die verwendete Elementkombination einen Einfluss auf die Beschaffenheit der Bandlücke. Quantenchemische Studien von *Snaith* und Mitarbeitern zu Edelmetall-Pnictogen-Elpasolithen zeigten, dass die Element-

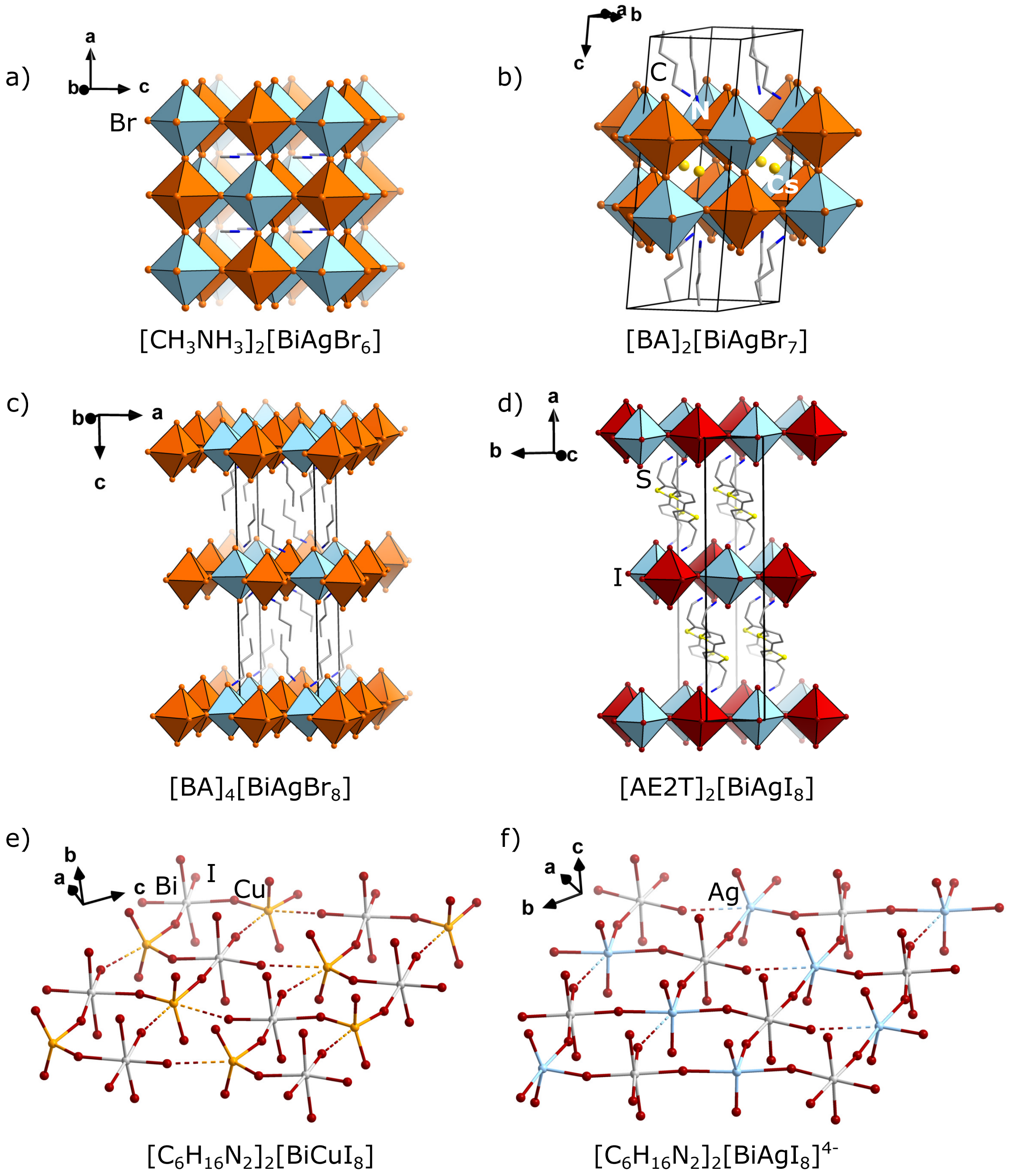

a) $[CH_3NH_3]_2[BiAgBr_6]$ b) $[BA]_2[BiAgBr_7]$ c) $[BA]_4[BiAgBr_8]$ d) $[AE2T]_2[BiAgI_8]$ e) $[C_6H_{16}N_2]_2[BiCuI_8]$ f) $[C_6H_{16}N_2]_2[BiAgI_8]^{4-}$

Abbildung 1.5: Verschiedene Halogenidobismutate mit ternärem Anion, dessen Struktur von der Elpasolithstruktur abgeleitet werden kann. $\{BiBr_6\}$-Oktaeder sind orange, $\{BiI_6\}$-Oktaeder rot, $\{AgBr_6\}$- und $\{AgI_6\}$-Oktaeder hellblau dargestellt: a) $[CH_3NH_3]_2[BiAgBr_6]$,[60] b) $[BA]_2Cs[BiAgBr_7]$ ($BA{=}CH_3(CH_2)_3NH_3$),[61] c) $[BA]_4[BiAgBr_8]$,[61] d) $[AE2T]_2[BiAgI_8]$ (AE2T=5,5′-diylbis(aminoethyl)-[2,2′-bithiophene]),[62] e) $[C_6H_{16}N_2]_2[BiCuI_8]\cdot 0.5H_2O$,[63] f) $[C_6H_{16}N_2]_2[BiAgI_8]\cdot 0.5H_2O$.[63]

kombination Bi-Cu-I die vielversprechendste Bandlücke von 1.6 eV erwarten lässt.[66] Bis dato konnten jedoch keine Elpasolithe dieser Elementkombination beobachtet werden. *Mitzi* und Mitarbeiter führten dies auf den kleinen Ionenradius des Cu^+-Kations zurück, weswegen es eine tetraedrische Koordination gegenüber der für Elpasolithe notwendigen oktaedrischen Koordination bevorzugt.[67] Silberkationen können auf Grund ihres größeren Ionenradius oktaedrisch koordiniert werden, eine Verbindung mit Elpasolithstruktur

vom Typ $[CH_3NH_3]_2[AgBiI_6]$ ist bisher aber noch nicht zugänglich, da die Bildung von konkurrierenden binären Bismutaten bevorzugt ist. *Mitzi* und Mitarbeiter konnten unter Verwendung eines Oligothiophens ein ternäres Silber-Iodidobismutat darstellen, dessen schichtartiges Anion einen Ausschnitt aus der Elpasolithstruktur darstellt.[62] Der Arbeitsgruppe um *Zheng* gelang die Synthese eines ternären Kupfer-Iodidobismutats, dessen Struktur ebenfalls von der Elpasolithstruktur abgeleitet werden kann. Aufgrund der Koordinationsumgebung des Kupfers, welche sehr stark verzerrt oktaedrisch ist, sollte hier allerdings besser von strangartigen Anionen geredet werden.[63]
Eine Auswahl der bereits untersuchten Gruppe-15-Verbindungen ist in Tabelle 1.1 aufgeführt. Hierbei werden nur die bisher diskutierten Strukturmotive und zu ihnen isostrukturelle Verbindungen mit anderer Elementkombination erwähnt.

Tabelle 1.1: Optische Bandlücken und Effizienzen einiger ausgewählter Halogenidoantimonate und -bismutate.

Material	Bandlücke [eV]	Effizienz [%]	Struktur
$Rb_3Sb_2I_9$[68]	2,1	0,66	Perowskit mit Leerstellen
$Cs_3Sb_2I_9$[69]	2,05	<0,1	Perowskit mit Leerstellen
$(CH_3NH_3)Sb_2I_9$[70]	2,14	0,49	
$Cs_3Bi_2I_9$[71]	2,03	1,09	diskrete Anionen
$(CH_3NH_3)Bi_2I_9$[58]	2,1	3,17	
$[CH_3NH_3]_2[AgBiBr_6]$[60]	2,0	-	Elpasolith
$[AE2T]_2AgBiI_8$[62]	2,0	-	ternäres Metallat

Aus Tabelle 1.1 wird deutlich, dass sowohl im Bezug auf die optische Bandlücke als auch auf die Effizienz der angestrebten Module, die Elementkombination Bismut-Iod die vielversprechendste zu sein scheint. Selbst diese Verbindungen weisen allerdings eine Bandlücke weitab des von *Shockley* und *Queiser* postulierten Bereichs auf, und können somit nur sehr geringe Effizienzen erzielen. Die strengen strukturellen Vorgaben an Perowskite und perowskitverwandte Strukturen gehen mit einer limitierten Anzahl möglicher Strukturmotive einher. Da Halogenidoantimonate und -bismutate für ihre strukturelle Vielfalt bekannt sind, sollten auch Verbindungen abseits der Perowskitstruktur auf ihre optischen Eigenschaften untersucht werden. Im Folgenden wird deshalb auf grundlegende und erweiterte Strukturmotive der Halogenidoantimonate und -bismutate, Synthesewege und Variationsmöglichkeiten eingegangen. Neben der Möglichkeit andere Metallkationen in die Elpasolithstruktur einzubinden, besteht auch die Möglichkeit die Struktur mit einem anderen Metall zu dotieren. *Karunadasa* und *Mitzi* gelang es die Ausgangsverbindung $Cs_2[AgBiBr_6]$ mit Tl^{3+}- beziehungsweise Sb^{3+}-Kationen zu dotieren, wodurch ebenfalls eine Reduktion der Bandlücke erreicht wurde.[72,73]

1.2. Halogenidoantimonate und -bismutate

Iodidometallate des Bismuts und Antimons können lumineszieren, sowie nicht lineare optische und Halbleitereigenschaften aufweisen.[74] Das macht sie für die Materialwissenschaften interessant. Des Weiteren sind sie meist luftstabil und bei Raumtemperatur zugänglich, was sie besonders interessant für technische Anwendungen macht.[75] Neben der bereits erwähnten Photovoltaik-Technik ist zum Beispiel eine Anwendung in LEDs oder Lasern denkbar.[76] Nichtsdestotrotz bleibt die Vorhersage und gezielte Synthese spezifischer Strukturen schwierig. Konzepte, die erfolgreich auf andere Hybridmaterialien angewandt wurden, wie die Verwendung von Prekusor-Einheiten um die Synthese des gewünschten Produktes zu steuern, können nicht auf Iodidometallate der Pentele angewandt werden. Grund hierfür ist die Labilität der Bindung zwischen Halogenid- und Pentelatom, die schnellen Dissoziations- und Assoziationsprozessen in Lösung unterliegen.[77] Da halbleitende und andere optoelektronischen Eigenschaften mit der Größe der anorganischen Einheit wachsen, ist die Kontrolle ihrer Struktur und Ausdehnung essenziell.

1.2.1. Grundlegende Strukturmotive

Halogenidoantimonate und -bismutate können aus den Elementtrihalogeniden durch Reaktion mit den Halogenwasserstoffen HX, z.B. in konzentrierter wässriger Lösung, oder durch Umsetzung mit anderen Halogeniden des Typs AX in organischen Lösungsmitteln erhalten werden. Hierbei kann A sowohl ein anorganisches Salz (NaI, KI, CsI, CuI) als auch eine organische Verbindung (PPh_4I, NH_4I, $N(CH_3)_4I$) sein.[78] Charakteristisch für die Substanzklasse ist ihre strukturelle Vielfalt. So können bei gleicher Zusammensetzung $[E^{15}_mX_n]^{p-}$ oft mehrere Strukturmotive erhalten werden. Als Beispiel seien hierbei die Anionen der Zusammensetzung $[Sb_6I_{22}]^{4-}$ zu nennen, die mit unterschiedlichen Kationen in vier verschiedenen Modifikationen auftreten können.[79,80,81] Als strukturdirigierende Faktoren können die Stöchiometrie der Edukte, die Wahl des Halogenids oder der räumliche Anspruch der Kationen dienen. Im Folgenden sollen die häufigsten Strukturmotive der Halogenidopentelate vorgestellt werden.

Einkernige Komplexanionen

Durch formale Addition von ein, zwei oder drei Halogenidliganden an die Elementtrihalogenide $E^{15}X_3$ können die einkernigen Komplexanionen mit der allgemeinen Formel $[E^{15}X_{3+n}]^{n-}$ erhalten werden, wobei n die Werte eins bis drei annehmen kann. Das einfachste dieser Komplexanionen ist $[EX_4]^-$, welches pseudo-trigonal bipyramidal aufgebaut ist, wobei die dritte Ecke der trigonalen Pyramidenbasis vom freien Elektronenpaar des Gruppe 15 Elements gebildet wird. Für die schweren Pentelelemente tritt dieses Strukturmotiv nicht diskret, sondern nur als Dimer oder Polymer auf, auf welche später eingegangen wird. Jedoch sind für Phosphor mehrere Verbindungen mit diskretem $[PX_4]^-$-Anion bekannt. Durch Addition von zwei Halogenidliganden an die Elementtrihalogenide wird das Anion $[\mathrm{EX}_5]^{2-}$ erhalten, welches eine quadratisch pyramidale Struktur aufweist. Hierbei weist das freie Elektronenpaar des Pentelatoms unter die Pyramidenbasis, sodass die Struktur auch als pseudo-oktaedrisch beschrieben werden kann. Auch dieses Strukturmotiv wird häufiger bei den leichteren Homologen der Pentele gefunden, tritt aber zum Beispiel auch in $[\mathrm{NH}_4]_2[\mathrm{SbCl}_5]$ auf. Durch Addition von drei Halogenidliganden wird letztlich das häufigste Strukturmotiv der Halogenidoantimonate und -bismutate, das $[\mathrm{EX}_6]^{3-}$-Oktaeder, erhalten.[82]

Mehrkernige Komplexanionen

Durch Verknüpfung der einkernigen Komplexanionen über gemeinsame Ecken, Kanten oder Flächen können die mehrkernigen Komplexanionen erhalten werden. In Abbildung 1.6 sind die zweikernigen Strukturmotive der Halogenidoantimonate und -bismutate, sowie die Häufigkeit der einzelnen Elementkombinationen dargestellt.

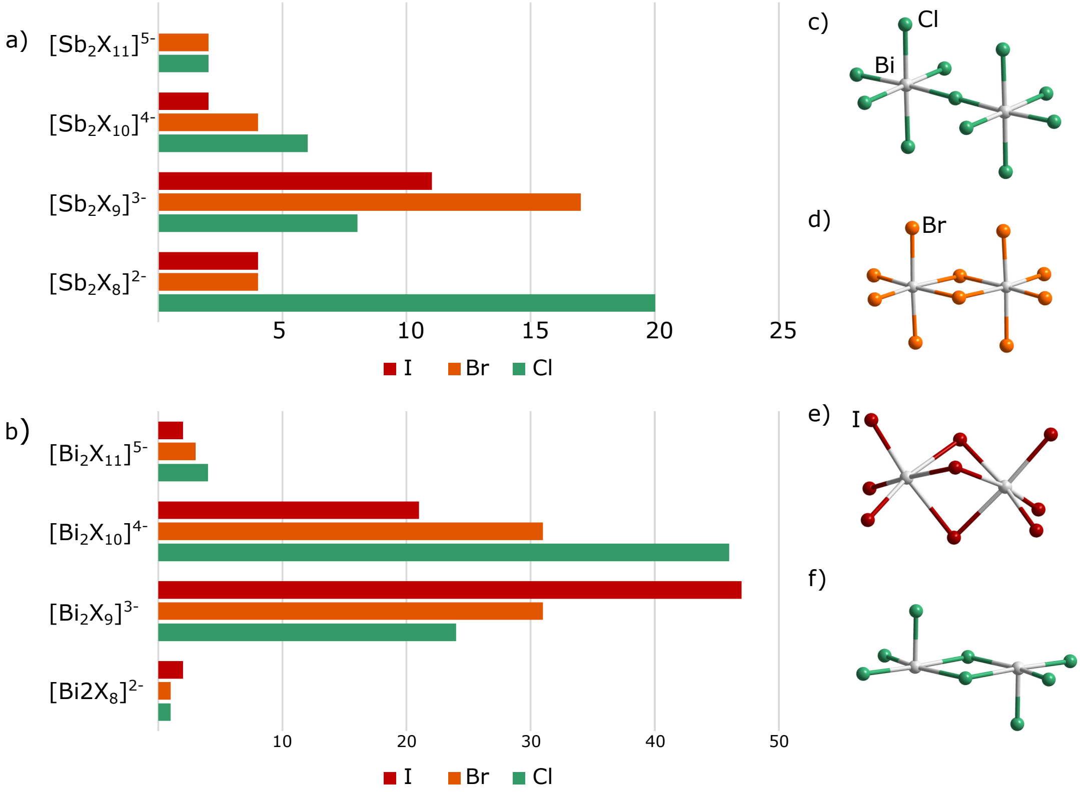

Abbildung 1.6: Häufigkeiten der zweikernigen Komplexanionen von: a) Antimon und b) Bismut (Daten aus der *Cambridge Structural Database*[83], abgerufen am 30.06.2020). Darstellung der zweikernigen Komplexanionen in: c) $[\mathrm{ImH}]_5[\mathrm{Bi}_2\mathrm{Cl}_{11}]$ (Im=Imidazol),[84] d) [4-4′$\mathrm{BipyH}_2]_2[\mathrm{Bi}_2\mathrm{Br}_{10}]$,[85] e) $[\mathrm{PPh}_4]_3[\mathrm{Bi}_2\mathrm{I}_9]\cdot\mathrm{CH}_2\mathrm{Cl}_2$,[86] f) $[\mathrm{BiC}_{l2}\cdot$ 18-Krone-6$]_2[\mathrm{Bi}_2\mathrm{Cl}_8]$.[87]

Auf den ersten Blick fällt auf, dass deutlich mehr Bismutate als Antimonate bekannt sind. Als häufigste Strukturmotive sind hierbei das $[\mathrm{E}^{15}_2\mathrm{X}_9]^{3-}$-Anion zu nennen, welches aus zwei flächenverknüpften $\{E^{15}X_6\}$-Oktaedern aufgebaut wird, sowie das $[E^{15}_2X_{10}]^{4-}$-Anion, welches aus zwei kantenverknüpften $\{E^{15}X_6\}$-Oktaedern besteht. Die eckenverknüpfte Variante $[E^{15}_2X_{11}]^{5-}$ tritt für Antimonate und Bismutate diskret nur sehr selten auf und wird häufiger als Polymer in Form eindimensionaler Stränge gefunden. Auffällig ist die Häufigkeit des $[E^{15}_2X_8]^{2-}$-Anions. Dieses wird nicht wie die anderen zweikernigen Komplexanion vom $\{E^{15}X_6\}$-Oktaeder, sondern von dem quadratisch pyramidalen $\{E^{15}X_5\}$ abgeleitet. Über eine Kantenverknüpfung von zwei dieser Bausteine in *trans*-Geometrie wird das erwähnte zweikernige Komplexanion erhalten, welches besonders häufig für die Elementkombination Antimon-Chlor anzutreffen ist.

1.2.2. Erweiterte Strukturmotive

Mehrkernige Komplexanionen und Trends

Durch formale Addition weiterer neutraler $\{E^{15}X_3\}$-Einheiten an die zweikernigen Komplexanionen können mehrkernige Komplexanionen erhalten werden, wobei der Verbrückungsgrad der Einheiten und die Ausdehnung der gebildeten Anionen stark variieren kann. Drei representative Beispiele sind in Abbildung 1.7 dargestellt.

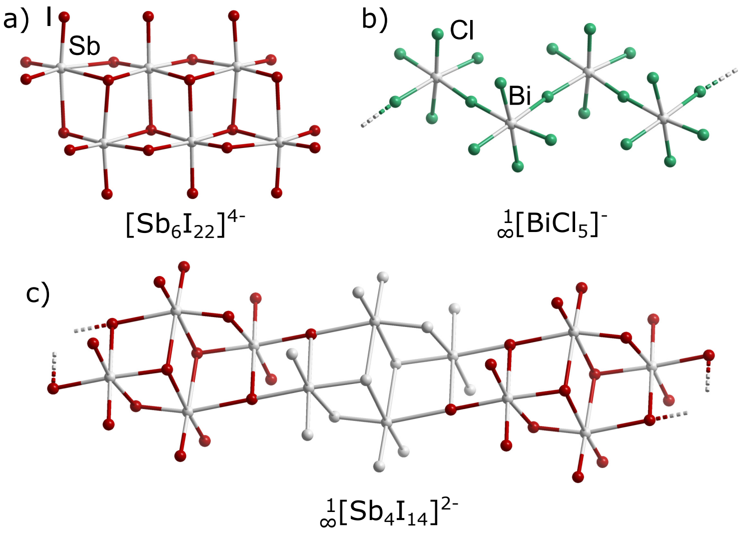

Abbildung 1.7: Ausschnitte aus den Kristallstrukturen einiger Halogenidopentelate mit mehrkernigem Komplexanion: a) $[Cp_2Fe]_4[Sb_6I_{22}]$,[80] b) $[NH_2(C_2H_4)_2O][BiCl_5]$,[88] c) $[C_{10}H_{16}N]_2[Sb_4I_{14}]$.[89]

Möglich sind sowohl diskrete Anionen, wie im $[Cp_2Fe]_4[Sb_6I_{22}]$,[90] einfache eindimensionale Stränge wie in $[NH_2(C_2H_4)_2O][BiCl_5]$[88] oder komplexere Stränge, die aus der Verknüpfung größerer diskreter Einheiten miteinander hervorgehen, wie in $[C_{10}H_{16}N]_2[Sb_4I_{14}]$.[89] Letzteres lässt sich eher für Iodidoantimonate und -bismutate finden, während für die leichteren Halogene eher Ketten aus kanten- oder eckenverknüpften Oktaedern auftreten. Des Weiteren werden für die leichteren Chlorido- und Bromidometallate häufiger

Verzerrungen der Koordinationspolyeder beobachtet, während die Iodidometallate meist unverzerrte Oktaeder aufweisen.[82]
Dieser Trend lässt sich auf einen unterschiedlichen stereochemischen Einfluss des freien Elektronenpaars am Pentelatom zurückführen. Nimmt man das VSEPR-Modell als Grundlage, wird für ein :ZL_6-Fragment mit einem freien Elektronenpaar ein überkapptes Oktaeder als Koordinationspolyeder angenommen. Mit steigender Elektronegativität der Liganden L kommt es zunehmend zu einer Verzerrung der O_h-Symmetrie zu einer C_{3v}-Symmetrie. Das freie nichtbindende Elektronenpaar hat laut VSEPR-Modell einen höheren sterischen Anspruch als ein bindendes Elektronenpaar, da es nur von einem positiven Atomrumpf angezogen wird. Im $\{BiI_6\}$ haben die großen wenig elektronegativen Iodidatome einen großen räumlichen Anspruch. Das freie Elektronenpaar ist somit wegen Platzmangels in der Ligandenhülle am Bismutatom lokalisiert und hat den Charakter eines „inerten“ s-Elektronenpaars. Die Chloridatome im $\{BiCl_6\}$ sind deutlich elektronegativer und kleiner als Iodidatome. Somit findet sich in der Ligandenhülle mehr Platz für das freie Elektronenpaar, welches sich mit größtmöglichem Abstand zu den Chloridatomen zu einer Fläche der oktaedrischen Koordinationssphäre ausrichtet. Durch gegenseitige Abstoßung zwischen den Bi-Cl-Bindungen und dem nichtbindenden Elektronenpaar am Bismutatom kommt es zu einer Aufweitung des entsprechenden Winkels, welche ebenfalls mit einer Aufweitung der von der Verzerrung betroffenen Atomabstände einhergeht.[78]

Ternäre Komplexanionen mit Heterometallatomen

Wie bereits in Abschnitt 1.2.1. diskutiert, kann die Einführung von Heterometallatomen in die Struktur von Halogenidobismutaten die Größe der optischen Bandlücke beeinflussen. Während die binären Bismutate eine große Strukturvielfalt zeigen, waren für Iodidobismutate mit ternärem Anion zu Beginn dieser Arbeit nur 14 Verbindungen, und für Iodidoantimonate mit ternärem Anion keine Verbindung bekannt. Ausschnitte aus den Kristallstrukturen sind in Abbildung 1.8 dargestellt.

Feldmann konnte die erste quarternäre Verbindung, welche aus eindimensionalen $[CuBi_5I_{19}]^{3-}$-Ketten besteht, bereits 2001 darstellen.[97] Eine Reihe von Heterometall-Iodidobismutaten konnten von der Arbeitsgruppe *Chen* in 2007 dargestellt werden. Sie berichteten über zwei polymere Silberbismutate, in welchen $[AgI_4]$-Tetraeder als Bindeglied zwischen $[Bi_xI_y]$-Einheiten agieren. Eine Reduktion der Bandlücke von 2,05 eV im eindimensionalen, strangartigem $[NEt_4]_{2n}[Bi_2Ag_2I_{10}]_n$ zu 1,93 eV im zweidimensionalen, netzartigem $[NEt_4]_{2n}[Bi_4Ag_2I_{16}]_n$ bestätigt die Korrelation zwischen den optoelektronischen Eigenschaften und der Dimensionalität des Anions.[96] Nichtsdestotrotz konnte *Chen* keine Hinweise finden, welche Parameter die Größe und Dimensionalität der anorganischen Einheit beeinflussen, da beide Verbindungen unter vergleichbaren solvothermalen Bedingungen dargestellt wurden. Auch die analoge Kupferverbindung zur bereits erwähn-

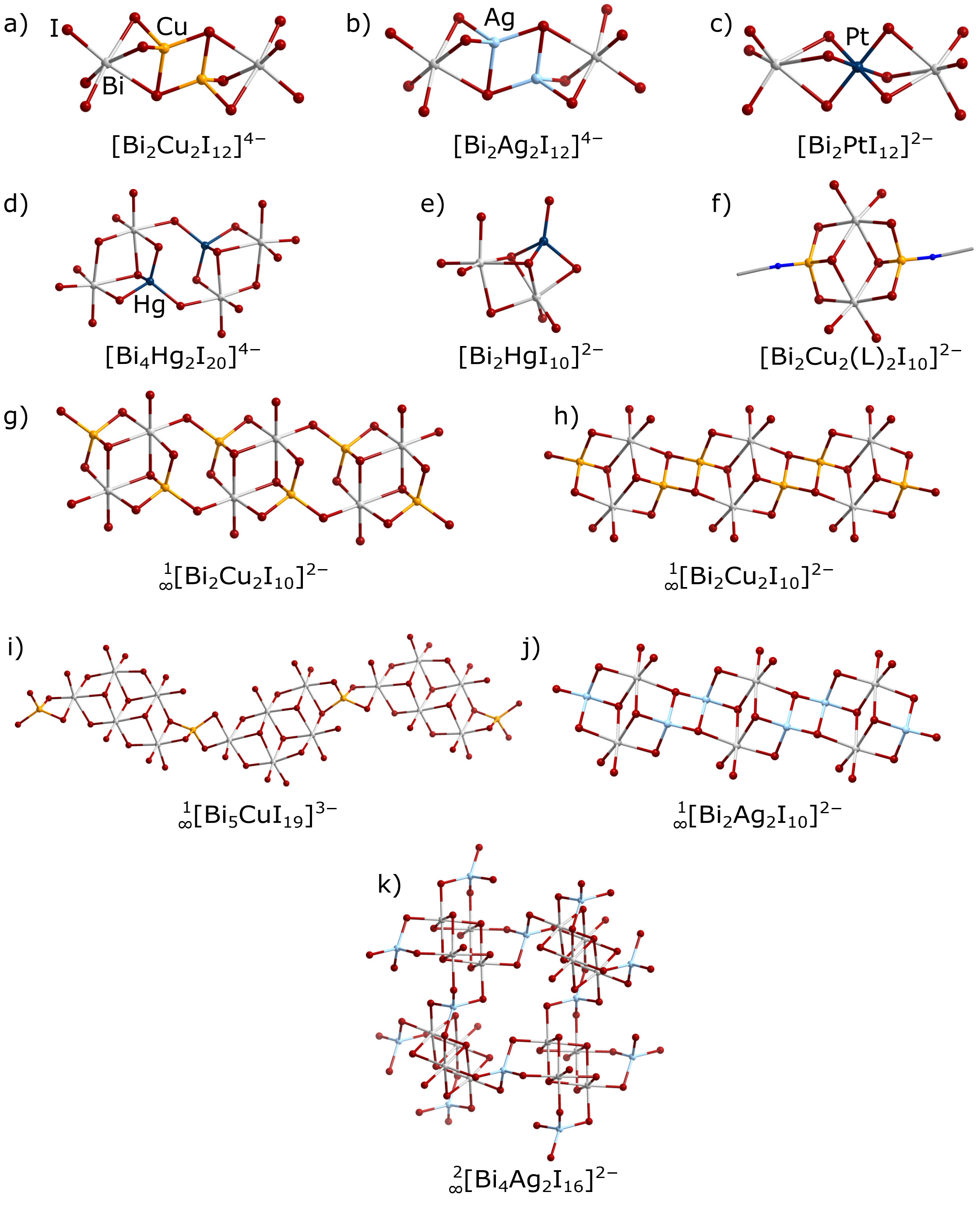

Abbildung 1.8: Ausschnitte aus den Kristallstrukturen der zu Beginn dieser Arbeit bekannten Iodidobismutate mit ternärem Anion: a) $[PPh_4]_4[Bi_2Cu_2I_{10}]$,[91] b) $[PPh_4]_4[Bi_2Ag_2I_{10}]$,[91] c) $[Na_4((CH_3)_2CO)_{15}][PtBi_2I_{12}]\cdot 3(CH_3)_2CO$, [92] d) $[NEt_4]_4[Bi_4Hg_2I_{20}]$,[93] e) $(N\textit{n}\text{-}Bu_4)_2[Bi_2HgI_{10}]$,[93] f) $[N\textit{n}\text{-}Bu_4][Cu_2(CH_3CN)_2Bi_2I_{10}]$,[94] g) $[Cu(CH_3CN)_4]_{2n}[Cu_2Bi_2I_{10}]_n$,[94] h) $[NEt_4]_{2n}[Cu_2Bi_2I_{10}]_n$,[94] i) $CuBi_7I_{19}(C_4H_8O_3H)_3(C_4H_8O_3H_2)$,[95] j) $[NEt_4]_{2n}[Bi_2Ag_2I_{10}]_n$,[96] k) $[NEt_4]_{2n}[Bi_4Ag_2I_{16}]_n$.[96]

ten Silberverbindung, $[NEt_4]_{2n}[Bi_2Cu_2I_{10}]_n$, konnte von *Chen* dargestellt werden.[94] Die Bandlücke konnte zu 1,89 eV ermittelt werden und ist somit kleiner als die Bandlücke der isostrukturellen Silberverbindung. Zusammenfassend zeigen die Ergebnisse einen positiven Einfluss von Kupferatomen und höherdimensionalen Netzwerken auf die optoelektronischen Eigenschaften von Iodidobismutaten in Hybridverbindungen. Weitere Untersuchungen in Richtung dreidimensionaler quarternärer Verbindungen sind somit vielversprechend.

Neben den Elementen der Kupfergruppe sind auch andere elektronenreiche Übergangsmetalle, wie die der Nickel- und Zinkgruppe vielversprechend. Ausschlaggebend ist hier die Tatsache, dass diese Übergangsmetallkationen von Halogenidliganden komplexiert werden können. Die elektronenärmeren Übergangsmetalle, wie Titan oder Mangan, kommen zwar auch in Perowskiten vor, können jedoch nicht von Halogenidatomen koordiniert werden, weswegen diese Elemente nur oxidische Perowskite ausbilden. *Sokolov* und Mitarbeitern gelang die Darstellung eines Platin-Iodidobismutats, in dem Platin eine ungewöhnliche oktaedrische Koordinationsumgebung aufweist.[92] *Chen* und Mitarbeiter berichteten über zwei Quecksilber-Iodidobismutate.[93] Die Ergebnisse zeigen, dass eine Synthese von Gruppe 10 und 12 Iodidobismutaten möglich ist.

Templatwirkung organischer Kationen

Mercier und Mitarbeiter konnten zeigen, dass die Verwendung von Verbindungen mit Kationen, die gerichtete intermolekulare Wechselwirkungen mit der anorganischen Einheit eingehen können, eine gewisse Kontrolle über die Dimensionalität des gebildeten Anions gewährleisten. In Hybrid-Iodidometallaten sind zwei Arten von intermolekularen Wechselwirkungen zwischen den Kationen möglich: Wasserstoffbrückenbindungen, wenn die organischen Kationen polare Kopfgruppen aufweisen, wie zum Beispiel Benzylammonium- oder Sulfoniumkationen, und π-π-Wechselwirkungen, wenn sie ein aromatisches Ringsystem aufweisen. Diese Wechselwirkungen können eine gezielte Packung der Kationen ermöglichen, wodurch die Verteilung der positiven Ladung gelenkt wird, was einen Templateffekt auf die Struktur des Anions ausübt. Ein Beispiel hierfür sind Wasserstoffbrückenbindungen in [L-Cystin][BiI_4], welches ein eindimensionales strangartiges Anion aufweist.[98] *Papavassilou* und Mitarbeiter berichteten bereits 1995 über ein Chloridobismutat, in dem Phenethylammoniumkationen die Bildung von Schichten begünstigen, in denen Kationen und Anionen voneinander getrennt sind. Hierbei arrangieren sich die Kationen so, dass die unpolaren Benzylringe von zwei benachbarten Schichten zueinander ausgerichtet sind, während die polaren Ammoniumgruppen in Richtung der Anionen weisen.[99]

Zu den neueren Ergebnissen, welche parallel zu dieser Arbeit entstanden, gehören ebenfalls die in Abbildung 1.5 b) bis f) dargestellten Verbindungen. Durch Verwendung eines Oligothiophen-Kations konnten *Mitzi* und Mitarbeiter ein ternäres Silber-Iodidobismutat darstellen, dessen schichtartiges Anion einen Ausschnitt aus der Elpasolithstruktur darstellt. Die Elementkombination Bismut und Iod lässt darüber hinaus eine niedrige Bandlücke erwarten. Die Synthese einer Verbindung dieser Elementkombination und Struktur war lange erfolglos, da die Konkurrenz zur Bildung von binären Bimutaten zu groß war.

Die Oligothiophen-Kationen weisen einen starken strukturdirigierenden Effekt auf, der schließlich die Bildung der Schichtstruktur templierte.[62]
Durch Verwendung von Butylammoniumkationen konnten *Karunadasa* und Mitarbeiter zeigen, dass formale „Schnitte“ durch die Elpasolithstruktur möglich sind, indem in der Synthese das Cs^+-Kation ganz oder teilweise durch Butylammoniumkationen ersetzt wird. Ausschnitte aus den Kristallstrukturen sind in Abbildung 1.5 b) und c) dargestellt. Für die Verbindung $[BA]_4[BiAgBr_8]$, welche Anionen mit einer Schichtdicke von n = 1 aufweist, konnte über quantenchemische Rechnungen eine direkte Bandlücke gefunden werden.[61] Für den Elpasolith $[CH_3NH_3][BiAgBr_6]$, der formal eine Schichtsicke von $n = \infty$ aufweist konnte eine indirekte Bandlücke von 2,0 eV bestimmt werden.[60]

Abschließend können zwei Faktoren zusammengefasst werden, die die Darstellung von Halogenidobismutaten und -antimonaten mit einer passenden Bandlücke für Anwendungen in der Photovoltaiktechnik ermöglichen. Zum einen ist die Elementkombination entscheidend, wobei die Iodidometallate gegenüber den leichteren Halogeniden aufgrund ihrer niedrigeren Bandlücke bevorzugt sind. Die Einbindung von Übergangsmetallkationen in die Anionenstruktur kann die Bandlücke zusätzlich senken. Zum anderen kann die Dimensionalität des Anions einen Einfluss auf die Bandlücke haben. Hierbei ist sie sowohl für die Größe der Bandlücke entscheidend, als auch für ihren direkten oder indirekten Charakter. Im Hinblick auf eine potentielle Anwendung ist die Darstellung von Metallaten mit Schichtstruktur, die auch in Dünnfilm-Elementen angewendet werden können, somit besonders interessant. Diese Ergebnisse motivierten die Forschungsfrage dieser Dissertation, die im folgenden Kapitel näher erläutert wird.

Motivation 2

Komplexe Halogenidoantimonate und -bismutate sind im Gegensatz zu den in der Einleitung vorgestellten Elpasoliten und perowskit-verwandten Metallaten nur wenig erforscht. Da die Halogenidopentelatanionen eine Vielzahl verschiedener Strukturen bilden können, die sich in der Art und Zahl der verknüpften Koordinationspolyeder unterscheiden, sollten hier eine große Zahl weiterer Verbindungen zugänglich sein. Bereits während meines Masterstudiums konnten wir den Einfluss von Münzmetallkationen auf die optischen und elektronischen Eigenschaften multinärer Iodidobismutate untersuchen. In meiner Masterarbeit konnte ich zeigen, dass sich dieses Reaktionssystem auch auf das leichtere Homologe Antimon übertragen lässt. Diese Untersuchungen zeigten bereits die strukturelle Vielfalt des Systems, machten aber auch deutlich, wie wenig bisher über Bildungsmechanismen und Eigenschaften der Materialklasse bekannt ist. Die Untersuchungen dieser Doktorarbeit sollen die bisher wenig erforschte Materialklasse um neue Verbindungen erweitern, und somit einen Beitrag zur Suche nach Substitutionsverbindungen für Iodidoplumbate in Hybrid-Perowskitsolarzellen leisten. In Anlehnung an die Erfolge der Bleihalogenid-Perowskit-Chemie ergaben sich für die geplanten Untersuchungen zwei Forschungsziele:

1. *Darstellung multinärer Halogenidoantimonate und -bismutate durch Einbindung von Übergangsmetallatomen in die Anionenstruktur.*

   Hierfür sollte zunächst der Einfluss unterschiedlicher Heterometallkationen auf die optischen Eigenschaften quarternärer Iodidobismutate und -antimonate untersucht werden. Der Fokus sollte hierbei auf den Metallen der Kupfergruppe liegen. Durch die zu erhaltenden Verbindungen können neue Erkenntnisse zum Einfluss von Heterometallkationen auf die Bindungssituation und die elektronischen Eigenschaften in Iodidopentelaten erhalten werden.

2. *Etablierung von Halogenidoantimonaten und -bismutaten als 2D-Materialien.*

   Durch die Verwendung von amphiphilen Kationen, wie etwa primären Ammoniumkationen, kann ein dirigierender Effekt der Kationen auf die Anionenstruktur ausgeübt werden. Der Fokus sollte hierbei auf der Darstellung von Verbindungen mit

Schichtstruktur liegen. Durch unterschiedliche Substituenten am Kation können die Eigenschaften der zu erhaltenden Materialien gezielt gesteuert werden.

Besondere Bedeutung sollte hierbei der grundlegenden Erforschung von Bildungsmechanismen, der Bindungssituation und der Struktur-Eigenschafts-Beziehungen zukommen. Die zu erhaltenden Verbindungen sollen über Röntgenbeugung an Pulvern und Einkristallen (PXRD und SCXRD), energiedispersive Röntgenspektroskopie (EDX), Infrarotspektroskopie (IR), Differenz-Thermoanalyse/Thermogravimetrie (DTA/TG), UV-Vis-Spektroskopie (UV-Vis) und Photolumineszenzmessungen (PL) charakterisiert werden. Die beiden Forschungsziele für diese Arbeit sind in Abbildung 2.1 nochmals zusammengefasst.

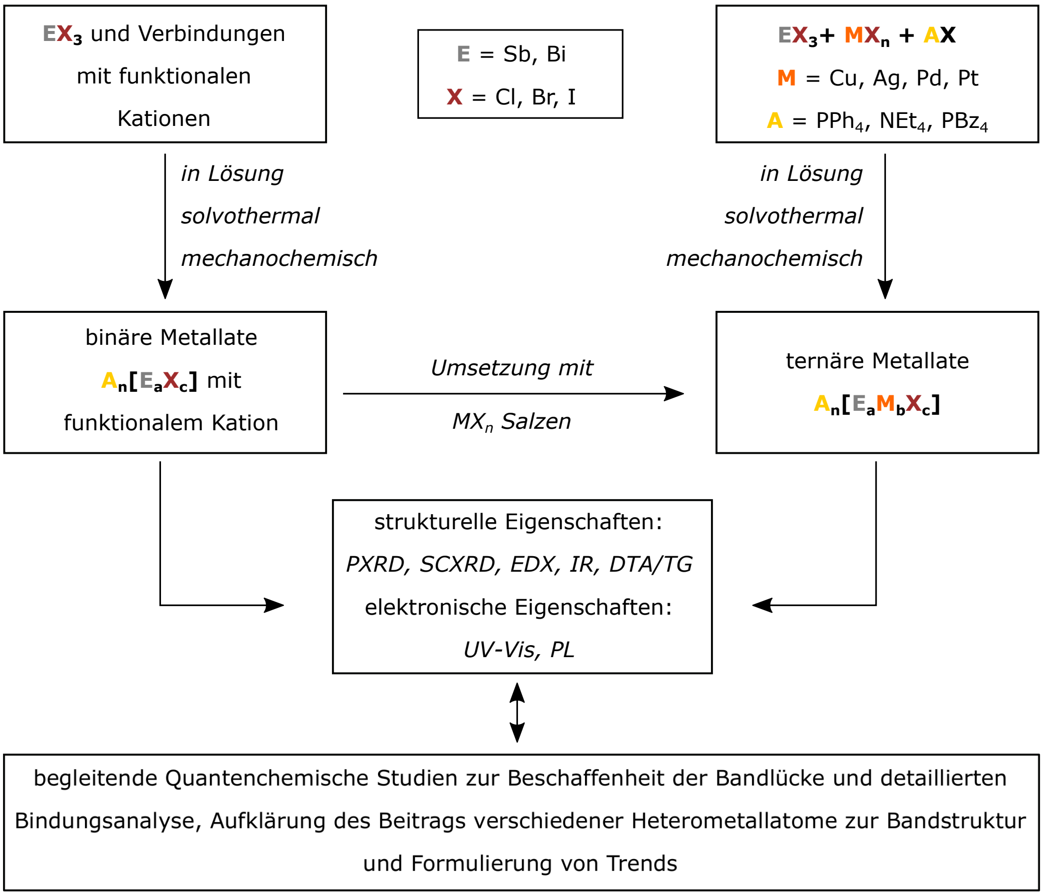

Abbildung 2.1: Übersicht der für diese Arbeit geplanten Experimente.

Kumulativer Teil 3

Im Rahmen der Untersuchungen dieses Promotionsprojektes sind bislang sechs veröffentlichte Publikationen entstanden. Zudem befindet sich ein weiterer Artikel in der Revision. Im Folgenden sind die zu dieser Promotionsschrift beitragenden Publikationen gelistet. Die elektronischen Zusatzinformationen sind in Anhang C zu finden. Alle publizierten Verbindungen werden im Folgenden anhand ihrer Nummerierung in der Originalpublikation benannt.

Inhalt

3.1. Surprising Discoveries on the Way to an Old Compound: Four Transient Iodido Antimonates

Natalie Dehnhardt, André Böth, Johanna Heine, *Dalton Transactions* **2019**, *48*, 5222-5229, DOI: 10.1039/C9DT00575G.

Abstract

During the synthesis of the literature-known iodido antimonate $[Cu(MeCN)_4]_4[Sb_3I_{11}]_2$ (MeCN = acetonitrile), four transient compounds, $[Cu(MeCN)_4]_4[Sb_6I_{22}] \cdot 2MeCN$ (**1**), $[Cu(MeCN)_4]_4[Sb_7I_{25}] \cdot MeCN$ (**2**), $[Cu(MeCN)_4]_4[Sb_{10}I_{34}]$ (**3**) and $[Cu(MeCN)_4]_4[Sb_8I_{28}]$ (**4**), were identified. The compounds appeared within hours or days and subsequently redissolved in the mother liquor, leading to $[Cu(MeCN)_4]_4[Sb_3I_{11}]_2$ as the final product. Single crystal X-ray analysis showed that all four compounds feature unprecedented anion motifs.

Zusammenfassung

In dieser Publikation wird über die Synthese und Charakterisierung von vier transienten Iodidoantimonaten berichtet. Alle Verbindungen wurden aus derselben Reaktion von Antimontriiodid (SbI_3) und Kupferiodid (CuI) in Acetonitril nach unterschiedlich langen Kristallisationszeiten und -temperaturen erhalten. Ursprüngliches Ziel dieser Synthesen war die Reproduktion der literaturbekannten Verbindung $[Cu(MeCN)_4]_2[Sb_3I_{11}]_2$ (**A**), um erste Erfahrungen mit dem Reaktionssystem SbI_3/CuI/Acetonitril zu gewinnen. Kristalle von **1** bis **4** wurden über Einkristall-Röntgenstrukturanalyse untersucht. Eine weiterführende Bulk-Analytik war nicht möglich, da die Kristalle außerhalb der Mutterlauge nur eine geringe Stabilität zeigten, die auf den schnellen Verlust von im Kristall gebundenem Acetonitril zurückzuführen ist. Besonders interessant ist der transiente Charakter der Verbindungen. Diese kristallisieren nacheinander, unter vollständigem Lösen der vorherigen Verbindung, aus der Mutterlauge aus. Werden SbI_3 und CuI im Verhältnis 1,5:1 in Acetonitril unter Reflux gelöst und die abgekühlte Reaktionslösung bei -18 °C gelagert, können nach vier Stunden orange Planken von $[Cu(MeCN)_4]_4[Sb_6I_{22}] \cdot 2MeCN$ (**1**) und gelbe Stäbe von $[Cu(MeCN)_4]_4[Sb_7I_{25}] \cdot MeCN$ (**2**) beobachtet werden. Versuche, die beiden Verbindungen unabhängig voneinander zu kristallisieren, waren erfolglos. Werden die Kristalle weiter in der Mutterlauge aufbewahrt, können nach zwei Tagen ausschließlich Kristalle von $[Cu(MeCN)_4]_4[Sb_{10}I_{34}]$ (**3**) beobachtet werden. Da diese in Form dunkelroter Blöcke kristallisierten ist eine klare Unterscheidung über den Habitus im Vergleich zu **1** und **2** möglich. Nach insgesamt sechs Tagen hat sich auch **3** wieder unter Bildung der literaturbekannten Verbindung **A**, deren Synthese das ursprüngliche Ziel dieser Untersuchung war, gelöst.

Wird die Reaktionslösung bei Raumtemperatur zur Kristallisation aufbewahrt kann nach drei Tagen Verbindung $[Cu(MeCN)_4]_4[Sb_8I_{28}]$ (**4**) beobachtet werden, die sich nach zwei Wochen unter Bildung von **A** wieder gelöst hat. Eine Übersicht über die transienten Umwandlungen ist zusammen mit Ausschnitten aus den Kristallstrukturen und Fotografien der Kristalle in Abbildung 3.1 dargestellt.

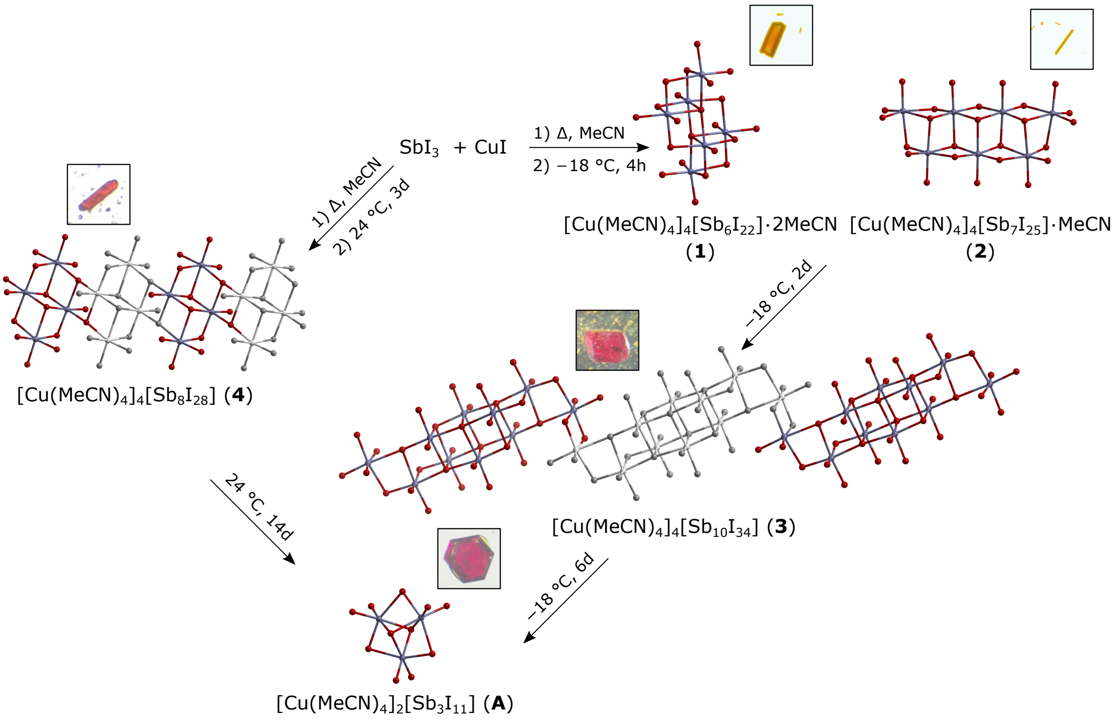

Abbildung 3.1: Übersicht der transienten Umwandlungen mit Ausschnitten aus den Kristallstrukturen von **1** bis **4**. Die Wiederholungseinheiten der polymeren Anionen von **3** und **4** sind grau hervorgehoben. Neben jedem Kristallstrukturausschnitt ist eine Fotografie eines Kristalls der entsprechenden Verbindung zu Verdeutlichung der verschiedenen Habitus gezeigt.

Eine optische Unterscheidung der einzelnen Spezies war auf Grund der sehr unterschiedlichen Habitus mit einem Lichtmikroskop möglich und wurde per Einkristalldiffraktometrie überprüft. Alle vier Verbindungen weisen ein neues Anionenmotiv auf. Das $[Sb_6I_{22}]^{4-}$-Anion in **1** stellt das vierte Isomer dieser Zusammensetzung dar und kristallisiert mit einer neuen Verknüpfung der $\{SbI_6\}$-Polyeder. Das Anion von **2** weist sieben kantenverknüpfte $\{SbI_6\}$-Oktaeder auf, deren Verknüpfungsmuster vom Cadmiumiodid-Strukturtyp abgeleitet werden kann. Es ist das erste Anion mit diesem Verknüpfungsmuster, das mit einer ungeraden Anzahl an Metallatomen kristallisiert. Verbindung **3** weist ein strangartiges Anion mit einer bisher unbekannten und ungewöhnlich großen Wiederholungseinheit auf. Das Anion von Verbindung **4** weist ebenfalls eine neue Kettenstruktur auf, jedoch mit einer kleineren Wiederholungseinheit.

Die einzelnen Übergänge zwischen den verschiedenen Verbindungen folgen hierbei einem zunehmenden Aggregationsgrad der Koordinationspolyeder, von kantenverknüpften Oktaedern in diskreten Anionen, über kantenverknüpfte Oktaeder in kettenförmigen Anionen zu allseits flächenverknüpften Oktaedern in der literaturbekannten Verbindung **A**. Da für die Verbindungen mit strangartigem Anion eine längere Kristallisationszeit nötig ist, ist ein Zusammenhang zwischen Komplexität der Verbindung und ihrer Kristallisationszeit möglich. Des Weiteren verdeutlichen die Ergebnisse die strukturelle Vielfalt der Iodidoantimonate und die Möglichkeit dieses Feld weiter zu erforschen, indem man einen Blick auf bereits bekannte Reaktionssysteme wirft.

Eigener Anteil

Die Verbindungen **1** und **3** wurden von mir bereits während meiner Masterarbeit synthetisiert. Im Rahmen meiner Promotion kam die Idee, durch regelmäßiges kontrollieren der Reaktionslösung den genauen Ablauf des Übergangs von einer Spezies zur nächsten beobachten zu können. Hierfür hat *André Böth* unter meiner Anleitung im Rahmen eines Forschungspraktikums Reaktionen reproduziert und den Kristallisationsverlauf mittels Lichtmikroskopie dokumentiert. Auf diese Weise konnten Kristalle von **2** und **4** erhalten werden. Die Einkristallmessung sowie Strukturlösung und -verfeinerung von **4** wurde von mir, **1** bis **3** von *Dr. Johanna Heine*, durchgeführt. Das Manuskript habe ich in Zusammenarbeit mit *Dr. Johanna Heine* verfasst.

Dalton
Transactions

PAPER

View Article Online
View Journal | View Issue

Cite this: *Dalton Trans.*, 2019, **48**, 5222

Received 7th February 2019,
Accepted 16th March 2019

DOI: 10.1039/c9dt00575g

rsc.li/dalton

Surprising discoveries on the way to an old compound: four transient iodido antimonates†

Natalie Dehnhardt, André Böth and Johanna Heine *

During the synthesis of the literature-known iodido antimonate $[Cu(MeCN)_4]_4[Sb_3I_{11}]_2$ (MeCN = acetonitrile), four transient compounds, $[Cu(MeCN)_4]_4[Sb_6I_{22}]\cdot 2MeCN$ (**1**), $[Cu(MeCN)_4]_4[Sb_7I_{25}]\cdot MeCN$ (**2**), $[Cu(MeCN)_4]_4[Sb_{10}I_{34}]$ (**3**) and $[Cu(MeCN)_4]_4[Sb_8I_{28}]$ (**4**), were identified. The compounds appeared within hours or days and subsequently re-dissolved in the mother liquor, leading to $[Cu(MeCN)_4]_4[Sb_3I_{11}]_2$ as the final product. Single crystal X-ray analysis showed that all four compounds feature unprecedented anion motifs.

Introduction

Halogenido metalates, especially of the heavy group 14 and 15 elements, show optical and electronic properties like photoluminescence,[1,2] ferroelectricity[3,4] and semiconductivity[5] which make them attractive for device applications.[6,7] Besides a facile processability at room temperature[8] especially metalates of antimony and bismuth often show only little sensitivity to air or moisture,[9] unlike the more extensively studied tin and lead halides.[10] Nonetheless, insights into the formation processes of these compounds in solution remain limited and have been mostly focused on $MAPbX_3$ (MA = methylammonium; X = Cl, Br, I) and related structures.[11]

These compounds are exemplary for the renaissance of iodido metalates as light absorbers in hybrid perovskite solar cells.[12] This emergent class of photovoltaic absorber materials reached power conversion efficiencies in prototype devices over 20%, based on formamidinium lead iodide.[13,14] The technology's bottlenecks are the toxicity of lead,[15] as well as the compound's sensitivity to heat and moisture.[16] A promising solution seems to be the heterovalent substitution of lead with bismuth or antimony.[17,18] Here, the antimonates have only recently come into focus.[19,20] This progress was based on a number of earlier works, for example by Mitzi and coworkers, who synthesized $Cs_3[Sb_2I_9]$ in two structural modifications featuring layered or molecular anions, and processed the compound into thin films with enhanced moisture stability.[21] The Mathews group showed that a substitution of Cs^+ with Rb^+ can template the formation of a layered structure when processed in solution,[22] while Jakubas prepared $[Sb_2I_9]^{3-}$ salts with organic imidazolium cations.[23] Recent investigations of the excitation dynamics in $MA_3[Sb_2I_9]$ have shown that using this compound and related materials for photovoltaics may be challenging,[24] but other applications such as hard radiation detection may hold more promise.[25] The interest in halogenido antimonates as absorption materials for photovoltaics is preceded by more fundamental investigations of their chemistry with much of the early work on iodido antimonates performed the 1980s by the group of Pohl.[26–32] Iodido antimonates and the closely related bismuthates show an expansive structural chemistry with MI_6 octahedra (M = Sb, Bi) as the main building block, connected *via* corner- edge- or face-sharing into anions of varying complexity. Antimony especially tends to form intricate discrete or 1D anions with diverse connectivity modes of the coordination polyhedra and flexible Sb–I interatomic distances.[33–36]

Siegfried Pohl investigated the structural chemistry of iodido antimonates nearly thirty years ago. Inspired by his work and looking to investigate the system $CuI/SbI_3/MeCN$ in preparation for the synthesis of ternary Cu/Sb/I anions, we repeated the synthesis of $[Cu(MeCN)_4]_4[Sb_3I_{11}]_2$.[31] Unexpectedly, we could identify four transient iodido antimonates crystallizing prior to the described compound. All four compounds possess anion motifs previously unknown for halogenido antimonates. Crystals of the products form within hours or days and dissolve entirely in the mother liquor subsequently, a phenomenon that has not been described for iodido pentelates yet. The results not only emphasize the structural variety of the material class, but also offer a first glimpse into the intricate kinetics involved in the formation processes.

Department of Chemistry and Material Sciences Center, Philipps-Universität Marburg, Hans-Meerwein-Straße, 35043 Marburg, Germany. E-mail: johanna.heine@chemie.uni-marburg.de

† Electronic supplementary information (ESI) available: Additional details of crystal structure refinement and analysis. CCDC 1881276–1881279. For ESI and crystallographic data in CIF or other electronic format see DOI: 10.1039/c9dt00575g

Experimental

General

Antimony triiodide (SbI_3) was synthesized from the elements according to literature procedure.[37] Copper(I) iodide (CuI) and acetonitrile were used as supplied from commercial sources.

Synthesis

$[Cu(MeCN)_4]_4[Sb_6I_{22}]\cdot 2MeCN$ (1), $[Cu(MeCN)_4]_4[Sb_7I_{25}]\cdot MeCN$ (2) and $[Cu(MeCN)_4]_4[Sb_{10}I_{34}]$ (3). SbI_3 (75 mg, 0.15 mmol) and CuI (20 mg, 0.1 mmol) were dissolved in 5 mL of acetonitrile by heating to reflux under magnetic stirring for 30 min. The hot reaction solution was left to cool to room temperature and stored for crystallization at −18 °C. Bright orange block-shaped crystals (**1**), as well as thin yellow planks (**2**) formed after four hours. After two days, dark red blocks (**3**) had crystallized. An isolation of bulk quantities of the crystals was not possible due to poor stability outside the mother liquor.

$[Cu(MeCN)_4]_4[Sb_8I_{28}]$ (4). SbI_3 (75 mg, 0.15 mmol) and CuI (20 mg, 0.1 mmol) were dissolved in 5 mL of acetonitrile by heating to reflux under magnetic stirring for 30 min. The hot reaction solution was left to cool to room temperature and stored for crystallization. Bright orange blocks crystallized after three days at room temperature. The crystals showed poor stability in air due to loss of acetonitrile.

Single crystal X-ray crystallography

Single crystal X-ray diffraction was performed at 100 or 110 K on a Bruker Quest D8 diffractometer with microfocus Mo Kα radiation and a Photon 100 (CMOS) detector for compound **1**, **2** and **3** and on a STOE IPDS2 diffractometer equipped with an imaging plate detector system using MoKα radiation with graphite monochromatization for compound **4**. The structures were solved using direct methods, refined by full-matrix least-squares techniques and expanded using Fourier techniques, using the ShelX software package[38–40] within the OLEX2 suite.[41] All non-hydrogen atoms were refined anisotropically unless indicated otherwise. Hydrogen atoms were assigned to idealized geometric positions and included in structure factors calculations. See ESI† for details on individual refinements. Pictures of the crystal structures were created using DIAMOND.[42] The data for **1–4** has also been deposited as CCDC 1881276–1881279.†

Results and discussion

Synthesis

The synthesis of **1** to **4** could be accomplished by following the method described by Pohl,[31] dissolving 0.15 mmol SbI_3 and 0.1 mmol CuI in 5 mL of acetonitrile by heating to reflux. The reaction solution was allowed to cool down to room temperature and was stored at −18 °C, leading to compounds **1** to **3**, or at room temperature, resulting in compound **4**. After few hours at −18 °C, orange and yellow crystals of **1** and **2** can be observed in the reaction solution. After few more hours, dark red blocks can be found in addition, until after two days, the crystals of **1** and **2** dissolved completely in the mother liquor and just dark red blocks of **3** can be found. After four more days, crystals of **3** disappeared, and only crystals of the known compound $[Cu(MeCN)_4]_4[Sb_3I_{11}]_2$ [31] are present now. An isolation of bulk samples of the compounds was not possible: **1**, **2** and **3** rapidly lose acetonitrile when taken from the mother liquor and attempts to store the crystals under acetonitrile atmosphere for additional investigations were not successful.

When storing the reaction solution at room temperature, bright orange rods can be observed, consisting of aggregates of single crystals of **4**. After two weeks, these crystals also dissolve in the mother liquor, forming once again the known compound $[Cu(MeCN)_4]_4[Sb_3I_{11}]_2$. Once again, an isolation of bulk quantities of **4** was not possible due to loss of acetonitrile.

Photographs of the single crystals are shown in Fig. 1, a schematic overview of the crystallization process is given in Fig. 2.

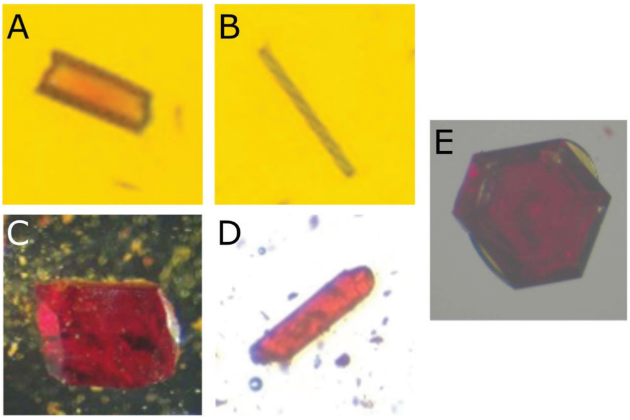

Fig. 1 Single crystals of **1** to **4** (A to D) and $[Cu(MeCN)_4]_4[Sb_3I_{11}]_2$ (E). Images of **1** and **2** were taken without removing the crystals from the reaction solution due to poor stability even in silicon oil.

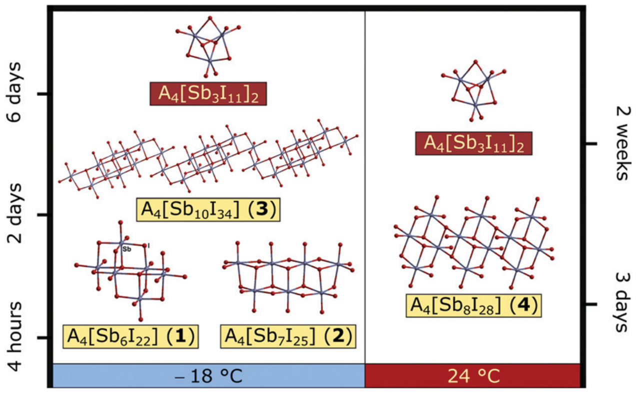

Fig. 2 Schematic overview of the crystallization process of compounds **1** to **4**. A = $[Cu(MeCN)_4]^+$, antimony atoms shown in grey, iodine atoms shown in red, solvate molecules in the formula of **1** and **2** omitted for brevity.

Description of the crystal structures

All four compounds feature the same cation, which consists of a Cu(I) ion coordinated by four acetonitrile ligands in a tetrahedral arrangement, shielding the charge of the Cu(I) ion and giving the cation a voluminous spherical shape. Thus, only little interactions between cation and anion are observed in compounds **1** to **4**. Selected crystal data are given in Table 1. It has to be noted that the crystal colors described here are lighter than in the photographs, due to the well-known thermochromism of iodido pentelates, shifting the compounds' color from orange or red at room temperature to yellow or orange at 100 K.[43]

Compound **1** crystallizes in the tetragonal crystal system in the space group $I4_1/a$. The anion consists of a discrete hexanuclear unit, constructed from $[SbI_6]^{3-}$ octahedra sharing common edges. Previously, three $[Sb_6I_{22}]^{4-}$ anions have been reported,[29,31,32] which can all be derived from the tetranuclear $[Sb_4I_{16}]^{4-}$,[44] whose structure can be understood as cutouts from layers in the CdI_2 structure.[45] As its isomers, compound **1** can be derived from $[Sb_4I_{16}]^{4-}$ by adding two neutral SbI_3 units to the anion. For this, different positions are possible. If the positions of the added SbI_3 units lie in the same plane as the metal atoms of the $[Sb_4I_{16}]^{4-}$ unit, another anion with CdI_2-like structure is obtained (isomer A).[31] If they lie behind and in front of the plane, two isomers are possible. In one case, the SbI_3 units are added to the $[Sb_4I_{16}]^{4-}$ unit in such a way that they complete the fragment to form a double cube structure (isomer B).[29]

In this case, each $[SbI_6]^{3-}$ octahedron has the same orientation, resulting in a close condensation of the octahedra and formation of μ_4-bridging iodine atoms. In the second case, the addition of two SbI_3 units results only in the formation of μ_3-bridging iodine atoms, resulting in face-sharing octahedra, instead of the corner-sharing octahedra found in the other isomers (isomer C).[32] The three different isomers are displayed in Fig. 3. In the case of compound **1**, the condensed SbI_3 units are situated above and below the plane of the four other Sb atoms. This structure has been described for the homologous bismuthate $[Bi_6I_{22}]^{4-}$.[46] In the unit cell of **1**, anions and cations arrange in a way that allows the formation of channels along the crystallographic *c*-axis. These channels are formed by the cations, while the anions occupy the voids between them. There are two different types of channels present, as displayed in Fig. 4, where they can be distinguished by the orientation of the acetonitrile ligands. While they are pointing inside the channel in type I, reducing its volume, they adopt a more compact arrangement in type II.

When regarding the packing of the channels along the *c*-axis, as shown in Fig. 5, it becomes clear that they can also be distinguished by a different symmetry operation. In type I, the cations are arranged along a fourfold screw axis, giving the channel a more open structure compared to the type II channels, where the cations are arranged along a fourfold rotoinversion axis. Along both channel types disordered acetonitrile molecules can be found (see ESI† for details). Single crystal X-ray diffraction indicated a composition of two molecules of acetonitrile per formula unit. This initiates a fast decomposition of the crystals in air and even silicon oil, as the solvate acetonitrile evaporates. The sensitivity to solvent loss is not unexpected, as Pohl has already described this issue for $[Cu(MeCN)_4]_4[Sb_3I_{11}]_2$.[31] As the solvate acetonitrile molecules are trapped inside the channels in **1**, they can only leave the crystal in one direction. The process can be observed macroscopically under the microscope as a rapid independent movement during decomposition.

Compound **2** crystallizes as yellowish needles in the monoclinic space group $P2_1$. The structure of the anion can also be derived from the CdI_2 structure. The known anions $[Sb_2I_{10}]^{4-}$,[47] $[Sb_4I_{16}]^{4-}$,[44] $[Sb_6I_{22}]^{4-}$ (ref. 31) and $[Sb_8I_{28}]^{4-}$ (ref. 27) can each be derived from the previous structure in the series by adding two SbI_3 units to it, while the metal atoms all lie in the same plane. With **2**, the first halogenido antimonate compound of this family with an odd number of metal atoms in the molecular anion was synthesized. The anion consists of seven edge-sharing SbI_6 octahedra and can be derived from

Table 1 Selected crystal data for compounds **1–4**

	1	**2**	**3**	**4**
Empirical formula	$C_{32}H_{48}Cu_4I_{22}N_{16}Sb_6$	$C_{34}H_{51}Cu_4I_{25}N_{17}Sb_7$	$C_{32}H_{48}Cu_4I_{34}N_{16}Sb_{10}$	$C_8H_{12}CuI_7N_4Sb_2$
M [g mol^{-1}]	4433.32	4976.82	6443.12	5438.22
Crystal color & shape	Yellow prism	Yellow plate	Orange block	Orange prism
Crystal system	Tetragonal	Monoclinic	Triclinic	Monoclinic
Space group	$I4_1/a$	$P2_1$	$P1$	$P2_1/c$
a [Å]	40.6216(12)	10.4510(6)	12.8463(4)	7.3965(2)
b [Å]	40.6216(12)	39.343(2)	13.0686(4)	16.7953(7)
c [Å]	12.3875(5)	13.3623(7)	19.1151(6)	21.6770(7)
α [°]	90	90	107.700(3)	90
β [°]	90	106.644(2)	94.743(3)	92.449(3)
γ [°]	90	90	93.000(3)	90
V [Å^3]	20 440.8(15)	5264.1(5)	3036.56(17)	2690.40(16)
Z	8	2	1	4
R_1 ($I > 2\sigma(I)$)	0.0434	0.0674	0.0350	0.0312
wR_2 (all data)	0.0895	0.1296	0.0801	0.0671
Flack		0.39(8)	0.23(5)	

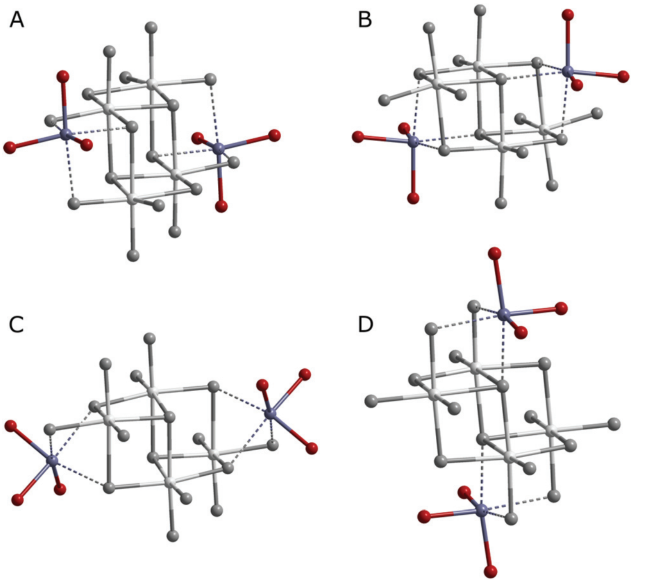

Fig. 3 Anionic motifs in the known $[Sb_6I_{22}]^{4-}$ isomers with the central $[Sb_4I_{16}]^{4-}$ unit highlighted in grey (A to C), and the anion in **1** (D).

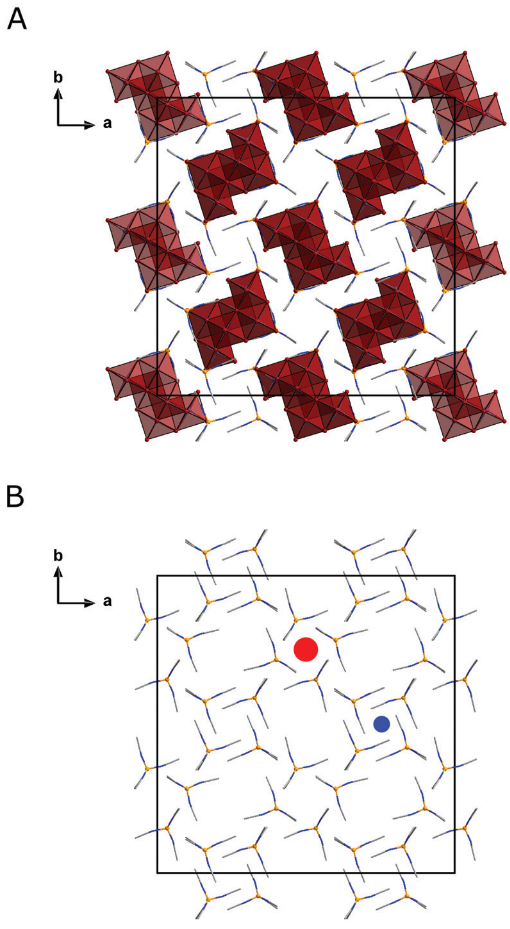

Fig. 4 Packing diagram of **1** with SbI_6 units shown as dark red polyhedra, copper atoms shown in orange, nitrogen atoms shown in blue and carbon atom shown in grey (A). Arrangement of the cations in **1** with a type I channel marked in blue and a type II channel marked in red (B).

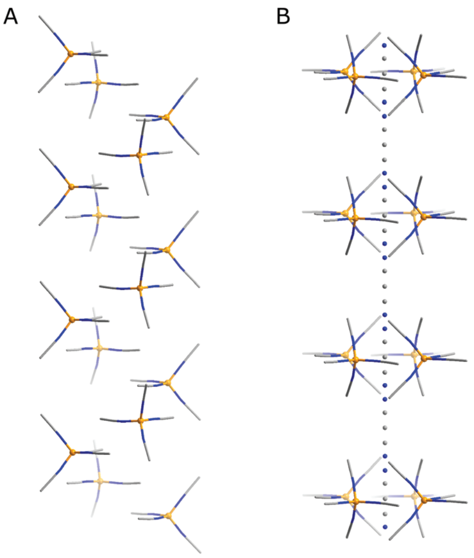

Fig. 5 Channels formed by the cations in **1**. A: Type I channel; B: Type II channel with captured acetonitrile.

the $[Sb_6I_{22}]^{4-}$ isomer B by formal addition of one SbI_3 unit. Excerpts of the crystal structure of **2** are shown in Fig. 6.

Compound **3** crystallizes in the triclinic space group $P1$, with an unusual 1D anion. The polymeric chains are formed of condensed $[Sb_{10}I_{34}]^{4-}$ building blocks. Compared to other iodido antimonates with chain-like anions, these building blocks are rather complex. Typically, polymeric anions with the formula $[SbI_5]^{2-}$ or $[SbI_4]^{-}$ are found,[44,48] consisting of corner- or edge-sharing $[SbI_6]^{3-}$ octahedra. Additionally, anions composed of small building blocks like $[Sb_3I_{10}]^{-}$, which are connected *via* common edges into a polymeric chain anion, are known.[27] The anion in **3** can be derived from the $[Sb_6I_{22}]^{4-}$ isomer C. This double cube with antimony and iodine atoms occupying the twelve edges is connected to two $[Sb_2I_{10}]^{4-}$ units *via* common iodine atoms of the opposite small faces of the

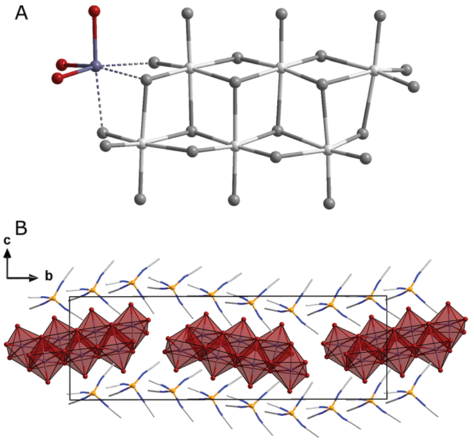

Fig. 6 Excerpt of the crystal structure of **2**. Anion in **2**, the central $[Sb_6I_{22}]$ unit is highlighted in grey (A). Packing diagram of **2** with the solvate acetonitrile omitted for clarity (B).

double cube. The decanuclear units are again connected by two bridging iodine atoms to form the polymeric chains shown in Fig. 7.

While a solution and refinement of the heavy atom structure is possible in $P\bar{1}$, the structure has to be solved in the non-centrosymmetric space group $P1$. The reason that this rare space group is observed here are the acetonitrile ligands coordinating the Cu(I) cation. When displaying them as the tetrahedral coordination sphere around the copper cation, it becomes clear that two different orientations of these tetrahedra are present and that these are incompatible with an inversion center, making a solution and refinement in $P1$ necessary (see ESI† for details). The different orientations of the $[\mathrm{Cu(MeCN)_4}]^+$ tetrahedra and the pseudo-center of inversion are highlighted in Fig. 8.

Compound **4** crystallizes in the monoclinic space group $P2_1/c$ as orange prisms. In contrast to compound **1** to **3**, **4** was obtained at room temperature. As **3**, it contains a chain-like anion, which shows a smaller repetition unit than **3**. It can also be derived from the $[\mathrm{Sb_4I_{16}}]^{4-}$ anion. Here, $[\mathrm{Sb_4I_{16}}]^{4-}$ units are connected over two common iodine atoms, forming polymeric chains as shown in Fig. 9.

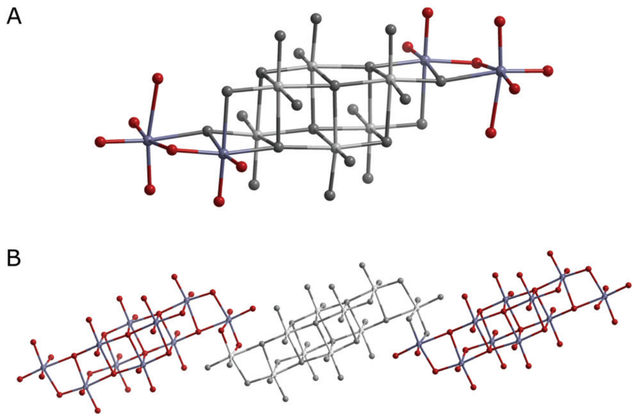

Fig. 7 Excerpts of the crystal structure of **3**. Anion in **3** with the central $[\mathrm{Sb_6I_{22}}]$ unit highlighted in dark grey (A). Polymeric chains of condensed $[\mathrm{Sb_{10}I_{34}}]$ units, highlighted in light grey, in **3** (B).

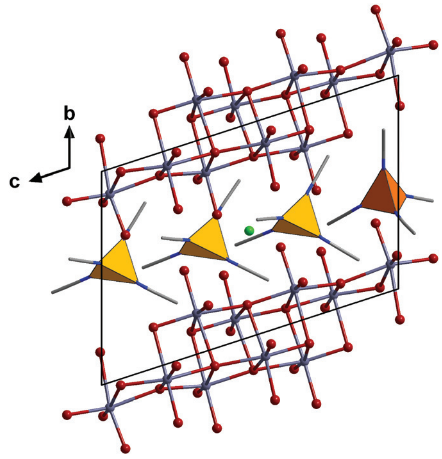

Fig. 8 Excerpt of the crystal structure of **3** with schematic $[\mathrm{Cu(MeCN)_4}]^+$ cations. Different orientations of the cations are highlighted in yellow and orange, the pseudo-center of inversion is marked in green.

The packing diagram of **4** reveals that the anionic chains arrange along the *ab* and *bc* plane of the unit cell, with two cations filling the voids between them. Similar to compound **2**, the chains show different orientations reminiscent of a herringbone-like arrangement. Corresponding to the 1D extension of the anion, the cations also adopt a stacked structure in the unit cell. An excerpt of the crystal structure is shown in Fig. 10. Iodido antimonates featuring anionic chains of the same composition are known,[30,49] yet a different mode of connection than in **4** is observed in these compounds, as shown in Fig. 11, where the chain motifs in $[\mathrm{Me_3NCH_2Ph}][\mathrm{Sb_2I_7}]$ ($\mathrm{Me_3NCH_2Ph}$ = benzyltrimethylammonium)[30] and **4** are compared.

Bond length and angles in **1–4** are within typical ranges (see ESI† for details). A closer look at the packing motifs of the $[\mathrm{Cu(MeCN)_4}]^+$ units in **1–4** and $[\mathrm{Cu(MeCN)_4}]_4[\mathrm{Sb_3I_{11}}]_2$, shown in Fig. 12, reveals the great flexibility of the cation and thus at least a part of the reason why such a wide range of iodido antimonate motifs can be stabilized. The cations do not merely act

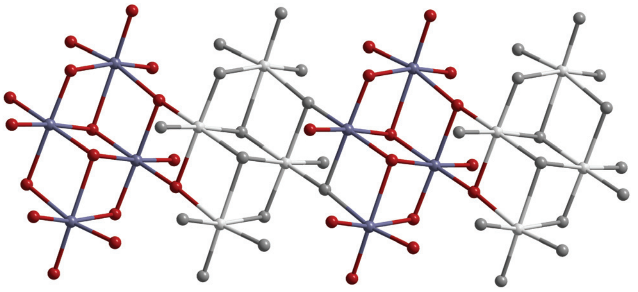

Fig. 9 Excerpt of an anionic chain in **4** with the repeating unit highlighted in grey.

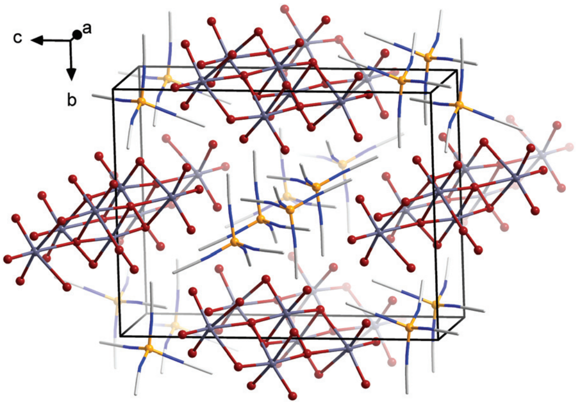

Fig. 10 Excerpt of the crystal structure of **4** showing the propagation of the anionic chains and the stacking of the cations along the crystallographic *a*-axis.

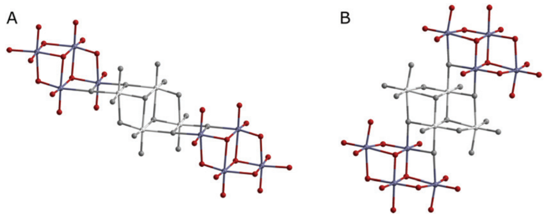

Fig. 11 Comparison of the chain connectivity in $[Me_3NCH_2Ph][Sb_2I_7]$ (A) and **4** (B) with the $[Sb_4I_{16}]$ unit shown in grey.

as approximately spherical counterions, but can interlock in different ways, a phenomenon that has been studied quite deeply for the more prominently used tetraphenylphosphonium ions and related systems by Dance and coworkers.[50]

Discussion

Although often hard to catch, the occurrence of transient phases during synthesis, crystallization and transformation has been observed in various classes of materials.[51] Nonetheless, to the best of our knowledge, the work presented here represents the first example of such transient phases in the chemistry of single crystalline halogenido metalates, despite the fundamental role of intermediate and metastable phases during the synthesis and application of lead halide perovskite materials and devices.[11] While unfortunately, the inclination of **1–4** towards rapid loss of solvent coupled with a comparatively long crystallization time has precluded us from performing detailed time-dependent powder X-ray diffraction studies either *ex situ* or *in situ*, a few observations can be made from the data at hand.

The reaction is initiated by dissolving the starting materials CuI and SbI_3 in hot acetonitrile. The stoichiometry chosen here corresponds to the final product $[Cu(MeCN)_4]_4[Sb_3I_{11}]_2$ (Cu : Sb : I → 2 : 3 : 11 or CuI : SbI_3 2 : 3). When the reaction solution is stored at −18 °C, the crystallization of two solvates, $[Cu(MeCN)_4]_4[Sb_6I_{22}]\cdot 2$ MeCN (**1**) and $[Cu(MeCN)_4]_4[Sb_7I_{25}]\cdot$MeCN (**2**) is observed. **1** features the same composition as the reaction stoichiometry (CuI : SbI_3 2 : 3), while **2** is more SbI_3-rich (CuI : SbI_3 2 : 3.5). The particular anion motifs found in these two compounds are unprecedented in the chemistry of halogenido antimonates, but molecular anions with nuclearities between two and eight are fairly common, suggesting that they are either present in solution or can rapidly assemble upon crystallization overriding the typically observed templating effects of the cations and leading to the crystallization of, in our case metastable, solvates.[34]

When the reaction is allowed to continue at −18 °C or conducted at room temperature, crystallization of $[Cu(MeCN)_4]_4[Sb_{10}I_{34}]$ (**3**) at the cost of **1** and **2** or direct crystallization of $[Cu(MeCN)_4]_4[Sb_8I_{28}]$ (**4**) are observed. Both **3** and **4** feature comparatively large chain-like anions that ostensibly take longer to assemble upon crystallization and both are SbI_3-rich with respect to the reaction stoichiometry (CuI : SbI_3 2 : 5 for **3**

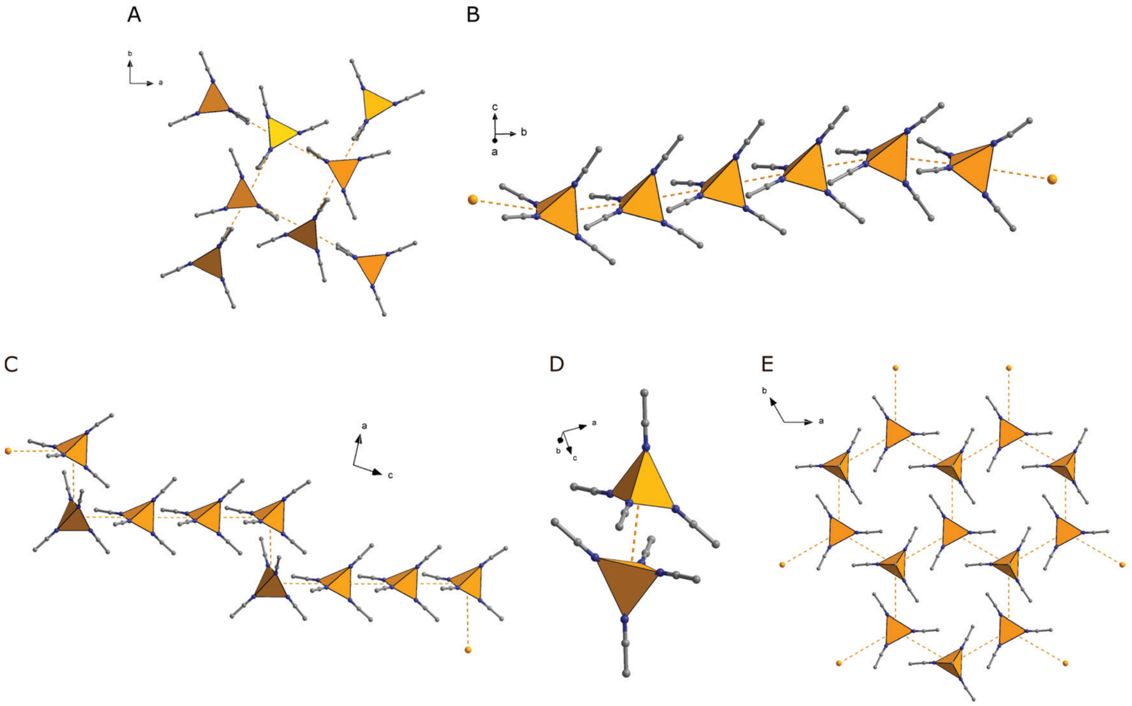

Fig. 12 Cation packing motifs in **1–4** (A–D) and $[Cu(MeCN)_4]_2[Sb_3I_{11}]$ (E), carbon shown in grey, nitrogen in blue, coordination polyhedral around Cu in orange. Shortest Cu⋯Cu distances drawn as dashed lines (**1**: 6 Å; **2**: 5 Å; **3**: 6 Å; **4**: 4 Å; $[Cu(MeCN)_4]_2[Sb_3I_{11}]$: 7 Å). Note that these do not represent bonding interactions and are merely a guide to the eye.

and 2 : 4 for **4**) providing an additional driving force towards further reaction. Independent of the reaction pathway, the sole and final product over the course of several days is the literature-known $[Cu(MeCN)_4]_4[Sb_3I_{11}]_2$, forming as thick hexagonal plates.

The question is of course, why does this compound not form immediately upon cooling the reaction solution? We suggest that the condensed anion motif $[Sb_3I_{11}]^{2-}$ forms only very slowly. Most halogenido pentelates can be assembled, at least conceptually, by adding either EX_3 or X^- to the basic building unit $[EX_6]^{3-}$. $[Sb_3I_{11}]^{2-}$ cannot be formed this way, instead requiring the formation of the rare penta-coordinate building block $[E_2X_8]^{2-}$,[28] and an addition of EX_3 with significant reorganization or an addition-elimination mechanism when adding EX_3 to $[E_2X_9]^{3-}$. Interestingly, the lone example of a iodido bismuthate with the same anion motif, $[M(1,10\text{-Phenanthroline})_3][Bi_3I_{11}]$ (M = Co, Fe, Zn) is also obtained after long reaction times of more than five days, in this case at elevated temperatures.[52]

Such simplistic deliberations are, of course, going to miss complexities that are bound to exist in the solution chemistry of the halogenido pentelates, which has so far remained poorly understood due to the lack of analytical access. Yet, they may help to explain our findings here and point toward a richer chemistry, controlled by kinetics as well as thermodynamics, in the synthesis of new members of this class of materials.

Conclusions

We have isolated four new, transient iodido antimonates $[Cu(MeCN)_4]_4[Sb_6I_{22}]\cdot 2MeCN$ (**1**), $[Cu(MeCN)_4]_4[Sb_7I_{25}]\cdot MeCN$ (**2**), $[Cu(MeCN)_4]_4[Sb_{10}I_{34}]$ (**3**) and $[Cu(MeCN)_4]_4[Sb_8I_{28}]$ (**4**), during the synthesis $[Cu(MeCN)_4]_4[Sb_3I_{11}]_2$, a compound described by Pohl nearly 30 years ago. The transient compounds feature complex, previously unknown anion motifs, broadening the structural chemistry of the halogenido pentelates. Our results highlight the importance of kinetics in the field of halogenido metalates and suggest that more new compounds may be found *en route* to those already known. This may allow new insights into the complex reaction kinetics of halogenido metalates.

Conflicts of interest

There are no conflicts to declare.

Acknowledgements

This work is funded by the SFB 1083. J. H. thanks Prof. Stefanie Dehnen, Philipps-Universität Marburg, for her constant support. N. D. thanks the Fonds der Chemischen Industrie and the Studienstiftung des Deutschen Volkes for their support.

Notes and references

1 C. Zhou, M. Worku, J. Neu, H. Lin, Y. Tian, S. Lee, Y. Zhou, D. Han, S. Chen, A. Hao, P. I. Djurovich, T. Siegrist, M.-H. Du and B. Ma, *Chem. Mater.*, 2018, **30**, 2374.

2 O. Nazarenko, M. R. Kotyrba, S. Yakunin, M. Aebli, G. Rainò, B. M. Benin, M. Wörle and M. V. Kovalenko, *J. Am. Chem. Soc.*, 2018, **140**, 3850.

3 W.-Q. Liao, Y. Zhang, C.-L. Hu, J.-G. Mao, H.-Y. Ye, P.-F. Li, S. D. Huang and R.-G. Xiong, *Nat. Commun.*, 2015, **6**, 7338.

4 N. Leblanc, N. Mercier, L. Zorina, S. Simonov, P. Auban-Senzier and C. Pasquier, *J. Am. Chem. Soc.*, 2011, **133**, 14924.

5 Y. Liu, Z. Yang, D. Cui, X. Ren, J. Sun, X. Liu, J. Zhang, Q. Wei, H. Fan, F. Yu, X. Zhang, C. Zhao and S. Liu, *Adv. Mater.*, 2015, **27**, 5176.

6 C. R. Kagan, D. B. Mitzi and C. D. Dimitrakopoulos, *Science*, 1999, **286**, 945.

7 X. Zhao, J. D. A. Ng, R. H. Friend and Z.-K. Tan, *ACS Photonics*, 2018, **5**, 3866.

8 D. B. Mitzi, *J. Mater. Chem.*, 2004, **14**, 2355.

9 J.-H. Chang, T. Doert and M. Ruck, *Z. Anorg. Allg. Chem.*, 2016, **642**, 736.

10 J. S. Manser, M. I. Saidaminov, J. A. Christians, O. M. Bakr and P. V. Kamat, *Acc. Chem. Res.*, 2016, **49**, 330.

11 W. A. Dunlap-Shohl, Y. Zhou, N. P. Padture and D. B. Mitzi, *Chem. Rev.*, 2019, **119**, 3193.

12 M. Saliba, J.-P. Correa-Baena, M. Grätzel, A. Hagfeldt and A. Abate, *Angew. Chem., Int. Ed.*, 2018, **57**, 2554.

13 M. A. Green, Y. Hishikawa, E. D. Dunlop, D. H. Levi, J. Hohl-Ebinger, M. Yoshita and A. W. H. Ho-Baillie, *Prog. Photovoltaics Res. Appl.*, 2019, **27**, 3.

14 Q. Jiang, Z. Chu, P. Wang, X. Yang, H. Liu, Y. Wang, Z. Yin, J. Wu, X. Zhang and J. You, *Adv. Mater.*, 2017, **29**, 1703852.

15 A. Babayigit, H.-G. Boyen and B. Conings, *MRS Energy Sustainability*, 2018, 5.

16 J. A. Christians, S. N. Habisreutinger, J. J. Berry and J. M. Luther, *ACS Energy Lett.*, 2018, **3**, 2136.

17 Z. Shi, J. Guo, Y. Chen, Q. Li, Y. Pan, H. Zhang, Y. Xia and W. Huang, *Adv. Mater.*, 2017, **2**, 1605005.

18 F. Giustino and H. J. Snaith, *ACS Energy Lett.*, 2016, **1**, 1233.

19 F. Jiang, D. Yang, Y. Jiang, T. Liu, X. Zhao, Y. Ming, B. Luo, F. Qin, J. Fan, H. Han, L. Zhang and Y. Zhou, *J. Am. Chem. Soc.*, 2018, **140**, 1019.

20 J.-P. Correa-Baena, L. Nienhaus, R. C. Kurchin, S. S. Shin, S. Wieghold, N. T. P. Hartono, M. Layurova, N. D. Klein, J. R. Poindexter, A. Polizzotti, S. Sun, M. G. Bawendi and T. Buonassisi, *Chem. Mater.*, 2018, **30**, 3734.

21 B. Saparov, F. Hong, J. Sun, H. Duan, W. Meng, S. Cameron, I. G. Hill, Y. Yan and D. B. Mitzi, *Chem. Mater.*, 2015, **27**, 5622.

22 P. C. Harikesh, H. K. Mulmudi, B. Ghosh, T. W. Goh, Y. T. Teng, S. Mhaisalkar and N. Mathews, *Chem. Mater.*, 2016, **28**, 7496.

23 M. Węcławik, A. Gągor, R. Jakubas, A. Piecha-Bisiorek, W. Medycki, J. Baran, P. Zielińskid and M. Gałązkae, *Inorg. Chem. Front.*, 2016, **3**, 1306.

24 M. Scholz, M. Morgenroth, K. Oum and T. Lenzer, *J. Phys. Chem. C*, 2018, **122**, 5854.

25 K. M. McCall, C. C. Stoumpos, S. S. Kostina, M. G. Kanatzidis and B. W. Wessels, *Chem. Mater.*, 2017, **29**, 4129.

26 S. Pohl, W. Saak, P. Mayer and A. Schmidpeter, *Angew. Chem., Int. Ed. Engl.*, 1986, **25**, 825.

27 S. Pohl, W. Saak and D. Haase, *Z. Naturforsch., B: J. Chem. Sci.*, 1987, **42**, 1493.

28 S. Pohl, W. Saak and D. Haase, *Angew. Chem., Int. Ed. Engl.*, 1987, **26**, 467.

29 S. Pohl, D. Haase, R. Lotz and W. Saak, *Z. Naturforsch., B: J. Chem. Sci.*, 1988, **43**, 1033.

30 S. Pohl, R. Lotz, D. Haase and W. Saak, *Z. Naturforsch., B: J. Chem. Sci.*, 1988, **43**, 1144.

31 S. Pohl, R. Lotz, W. Saak and D. Haase, *Angew. Chem., Int. Ed. Engl.*, 1989, **28**, 344.

32 S. Pohl, M. Peters, D. Haase and W. Saak, *Z. Naturforsch., B: J. Chem. Sci.*, 1994, **49**, 741.

33 G. A. Fisher and N. C. Norman, *Adv. Inorg. Chem.*, 1994, **41**, 233.

34 N. Mercier, N. Louvain and W. Bi, *CrystEngComm*, 2009, **11**, 720.

35 L. M. Wu, X. T. Wu and L. Chen, *Coord. Chem. Rev.*, 2009, **253**, 2787.

36 S. A. Adonin, M. N. Sokolov and V. P. Fedin, *Coord. Chem. Rev.*, 2016, **312**, 1.

37 J. Trotter and T. Zobel, *Z. Kristallogr.*, 1966, **123**, 67.

38 G. M. Sheldrick, *Acta Crystallogr., Sect. A: Found. Crystallogr.*, 2008, **64**, 112.

39 G. M. Sheldrick, *Acta Crystallogr., Sect. A: Found. Adv.*, 2015, **71**, 3.

40 G. M. Sheldrick, *Acta Crystallogr., Sect. C: Struct. Chem.*, 2018, **71**, 3.

41 O. V. Dolomanov, L. J. Bourhis, R. J. Gildea, J. A. K. Howard and H. Puschmann, *J. Appl. Crystallogr.*, 2009, **42**, 339.

42 K. Brandenburg, *Diamond*, Crystal Impact GbR, Bonn, Germany, 2005.

43 A. Gągor, G. Banach, M. Węcławik, A. Piecha-Bisiorek and R. Jakubas, *Dalton Trans.*, 2017, **46**, 16605.

44 A. J. Dennington and M. T. Weller, *Dalton Trans.*, 2018, **47**, 3469.

45 R. M. Bozorth, *J. Am. Chem. Soc.*, 1922, **44**, 2232.

46 A. M. Goforth, M. A. Tershansy, M. D. Smith, L. J. Peterson and H.-C. zur Loye, *Acta Crystallogr., Sect. C: Cryst. Struct. Commun.*, 2006, **62**, 381.

47 B. V. Bukvetskij, T. V. Storozhuk, A. G. Mirochnik, N. V. Petrochenkova and V. E. Karasev, *Zh. Neorg. Khim.*, 2004, **49**, 47.

48 G. A. Mousdis, N.-M. Ganotopoulos, H. Barkaoui, Y. Abid, V. Psycharis, A. Savvidou and C. P. Raptopoulou, *Eur. J. Inorg. Chem.*, 2017, 3401.

49 G. J. Perpétuo and J. Janczaka, *Acta Crystallogr., Sect. E: Struct. Rep. Online*, 2005, **61**, m2003.

50 I. Dance and M. Scudder, *CrystEngComm*, 2009, **11**, 2233–2247.

51 N. Pienack and W. Bensch, *Angew. Chem., Int. Ed.*, 2011, **50**, 2014.

52 A. M. Goforth, M. A. Tershansy, M. D. Smith, L. Peterson Jr., J. G. Kelley, W. J. I. DeBenedetti and H.-C. zur Loye, *J. Am. Chem. Soc.*, 2011, **133**, 603.

3.2. Divergent Optical Properties in an Isomorphous Family of Multinary Iodido Pentelates

Natalie Dehnhardt, Philip Klement, Sangam Chatterjee, Johanna Heine, *Inorganic Chemistry* **2019**, *58*, 10983-10990, DOI: 10.1021/acs.inorgchem.9b01466.

Abstract

Multinary organic inorganic metal halide materials beyond the perovskite motif can help to address both fundamental aspects such as the electronic interactions between different metalate building units and practical issues like stability and ease of preparation in this new field of research. However, such multinary compounds have remained quite rare for the halogenido pentelates, as the formation of simpler side phases can be a significant hindrance. Here, we report a family of four new multinary iodidopentelates $(PPh_4)_2ECu_2I_7$(nitrile) (E = Sb, Bi; nitrile = acetonitile or propionitrile), including the first metalate with a CuISb unit. The compounds can be obtained by facile solution or mechanochemical methods and display good stability up to 160 °C. A comparison with compounds containing binary anions $[EI_6]^{3-}$ reveals that, unexpectedly, the addition of the iodido cuprate unit causes a blue-shift in the absorption of the antimonates but a red-shift in the bismuthates. Photoluminescence investigations at 10 K show that the compounds display broad luminescence bands that correspond well with the trend in their onset of absorption. Overall, the work highlights that multinary, non-perovskite halogenido metalates can be a valuable expansion of the chemistry of metal halide perovskites.

Zusammenfassung

Während Halogenidopentelate mit Strukturmotiven, die Ausschnitte aus der Perowskitstruktur darstellen, im letzten Jahrzent intensiv erforscht wurden, zogen multinäre Pentelate abseits des Perowskit-Motivs nur wenig Aufmerksamkeit auf sich. Dabei bieten sie die Möglichkeit, diese Materialklasse in Bezug auf Elementsubstitutionen, damit verbundenen Eigenschaften und Stabilität detaillierter zu verstehen, da eine Vielzahl an anionischen Strukturmotiven und Elementkombinationen zugänglich sein sollte. In dieser Publikation wird über vier neue multinäre Kupfer-Iodidopentelate berichtet, unter ihnen die ersten multinären Antimonate die eine Cuprat-Einheit enthalten. Alle vier Verbindungen sind isomorph und unterscheiden sich durch das enthaltene Pentelatom (Sb, Bi) und das am Cu2-Atom koordinierende Nitril (Acetonitril=MeCN, Propionitril=EtCN).

Die Struktur der entsprechenden Anionen $(PPh_4)_2ECu_2I_7$(Nitril) in **1** bis **4** kann als ein $[EI_6]^{3-}$-Oktaeder, welches über eine gemeinsame Fläche mit einer $\{Cu_2I_4\text{Nitril}\}$-Einheit verbrückt ist, betrachtet werden. Zwei Ausschnitte aus der Kristallstruktur von **1** sind in Abbildung 3.2 a) und b) gezeigt.

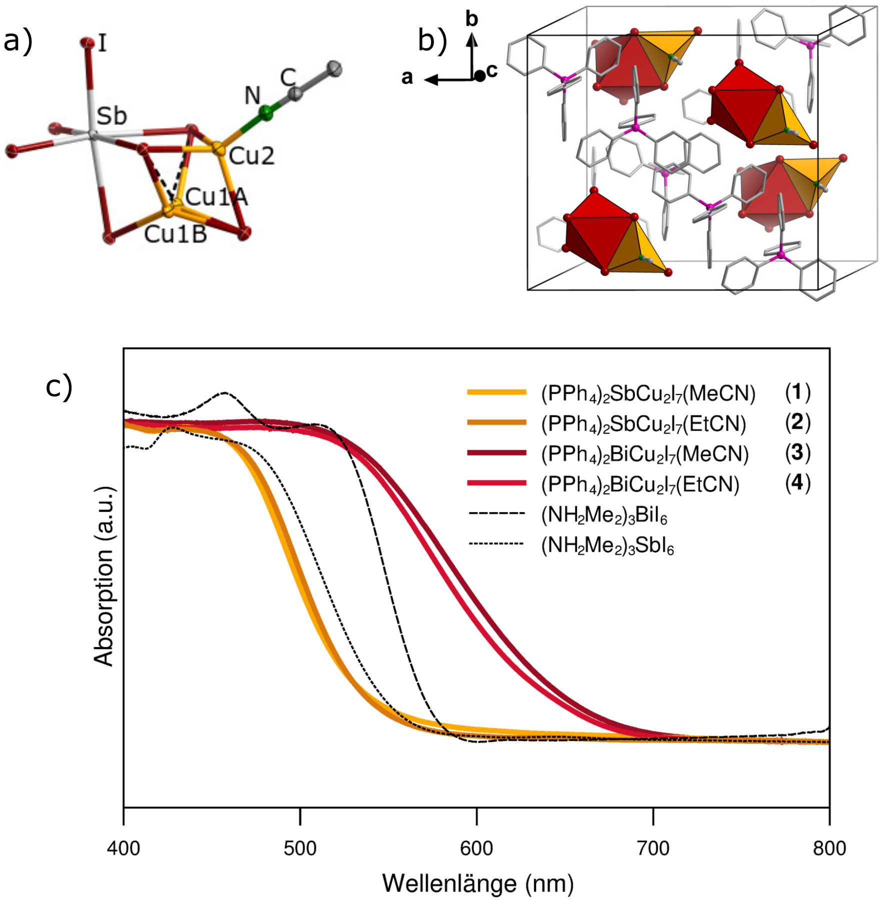

Abbildung 3.2: a) Molekülstruktur des Anions in **1**. Das Cu1-Atom ist über zwei Positionen fehlgeordnet, Ellipsoide sind mit 50 % Aufenthaltswahrscheinlichkeit, Wasserstoffatome nicht dargestellt. b) Ausschnitt aus der Kristallstruktur von **1**. Zur besseren Übersicht sind die Anionen in Polyederdarstellung abgebildet. c) UV-Vis-Spektren von **1** bis **4** im Vergleich zu zwei binären Metallaten.

Die Synthese der Verbindungen kann aus Lösung oder auf mechanochemischem Weg erfolgen, indem stöchiometrische Mischungen der entsprechenden Elementtrihalogenide EI_3 (E=Sb, Bi) mit Kupferiodid (CuI) und Tetraphenylphosphoniumiodid (PPh_4I) in dem jeweiligen Nitril umgesetzt werden. Kristalle der entsprechenden Verbindungen konnten bereits nach wenigen Stunden erhalten werden.

Mikrokristalline Pulver der Verbindungen konnten über *liquid assisted grinding* dargestellt werden. Diese Synthesemethode ermöglicht eine schnelle und saubere Synthese der Zielverbindungen mit nur einer sehr geringen Menge Lösungsmittel und kommt ohne weiteres Erhitzen aus.

Alle Proben wurden über Röntgenbeugung, Elementaranalyse, Infrarotspektroskopie, Thermogravimetrie und UV-Vis-Spektroskopie charakterisiert. Von den beiden Propionitrilverbindungen **2** und **4** wurden des Weiteren Photolumineszenzspektren aufgenommen. Die thermogravimetrische Analyse zeigt einen Masseverlust von 2-3 % zwischen 160 °C und

170 °C, der mit dem Verlust der Nitrilliganden am Cu2-Atom korrespondiert. Um neben der Stabilität der Verbindungen auch deren optische Eigenschaften zu untersuchen, wurden UV-Vis-Spektren aufgenommen. Die Farbe der Verbindungen, orange im Falle der Antimonate, dunkelrot im Falle der Bismutate, zeigt bereits, dass die Substitution des Hauptgruppenmetalls einen großen Einfluss auf die Absorptionseigenschaften des jeweiligen Materials hat. Diese können durch die Absorptionsspektren bestätigt werden, die eine Absorptionskante bei 530 nm für die Antimonverbindungen **1** und **2** und bei 650 nm für die Bismutverbindungen **3** und **4** zeigen. Die Absorptionsspektren sind in Abbildung 3.2 c) dargestellt.
Da auch das verknüpfende Übergangsmetall die optischen Eigenschaften beeinflussen kann, wurden zwei Referenzverbindungen synthetisiert. Diese enthalten jeweils mononukleare $[EI_6]^{3-}$-Anionen, ein Baustein der auch in den Anionen in **1** bis **4** vorkommt. Ein Vergleich der Absorptionsspektren lässt somit eine Abschätzung des Einflusses der Cu_2I_4Nitril-Einheiten auf die optischen Eigenschaften der dargestellten multinären Pentelate zu. Die Ergebnisse zeigen eine deutliche Rotverschiebung um 70 nm der Absorptionskanten der Bismutverbindungen **3** und **4**, verglichen mit der binären Referenzverbindung. Für die Antimonate wird hingegen eine entgegengesetzte Verschiebung um 30 nm in Richtung kürzerer Wellenlängen beobachtet. Die Photolumineszenzspektren bei 4 K zeigen breite Banden bei 1,80 eV (Bi) und 1,96 eV (Sb). Die Substitution des Hauptgruppenmetalls geht somit mit einer Verschiebung der Bande um 80 nm einher, was die Erkenntnisse aus den Absorptionsmessungen nochmals unterstreicht. Der unterschiedliche Einfluss der Cuprat-Einheit auf die optischen Eigenschaften macht deutlich, dass unterschiedliche elektronische Wechselwirkungen zwischen der Cuprat-Einheit und dem Antimon-, respektive Bismutatom in **1** bis **4** herrschen müssen, welche letztendlich zu den abweichenden optischen Eigenschaften führen.

Eigener Anteil

Das Strukturmotiv der dargestellten Pentelate wurde erstmals 2016 von *Hendrik Borkowski* beobachtet, der $(PPh_4)_2BiCu_2I_7(CH_3CN)$ (**3**) in seiner Masterarbeit synthetisierte. Alle weiteren Synthesen wurden von mir geplant, optimiert und durchgeführt, mit Ausnahme von $(PPh_4)_2SbCu_2I_7(CH_3CN)$ (**1**), welche von *Ana Pons Gomez* im Rahmen ihrer Bachelorarbeit unter meiner Anleitung durchgeführt wurde. Neben der Synthese in Lösung habe ich eine mechanochemische Syntheseroute entwickelt. Alle Verbindungen wurden über Röntgenbeugung an Einkristallen und Pulvern, UV-Vis-Spektroskopie, Infrarot-Spektroskopie, Thermogravimetrie und gekoppelte Differenzkalorimetrie sowie CHN-Elementaranalyse charakterisiert und identifiziert. Alle Ergebnisse wurden von mir ausgewertet und für die Publikation aufbereitet. Einkristallmessungen sowie Strukturlösung und -verfeinerung von **1** und **4** wurden von mir, von **2** und **3** von *Dr. Johanna Heine*, durchgeführt. Pulverdiffraktogramme, UV-Vis-Spektren und Infrarotspektren wurden von mir aufgenommen. Photolumineszenzspektren wurden von *Philip Klement* aus der Arbeitsgruppe von *Prof. Dr. Sangam Chatterjee* aufgenommen und ausgewertet. Thermogravimetrie und gekoppelte Differenzkalorimetrie wurden von *Uwe Justus* durchgeführt. Die CHN-Elementaranalyse wurde von der zentralen Abteilung für Massenspektrometrie und Elementaranalyse der Philipps-Universität Marburg durchgeführt. An der Erstellung des Manuskripts wirkten alle Co-Autoren mit.

Inorganic Chemistry
Article
Cite This: Inorg. Chem. 2019, 58, 10983−10990
pubs.acs.org/IC

Divergent Optical Properties in an Isomorphous Family of Multinary Iodido Pentelates

Natalie Dehnhardt,[†] Philip Klement,[‡] Sangam Chatterjee,[‡] and Johanna Heine*,[†]

[†]Department of Chemistry and Material Sciences Center, Philipps-Universität Marburg, Hans-Meerwein-Straße, 35043 Marburg, Germany

[‡]Institute of Experimental Physics I and Center for Materials Research (ZfM), Justus Liebig University Giessen, Giessen, Germany

Supporting Information

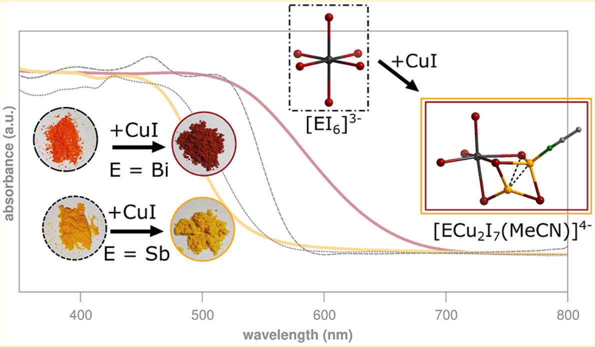

ABSTRACT: Multinary organic−inorganic metal halide materials beyond the perovskite motif can help to address both fundamental aspects such as the electronic interactions between different metalate building units and practical issues like stability and ease of preparation in this new field of research. However, such multinary compounds have remained quite rare for the halogenido pentelates, as the formation of simpler side phases can be a significant hindrance. Here, we report a family of four new multinary iodido pentelates $[PPh_4]_2[ECu_2I_7(\text{nitrile})]$ (E = Sb, Bi; nitrile = acetonitile or propionitrile), including the first metalate with a Cu−I−Sb unit. The compounds can be obtained by facile solution or mechanochemical methods and display good stability up to 160 °C. A comparison with compounds containing binary anions $[EI_6]^{3-}$ reveals that, unexpectedly, the addition of the iodido cuprate unit causes a blue-shift in the absorption of the antimonates but a red-shift in the bismuthates. Photoluminescence investigations at 10 K show that the compounds display broad luminescence bands that correspond well with the trend in their onset of absorption. Overall, the work highlights that multinary, non-perovskite halogenido metalates can be a valuable expansion of the chemistry of metal halide perovskites.

INTRODUCTION

Metal halide perovskite materials have seen enormous progress from the earliest reports[1,2] to crystal engineering of the dimensionality and properties of tin halide perovskites,[3,4] their first use in photovoltaics (PV),[5] and the recent successful development of highly efficient PV devices[6−8] using lead iodide perovskites[9,10] such as $(CH_3NH_3)PbI_3$.[11,12] Still, with regard to large-scale application, issues of toxicity[13] and long-term stability[14] remain to be addressed and are currently under intense investigation.

One way to alleviate the toxicity of the perovskite materials is by replacement of lead with bismuth, whose compounds have generally proven to be much more benign.[15] However, replacing Pb^{2+} with Bi^{3+} leads to a distinctly different structural chemistry. For example, the reaction of BiI_3 with CH_3NH_3I yields $(CH_3NH_3)_3Bi_2I_9$,[16] a bismuthate with molecular $Bi_2I_9^{3-}$ anions comprised of two face-sharing octahedra. The compound exhibits highly localized exciton dynamics[17] and prototype PV devices have shown only moderate efficiencies,[18] although for other types of applications, such as memristors,[19] hard radiation detectors,[20] and luminescent nanoparticles,[21] this and related materials appear more promising. Using bismuthates with anions of higher dimensionality should in principle improve PV device performance due to lower band gaps and improved charge transport properties.[22,23] However, despite their rich structural chemistry,[24−26] iodido bismuthates are typically limited to molecular anions or strand-like topologies. The exception to this are layered anions in $(H_2AEQT)Bi_{2/3}I_4$ (AEQT = 5,5‴-bis(aminoethyl)-2,2′:5′,2″:5″,2‴-quaterthiophene)[27] and $A_3Bi_2I_9$[28,29] (A = K, Rb).[30−32] Similar observations have been made for the structural chemistry[33,34] and PV device performance[35−38] of the closely related but much less studied iodido antimonates.[39]

To expand the limits of halogenido pentelate chemistry, one approach has been the heterovalent substitution of Pb^{2+} with Bi^{3+} or Sb^{3+} and a monovalent cation such as Ag^+.[40] This way, double perovskites $AE^{(III)}AgX_6$ (A = Cs, CH_3NH_3; E = Sb, Bi; X = Cl, Br, I)[41−45] have been developed that show promising properties, as demonstrated in PV devices,[46] that can also be improved upon by doping.[47,48] Similar to lead halide perovskites, the dimensionality of double perovskites can be controlled with the use of larger organic cations.[49] In a different approach, multinary, layered (111) perovskites such as $Cs_4CuSb_2Cl_{12}$ can be obtained.[50] Aside from the replication of different perovskite motifs, Rudorffites of composition Ag/Bi/I have recently generated a lot of interest as light-absorbing materials as well.[51−55]

Received: May 20, 2019
Published: August 7, 2019

DOI: 10.1021/acs.inorgchem.9b01466
Inorg. Chem. 2019, 58, 10983−10990

Despite this, very few compounds featuring ternary anions $[M_xE_yI_z]^{q-}$ that go beyond the perovskite motif have been reported to date: The works of Feldmann[56] and Chen[57−59] demonstrated the general feasibility of including transition metal ions such as Cu^+, Ag^+, and Hg^{2+} in iodido bismuthates, and Adonin[60] extended this chemistry to include the first iodido bismuthate with Pt^{4+}. In our group, we showed that the isostructural silver and copper iodido bismuthates $[PPh_4]_4[Bi_2M_2I_{12}]$ (M = Cu, Ag) can serve as model compounds for a deeper understanding of the influence of the metal M on the optical properties of iodido bismuthates.[61] Pike and co-workers presented a number of mixed ligand metalates in the Cu/Bi/I system.[62] For iodido antimonates, no compound featuring a ternary anion except for the double perovskite $(CH_3NH_3)_2AgSbI_6$ is known.[63]

In this work, we introduce $[PPh_4]_2[ECu_2I_7(\text{nitrile})]$ (E = Sb, Bi; nitrile = acetonitile or propionitrile), an isomorphous family of compounds that allows for a comparison of the divergent effects of Sb/Bi substitution on the optical properties of copper iodido pentelates. The antimony compounds represent the first examples of multinary Sb/M/I anions beyond the double perovskite motif.

■ EXPERIMENTAL SECTION

General. BiI_3 and SbI_3 were synthesized from the elements according to literature procedures.[64,65] Tetraphenylphosphonium iodide (PPh_4I, 98%) and CuI were used as supplied from commercial sources. The reference compounds $[NH_2Me_2]_3[EI_6]$ were prepared according to a modified literature procedure (see the Supporting Information for details).[66] CHN analysis was carried out on an Elementar CHN-analyzer. Thermal analysis was conducted on a Netzsch STA 409 CD instrument from 25 to 1200 °C with a heating rate of 10 °C min^{-1} in a constant flow of 150 mL min^{-1} Ar. Powder patterns were recorded on a STADI MP (STOE Darmstadt) powder diffractometer, with Cu Kα1 radiation with $\lambda = 1.54056$ Å at room temperature in transmission mode. IR spectra were measured on a Bruker Tensor 37 FT-IR spectrometer equipped with an ATR-Platinum measuring unit.

Synthesis in Solution. *$[PPh_4]_2[SbCu_2I_7(CH_3CN)]$ (1).* SbI_3 (50 mg, 0.1 mmol), CuI (38 mg, 0.2 mmol), and PPh_4I (94 mg. 0.2 mmol) were dissolved in 10 mL of acetonitrile by heating to boiling under magnetic stirring for 30 min. The hot reaction solution was slowly cooled to room temperature and stored for crystallization. Bright orange block-shaped crystals precipitated after 1 h at room temperature. The crystals were isolated by filtration (yield: 94.2 mg, 0.05 mmol, 50%). Data for **1**: Anal. Calcd for $C_{50}H_{43}NSbCu_2I_7P_2$ (M = 1856.92 g mol^{-1}): C, 32.34; H, 2.33; N, 0.75%. Found: C, 32.41; H, 2.409; N, 0.78%.

$[PPh_4]_2[SbCu_2I_7(CH_3CH_2CN)]$ (2). SbI_3 (50 mg, 0.1 mmol), CuI (38 mg, 0.2 mmol), and PPh_4I (94 mg. 0.2 mmol) were dissolved in 10 mL of propionitrile by heating to boiling under magnetic stirring for 30 min. The hot reaction solution was slowly cooled to room temperature and stored for crystallization. Bright orange block-shaped crystals precipitated after 2 h at room temperature. The crystals were isolated by filtration (yield: 41 mg, 0.022 mmol, 22%). Data for **2**: Anal. Calcd for $C_{51}H_{45}NSbCu_2I_7P_2$ (M = 1870.95 g mol^{-1}): C, 32.74; H, 2.42; N, 0.75%. Found: C, 32.82; H, 2.581; N, 0.81%.

$[PPh_4]_2[BiCu_2I_7(CH_3CN)]$ (3). BiI_3 (59 mg, 0.1 mmol), CuI (38 mg, 0.2 mmol), and PPh_4I (94 mg. 0.2 mmol) were dissolved in 10 mL of acetonitrile by heating to boiling under magnetic stirring for 30 min. The hot reaction solution was slowly cooled to room temperature and stored for crystallization. Dark red block-shaped crystals precipitated after 3 days at room temperature. The crystals were isolated by filtration (yield: 98.1 mg, 0.05 mmol, 50%). Data for **3**: Anal. Calcd for $C_{50}H_{43}NBiCu_2I_7P_2$ (M = 1944.15 g mol^{-1}): C, 30.89; H, 2.23; N, 0.72%. Found: C, 31.05; H, 2.404; N, 0.76%.

$[PPh_4]_2[BiCu_2I_7(CH_3CH_2CN)]$ (4). BiI_3 (59 mg, 0.1 mmol), CuI (38 mg, 0.2 mmol), and PPh_4I (94 mg. 0.2 mmol) were dissolved in 5 mL of propionitrile by heating to boiling under magnetic stirring for 30 min. The hot reaction solution was slowly cooled to room temperature and stored for crystallization. Dark red block-shaped crystals precipitated after 2 h at room temperature. The crystals were isolated by filtration (yield: 48.9 mg, 0.025 mmol, 25%). Data for **4**: Anal. Calcd for $C_{51}H_{45}NBiCu_2I_7P_2$ (M = 1958.18 g mol^{-1}): C, 31.28; H, 2.32; N, 0.72%. Found: C, 31.44; H, 2.383; N, 0.76%.

Mechanochemical Preparation. Microcrystalline powders of **1**−**4** could be obtained by liquid assisted grinding (LAG) of a mixture of 0.1 mmol of EI_3, 0.2 mmol of CuI, and 0.2 mmol of PPh_4I for 3 min in 1 mL of the required nitrile, using a porcelain mortar. PXRD patterns confirmed the presence of the products and the absence of any crystalline starting materials or byproducts such as compounds with binary anions (Figure S20).

X-ray Crystallography. Single crystal X-ray determination was performed on a Bruker Quest D8 diffractometer with microfocus Mo Kα radiation and a Photon 100 (CMOS) detector or on a STOE IPDS2 diffractometer equipped with an imaging plate detector system using Mo Kα radiation with graphite monochromatization. The structures were solved using direct methods, refined by full-matrix least-squares techniques, and expanded using Fourier techniques, using the Shelx software package[67−69] within the OLEX2 suite.[70] Pictures of the crystal structures were created using DIAMOND.[71] Additional details on the refinement of each structure can be found in the Supporting Information.

Optical Characterization. Low-temperature PL measurements were conducted in a continuous-flow liquid He coldfinger cryostat cooled to 10 K with the sample in a vacuum. A Ti:sapphire laser was frequency-doubled for excitation (400 nm), and the excitation light was focused into a 3 μm diameter spot (390 μW excitation power) using a confocal beam path with all-reflective optics. PL was spectrally filtered through a $^1/_4$ m monochromator (Oriel MS260i) and detected on a Si charge-coupled device camera (Andor DU440). Optical absorption spectra were recorded on a Varian Cary 5000 UV/Vis/NIR spectrometer in the range 200−800 nm in diffuse reflectance mode employing a Praying Mantis accessory (Harrick). For ease of viewing, raw data was transformed from % reflectance R to absorbance A according to $A = \log(1/R)$, which yields estimates comparable to the widely used Kubelka−Munk relation.[72]

■ RESULTS AND DISCUSSION

Synthesis. The synthesis of $[PPh_4]_2[ECu_2I_7(CH_3CN)]$ and $[PPh_4]_2[MCu_2I_7(CH_3CH_2CN)]$ (M = Sb, Bi) single crystals was accomplished by dissolving stochiometric ratios of the reactants in hot acetonitrile or propionitrile, respectively. The clear bright orange (Sb) and red (Bi) reaction solutions were allowed to cool to ambient temperature. After a few hours, orange blocks of $[PPh_4]_2[SbCu_2I_7(CH_3CN)]$ (**1**) and $[PPh_4]_2[SbCu_2I_7(CH_3CH_2CN)]$ (**2**) and dark red blocks of $[PPh_4]_2[BiCu_2I_7(CH_3CN)]$ (**3**) and $[PPh_4]_2[BiCu_2I_7(CH_3CH_2CN)]$ (**4**) were obtained. Crystals of **1** and **3** are displayed in Figure 1. Microcrystalline powders of the title compounds could be obtained via liquid assisted grinding (LAG) of a stoichiometric mixture of the reactants with the respective nitrile (see also Figure 1C and D). This method allows a rapid and clean synthesis using a minimal amount of solvent (1 mL) and no further heating and yields products with very good crystallinity. For **1** and **3**, we also found that the compounds could be quantitatively obtained as microcrystalline powders by evaporating the solvent on a rotary evaporator. This is in contrast to our findings when using ketones in the PPh_4/Cu/Bi/I system, where the use of nonstoichiometric reactant mixtures and careful control of crystallization conditions was necessary to avoid the formation of byproducts.[61]

DOI: 10.1021/acs.inorgchem.9b01466
Inorg. Chem. 2019, 58, 10983−10990

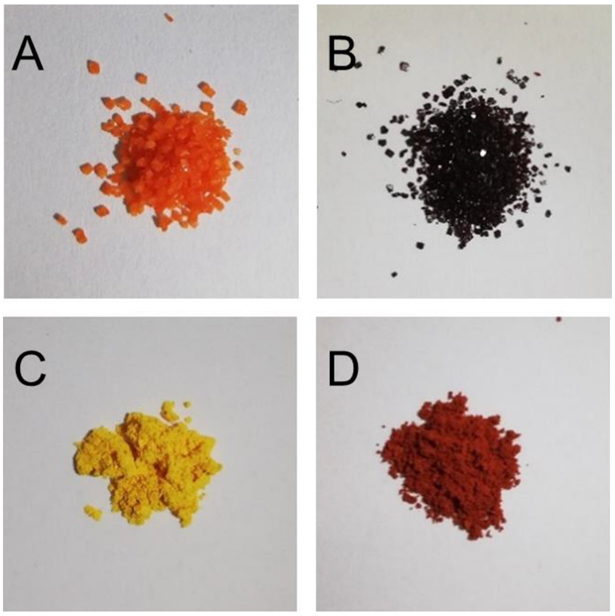

Figure 1. Photographs of crystals of **1** (A) and **3** (B) as well as microcrystalline powders of **1** (C) and **3** (D) with side length equal to about 1 cm.

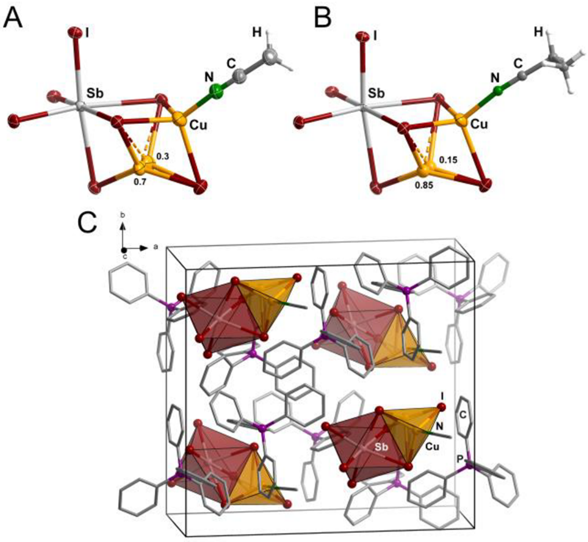

Figure 2. Structures of the anions in **1** (A) and **2** (B) with occupancies given for the disordered Cu atoms. Ellipsoids shown at 70% probability. Only the majority component of the disordered CH_3CH_2CN ligand is shown for **2**. Disordered atoms were refined isotropically in **2**. (C) Packing in the crystal structure of **1**; atoms and bonds shown in ball-and-stick representation.

Description of the Crystal Structures. The four isomorphous iodido metalates crystallize in the monoclinic space group *Cc* (Table 1). The structure of the iodido metalate anions can be described as a EI_6 octahedron, connected to a Cu_2I_4(nitrile) unit via a common face. Crystal structures are shown in Figure 2.

Interatomic distances within the anions are very similar throughout the series, as shown in Table 2. E–I distances are shorter for terminal and longer for bridging iodine atoms and very similar to values found for dinuclear $[E_2I_9]^{3-}$ ions.[73]

One of the Cu atoms is disordered over two positions in compounds **1**–**3**. The position with major (or in the case of **4**, full) occupation can be described as trigonally coordinated, as the Cu atom lies nearly directly within the plane of the coordinating iodine atoms. The second position, displaying occupancies of 0.3, 0.25, and 0.15 in **1**, **2**, and **3**, respectively, is closer to a tetrahedral coordination environment but still significantly distorted. Figure S5 illustrates the relevant interatomic distances in both positions for compound **1**.

The second copper atom as well as the nitrile ligand likely have a significant influence on this disorder, as an ideal tetrahedrally coordinated position, which would be more favorable with respect to shorter, more uniform Cu–I bonds, generates unphysically short Cu–Cu distances between the two copper atoms. Due to the distorted coordination environments of the copper atoms, two sets of Cu–I distances are observed, shorter ones below 2.8 Å and longer ones above

Table 1. Summary of Crystallographic Data for 1–4 (see the Supporting Information for Additional Details)

	1	2	3	4
empirical formula	$C_{50}H_{43}Cu_2I_7NP_2Sb$	$C_{51}H_{45}Cu_2I_7NP_2Sb$	$C_{50}H_{43}BiCu_2I_7NP_2$	$C_{51}H_{45}BiCu_2I_7NP_2$
formula weight/g·mol^{-1}	1856.92	1870.95	1944.26	1958.18
crystal system	monoclinic			
space group	*Cc*			
a/Å	19.5958(8)	19.7444(8)	19.6722(9)	19.6427(7)
b/Å	17.2708(5)	17.4660(7)	17.3553(8)	17.5050(4)
c/Å	16.7887(8)	16.9029(7)	16.8568(8)	16.8610(5)
β/deg	103.833(3)	104.0120(10)	103.836(2)	104.022(3)
V/Å^3	5517.1(4)	5655.6(4)	5588.2(5)	5624.8(3)
Z	4			
ρ_{calc}/g·cm^{-3}	2.236	2.197	2.311	2.312
independent reflections	16822	10288	9832	18208
R(int)	0.0512	0.0389	0.0349	0.0415
R_1 ($I > 2\sigma(I)$)	0.0311	0.0149	0.0142	0.0310
wR_2 (all data)	0.0653	0.0295	0.0315	0.0751
S (all data)	0.840	1.075	0.918	1.017
$\Delta\rho_{max}$, $\Delta\rho_{min}$/e·Å^{-3}	1.66/−1.33	0.67/−0.85	0.49/−0.71	3.60/−1.65
Flack parameter	−0.02(2)	0.000(6)	0.0136(2)	−0.024(3)

DOI: 10.1021/acs.inorgchem.9b01466
Inorg. Chem. 2019, 58, 10983–10990

Table 2. Comparison of E−I, Cu−I, Cu···Cu, E···Cu, Cu−N, and N−C Distances of Compounds **1**−**4** in Å

	E−I	Cu−I	Cu···Cu	E···Cu	Cu−N	N−C
1	2.849−3.207	2.458−3.335	2.416−2.484	3.434−3.429	1.943	1.130
2	2.872−3.298	2.443−3.470	2.420−2.509	3.498−3.505	1.938−1.952	1.125−1.144
3	2.937−3.270	2.469−3.350	2.422−2.493	3.464−3.368	1.937	1.145
4	2.952−3.279	2.489−3.465	2.500	3.510	1.940	1.140

3.0 Å, longer than the sum of the atomic or ionic radii (2.7 or 2.8 Å respectively) but still well below the sum of the van der Waals radii of 4.4 Å.[74] Extensive disorder in the Cu(I) positions is a common phenomenon in iodido cuprate compounds,[75] so it is not surprising to see it here as well.

A graphic comparison of the atomic distances and angles, shown in Figure 3, shows that the substitution of the central Sb atom with Bi has little impact on the structure of the anion. In contrast, more pronounced changes can be observed when changing the ligand from acetonitrile to propionitrile. The nitrile ligand also has an influence on the disordered Cu atom position, as the trigonal coordination is more strongly preferred over the distorted tetrahedral one in both propionitrile compounds.

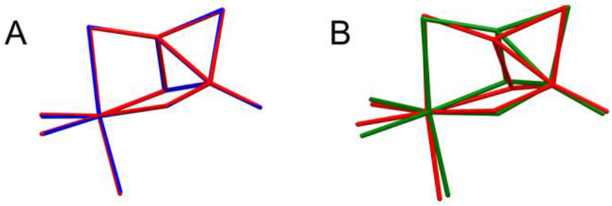

Figure 3. Comparison of atomic distances and angles. The organic ligands are represented by their nitrogen positions. For the disordered Cu atom, preferred positions were chosen. (A) Comparison of propionitril compounds **2** (Sb, blue) and **4** (Bi, red). (B) Comparison of bismuth compounds **3** (acetonitrile, red) and **4** (propionitrile, green).

Intermetallic Cu···Cu distances are uniform across the series and fairly short, below the interatomic distance of 2.56 Å found in metallic copper,[76] although similar distances have been found in a number of halogenido cuprates.[77,78] In contrast, E···Cu distances are equally uniform but longer than typical Sb−Cu (e.g., 2.57 Å in $[Cu_4I_4(Sb^iPr_3)_4]$[79]) or Bi−Cu bonds (e.g., 2.74 Å in $[(Me_3Si)_2BiCu(PMe_3)_3]$[80]), suggesting little direct interaction between the respective metal atoms.

The polar nature of the compounds, as manifested by the non-centrosymmetric space group *Cc*, suggests that, similar to other polar halogenido metalates, they may also be candidate materials for second harmonic generation as well as ferroelectrics.[81,82]

Stability. All four compounds are fairly stable: Thermal decomposition proceeds via a first weight loss step that corresponds to the loss of the respective nitrile ligand between 160 and 175 °C. A second weight loss step sets in at 310 °C for the antimony and 380 °C for the bismuth compounds, indicating a possible onset of EI_3 sublimation concomitant with additional decomposition reactions (see Figures S6−S9). **1**−**4** are also stable against air and moisture, but after several weeks, a deepening of the crystal color can be observed, indicating surface level degradation.

Optical Properties. As illustrated in Figure 1, the incorporated main group metal in compounds **1**−**4** has a striking influence on the crystals' colors. While the antimony compounds are bright orange, the bismuth compounds are dark red. Optical absorption spectra of the microcrystalline powders obtained in diffuse reflection reveal that the nitrile ligands have little influence on the absorption properties, as expected. **1** and **2** show an onset of absorption at 530 nm, while the bismuth compounds **3** and **4** display an onset of absorption at 650 nm (Figure 4).

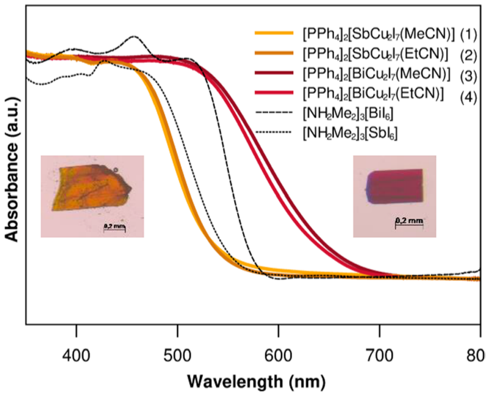

Figure 4. Optical absorption spectra from diffuse reflectance measurements of microcrystalline powders of **1**−**4** and the reference compounds $[NH_2Me_2]_3[EI_6]$. Photographs of crystals of **1** (left) and **3** (right) are shown as insets.

These results, a lighter color in the iodido antimonates compared to the bismuthates, are well in line with literature examples of compounds containing binary E/I anions.[83] In contrast, double perovskites show a different behavior: Here, a decrease in band gap is observed in the solid solution series $Cs_2Ag(Bi_{1-x}Sb_x)Br_6$ with increasing antimony content.[48] However, this effect is not reproduced in the two iodides $(MA)_2AgEI_6$ (E = Sb, Bi) which are very similar in their onset of absorption.[45,63] Computational results for the hypothetical double perovskites Cs_2CuEI_6 suggest a similar behavior as that observed for the silver bromide compounds,[84] although an experimental confirmation of this is likely to remain impossible.[85]

To directly estimate the influence of the coordination of the dinuclear copper unit on the EI_6 anion in **1**−**4**, we have prepared two reference compounds $[NH_2Me_2]_3[EI_6]$ that feature mononuclear $[EI_6]^{3-}$ anions.[66] For the antimonates, the onset of absorption is blue-shifted ca. 30 nm going from the binary to the ternary anion. In contrast to this, for the bismuthates, the onset of absorption is red-shifted ca. 70 nm going from binary to ternary anions.

It has been observed that the optical properties of halogenido tetrelates and pentelates do not solely depend on the nature of the metalate anion and its dimensionality. Other factors such as halide−halide interactions or the orientation and separation of the anions can have a noticeable influence.[11]

DOI: 10.1021/acs.inorgchem.9b01466
Inorg. Chem. 2019, 58, 10983−10990

However, these additional factors should contribute in an identical way in both the antimony and the bismuth compounds, as both the dimethylammonium compounds as well as **1**−**4** are isomorphous. Thus, our results point to a significant difference in the electronic interactions with the iodido cuprate unit between antimony and bismuth, resulting in divergent optical properties of the ternary metalates.

This interpretation is further supported by low-temperature PL measurements of single crystals **2** and **4** (Figure 5). We observe one pronounced broad peak at 1.96 eV (600 nm) for the antimonate **2** and one narrower peak at 1.80 eV (680 nm) for the bismuthate **4**. Thus, the substitution of Bi for Sb produces a red-shift of the PL by 160 meV (80 nm) and a reduction of the line width by one-half. This is accompanied by the intensity decreasing by two-thirds as it was recorded under identical experimental conditions. This is in good agreement with the shift of the onset of absorption (Figure 4).

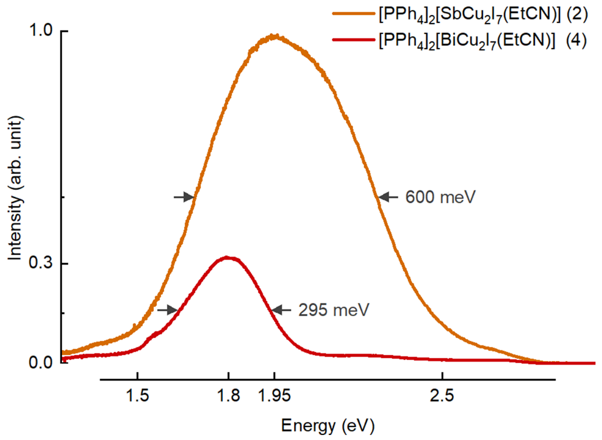

Figure 5. Low-temperature photoluminescence spectra of the antimonate **2** and bismuthate **4** (orange and red lines) at 10 K.

Neutral copper halide clusters are well-known for featuring intense emissions in the visible spectrum even at room temperature.[86] Iodido cuprates are less prominent but can also show good luminescence properties.[87,88] Iodido pentelates are even less studied in this respect,[89] but some comprehensive data is available for $Cs_3E_2I_9$ compounds. In the bulk phases, weak, broad luminescence bands are observed at room temperature.[29] In contrast, nanoparticles of $Cs_3Sb_2I_9$ display bright, narrow room temperature luminescence,[90] while those of $Cs_3Bi_2I_9$ show a broader, less intense band.[21] Reference luminescence data on multinary iodido pentelates is limited to a single example, colloidal nanoparticles of the double perovskite Cs_2AgBiI_6, where a broad peak at 575 nm with a low quantum efficiency was observed,[91] a behavior similar to nanoparticles of the binary $Cs_3Bi_2I_9$.[21] Additionally, the single crystalline 2D double perovskite $[AE2T]_2AgBiI_8$ (AE2T = 5,5-diylbis(aminoethyl)-[2,2-bithiophene]) was reported to not display significant luminescence even at 78 K.[92]

While more in-depth studies of our compounds' optical properties are planned as part of our future work, we suggest that our results can be viewed as akin to the findings for the binary pentelates, with bulk luminescence properties strongly dominated by quenching trap states. Still, especially the more strongly emitting antimonates are good candidates for the synthesis of nanoparticles.

■ CONCLUSION

In conclusion, we have shown that new multinary iodido pentelates can be prepared via a clean and efficient route and that going from binary E/I to ternary Cu/E/I anions has a distinctly different effect on the compounds' optical properties for antimonates and bismuthates. We hope that our work demonstrates that halogenido metalates going beyond the perovskite motif are a promising class of materials, both as a point of reference for perovskites as well as on their own.

■ ASSOCIATED CONTENT

Ⓢ Supporting Information

The Supporting Information is available free of charge on the ACS Publications website at DOI: 10.1021/acs.inorgchem.9b01466.

> Additional crystallographic details, thermal analysis, powder diffraction, IR spectroscopy, and optical properties (PDF)

Accession Codes

CCDC 1914215−1914218 contain the supplementary crystallographic data for this paper. These data can be obtained free of charge via www.ccdc.cam.ac.uk/data_request/cif, or by emailing data_request@ccdc.cam.ac.uk, or by contacting The Cambridge Crystallographic Data Centre, 12 Union Road, Cambridge CB2 1EZ, UK; fax: +44 1223 336033.

■ AUTHOR INFORMATION

Corresponding Author

*E-mail: johanna.heine@chemie.uni-marburg.de.

ORCID

Philip Klement: 0000-0001-7044-713X
Sangam Chatterjee: 0000-0002-0237-5880
Johanna Heine: 0000-0002-6795-5288

Notes

The authors declare no competing financial interest.

■ ACKNOWLEDGMENTS

This work is funded by the SFB 1083. J.H. thanks Prof. Stefanie Dehnen for her support. N.D. thanks the Fonds der Chemischen Industrie and the Studienstiftung des Deutschen Volkes for their support. S.C. acknowledges financial support by the Heisenberg programme (CH660/2). The authors thank Benjamin Gunschera for his help in preparing the $[NH_2Me_2]_3[EI_6]$ reference compounds.

■ REFERENCES

(1) Wells, H. L. Über die Cäsium- und Kalium-Bleihalogenide. *Z. Anorg. Chem.* **1893**, *3*, 195−210.

(2) Møller, C. K. Crystal Structure and Photoconductivity of Cæsium Plumbohalides. *Nature* **1958**, *182*, 1436.

(3) Mitzi, D. B.; Feild, C. A.; Harrison, W. T. A.; Guloy, A. M. Conducting Tin Halides with a Layered Organic-Based Perovskite Structure. *Nature* **1994**, *369*, 467−469.

(4) Mitzi, D. B. Templating and Structural Engineering in Organic-Inorganic Perovskites. *J. Chem. Soc., Dalton Trans.* **2001**, 1−12.

(5) Kojima, A.; Teshima, K.; Shirai, Y.; Miyasaka, T. Organometal Halide Perovskites as Visible-Light Sensitizers for Photovoltaic Cells. *J. Am. Chem. Soc.* **2009**, *131*, 6050−6051.

(6) Saliba, M.; Correa-Baena, J.-P.; Grätzel, M.; Hagfeldt, A.; Abate, A. Perovskite Solar Cells: From the Atomic Level to Film Quality and Device Performance. *Angew. Chem., Int. Ed.* **2018**, *57*, 2554−2569.

(7) Jena, A. K.; Kulkarni, A.; Miyasaka, T. Halide Perovskite Photovoltaics: Background, Status, and Future Prospects. *Chem. Rev.* **2019**, *119*, 3036−3103.

(8) Green, M. A.; Hishikawa, Y.; Dunlop, E. D.; Levi, D. H.; Hohl-Ebinger, J.; Yoshita, M.; Ho-Baillie, A. W. H. Solar Cell Efficiency Tables (Version 53). *Prog. Photovoltaics* **2019**, *27*, 3−12.

(9) Weber, D. $CH_3NH_3PbX_3$, ein Pb(II)-System mit kubischer Perowskitstruktur. *Z. Naturforsch., B: J. Chem. Sci.* **1978**, *33b*, 1443−1445.

(10) Baikie, T.; Fang, Y.; Kadro, J. M.; Schreyer, M.; Wei, F.; Mhaisalkar, S. G.; Grätzel, M.; White, T. J. Synthesis and Crystal Chemistry of the Hybrid Perovskite $(CH_3NH_3)PbI_3$ for Solid-State Sensitised Solar Cell Applications. *J. Mater. Chem. A* **2013**, *1*, 5628−5641.

(11) Saparov, B.; Mitzi, D. B. Organic−Inorganic Perovskites: Structural Versatility for Functional Materials Design. *Chem. Rev.* **2016**, *116*, 4558−4596.

(12) Manser, J. S.; Christians, J. A.; Kamat, P. V. Intriguing Optoelectronic Properties of Metal Halide Perovskites. *Chem. Rev.* **2016**, *116*, 12956−13008.

(13) Babayigit, A.; Boyen, H.-G.; Conings, B. Environment versus sustainable energy: The case of lead halide perovskite-based solar cells. *MRS Energy & Sustainability* **2018**, DOI: 10.1557/mre.2017.17.

(14) Boyd, C. C.; Cheacharoen, R.; Leijtens, T.; McGehee, M. D. Understanding Degradation Mechanisms and Improving Stability of Perovskite Photovoltaics. *Chem. Rev.* **2019**, *119*, 3418−3451.

(15) Yang, N.; Sun, H. Biocoordination Chemistry of Bismuth: Recent Advances. *Coord. Chem. Rev.* **2007**, *251*, 2354−2366.

(16) Eckhardt, K.; Bon, V.; Getzschmann, J.; Grothe, J.; Wisser, F. M.; Kaskel, S. Crystallographic Insights into $(CH_3NH_3)_3(Bi_2I_9)$: A New Lead-Free Hybrid Organic−Inorganic Material as a Potential Absorber for Photovoltaics. *Chem. Commun.* **2016**, *52*, 3058−3060.

(17) Scholz, M.; Flender, O.; Oum, K.; Lenzer, T. Pronounced Exciton Dynamics in the Vacancy-Ordered Bismuth Halide Perovskite $(CH_3NH_3)_3Bi_2I_9$ Observed by Ultrafast UV−vis−NIR Transient Absorption Spectroscopy. *J. Phys. Chem. C* **2017**, *121*, 12110−12116.

(18) Jain, S. M.; Phuyal, D.; Davies, M. L.; Li, M.; Philippe, B.; De Castro, C.; Qiu, Z.; Kim, J.; Watson, T.; Tsoi, W. C.; Karis, O.; Rensmo, H.; Boschloo, G.; Edvinsson, T.; Durrant, J. R. An Effective Approach of Vapour Assisted Morphological Tailoring for Reducing Metal Defect Sites in Lead-Free, $(CH_3NH_3)_3Bi_2I_9$ Bismuth-Based Perovskite Solar Cells for Improved Performance and Long-Term Stability. *Nano Energy* **2018**, *49*, 614−624.

(19) Hu, Y.; Zhang, S.; Miao, X.; Su, L.; Bai, F.; Qiu, T.; Liu, J.; Yuan, G. Ultrathin $Cs_3Bi_2I_9$ Nanosheets as an Electronic Memory Material for Flexible Memristors. *Adv. Mater. Interfaces* **2017**, *4*, 1700131.

(20) McCall, K. M.; Liu, Z.; Trimarchi, G.; Stoumpos, C. C.; Lin, W.; He, Y.; Hadar, I.; Kanatzidis, M. G.; Wessels, B. W. α-Particle Detection and Charge Transport Characteristics in the $A_3M_2I_9$ Defect Perovskites (A = Cs, Rb; M = Bi, Sb). *ACS Photonics* **2018**, *5*, 3748−3762.

(21) Yang, B.; Chen, J.; Hong, F.; Mao, X.; Zheng, K.; Yang, S.; Li, Y.; Pullerits, T.; Deng, W.; Han, K. Lead-Free, Air-Stable All-Inorganic Cesium Bismuth Halide Perovskite Nanocrystals. *Angew. Chem., Int. Ed.* **2017**, *56*, 12471−12475.

(22) Li, T.; Hu, Y.; Morrison, C. A.; Wu, W.; Han, H.; Robertson, N. Lead-free pseudo-three-dimensional organic−inorganic iodobismuthates for photovoltaic applications. *Sustainable Energy Fuels* **2017**, *1*, 308−316.

(23) Usoltsev, A. N.; Elshobaki, M.; Adonin, S. A.; Frolova, L. A.; Derzhavskaya, T.; Abramov, P. A.; Anokhin, D. V.; Korolkov, I. V.; Luchkin, S. Yu.; Dremova, N. N.; Stevenson, K. J.; Sokolov, M. N.; Fedin, V. P.; Troshin, P. A. Polymeric Iodobismuthates $\{[Bi_3I_{10}]\}$ and $\{[BiI_4]\}$ with N-Heterocyclic Cations: Promising Perovskite-Like Photoactive Materials for Electronic Devices. *J. Mater. Chem. A* **2019**, *7*, 5957−5966.

(24) Lazarini, F. Structure of Diethylammonium Enneaiododibismuthate(III). *Acta Crystallogr., Sect. C: Cryst. Struct. Commun.* **1987**, *C43*, 875−877.

(25) Krautscheid, H. Synthese und Kristallstrukturen von $[Li(thf)_4]_2[Bi_4I_{14}(thf)_2]$, $[Li(thf)_4]_4[Bi_5I_{19}]$ und $(Ph_4P)_4[Bi_6I_{22}]$. *Z. Anorg. Allg. Chem.* **1994**, *620*, 1559−1564.

(26) Papavassiliou, G. C.; Koutselas, I. B.; Terzis, A.; Raptopouloir, C. P. Preparation and Characterization of $(C_6H_5CH_2CH_2NH_3)_4BiI_7\cdot H_2O$, $(C_6H_5CH_2CH_2NH_3)BiBr_6$ and $(C_6H_5CH_2CH_2NH_3)_3BiCl_6$. *Z. Naturforsch., B: J. Chem. Sci.* **1995**, *50*, 1566−1569.

(27) Mitzi, D. B. Organic-Inorganic Perovskites Containing Trivalent Metal Halide Layers: The Templating Influence of the Organic Cation Layer. *Inorg. Chem.* **2000**, *39*, 6107−6113.

(28) Lehner, A. J.; Fabini, D. H.; Evans, H. A.; Hébert, C.-A.; Smock, S. R.; Hu, J.; Wang, H.; Zwanziger, J. W.; Chabinyc, M. L.; Seshadri, R. Crystal and Electronic Structures of Complex Bismuth Iodides $A_3Bi_2I_9$ (A = K, Rb, Cs) Related to Perovskite: Aiding the Rational Design of Photovoltaics. *Chem. Mater.* **2015**, *27*, 7137−7148.

(29) McCall, K. M.; Stoumpos, C. C.; Kostina, S. S.; Kanatzidis, M. G.; Wessels, B. W. Strong Electron−Phonon Coupling and Self-Trapped Excitons in the Defect Halide Perovskites $A_3M_2I_9$ (A = Cs, Rb; M = Bi, Sb). *Chem. Mater.* **2017**, *29*, 4129−4145.

(30) Wu, L.-M.; Wu, X.-T.; Chen, L. Structural Overview and Structure−Property Relationships of Iodoplumbate and Iodobismuthate. *Coord. Chem. Rev.* **2009**, *253*, 2787−2804.

(31) Mercier, N.; Louvain, N.; Bi, W. Structural Diversity and Retro-Crystal Engineering Analysis of Iodometalate Hybrids. *CrystEngComm* **2009**, *11*, 720−734.

(32) Adonin, S. A.; Sokolov, M. N.; Fedin, V. P. Polynuclear Halide Complexes of Bi(III): From Structural Diversity to the New Properties. *Coord. Chem. Rev.* **2016**, *312*, 1−21.

(33) Pohl, S.; Saak, W.; Mayer, P.; Schmidpeter, A. $[Sb_3I_{10}^-]$—A Polymeric Anion with Transitions from Trigonal Pyramidal to Octahedral Coordination of Antimony(III). *Angew. Chem., Int. Ed. Engl.* **1986**, *25*, 825−825.

(34) Pohl, S.; Lotz, R.; Saak, W.; Haase, D. Structural Diversity in Iodoantimonates; the Anions $Sb_3I_{11}^{2-}$, $Sb_5I_{18}^{3-}$ and $Sb_6I_{22}^{4-}$. *Angew. Chem., Int. Ed. Engl.* **1989**, *28*, 344−345.

(35) Harikesh, P. C.; Mulmudi, H. K.; Ghosh, B.; Goh, T. W.; Teng, Y. T.; Thirumal, K.; Lockrey, M.; Weber, K.; Koh, T. M.; Li, S.; Mhaisalkar, S.; Mathews, N. Rb as an Alternative Cation for Templating Inorganic Lead-Free Perovskites for Solution Processed Photovoltaics. *Chem. Mater.* **2016**, *28*, 7496−7504.

(36) Boopathi, K. M.; Karuppuswamy, P.; Singh, A.; Hanmandlu, C.; Lin, L.; Abbas, S. A.; Chang, C. C.; Wang, P. C.; Li, G.; Chu, C. W. Solution-Processable Antimony-Based Lightabsorbing Materials Beyond Lead Halide Perovskites. *J. Mater. Chem. A* **2017**, *5*, 20843−20850.

(37) Zuo, C.; Ding, L. Lead-free Perovskite Materials $(NH_4)_3Sb_2I_xBr_{9-x}$. *Angew. Chem., Int. Ed.* **2017**, *56*, 6528−6532.

(38) Singh, A.; Boopathi, K. M.; Mohapatra, A.; Chen, Y. F.; Li, G.; Chu, C. W. Photovoltaic Performance of Vapor-Assisted Solution-Processed Layer Polymorph of $Cs_3Sb_2I_9$. *ACS Appl. Mater. Interfaces* **2018**, *10*, 2566−2573.

(39) Fisher, G. A.; Norman, N. C. The Structures of the Group 15 Element(III) Halides and Halogenoanions. *Adv. Inorg. Chem.* **1994**, *41*, 233−271.

(40) Volonakis, G.; Filip, M. R.; Haghighirad, A. A.; Sakai, N.; Wenger, B.; Snaith, H. J.; Giustino, F. Lead-Free Halide Double Perovskites via Heterovalent Substitution of Noble Metals. *J. Phys. Chem. Lett.* **2016**, *7*, 1254−1259.

(41) Slavney, A. H.; Hu, T.; Lindenberg, A. M.; Karunadasa, H. I. A Bismuth-Halide Double Perovskite with Long Carrier Recombination Lifetime for Photovoltaic Applications. *J. Am. Chem. Soc.* **2016**, *138*, 2138−2141.

(42) McClure, E. T.; Ball, M. R.; Windl, W.; Woodward, P. M. Cs_2AgBiX_6 (X = Br, Cl): New Visible Light Absorbing, Lead-Free Halide Perovskite Semiconductors. *Chem. Mater.* **2016**, *28*, 1348−1354.

(43) Giustino, F.; Snaith, H. J. Toward Lead-Free Perovskite Solar Cells. *ACS Energy Lett.* **2016**, *1*, 1233−1240.

(44) Wei, F.; Deng, Z.; Sun, S.; Zhang, F.; Evans, D. M.; Kieslich, G.; Tominaka, S.; Carpenter, M. A.; Zhang, J.; Bristowe, P. D.; Cheetham, A. K. Synthesis and Properties of a Lead-Free Hybrid Double Perovskite: $(CH_3NH_3)_2AgBiBr_6$. *Chem. Mater.* **2017**, *29*, 1089−1094.

(45) Cheng, P.; Wu, T.; Li, Y.; Jiang, L.; Deng, W.; Han, K. Combining theory and experiment in the design of a lead-free $((CH_3NH_3)_2AgBiI_6)$ double perovskite. *New J. Chem.* **2017**, *41*, 9598−9601.

(46) Greul, E.; Petrus, M. L.; Binek, A.; Docampo, P.; Bein, T. Highly Stable, Phase Pure $Cs_2AgBiBr_6$ Double Perovskite Thin Films for Optoelectronic Applications. *J. Mater. Chem. A* **2017**, *5*, 19972−19981.

(47) Slavney, A. H.; Leppert, L.; Bartesaghi, D.; Gold-Parker, A.; Toney, M. F.; Savenije, T. J.; Neaton, J. B.; Karunadasa, H. I. Defect-Induced Band-Edge Reconstruction of a Bismuth-Halide Double Perovskite for Visible-Light Absorption. *J. Am. Chem. Soc.* **2017**, *139*, 5015−5018.

(48) Du, K.-z.; Meng, W.; Wang, X.; Yan, Y.; Mitzi, D. B. Bandgap Engineering of Lead-Free Double Perovskite $Cs_2AgBiBr_6$ through Trivalent Metal Alloying. *Angew. Chem., Int. Ed.* **2017**, *56*, 8158−8162.

(49) Connor, B. A.; Leppert, L.; Smith, M. D.; Neaton, J. B.; Karunadasa, H. I. Layered Halide Double Perovskites: Dimensional Reduction of $Cs_2AgBiBr_6$. *J. Am. Chem. Soc.* **2018**, *140*, 5235−5240.

(50) Vargas, B.; Ramos, E.; Pérez-Gutiérrez, E.; Alonso, J. C.; Solis-Ibarra, D. A Direct Bandgap Copper−Antimony Halide Perovskite. *J. Am. Chem. Soc.* **2017**, *139*, 9116−9119.

(51) Kim, Y.; Yang, Z.; Jain, A.; Voznyy, O.; Kim, G.-H.; Liu, M.; Quan, L. N.; García de Arquer, F. P.; Comin, R.; Fan, J. Z.; Sargent, E. H. Pure Cubic-Phase Hybrid Iodobismuthates $AgBi_2I_7$ for Thin-Film Photovoltaics. *Angew. Chem., Int. Ed.* **2016**, *55*, 9586−9590.

(52) Xiao, Z.; Meng, W.; Mitzi, D. B.; Yan, Y. Crystal Structure of $AgBi_2I_7$ Thin Films. *J. Phys. Chem. Lett.* **2016**, *7*, 3903−3907.

(53) Sansom, H. C.; Whitehead, G. F. S.; Dyer, M. S.; Zanella, M.; Manning, T. D.; Pitcher, M. J.; Whittles, T. J.; Dhanak, V. R.; Alaria, J.; Claridge, J. B.; Rosseinsky, M. J. $AgBiI_4$ as a Lead-Free Solar Absorber with Potential Application in Photovoltaics. *Chem. Mater.* **2017**, *29*, 1538−1549.

(54) Khazaee, M.; Sardashti, K.; Sun, J.-P.; Zhou, H.; Clegg, C.; Hill, I. G.; Jones, J. L.; Lupascu, D. C.; Mitzi, D. B. A Versatile Thin-Film Deposition Method for Multidimensional Semiconducting Bismuth Halides. *Chem. Mater.* **2018**, *30*, 3538−3544.

(55) Kulkarni, A.; Jena, A. K.; Ikegami, M.; Miyasaka, T. Performance Enhancement of $AgBi_2I_7$ Solar Cells by Modulating a Solvent-Mediated Adduct and Tuning Remnant BiI_3 in One-Step Crystallization. *Chem. Commun.* **2019**, *55*, 4031−4034.

(56) Feldmann, C. $CuBi_7I_{19}(C_4H_8O_3H)_3(C_4H_8O_3H_2)$, a Novel Complex Bismuth Iodide Containing One-Dimensional $[CuBi_5I_{19}]^{3-}$ Chains. *Inorg. Chem.* **2001**, *40*, 818−819.

(57) Chai, W.-X.; Wu, L.-M.; Li, J.-Q.; Chen, L. Silver Iodobismuthates: Syntheses, Structures, Properties, and Theoretical Studies of $[Bi_2Ag_2I_{10}{}^{2-}]_n$ and $[Bi_4Ag_2I_{16}{}^{2-}]_n$. *Inorg. Chem.* **2007**, *46*, 1042−1044.

(58) Chai, W.-X.; Wu, L.-M.; Li, J.-Q.; Chen, L. A Series of New Copper Iodobismuthates: Structural Relationships, Optical Band Gaps Affected by Dimensionality, and Distinct Thermal Stabilities. *Inorg. Chem.* **2007**, *46*, 8698−8704.

(59) Yuan, M. W.; Li, L. H.; Chen, L. Syntheses, Structures, and Theoretical Studies of New Mercury Iodobismuthates: $(Et_4N)_4(Bi_4Hg_2I_{20})$ and $(nBu_4N)_2(Bi_2HgI_{10})$. *Z. Anorg. Allg. Chem.* **2009**, *635*, 1645−1649.

(60) Adonin, S. A.; Sokolov, M. N.; Smolentsev, A. I.; Kozlova, S. G.; Fedin, V. P. $[PtBi_2I_{12}]^{2-}$: The First Polyiodobismuthate Containing an Octahedral Heterometallic Unit. *Dalton Trans.* **2013**, *42*, 9818−9821.

(61) Dehnhardt, N.; Borkowski, H.; Schepp, J.; Tonner, R.; Heine, J. Ternary Iodido Bismuthates and the Special Role of Copper. *Inorg. Chem.* **2018**, *57*, 633−640.

(62) Kelly, A. W.; Wheaton, A. M.; Nicholas, A. D.; Barnes, F. H.; Patterson, H. H.; Pike, R. D. Iodobismuthate(III) and Iodobismuthate(III)/Iodocuprate(I) Complexes with Organic Ligands. *Eur. J. Inorg. Chem.* **2017**, *2017*, 4990−5000.

(63) Li, Y.-J.; Wu, T.; Sun, L.; Yang, R.-X.; Jiang, L.; Cheng, P.-F.; Hao, Q.-Q.; Wang, T.-J.; Lu, R.-F.; Deng, W.-Q. Lead-free and stable antimony−silver-halide double perovskite $(CH_3NH_3)_2AgSbI_6$. *RSC Adv.* **2017**, *7*, 35175−35180.

(64) Ruck, M. Darstellung und Kristallstruktur von fehlordnungsfreiem Bismuttriiodid. *Z. Kristallogr. - Cryst. Mater.* **1995**, *210*, 650−655.

(65) Trotter, J.; Zobel, T. The crystal structure of SbI_3 and BiI_3. *Z. Kristallogr.* **1966**, *123*, 67−72.

(66) Lindsjö, M.; Fischer, A.; Kloo, L. Anionic Diversity in Iodobismuthate Chemistry. *Z. Anorg. Allg. Chem.* **2005**, *631*, 1497−1501.

(67) Sheldrick, G. M. A Short History of SHELX. *Acta Crystallogr., Sect. A: Found. Crystallogr.* **2008**, *A64*, 112−122.

(68) Sheldrick, G. M. SHELXT − Integrated Space-Group and Crystal-Structure Determination. *Acta Crystallogr., Sect. A: Found. Adv.* **2015**, *A71*, 3−8.

(69) Sheldrick, G. M. Crystal Structure Refinement with SHELXL. *Acta Crystallogr., Sect. C: Struct. Chem.* **2015**, *C71*, 3−8.

(70) Dolomanov, O. V.; Bourhis, L. J.; Gildea, R. J.; Howard, J. A. K.; Puschmann, H. OLEX2: A Complete Structure Solution, Refinement and Analysis Program. *J. Appl. Crystallogr.* **2009**, *42*, 339−341.

(71) Brandenburg, K. *Diamond*; Crystal Impact GbR: Bonn, Germany, 2005.

(72) Boldish, S. I.; White, W. B. Optical Band Gaps of Selected Ternary Sulfide Minerals. *Am. Mineral.* **1998**, *83*, 865−871.

(73) Węcławik, M.; Gągor, A.; Jakubas, R.; Piecha-Bisiorek, A.; Medycki, W.; Baran, J.; Zieliński, P.; Gałązka, M. Structure−Property Relationships in Hybrid $(C_3H_5N_2)_3[Sb_2I_9]$ and $(C_3H_5N_2)_3[Bi_2I_9]$ Isomorphs. *Inorg. Chem. Front.* **2016**, *3*, 1306−1316.

(74) Alvarez, S. A cartography of the van der Waals territories. *Dalton Trans.* **2013**, *42*, 8617−8636.

(75) Hartl, H.; Mahdjour-Hassan-Abadi, F. $[(C_6H_5)_4P][Cu_3I_4]$ − The First Compound with a Helical Chain of Face-Sharing Tetrahedra as a Structural Element. *Angew. Chem., Int. Ed. Engl.* **1994**, *33*, 1841−1842.

(76) Robert, M. C.; Saravanan, R.; Saravana Kumar, K.; Rani, M. P. Structural Analysis of Al, Ni and Cu Using the Maximum Entropy Method, Multipole and Pair Distribution Function. *Z. Naturforsch., A: Phys. Sci.* **2009**, *64*, 361−369.

(77) Hartl, H.; Mahdjour-Hassan-Abadi, F. $[Cu_5I_7]^{2-}$ - An Isopolyanion with Cyclic Face-to-Face Linking of CuI_4 Tetrahedra. *Angew. Chem., Int. Ed. Engl.* **1984**, *23*, 378−379.

(78) Jagner, S.; Helgesson, G. On the Coordination Number of the Metal in Crystalline Halogenocuprates(I) and Halogenoargentates(I). *Adv. Inorg. Chem.* **1991**, *37*, 1−45.

(79) Taylor, W. V.; Soto, U. H.; Lynch, V. M.; Rose, M. J. Antimony-Supported Cu_4I_4 Cuboid with Short Cu−Cu Bonds: Structural Premise for Near-Infrared Thermoluminescence. *Inorg. Chem.* **2016**, *55*, 3206−3208.

(80) Fenske, D.; Rothenberger, A.; Wieber, S. Synthesis and Crystal Structure of $[(Me_3Si)_2BiCu(PMe_3)_3]$ - the First Complex with a Bismuth-Copper Bond. *Z. Anorg. Allg. Chem.* **2003**, *629*, 929−930.

(81) Liao, W.-Q.; Zhang, Y.; Hu, C.-L.; Mao, J.-G.; Ye, H.-Y.; Li, P.-F.; Huang, S. D.; Xiong, R.-G. A lead-halide perovskite molecular ferroelectric semiconductor. *Nat. Commun.* **2015**, *6*, 7338.

(82) Wojciechowska, M.; Gągor, A.; Piecha-Bisiorek, A.; Jakubas, R.; Ciżman, A.; Zaręba, J. K.; Nyk, M.; Zieliński, P.; Medycki, W.; Bil, A. Ferroelectricity and Ferroelasticity in Organic Inorganic Hybrid $(Pyrrolidinium)_3[Sb_2Cl_9]$. *Chem. Mater.* **2018**, *30*, 4597−4608.

(83) Dennington, A. J.; Weller, M. T. Synthesis, Structure and Optoelectronic Properties of Hybrid Iodobismuthate & Iodoantimonate Semiconducting Materials. *Dalton Trans.* **2018**, *47*, 3469−3484.

(84) Volonakis, G.; Filip, M. R.; Haghighirad, A. A.; Sakai, N.; Wenger, B.; Snaith, H. J.; Giustino, F. Lead-Free Halide Double Perovskites via Heterovalent Substitution of Noble Metals. *J. Phys. Chem. Lett.* **2016**, *7*, 1254−1259.

(85) Xiao, Z.; Du, K.-Z.; Meng, W.; Mitzi, D. B.; Yan, Y. Chemical Origin of the Stability Difference between Copper(I)- and Silver(I)-Based Halide Double Perovskites. *Angew. Chem., Int. Ed.* **2017**, *56*, 12107−12111.

(86) Ford, P. C.; Cariati, E.; Bourassa, J. Photoluminescence Properties of Multinuclear Copper(I) Compounds. *Chem. Rev.* **1999**, *99*, 3625−3647.

(87) Pfitzner, A.; Schmitz, D. Two New Modifications of $[P(C_6H_5)_4]_2[Cu_2I_4]$. *Z. Anorg. Allg. Chem.* **1997**, *623*, 1555−1560.

(88) Jalilian, E.; Liao, R.-Z.; Himo, F.; Brismar, H.; Laurell, F.; Lidin, S. Luminescence Properties of the $Cu_4I_6^{2-}$ Cluster. *CrystEngComm* **2011**, *13*, 4729−4734.

(89) Garcia-Fernandez, A.; Marcos-Cives, I.; Platas-Iglesias, C.; Castro-Garcia, S.; Vazquez-Garcia, D.; Fernandez, A.; Sanchez-Andujar, M. Diimidazolium Halobismuthates $[Dim]_2[Bi_2X_{10}]$ (X = Cl^-, Br^-, or I^-): A New Class of Thermochromic and Photoluminescent Materials. *Inorg. Chem.* **2018**, *57*, 7655−7664.

(90) Pal, J.; Manna, S.; Mondal, A.; Das, S.; Adarsh, K. V.; Nag, A. Colloidal Synthesis and Photophysics of $M_3Sb_2I_9$ (M = Cs and Rb) Nanocrystals: Lead-Free Perovskites. *Angew. Chem., Int. Ed.* **2017**, *56*, 14187−14191.

(91) Yang, B.; Chen, J.; Yang, S.; Hong, F.; Sun, L.; Han, P.; Pullerits, T.; Deng, W.; Han, K. Lead-Free Silver-Bismuth Halide Double Perovskite Nanocrystals. *Angew. Chem., Int. Ed.* **2018**, *57*, 5359−5363.

(92) Jana, M. K.; Janke, S. M.; Dirkes, D. J.; Dovletgeldi, S.; Liu, C.; Qin, X.; Gundogdu, K.; You, W.; Blum, V.; Mitzi, D. B. Direct-Bandgap 2D Silver−Bismuth Iodide Double Perovskite: The Structure-Directing Influence of an Oligothiophene Spacer Cation. *J. Am. Chem. Soc.* **2019**, *141*, 7955−7964.

DOI: 10.1021/acs.inorgchem.9b01466
Inorg. Chem. 2019, 58, 10983−10990

3.3. Synthesis of a two-dimensional organic–inorganic bismuth iodide metalate through in situ formation of iminium cations

Natalie Dehnhardt, Jan-Niclas Luy, Marvin Szabo, Mirco Wende, Ralf Tonner, Johanna Heine, *Chemical Communications* **2019**, *55*, 14725 - 14728, DOI: 10.1039/c9cc06625j.

Abstract

$(Me_2C{=}NMe_2)Bi_2I_7$ represents a new layered organic–inorganic iodido bismuthate. It displays an unprecedented anion topology, a low band gap and good stability. Advanced electronic structure analysis finds the I-I interactions to be decisive for the compound's structural and electronic properties.

Zusammenfassung

Im Rahmen dieser Publikation wird über ein Iodidobismutat, welches mit Iminiumkationen als Gegenionen kristallisiert, berichtet. Bei der Verbindung $(Me_2C{=}NMe_2)Bi_2I_7$ handelt es sich um das erste anorganisch-organische Iodidobismutat mit vollbesetzten Metallpositionen, dass eine Schichtstruktur ausbildet. Die Schichten bestehen aus Strängen aus kantenverknüpften $\{BiI_6\}$-Oktaedern, die untereinander über gemeinsame Ecken verknüpft sind, wodurch eine 6^3-Netzstruktur erhalten wird. Ausschnitte aus den Kristallstrukturen sind in Abbildung 3.3 a) und b) dargestellt.

Die Verbindung ist ungewöhnlich dunkel, absorbiert im roten Bereich des elektromagnetischen Spektrums bei 671,5 nm und weist eine ungewöhnlich niedrige Bandlücke von 1,87 eV auf, welche über quantenchemische Methoden bestimmt wurde.

$(Me_2C{=}NMe_2)Bi_2I_7$ kann aus stöchiometrischer Mischung von Bismuttriiodid (BiI_3) und Dimethylammoniumiodid in trockenem Aceton unter Argonatmosphäre erhalten werden. Hierbei kommt es zu einer *in-situ* Kondensation des Dimethylammoniumkations mit Acteon, bei der unter Freisetzung eines Äquivalentes Wasser ein Iminiumkation entsteht. Einkristalle konnten nach 24 Stunden als dunkelrote Blöcke erhalten werden. Des Weiteren kann die Verbindung auch aus konzentrierter Lösung als mikrokristallines Pulver mit 62 % Ausbeute ausgefällt werden. Die Stabilität von $(Me_2C{=}NMe_2)Bi_2I_7$ wurde über Thermogravimetrie untersucht. Die Analyse zeigt eine vollständige Zersetzung der Verbindung bei 290 °C, welche mit einem Masseverlust von 98,4 % einhergeht. Die Differenzkalorimetrie zeigt einen endothermen Peak bei 258 °C. Dieser konnte von uns in weiteren Experimenten als Sublimationspunkt verifiziert werden. Des Weiteren wurde der Alterungsprozess von $(Me_2C{=}NMe_2)Bi_2I_7$ über Röntgenpulverdiffraktometrie kontrolliert. Auch nach fünf Monaten an Luft zeigt das Diffraktogramm keine zusätzlichen Reflexe oder einen

Anstieg des amorphen Untergrundes, die auf ein Zersetzen der Verbindung hindeuten würden. Das UV-Vis-Spektrum der Verbindung wurde in diffuser Reflexion an gemörserten Einkristallen gemessen. Es zeigt eine Absorptionskante bei 671,5 nm und somit eine starke Rotverschiebung der Absorptionskante, verglichen mit anderen Iodidobismutaten. Ein in Abbildung 3.3 c) und d) dargestellter Vergleich der Absorptionsspektren sowie mikrokristallinen Pulvern von BiI$_3$, (Me$_2$C=NMe$_2$)Bi$_2$I$_7$, (HPy)BiI$_4$ (HPy=Pyridinium) und (NMe$_2$H$_2$)$_3$BiI$_6$ zeigt, dass eine Reduzierung der Ausdehnung des Anions von einem dreidimensionalem Netzwerk hin zu isolierten Anionen mit einer Blauverschiebung der Absorptionskante einhergeht.

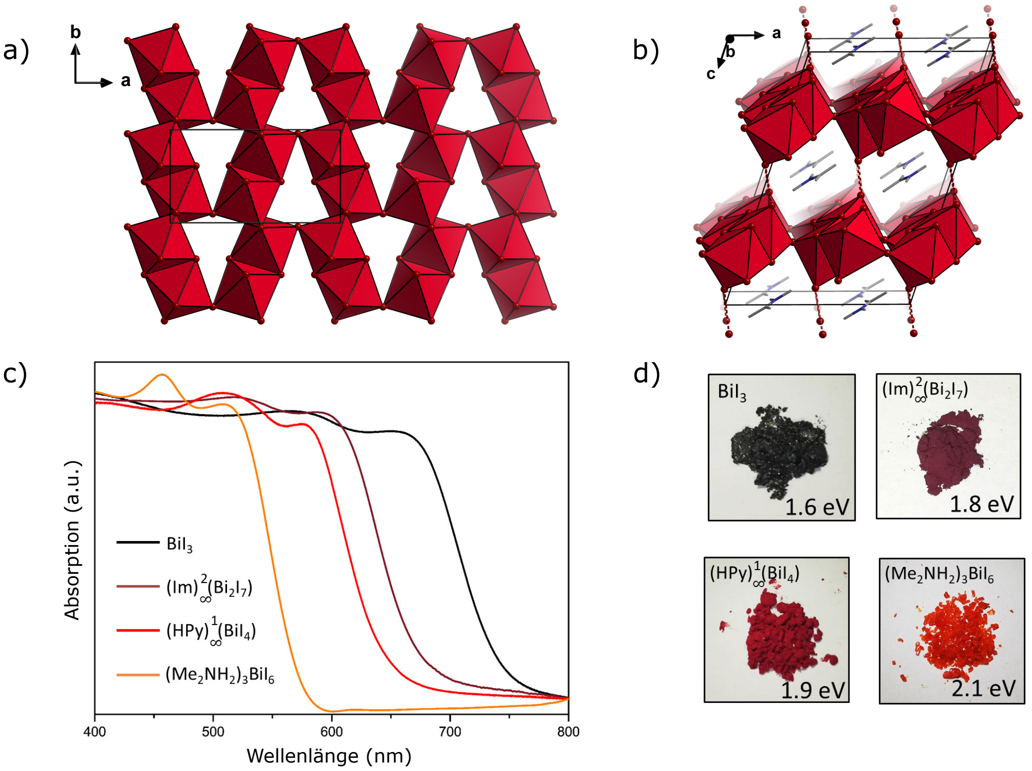

Abbildung 3.3: Ausschnitte aus der Kristallstruktur von (Me$_2$C=NMe$_2$)Bi$_2$I$_7$ a) entlang der kristallographischen *c*-Achse. b) entlang der kristallographischen *b*-Achse mit hervorgehobenen Iod-Iod-Abständen. Zur besseren Übersicht wurde die Polyederdarstellung für die anorganische Einheit gewählt. c) und d) UV-Vis-Spektrum und Fotografien von mikrokristallinen Pulvern von (Me$_2$C=NMe$_2$)Bi$_2$I$_7$ im Vergleich zu ausgewählten Verbindungen.

Für schichtartige Anionen wie in (Me$_2$C=NMe$_2$)Bi$_2$I$_7$ würde somit eine Absorptionskante bei höheren Wellenlängen als für ein molekulares Bismutat erwartet werden. Für das schon bekannte rein anorganische Bismutat Rb$_3$Bi$_2$I$_9$, welches ebenfalls eine Schichtstruktur aufweist, wird allerdings eine Absorptionskante bei 2,1 eV (590 nm) erhalten. Die Rotverschiebung der Absorptionskante im Vergleich zu Rb$_3$Bi$_2$I$_9$ kann durch die kurzen Iod-Iod Abstände von 3,8 Å erklärt werden. Um diese Iod-Iod-Abstände und deren Einfluss auf die optischen Eigenschaften genauer zu untersuchen wurden quantenchemische Rechnungen durchgeführt. Zunächst wurde die Bandlücke mit DFT-Methoden unter Verwendung des PBE Funktionals und des Tz2P+ Basissatzes berechnet. Hierbei wurde die Periodizität der Verbindung mittels Dispersionskorrektur über DFT-D3 berücksichtigt. Der erhaltene Wert von 1,87 eV stimmt gut mit dem experimentell erhaltenen Wert von 1,8 eV überein. Die Analyse der Zustandsdichte ergab, dass die Valenzbandkante hauptsächlich von Zuständen an den Iodatomen beherrscht wird, während am Leitungsband gleiche Beiträge von Bismut- und Iodatomen zu finden sind. Um den genauen Charakter der Iod-Iod-Wechselwirkung zu untersuchen, wurden Populationsanalysen (Crystal orbital Hamilton population) durchgeführt. Nahe der *Fermi*-Energie werden antibindende Beiträge, hervorgerufen durch nichtbindende Elektronenpaarrepulsion (electron pair repulsion), gefunden. Eine detaillierte Untersuchung der Bindungssituation wurde über pEDA (periodic energy decomposition analysis) durchgeführt. Sie ergaben einen gleichen Beitrag von Dispersions- und elektronischen Wechselwirkungen zwischen den Schichten. Wird diese Wechselwirkung reduziert, indem der Abstand zwischen den Schichten vergrößert wird, verringert sich der antibindende Beitrag nahe der Fermi-Energie, womit eine Vergrößerung der Bandlücke einhergeht.

Eigener Anteil

Die erste Synthese von $(Me_2C{=}NMe_2)Bi_2I_7$ wurde von *Marvin Szabo* im Rahmen eines Forschungspraktikums unter meiner Anleitung durchgeführt. *Mirco Wende* optimierte die Synthese im Rahmen einer studentischen Hilfskraftstelle unter meiner Betreuung. $(Me_2C{=}NMe_2)Bi_2I_7$ wurde über Röntgenbeugung am Einkristall und Pulver, UV-Vis-, Infrarot- und Raman-Spektroskopie, Thermogravimetrie und gekoppelte Differenzkalorimetrie sowie CHN-Elementaranalyse charakterisiert und identifiziert. Alle Ergebnisse wurden von mir ausgewertet und für die Publikation aufbereitet. Die Einkristallmessung sowie Strukturlösung und -verfeinerung wurde von *Dr. Johanna Heine* durchgeführt. Pulverdiffraktogramme, UV-Vis- und Infrarotspektren wurden von mir aufgenommen. Die Raman-Spektroskopie erfolgte durch *Dr. Istemi Kuzu.* Thermogravimetrie und gekoppelte Differenzkalorimetrie wurden von *Uwe Justus* durchgeführt. Die CHN-Elementaranalyse wurde von der zentralen Abteilung für Massenspektrometrie und Elementaranalyse der Philipps-Universität Marburg vorgenommen. Quantenchemische Rechnungen wurden in der Arbeitsgruppe von *Pro. Dr. Ralf Tonner* von *Jan-Niclas Luy* durchgeführt. Die Erstellung der Manuskripts erfolgte unter Beteiligung aller Co-Autoren.

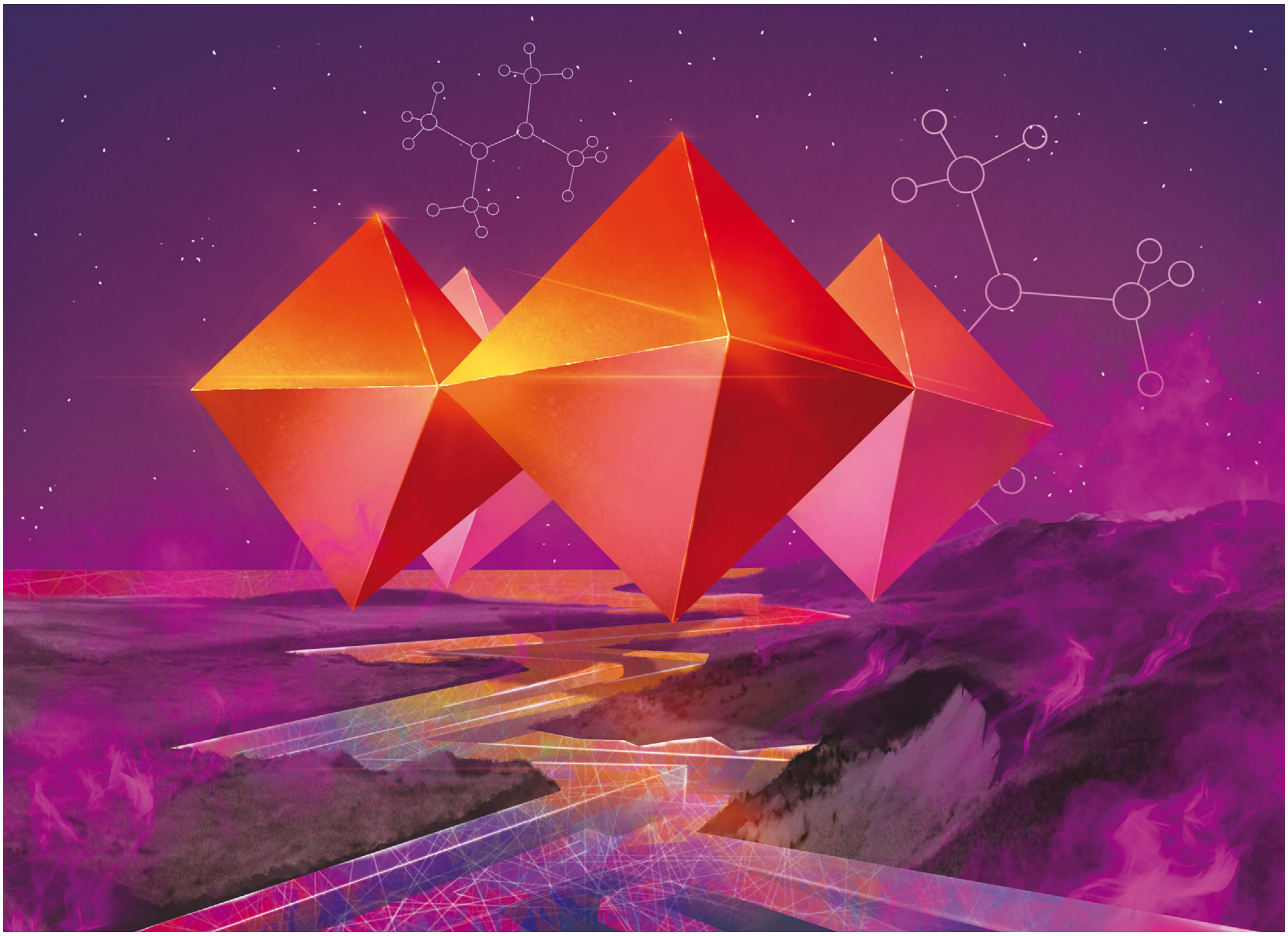

Showcasing research from Ralf Tonner's and Johanna Heine's group, Department of Chemistry and Collaborative Research Center 1083, Philipps-Universität, Marburg, Germany.
Image designed and illustrated by Leander Aurel Taubner.

Synthesis of a two-dimensional organic–inorganic bismuth iodide metalate through *in situ* formation of iminium cations

$(Me_2C{=}NMe_2)Bi_2I_7$ represents a new layered organic–inorganic iodido bismuthate. It displays an unprecedented anion topology, a low band gap and good stability. Advanced electronic structure analysis finds the I···I interactions to be decisive for the compound's structural and electronic properties.

As featured in:


ChemComm

See Ralf Tonner,
Johanna Heine *et al.*,
Chem. *Commun*., 2019, **55**, 14725.

ROYAL SOCIETY OF CHEMISTRY | Celebrating IYPT 2019

rsc.li/chemcomm

Registered charity number: 207890

ChemComm

COMMUNICATION

View Article Online
View Journal | View Issue

Cite this: *Chem. Commun.*, 2019, **55**, 14725

Received 26th August 2019,
Accepted 26th October 2019

DOI: 10.1039/c9cc06625j

rsc.li/chemcomm

Synthesis of a two-dimensional organic–inorganic bismuth iodide metalate through *in situ* formation of iminium cations†

Natalie Dehnhardt, Jan-Niclas Luy, Marvin Szabo, Mirco Wende, Ralf Tonner * and Johanna Heine *

$(Me_2C{=}NMe_2)Bi_2I_7$ represents a new layered organic–inorganic iodido bismuthate. It displays an unprecedented anion topology, a low band gap and good stability. Advanced electronic structure analysis finds the I···I interactions to be decisive for the compound's structural and electronic properties.

Lead halide perovskites like $(CH_3NH_3)PbI_3$ are prominent materials due to their excellent semiconductor properties[1] and successful application in solar cells,[2] photocatalysis[3] and LEDs.[4] Layered perovskites such as $(C_4H_9NH_3)PbI_4$[5,6] offer the benefit of greater stability and allow the use of larger, functional organic cations while maintaining the good semiconductor properties of their parent perovskites.[7] However, the toxicity of lead compounds has prompted researchers to look to related halogenido metalates for alternatives. Iodido bismuthates appear promising, as bismuth compounds are typically non-toxic.[8] Compounds like $(CH_3NH_3)_3Bi_2I_9$, which features dinuclear $Bi_2I_9^{3-}$ anions,[9] have been tested in photovoltaic devices, but only show moderate efficiencies up to 3.17% after significant efforts at optimization.[10] In contrast, lead halide perovskite solar cells currently reach well above 20%.[11] One reason for this difference in properties lies in the structural chemistry of the iodido bismuthates: while iodido plumbates readily feature layer or network anions, bismuthates are mostly limited to molecular or chain-like anions.[12] Only two types of iodido bismuthates with a layered anion have been reported to date: the all-inorganic family $A_3Bi_2I_9$ (A = K, Rb)[13] featuring (111) perovskite layers, and $(H_2AEQT)Bi_{2/3}I_4$ (AEQT = 5,5‴-bis-(aminoethyl)-2,2′:5′,2″:5″,2‴-quaterthiophene), featuring a metal-deficient (001) perovskite layer.[14] However, the synthesis of the layered mixed halide bismuthate $(TMP)_{1.5}[Bi_2I_7Cl_2]$, (TMP = *N*,*N*,*N*′,*N*′-tetramethyl-piperazine)[15] suggests that more organic–inorganic, layered iodido bismuthates should be available if the right type of counterion can be found.

A family of organic cations that has been largely overlooked in the context of metal halide materials are iminium ions ($R_2C{=}NR_2^+$; R = H, organic group). They are well known as reactive intermediates and reagents in organic chemistry,[16] but they are also known for their tendency to hydrolyze.[17] This reactivity suggests that they are difficult to work with in the preparation of robust materials, yet in early studies of iminium cations, halogenido metalate anions were used to isolate these species.[18] Later work demonstrated that compounds containing iminium cations are readily available with numerous substitution patterns[19] and easy to isolate as single crystals.[20] More recently, cuprates and argentates featuring $(Me_2C{=}NMe_2)^+$ were prepared by *in situ* condensation of dimethylamine and acetone.[21]

Here, we present $(Me_2C{=}NMe_2)Bi_2I_7$ (**1**), a layered organic–inorganic iodido bismuthate, the first example of a layer with fully occupied metal positions in this class of compounds. We investigate the synthesis and reactivity, crystal structure and optical properties of **1**, revealing its unique topology, high stability and low band gap. We use quantum chemical methods to analyze the compound's electronic properties and demonstrate a new method to characterize and quantify iodine–iodine contacts in extended solids. We also discuss why our findings are relevant to lead halide perovskites and how the facile preparation of iminium cations opens up new opportunities for metal halide materials in general.

$(Me_2C{=}NMe_2)Bi_2I_7$ (**1**) is obtained by heating stoichiometric amounts of BiI_3 and $(NMe_2H_2)I$ in acetone (Scheme 1).

1 crystallizes in *P*2/*n* (No. 13) as black blocks. Fig. 1 shows an overview of the crystal structure. Bond lengths in both the cation and anion are in good agreement with literature reports

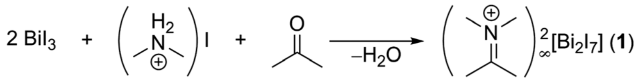

Scheme 1 Synthesis of **1**.

Department of Chemistry and Material Sciences Center, Philipps-Universität Marburg, Hans-Meerwein-Straße, 35043 Marburg, Germany.
E-mail: tonner@chemie.uni-marburg.de, johanna.heine@chemie.uni-marburg.de

† Electronic supplementary information (ESI) available: Synthesis, crystallographic details, thermal analysis, powder patterns, IR and Raman spectra, absorption spectra, details of computational studies. CCDC 1939881. For ESI and crystallographic data in CIF or other electronic format see DOI: 10.1039/c9cc06625j

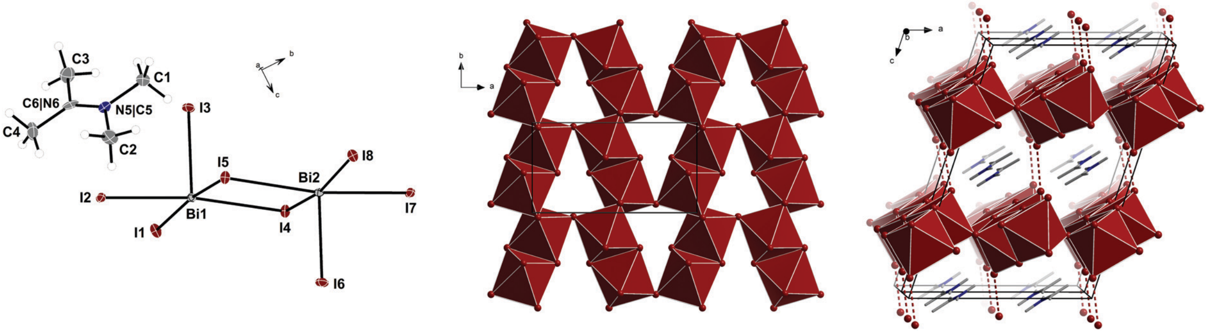

Fig. 1 Asymmetric unit of **1**, ellipsoids at 50% probability, only majority position shown (left). View along the *c* axis, cations omitted (middle). Excerpt with I–I interactions below 4 Å marked with dashed lines (right).

(Tables S3 and S4, ESI†). The iodido bismuthate layers feature the well-known motif of $\{BiI_4\}$ chains of edge-sharing $\{BiI_6\}$ octahedra.[12] These chains are connected into layers by additional edge-sharing with adjacent strands. The resulting topology is a 6^3-honeycomb net. To the best of our knowledge, the anion motif found in **1** is unique among metalates, although related metal halide layers with six-membered rings are known, *e.g.* in BiI_3,[22] $(pipzH_2)Mn_2F_8$ (pipz = piperazine)[23] or the triple-layered anion in $(H_2mpz)_2Pb_3Br_{10}$ (mpz = 1-methylpiperazine).[24] The layers in **1** are further connected into a pseudo-network *via* iodine–iodine interactions.

1 starts to decompose at 290 °C (Fig. S2, ESI†), similar to layered organic–inorganic iodido plumbates.[5] We also tested the stability of **1** against humidity, as the tendency of iminium cations to hydrolyze might be expected to translate to the metalate as well. However, when a powdered sample of **1** is stored in humid air for 24 h, no change in powder pattern is observed (Fig. S4, ESI†). Additionally, long term stability was investigated on a sample that was aged in air for 5 months. Here, no significant decomposition was observed in the powder diffractogram as well (Fig. S4, ESI†). The absorption spectrum of **1**, measured in diffuse reflectance, shows an onset of absorption at 1.8 eV (Fig. S7, ESI†). A comparison with the spectra of BiI_3 and $(Hpy)BiI_4$[25] (Hpy = pyridinium) highlights the effect of metalate formation and changing anion dimensionality (Fig. 2): the onset of absorption is blue-shifted going from BiI_3 to **1** to $(Hpy)BiI_4$, which features chain-like anions, as expected from general principles of dimensionality reduction in metalates.[26] Weller has shown that iodido bismuthate band gaps correlate not only with the anion dimensionality, but also with the presence of iodine–iodine interactions between anions, which typically lower the band gap.[27] We suggest that it is these interactions, also found in **1**, that cause a red-shifted onset of absorption in comparison with $Rb_3Bi_2I_9$, composed of (111) perovskite layers, where a band gap of 2.1 eV[13] has been reported and no interlayer iodine–iodine interactions below 4 Å occur. Revealing the nature of these interlayer interactions and their impact on the band gap motivated our computational investigations for **1**.

Following our previous work,[28] we chose density functional theory (DFT) approaches based on the PBE functional with dispersion correction by the DFT-D3 method and consideration of scalar and spin–orbit relativistic effects taking into account the full periodicity of the system (see ESI†). The calculated band gap of 1.87 eV (TB09) is in excellent agreement with the experimental value of 1.8 eV (Table S6, ESI†). An analysis of the projected density of states (pDOS) shows that the valence band edge is mostly composed of orbitals located at the iodine atoms, while the conduction band consists of equal contributions of Bi- and I-based orbitals (Fig. 3). Plotting the orbitals at the *Γ*-point confirms these assignments in a real-space picture and demonstrates that the highest occupied crystal orbital (HOCO) consists of non-bonding electron pairs at the iodine atoms while the lowest unoccupied crystal orbital (LUCO) additionally features contributions from antibonding Bi–I orbitals. These orbitals are delocalized over the whole unit cell, indicating good carrier mobility. This picture is similar to results derived for $Rb_3Bi_2I_9$.[13] In contrast, layered lead-based perovskites typically show a higher contribution of the metal-based orbitals to the valence and conduction bands.[6] The interlayer interaction between the iodine atoms was previously found to be an important element for the crystal packing and electronic structure of iodido metalates.[27]

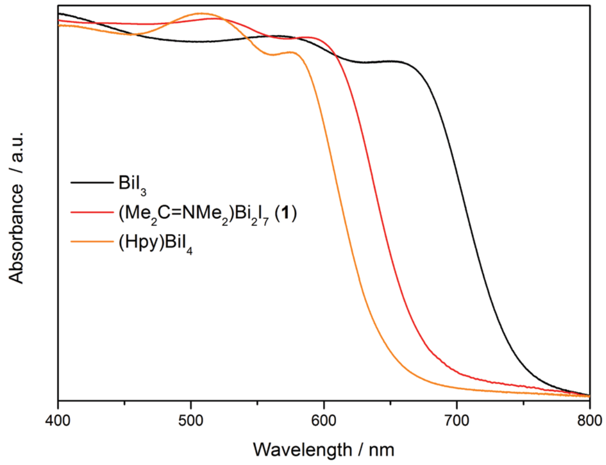

Fig. 2 Absorption spectra of BiI_3, **1** and $(HPy)BiI_4$, measured in diffuse reflection.

But the exact nature of these interactions has not been revealed up to now. Thus, we performed an in-depth analysis of the underlying principles governing the I···I interaction by a combination of several advanced tools for bonding analysis. In

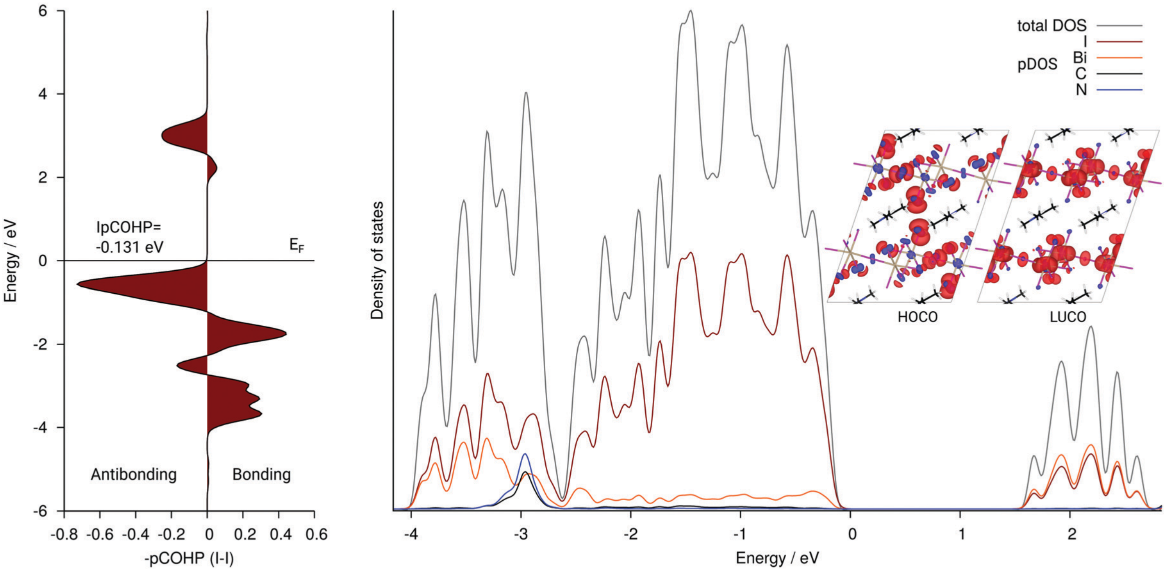

Fig. 3 Negative of the pCOHP (PBE-D3) values of the interlayer I$\cdots$I interaction (left); total and partial density of states (pDOS, TB09) with insets of the highest occupied (HOCO) and lowest unoccupied crystal orbital (LUCO) at the Γ-point (right).

Fig. 3, we show the projected Crystal Orbital Hamilton Population (pCOHP[29]) of the I$\cdots$I interaction. In agreement with the results from the pDOS analysis, an antibonding contribution stemming from non-bonding electron pair repulsion is found close to the Fermi energy. The integrated pCOHP (IpCOHP) amounts to −0.131 eV indicating an overall slightly attractive interaction. The topological analysis by the atoms in molecules (AIM) method[30] shows an increased but small electron density at the bond critical points for the interlayer I$\cdots$I interactions compared to the intralayer contacts and a positive value for the second derivative of the electron density (Laplacian, $\nabla^2\rho$) supporting the notion of a non-covalent interaction (Table S7, ESI†).

A quantitative analysis of this interaction was carried out with our recently developed energy decomposition analysis for extended systems (pEDA). This analysis decomposes the bonding energy between two fragments in terms of well-defined energy contributions that help to gain a qualitative understanding of the bonding interaction from quantitative results. It is thus possible to distinguish effects from quasiclassical electrostatic interactions (ΔE_{elstat}), Pauli repulsion (ΔE_{Pauli}) and orbital interactions (ΔE_{orb}). Dispersion contributions to the bonding are derived from the DFT-D3 scheme (ΔE_{int}(disp)) and added to the sum of the electronic interaction terms (ΔE_{int}(elec)) to give the total interaction energy (ΔE_{int}).[31–33] Notably, the layered structure of **1** enables an analysis of a 3-dimensional solid not composed of molecular units with an EDA method for the first time, since commonly a reasonable fragmentation is not possible. Here, the fragmentation is done by including one layer of organic and inorganic component each as sketched in Fig. S8a (ESI†) to form a double layer as one fragment. The pEDA results for **1** are summarized in Table S8 (ESI†). Surprisingly, the interaction energy between these double layers stems nearly equally from dispersion (53%) and electronic (47%) contributions indicating a more complex situation than pure van-der-Waals binding. A further look into the attractive pEDA terms shows that the electrostatic interaction is dominating (56%) which can be understood by the ionic nature of the organic and inorganic layers, respectively. Nevertheless, a significant orbital interaction (44%) is found, indicating covalent bonding contributions. These orbital interactions were further analyzed with the Natural Orbitals for Chemical Valence (NOCV) approach,[33,34] identifying iodine–iodine charge shift as the major contribution (Fig. S8 and S9, ESI†).

But how does this I–I interaction effect the band edges? To this end we reduced this interaction by increasing the interlayer I–I distance from 3.692 to 4.047 Å (9.6%) while keeping the other structural parameters constant. A pCOHP analysis (Fig. S10, ESI†) reveals that the antibonding contribution close to the Fermi energy decreases more than its bonding counterparts leading to a decreased IpCOHP of −0.051 eV. In addition, the HOCO is shifted to slightly lower energies (−0.1 eV). This shows that the interlayer I$\cdots$I interaction leads to a smaller band gap, implying the possibility of band gap tuning by controlling the iodine–iodine distances.

We want to highlight another aspect of our findings: the facile synthesis and inclusion of the iminium cations in **1**, and its relevance to the synthesis of metal halide perovskites. Dimethylformamide, a common solvent in metal halide perovskite synthesis, can form dimethylamine as a decomposition product[35] and subsequently $(NMe_2H_2)^+$ cations in the presence of acids, a phenomenon that has already been observed in $CsPbI_3$ perovskites.[36] Our results indicate that a further reaction towards iminium cations may occur when ketones are added to the reaction mixture, for example during the synthesis of nanoparticles.[37] The partial inclusion of larger organic cations in lead halide perovskites does not necessarily change the crystal structure, but can have significant effects on optical properties and stability.[38] While this may occur accidentally, it can also be used deliberately to tune the properties of mixed cation perovskite materials.[39] On a broader scope, the wide range of possible starting materials for iminium ions – amines and ketones or aldehydes – allows for targeting specific cation sizes and shapes that were previously unavailable and may yield unique new anion topologies and material properties, not only for halogenido bismuthates, but metalates in general.

In summary, we show that layered organic–inorganic iodido bismuthates are available given the right cation: $(\mathrm{Me_2C{=}NMe_2})\mathrm{Bi_2I_7}$ combines a simple synthetic access with a layered anion topology, low band gap and good stability and thus holds great promise for material applications. Our computational investigations show a band gap in good agreement with experiment and characterize it as a I → σ*(Bi–I) transition. Using energy decomposition analysis for the first time in an inorganic 3D system, we quantitatively and qualitatively elucidate the I···I interactions found as structural elements with dispersion interactions and polarization of the iodine atoms as the major bonding contributions. Our results highlight iminium cations as prime counterion templating candidates for new metalate materials with unprecedented anion topologies.

This work is funded by the DFG *via* the SFB 1083. J. H. thanks Prof. Stefanie Dehnen for her constant support. N. D. thanks the Fonds der Chemischen Industrie and the Studienstiftung des Deutschen Volkes for their support. We thank the HLR Stuttgart, HRZ Marburg, and Goethe-HLR Frankfurt for computational resources, Jakob Möbs for preparing reference compounds, Dr Istemi Kuzu for recording the Raman spectrum and Dr Robert Wilson for helpful discussions.

Conflicts of interest

There are no conflicts to declare.

References

1 C. C. Stoumpos and M. G. Kanatzidis, *Adv. Mater.*, 2016, **28**, 5778–5793.
2 A. K. Jena, A. Kulkarni and T. Miyasaka, *Chem. Rev.*, 2019, **119**, 3036–3103.
3 X. Zhu, Y. Lin, Y. Sun, M. C. Beard and Y. Yan, *J. Am. Chem. Soc.*, 2019, **141**, 733–738.
4 L. N. Quan, B. P. Rand, R. H. Friend, S. G. Mhaisalkar, T.-W. Lee and E. H. Sargent, *Chem. Rev.*, 2019, **119**, 7444–7477.
5 D. B. Mitzi, *Chem. Mater.*, 1996, **8**, 791–800.
6 C. C. Stoumpos, D. H. Cao, D. J. Clark, J. Young, J. M. Rondinelli, J. I. Jang, J. T. Hupp and M. G. Kanatzidis, *Chem. Mater.*, 2016, **28**, 2852–2867.
7 L. Mao, C. C. Stoumpos and M. G. Kanatzidis, *J. Am. Chem. Soc.*, 2019, **141**, 1171–1190.
8 H. Li, R. Wang and H. Sun, *Acc. Chem. Res.*, 2019, **52**, 216–227.
9 K. Eckhardt, V. Bon, J. Getzschmann, J. Grothe, F. M. Wisser and S. Kaskel, *Chem. Commun.*, 2016, **52**, 3058–3060.
10 S. M. Jain, D. Phuyal, M. L. Davies, M. Li, B. Philippe, C. De Castro, Z. Qiu, J. Kim, T. Watson, W. C. Tsoi, O. Karis, H. Rensmo, G. Boschloo, T. Edvinssonand and J. R. Durrant, *Nano Energy*, 2018, **49**, 614–624.
11 M. A. Green, Y. Hishikawa, E. D. Dunlop, D. H. Levi, J. Hohl-Ebinger, M. Yoshita and A. W. Y. Ho-Baillie, *Prog. Photovolt. Res. Appl.*, 2019, **27**, 3–12.
12 N. Mercier, N. Louvain and W. Bi, *CrystEngComm*, 2009, **11**, 720–734.
13 A. J. Lehner, D. H. Fabini, H. A. Evans, C.-A. Hébert, S. R. Smock, J. Hu, H. Wang, J. W. Zwanziger, M. L. Chabinyc and R. Seshadri, *Chem. Mater.*, 2015, **27**, 7137–7148.
14 D. B. Mitzi, *Inorg. Chem.*, 2000, **39**, 6107–6113.
15 M.-Q. Li, Y.-Q. Hu, L.-Y. Bi, H.-L. Zhang, Y. Wang and Y.-Z. Zheng, *Chem. Mater.*, 2017, **29**, 5463–5467.
16 A. Erkkilä, I. Majander and P. M. Pihko, *Chem. Rev.*, 2007, **107**, 5416–5470.
17 H. G. Reiber and T. D. Stewart, *J. Am. Chem. Soc.*, 1940, **62**, 3026–3030.
18 M. Lamchen, W. Pugh and A. M. Stephen, *J. Chem. Soc.*, 1954, 4418–4425.
19 N. J. Leonard and J. V. Paukstelis, *J. Org. Chem.*, 1963, **28**, 3021–3024.
20 L. M. Trefonas, R. L. Flurry Jr., R. Majeste, E. A. Meyers and R. F. Copeland, *J. Am. Chem. Soc.*, 1966, **88**, 2145–2149.
21 R. Hehl and G. Thiele, *Z. Anorg. Allg. Chem.*, 2000, **626**, 2167–2172.
22 M. Ruck, *Z. Kristallogr.*, 1995, **210**, 650–655.
23 R. Stief and W. Massa, *Z. Anorg. Allg. Chem.*, 2006, **632**, 797–800.
24 L. Mao, P. Guo, M. Kepenekian, I. Hadar, C. Katan, J. Even, R. D. Schaller, C. C. Stoumpos and M. G. Kanatzidis, *J. Am. Chem. Soc.*, 2018, **140**, 13078–13088.
25 T. Li, Y. Hu, C. A. Morrison, W. Wu, H. Han and N. Robertson, *Sustainable Energy Fuels*, 2017, **1**, 308–316.
26 E. G. Tulsky and J. R. Long, *Chem. Mater.*, 2001, **13**, 1149–1166.
27 A. J. Dennington and M. T. Weller, *Dalton Trans.*, 2018, **47**, 3469–3484.
28 N. Dehnhardt, H. Borkowski, J. Schepp, R. Tonner and J. Heine, *Inorg. Chem.*, 2018, **57**, 633–640.
29 R. Dronskowski and P. E. Blöchl, *J. Phys. Chem.*, 1993, **97**, 8617–8624.
30 R. F. W. Bader, *Chem. Rev.*, 1991, **91**, 893–928.
31 Dispersion interactions are of course electronic in origin as well. Distinguishing them from the electrostatic and overlap-based terms in the pEDA nevertheless gives us additional insight into the nature of the chemical bond.
32 M. Raupach and R. Tonner, *J. Chem. Phys.*, 2015, **142**, 194105.
33 L. Pecher and R. Tonner, *Wiley Interdiscip. Rev.: Comput. Mol. Sci.*, 2018, e1401.
34 M. P. Mitoraj, A. Michalak and T. Ziegler, *J. Chem. Theory Comput.*, 2009, **5**, 962–975.
35 S. Ding and N. Jiao, *Angew. Chem., Int. Ed.*, 2012, **51**, 9226–9237.
36 W. Ke, I. Spanopoulos, C. C. Stoumpos and M. G. Kanatzidis, *Nat. Commun.*, 2018, **9**, 4785.
37 Q. A. Akkerman, S. G. Motti, A. R. S. Kandada, E. Mosconi, V. D'Innocenzo, G. Bertoni, S. Marras, B. A. Kamino, L. Miranda, F. De Angelis, A. Petrozza, M. Prato and L. Manna, *J. Am. Chem. Soc.*, 2016, **138**, 1010–1016.
38 I. Spanopoulos, W. Ke, C. C. Stoumpos, E. C. Schueller, O. Y. Kontsevoi, R. Seshadri and M. G. Kanatzidis, *J. Am. Chem. Soc.*, 2018, **140**, 5728–5742.
39 W. Ke, I. Spanopoulos, Q. Tu, I. Hadar, X. Li, G. S. Shekhawat, V. P. Dravid and M. G. Kanatzidis, *J. Am. Chem. Soc.*, 2019, **141**, 8627–8637.

3.4. Multinary Halogenido Bismuthates Beyond the Double Perovskite Motif

Natalie Dehnhardt, Hayden Paneth, Nikolas Hecht, Johanna Heine, *Inorganic Chemistry* **2020**, *59*, 6, 3394-3405, DOI: 10.1021/acs.inorgchem.9b03287.

Abstract

Both lead halide perovskites and bismuth based double perovskites have generated intense research interest in the last few years. There is, however, a broader class of bismuthates that transcends the double perovskite motif. These multinary halogenido bismuthates remain severely underexplored and offer rich research opportunities with regard to new structure motifs and material properties. In this Forum article, we want to provide both an overview of the work on this class of compounds that has been done in the last two decades and an example how new compounds can be obtained and which challenges are associated with their synthesis. We present the synthesis and characterization of six new bismuthates, $(PBz_4)_3Bi_3Br_{12}$ (**1**) $(PBz_4)_2(MeCN)_2Cu_2Bi_2Br_{10}$ (**2**), $(PBz_4)Bi_2I_7$ (**3**), $(PBz_4)_2(MeCN)_2Cu_2Bi_2I_{10}$ (**4**), $(PBz_4)_2AgBi_2I_9$ (**5**) and $(PBz_4)_3Bi_3I_{12} \cdot C_4H_8O$ (**6**) based on the tetrabenzylphosphonium cation PBz_4^+. **2**, **4** and **5** represent new multinary bismuthates, featuring both a familiar anion motif with a new element combination in **2** and a previously unknown anionic chain in **5**. We use this series of compounds to further elucidate the influence of anion composition, nuclearity and dimensionality on the compounds' onset of absorption and un-cover that an additional factor has to play a role in copper iodido bismuthates.

Zusammenfassung

Diese Veröffentlichung erschien im Rahmen des *Inorganic Chemistry*-Forums *„Bismuth-The Magic Element“* und gliedert sich in zwei Teile. Im ersten Teil wird ähnlich zu einem Übersichtsartikel der aktuelle Forschungsstand auf dem Gebiet der multinären Halogenidometallate erörtert und besondere Herausforderungen und Eigenschaften der Verbindungsklasse erläutert. Im zweiten Teil werden die Erkenntnisse des ersten Teils anhand einer Serie von sechs neuen Halogenidometallaten, die mit dem Tetrabenzylphosphoniumkation kristallisieren, angewandt und beispielhaft untersucht. Unter den dargestellten Verbindungen befinden sich sowohl solche mit bereits bekannter Anionenstruktur $(PBz_4)_3Bi_3Br_{12}$ (**1**), $(PBz_4)Bi_2I_7$ (**3**), $(PBz_4)_2(MeCN)_2Cu_2Bi_2I_{10}$ (**4**) und $(PBz_4)_3Bi_3I_{12} \cdot C_4H_8O$ (**6**) sowie das erste multinäre Kupfer-Bromidobismutat $(PBz_4)_2(MeCN)_2Cu_2Bi_2Br_{10}$ (**2**), welches eine bekannte Anionenstruktur in neuer Elementkombination aufweist, und das Silber-Iodidobismutat $(PBz_4)_2AgBi_2I_9$ (**5**) mit einem bisher unbekannten kettenförmigen Anion. Ausschnitte aus den Kristallstrukturen sind

in Abbildung 3.4 dargestellt.

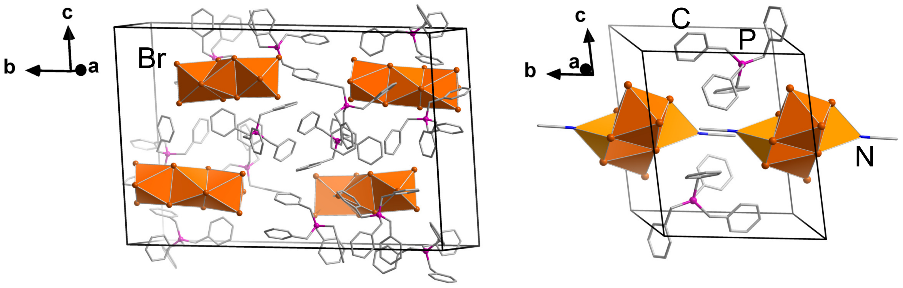

$(PBz_4)_3Bi_3Br_{12}$ (**1**) $(PBz_4)_2(MeCN)_2Cu_2Bi_2Br_{10}$ (**2**)

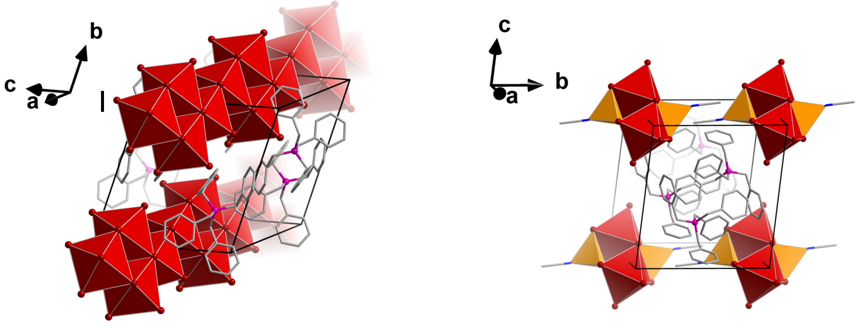

$(PBz_4)Bi_2I_7$ (**3**) $(PBz_4)_2(MeCN)_2Cu_2Bi_2I_{10}$ (**4**)

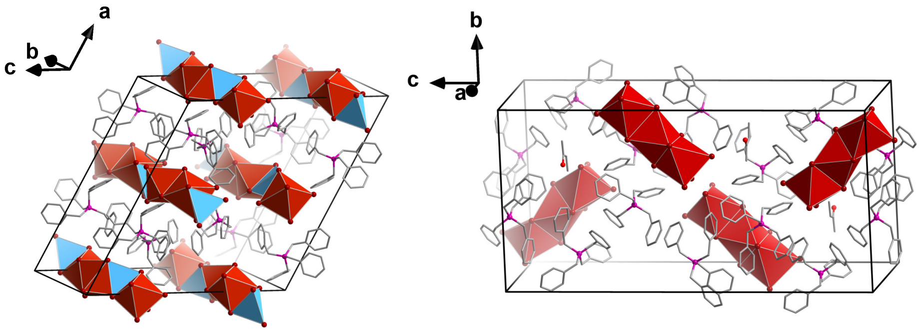

$(PBz_4)_2AgBi_2I_9$ (**5**) $(PBz_4)_3Bi_3I_{12}\cdot(C_4H_8O)$ (**6**)

Abbildung 3.4: Ausschnitte aus den Kristallstrukturen der in „Multinary Halgenido Bismuthates Beyond the Double Perovskite Motif“ publizierten Strukturen.

Die Verbindungen **1** bis **4** konnten aus stöchiometrischen Mischung der Edukte in heißem Aceonitril erhalten werden. Werden Bismuttribromid und Tetrabenzylphosphoniumbromid in heißem Acetonitril für 30 Minuten refluxiert und anschließend filtriert, können nach einem Tag helle, gelbe, blockförmige Kristalle von **1** erhalten werden. Bei der Synthese von **2** kommt zusätzlich Kupfer-I-bromid zum Einsatz, was das Arbeiten unter inerten Bedingungen notwendig macht, da ansonsten eine schnelle Oxidation zu Kupfer-II-bromid erfolgt, was an einem Farbwechsel der gelben Reaktionslösung zu grün zu beobachten ist. Für die Darstellung von **3** und **4** kamen Bismuttriiodid und Tetrabenzylphosphoniumhexafluorophosphat $(PBz_4)PF_6$ zum Einsatz. Die Verwendung von $(PBz_4)PF_6$ machte den

Einsatz einer weiteren Iodidquelle erforderlich, in deren Anwesenheit es zur Bildung der gewünschten Iodidobismutate kommen kann.

Hierbei hat sich Natriumiodid als geeignet erwiesen, da es eine entsprechend gute Löslichkeit in Acetonitril besitzt, jedoch kein Einbau von Natriumionen in die Kristallstruktur erfolgt. Die Verwendung von Kaliumiodid führte hingegen stets zum Auftreten großer amorpher Niederschläge, die eine saubere Kristallisation verhinderten. Zusätzlich war für die Verbindungen **2** bis **4** eine Aufkonzentration der Reaktionslösung nötig, um eine Kristallisation zu erreichen.

Die Verbindungen **5** und **6** konnten im Gegensatz zu **1** bis **4** nur aus nicht- stöchiometrischen Reaktionsmischungen erhalten werden. Hier erwies sich 2-Butanon als geeigneteres Lösungsmittel, da aus Acetonitril meist schnell binäre Bismutate kristallisieren, wodurch die Bildung von multinären Bismutaten, die meist eine längere Kristallisationszeit aufweisen, verhindert wird. Trotzdem konnte auch aus 2-Butanon die Co-Kristallisation von dem binären Iodidobismutat **6** nicht verhindert werden.

Verbindung **5** weist ein bisher unbekanntes Anion auf, welches aus kantenverknüpften $\{Bi_2I_9\}$- und $\{AgI_4\}$-Einheiten besteht, die zu einer Kette propagieren. Auf Grund des ähnlichen Habitus der Kristalle war eine Unterscheidung zu **6** nur über Röntgenbeugung möglich, worüber einige Kristalle isoliert werden konnten.

Mit Ausnahme von **5** wurden alle Verbindungen über UV-Vis-Spektroskopie charakterisiert. Hierbei ermöglicht ein direkter Vergleich der binären Bismutate **1** und **6** mit den multinären Bismutaten **2** und **4** den Einfluss der zusätzlichen Kupferhalogenideinheiten auf die optischen Eigenschaften der Verbindungen. Für die Bromidobismutate **1** und **2** wird eine Rotverschiebung von 0,24 eV vom binären zum multinären Bismutat beobachtet. Dieser Trend ist schon für Iodidobismutate bekannt und kann somit für die bisher unbekannten ternären Bromidobismutate bestätigt werden.

Der selbe Trend wäre somit auch für den Übergang von Verbindung **6** zu **4** zu erwarten gewesen. Das ternäre Bismutat **4** zeigt allerdings ähnliche Absorptionseigenschaften wie die binären Bismutate **3** und **6**. Der Vergleich mit der Literatur bestätigt die von uns gefundene Bandkante bei 2,03 eV für das literaturbekannte Anion in **4**.[94]

Für ein in unserer Arbeitsgruppe synthetisiertes und unter Abschnitt 3.2. diskutiertes Kupfer-Iodidobismutat, $(PPh_4)_2Cu_2(MeCN)BiI_7$, welches wie **4** diskrete Anionen mit einem von Acetronitril koordinierten Kupferatom enthält, wird eine Absorptionskante von 1,8 eV beobachtet. Dieser Wert liegt deutlich unter dem für **4** erhaltenen Wert. Ein Vergleich der Strukturmotive offenbart unterschiedliche Verknüpfungsmuster zwischen den $\{BiI_6\}$- und $\{CuI_4\}$- bzw. $\{CuI_3MeCN\}$-Einheiten. Während die Einheiten in der bekannten Verbindung $(PPh_4)_2Cu_2(MeCN)BiI_7$ flächenverknüpft sind, weisen sie in **4** eine Kantenverknüpfung auf. Dies lässt den Rückschluss zu, dass nicht nur die Nuklearität und Dimensionalität von Halogenidobismutaten einen Einfluss auf die optischen Eigenschaften haben, sondern zusätzlich auch das Verknüpfungsmuster zwischen den einzelnen

Koordinationspolyedern eine Rolle spielt.

Eigener Anteil

Alle Synthesen wurden von mir geplant und von *Nikolas Hecht* und *Hayden Paneth* im Rahmen von Forschungspraktika durchgeführt. Hierbei synthetisierte *Nikolas Hecht* die (PBz_4)-Salze sowie die beiden Bromidobismutate **1** und **2**, während die Iodidobismutate **3** bis **6** von Hayden Paneth dargestellt wurden. Alle Reaktionen wurden von mir reproduziert und optimiert. Alle Verbindungen wurden über Röntgenbeugung an Einkristallen und Pulvern, alle außer **5** über UV-Vis- und Infrarot-Spektroskopie sowie CHN-Elementaranalyse charakterisiert und identifiziert. Alle Ergebnisse wurden von mir ausgewertet und für die Publikation aufbereitet. Einkristallmessung sowie Strukturlösung und -verfeinerung von **6** wurde von mir, von **1** bis **5** von *Dr. Johanna Heine*, durchgeführt. Pulverdiffraktogramme, UV-Vis-Spektren und Infrarotspektren wurden von mir aufgenommen. Die CHN-Elementaranalyse wurde von der zentralen Abteilung für Massenspektrometrie und Elementaranalyse der Philipps-Universität Marburg durchgeführt. Das Manuskript habe ich in Zusammenarbeit mit *Dr. Johanna Heine* verfasst.

Inorganic Chemistry

pubs.acs.org/IC Forum Article

Multinary Halogenido Bismuthates beyond the Double Perovskite Motif

Natalie Dehnhardt, Hayden Paneth, Nikolas Hecht, and Johanna Heine*

Cite This: *Inorg. Chem.* 2020, 59, 3394−3405

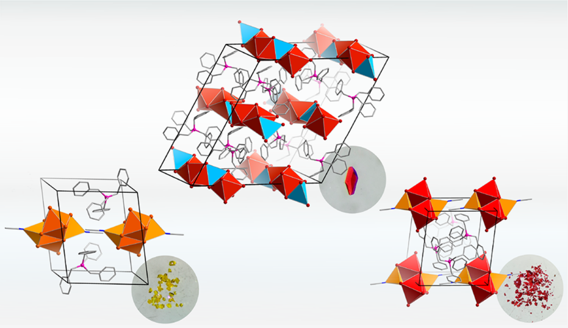

ABSTRACT: Both lead halide perovskites and bismuth-based double perovskites have generated intense research interest in the past few years. There is, however, a broader class of bismuthates that transcends the double perovskite motif. These multinary halogenido bismuthates remain severely underexplored and offer rich research opportunities with regard to new structure motifs and material properties. In this Forum Article, we want to provide both an overview of the work on this class of compounds that has been done in the last 2 decades and an example of how new compounds can be obtained and which challenges are associated with their synthesis. We present the synthesis and characterization of six new bismuthates, $(PBz_4)_3Bi_3Br_{12}$ (**1**) $(PBz_4)_2(MeCN)_2Cu_2Bi_2Br_{10}$ (**2**), $(PBz_4)Bi_2I_7$ (**3**), $(PBz_4)_2(MeCN)_2Cu_2Bi_2I_{10}$ (**4**), $(PBz_4)_2AgBi_2I_9$ (**5**), and $(PBz_4)_3Bi_3I_{12}\cdot C_4H_8O$ (**6**), based on the tetrabenzylphosphonium cation PBz_4^+. **2**, **4**, and **5** represent new multinary bismuthates, featuring both a familiar anion motif with a new element combination in **2** and a previously unknown anionic chain in **5**. We use this series of compounds to further elucidate the influence of the anion composition, nuclearity, and dimensionality on the compounds' onset of absorption and discover that an additional factor, the connectivity between coordination polyhedra, plays a role in copper iodido bismuthates.

■ INTRODUCTION

Halogenido bismuthates are a class of compounds with a rich history, as exemplified by Dragendorff's reagent, an acidic aqueous solution of a bismuth salt and an alkali-metal iodide.[1] The reagent was used to detect alkaloids NR_3 as colorful and characteristic precipitates $[HNR_3][Bi_xI_y]$ in early forensic chemistry and is still in use today.[2] This very early synthesis of what can be described as hybrid organic−inorganic halogenido metalates sparked continued interest in using halogenido bismuthates as counterions to isolate sensitive organic and inorganic ions like iminium[3] or tellurium cations.[4] All-inorganic halogenido bismuthates like $Cs_3Bi_2I_9$ were also studied early on as researchers tried to elucidate the nature of double salts, likely owed, in part, to the ready availability of both the starting materials and the compounds themselves to chemists of the late 19th century.[5] They were also among the first structurally characterized halogenido bismuthates.[6]

The first crystal structures of halogenido bismuthates with organic counterions[7,8] started to reveal the reason for the wide variety of compositions that researchers had noted before:[9,10] In contrast to other halogenido metalates like ferrates or aluminates, bismuthates show a rich structural chemistry based on corner-, edge-, and face-sharing $\{BiX_6\}$ octahedra for X = Cl, Br, and I, which will be the focus of our discussion here.[11]

Today, over 40 different anion motifs are known,[12−15] mostly polynuclear molecular anions and chains, while layers have remained rare[16,17] and 3D network anions are unknown. Figure 1 illustrates a number of representative anion motifs. The semiconductor nature of halogenido bismuthates gives rise to properties like luminescence[18] and thermochromism,[19] and the combination with specific organic cations can produce effects like photochromism[20] or enhanced conductivity.[21]

Much of the current interest focuses on the potential of halogenido bismuthates to replace hybrid organic−inorganic lead halide perovskite materials[22] with a less toxic and more stable alternative. However, attempts to directly transpose the synthesis of $APbX_3$ [e.g., A = CH_3NH_3 (MA) or Cs] to the halogenido bismuthates lead to the $A_3Bi_2X_9$ family. Here, two different anion motifs are known, depending on the nature of A and X: One motif consists of molecular $[Bi_2X_9]^{3-}$ ions built from two face-sharing octahedra. The second motif is a rare example of a layered anion, consisting of double layers of corner-sharing $\{BiX_6\}$ octahedra.[23,24] Compounds like $(MA)_3Bi_2I_9$ and $Cs_3Bi_2I_9$, both featuring the molecular anion motif, have been intensely studied, but solar cell efficiencies have remained much lower than those for the lead-based

Special Issue: Bismuth - The Magic Element

Received: November 8, 2019
Published: February 20, 2020

https://dx.doi.org/10.1021/acs.inorgchem.9b03287
Inorg. Chem. 2020, 59, 3394−3405

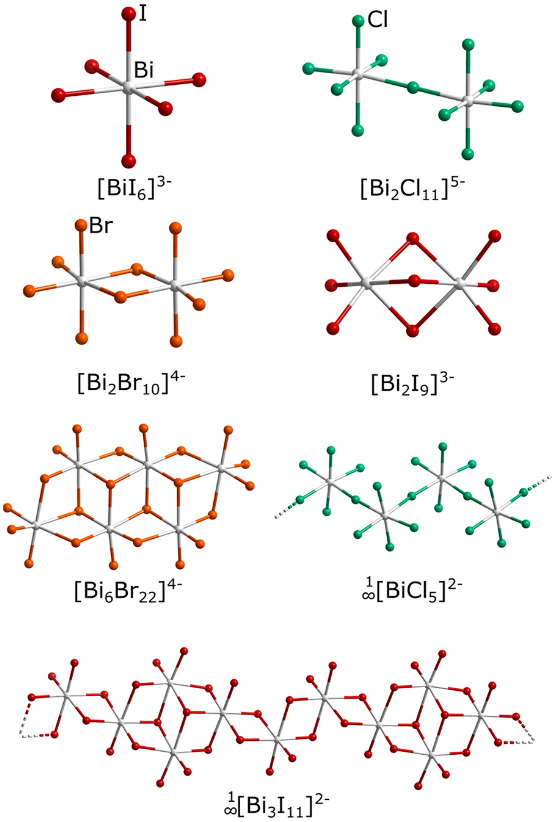

Figure 1. Representative halogenido bismuthate anion motifs found in $(TTF)_3BiI_6$,[21] $(C_3N_2H_5)_5Bi_2Cl_{11}$,[35] $(Dim)_2Bi_2Br_{10}$,[18] $(N(CH_3)_4)_3Bi_2I_9$,[36] $(PPh_4)_4Bi_6Br_{22}$,[37] $(NH_2(C_2H_4)_2O)BiCl_5$,[38] and $(H_2TMDP)Bi_3I_{11}\cdot H_2O$.[39]

counterparts.[25−30] Instead, the $A_3Bi_2X_9$ family appears to be more suitable for applications like X-ray and α-particle detectors,[31,32] luminescent nanoparticles,[33] and photocatalysis.[34]

As a way to emulate the structure of lead halide perovskites more closely, researchers have begun to reinvestigate double perovskites.[40] This class of compounds, also called elpasolites, represents a superstructure of perovskites, with a composition A_2MBiX_6 (e.g., A = Cs or MA and M = Ag, Tl, or Na), as illustrated in Figure 2. Halide double perovksites like $Cs_2NaBiCl_6$ have been known since 1972,[41] but recent efforts have resulted in the addition of compounds like $A_2AgBiBr_6$ and $Cs_2TlBiBr_6$.[42−47] $Cs_2AgBiBr_6$ has been investigated intensely and shown to have promising optical properties.[48,49] Indeed, both the fabrication of solar cells showing an efficiency of 2.5%[50] and the preparation of nanoparticles for luminescence[51] and photocatalysis[52] have been successful. Similar to the dimensional reduction in lead halide perovskites,[53] where compounds like $(BA)_2PbI_4$ (BA = butylammonium) with Pb−I layers can be prepared,[54] double perovksites like $(BA)_4AgBiBr_8$,[55] $(PEA)_4AgBiBr_8$ (PEA = phenylethylammonium),[56] or $(AE2T)_2AgBiI_8$ (AE2T = 5′-diylbis(aminoethyl)-[2,2′-bithiophene])[57] feature Ag−Bi−X layers (Figure 2). However, the chemistry of double perovksites remains limited in the sense that only M ions capable of adopting an octahedral coordination environment can be used, and for A_2MBiX_6, the Goldschmidt tolerance factor limits the choice of cations A in a fashion similar to that in perovskites.[58,59]

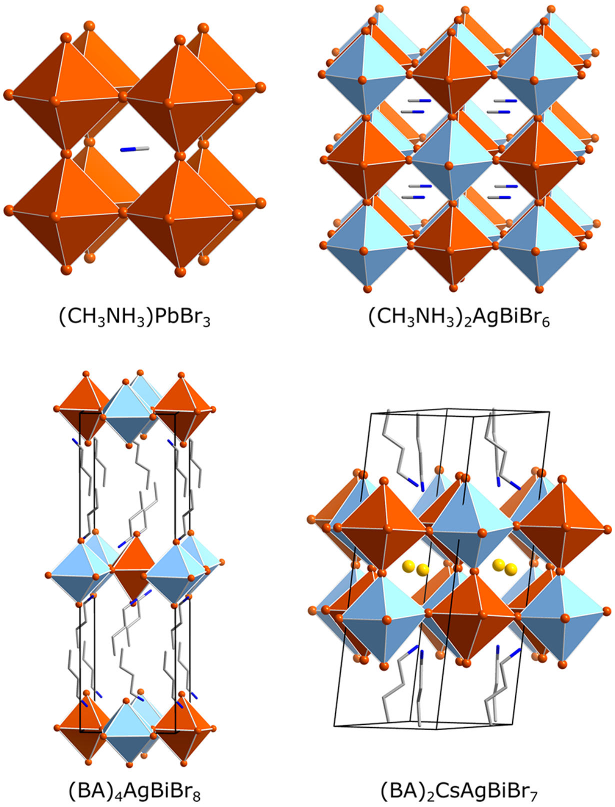

Figure 2. Comparison of the crystal structures of perovskite $(MA)PbBr_3$[60] (top left) and double perovskite $(MA)_2AgBiBr_6$[61] (top right). Crystal structures of the layered double perovskites $(BA)_4AgBiBr_8$ (bottom left) and $(BA)_2CsAgBiBr_7$[55] (bottom right). $\{PbBr_6\}$ and $\{BiBr_6\}$ octahedra are shown in orange and $\{AgBr_6\}$ octahedra in light blue. C is shown in gray, N in blue, and Cs in yellow. Only one orientation of the $CH_3NH_3^+$ cations is shown.

The questions that we want to address in this Forum Article are as follows: What happens if you go beyond the double perovskite motif? Which multinary bismuthates are available? What is the role of the cation A in this case? How can the optoelectronic properties of these compounds be understood? As a first step in answering these questions, we will give an account of the current knowledge about these nonperovskite multinary bismuthates. In a second step, we will show how the insights derived from these examples can help to prepare a new family of these compounds based on tetrabenzylphosphonium counterions that feature both familiar and new multinary anion motifs.

In stark contrast to the large number of different anion motifs and hundreds of individual examples for simple halogenido bismuthates, multinary halogenido bismuthates containing a second metal M within the metalate anion have remained rare. For all-inorganic compounds, only one nonperovskite example with alkali-metal cations, $Rb_4Ag_2BiBr_9$, is known.[62] Compounds like $(Bi_9)_4Bi_3Pb_9Br_{47}$, $AuBi_{14-\delta}Sn_{2+\delta}X_{21-\delta}$ ($\delta \approx 0.4$), and $PdBi_{15-\delta}Sn_{1+\delta}X_{21-\delta}$ ($\delta \approx 0.6$) with X = Cl and Br are also multinary halogenido bismuthates, although here the metalate is primarily used as a matrix in the isolation of cationic metal clusters.[63,64]

For organic−inorganic compounds, only 18 compounds with 12 different anion motifs have been reported (Figure 3). The first reported example $[Bi_2(C_4H_8O_3H)_3(C_4H_8O_3H_2)]$-

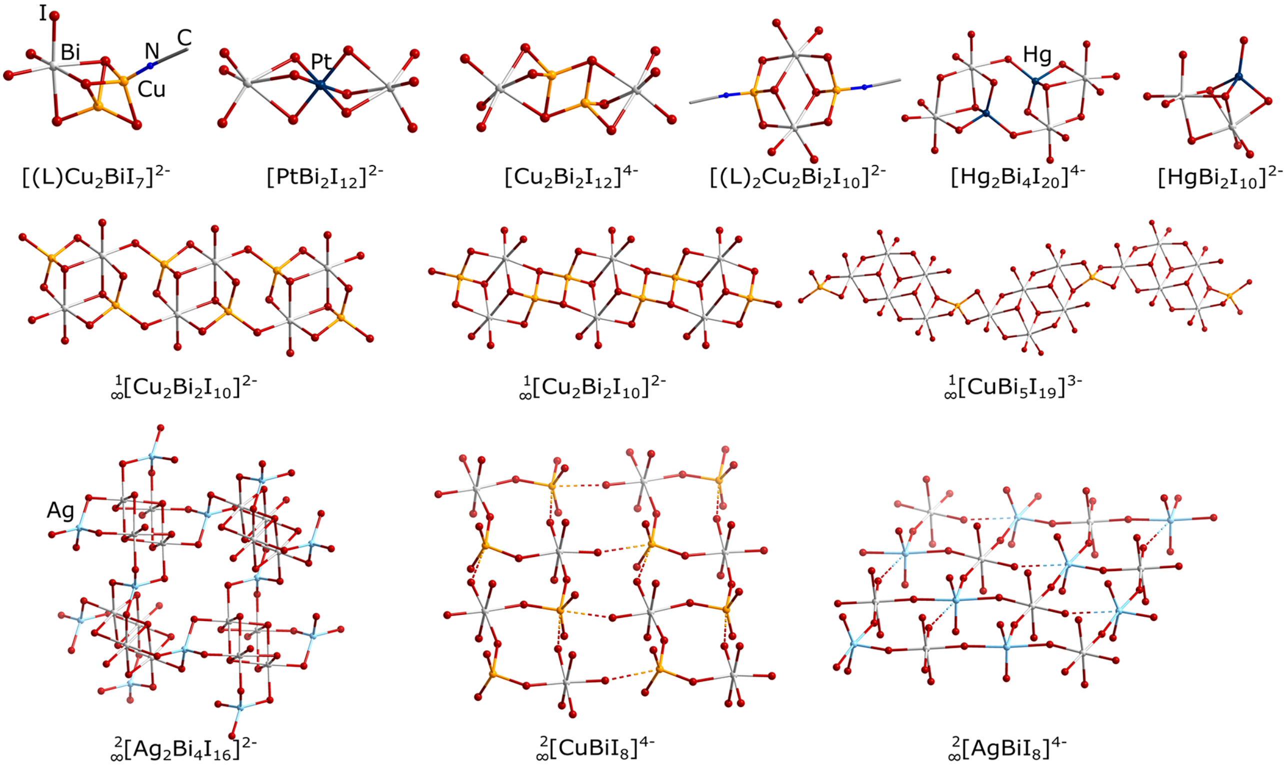

Figure 3. Examples of anion motifs in organic−inorganic multinary bismuthates (top left to bottom right with molecular anions in the top row, chainlike examples in the middle row, and layered anions in the bottom row): $(PPh_4)_2(L)Cu_2BiI_7$ (L = MeCN),[75] $(Na_4((CH_3)_2CO)_{15})[PtBi_2I_{12}]_2$,[69] $(PPh_4)_4Cu_2Bi_2I_{12}$,[74] $(n\text{-}Bu_4N)_2(CH_3CN)_2Cu_2Bi_2I_{10}$,[67] $(Et_4N)_4Hg_2Bi_4I_{20}$,[68] $(n\text{-}Bu_4N)_2HgBi_2I_{10}$,[68] $(Cu(CH_3CN)_4)_2Cu_2Bi_2I_{10}$,[67] $(Et_4N)_2M_2Bi_2I_{10}$,[66,67] $(Bi_2(C_4H_8O_3H)_3(C_4H_8O_3H_2))CuBi_5I_{19}$,[65] $(Et_4N)_2Ag_2Bi_4I_{16}$,[66] and $(C_6H_{16}N_2)_2MBiI_8$ with M = Cu and Ag.[72]

$CuBi_5I_{19}$ features a complex cation comprised of a dinuclear bismuth polyol complex and $[Bi_5I_{19}]^{4-}$ units interconnected into chains by disordered Cu^+ ions.[65] The Chen group prepared a number of different multinary bismuthates: $(n\text{-}Bu_4N)_2(CH_3CN)_2Cu_2Bi_2I_{10}$, which features a molecular anion where the Cu atoms are capped by acetonitrile ligands, $(Et_4N)_2M_2Bi_2I_{10}$ (M = Cu, Ag) and $(Cu(CH_3CN)_4)_2Cu_2Bi_2I_{10}$, with dissimilar but closely related chain motifs, which can be understood as condensation products of $[(CH_3CN)_2Cu_2Bi_2I_{10}]^{2-}$ anions, and $(Et_4N)_2Ag_2Bi_4I_{16}$, where $[Bi_4I_{16}]^{4-}$ units are connected by Ag^+ ions into a layered anion.[66,67] A comparison of the two isostructural copper and silver compounds by absorption spectroscopy and with density functional theory methods gave a first indication that the two group 11 elements behave quite differently in multinary bismuthates. Chen and co-workers also presented the first and only mercury-based examples $(Et_4N)_4Hg_2Bi_4I_{20}$ and $(n\text{-}Bu_4N)_2HgBi_2I_{10}$, both composed of molecular anions.[68] Adonin and co-workers also showed that Pt^{4+} can be included in multinary bismuthates with $(Na_4((CH_3)_2CO)_{15})[PtBi_2I_{12}]_2$, which contains a trinuclear molecular anion.[69] Only a singular example of a multinary bromido bismuthate, prepared by the Mehring group, is known: $(\{FeCp^*(CO)_2\}_2Br)_2Bi_6Br_{22}\{FeCp^*(CO)_2\}_2$, where the familiar $[Bi_6Br_{22}]^{4-}$ anion is decorated with two $FeCp^*(CO)_2$ units at two of its terminal Br atoms.[70] Pike and co-workers expanded upon the earlier work by Chen and presented $(Bu_4N)_2L_nCu_2Bi_2I_{10}$ [n = 1, L = Py; n = 2, L = PPh_3, $P(OPh)_3$], highlighting the versatility of the molecular $[L_nCu_2Bi_2I_{10}]^{2-}$ motif.[71] The two compounds $(C_6H_{16}N_2)_2MBiI_8$ (M = Cu, Ag; $C_6H_{14}N_2$ = 1,4-cyclohexanediamine) represent an interesting border case between the double perovskite and nonperovskite motifs.[72] Both compounds feature what can be approximated as M−Bi−I double perovskite layers. However, the coordination environment around the M atoms deviates strongly from the ideal octahedron, especially for Cu. This can be well understood because Cu^+ is unable to accommodate octahedral coordination.[73] A comparison of the optical absorption properties of the two isostructural compounds shows, similar to the findings of the Chen group, that the copper compound has a band gap that is about 0.25 eV smaller than the silver homologue. Our group has prepared the multinary bismuthates $(PPh_4)_4M_2Bi_2I_{12}$ (M = Cu, Ag)[74] and $(PPh_4)_2(L)Cu_2BiI_7$ (L = MeCN, EtCN),[75] both of which feature molecular anions and confirm the previous findings with regard to the influence of copper on the band gap of multinary iodido bismuthates.

When asking what can be learned from these examples, we first have to highlight that the amount of data at hand is still very small. Nonetheless, a few observations and a working hypothesis can be put forth. It seems conspicuous that only one bromido bismuthate and no chlorido bismuthate can be found among the nonperovskite organic−inorganic bismuthates. However, as shown by both the availability of a number of double perovskites with Cl and Br and our findings outlined below, this appears to be due to the fact that these compounds remain underexplored and not because they might be generally less readily available. With regard to the metal M used in multinary bismuthates, Cu^+ and Ag^+ are clearly featured most often. Both the halogenido cuprates and argentates have a rich structural chemistry on their own, highlighting their versatility.[76−80] Their flexibility with regard to their coordination environment makes them especially suitable for the synthesis of multinary metalates. However, even within the small number of known multinary halogenido bismuthates, other metals, like Hg^{2+} and Pt^{4+}, have been employed successfully, hinting toward a larger range of candidates for M. The observation that not only halogenido metalate fragments like $\{CuI_4\}$ tetrahedra but also mixed tetrahedral complex fragments like $\{CuI_3(L)\}$ with a number of different ligands L can be found suggests another path toward the modification of multinary bismuthates by changing both the electronics and sterics of L.

With regard to the observed anion motifs, it is noticeable that the halogenido bismuthate fragments are often multinuclear, e.g., $[Bi_2I_{10}]^{4-}$ or $[Bi_4I_{16}]^{4-}$, and represent anion types that are also found in simple halogenido bismuthates. These fragments are then either decorated or interconnected by M atoms to form the overall metalate anion.

The optical and electronic properties of metalate compounds are of prime importance for possible semiconductor applications. Table 1 shows the band gap (or the onset of absorption) for those multinary bismuthates where data are available. Obviously, several factors can affect the optical band gap in these compounds, from the nature of M, anion size and dimensionality, and ratio of M to Bi to the connectivity between BiX_6 and MX_n octahedra and possibly others. A quantification remains difficult because a direct comparison of the compounds is only viable for the isostructural Cu/Ag pairs discussed above. Still, some general trends can be noted for multinary iodido bismuthates despite the small data set: The incorporation of Cu^+ appears to lead to lower band gaps, both in contrast to similar Ag^+ compounds and compared to simple iodido bismuthates, with the exception of $(n\text{-}Bu_4N)_2(CH_3CN)_2Cu_2Bi_2I_{10}$,[67] which we will analyze in more detail in the discussion part below. Similar to Ag^+, Hg^{2+} does not seem to have a large effect on the compounds' band gap; here the optical properties are largely dominated by the respective bismuthate anion fragment. Expectedly, the anion dimensionality appears to play a role as well, with layer-like anions representing the compounds with the lowest band gaps among the two series of copper and silver iodido bismuthates. However, more multinary bismuthates need to be analyzed to obtain a clearer picture of the interrelationships of different factors.

Table 1. Band Gaps (Where Available) for Organic−Inorganic Multinary Bismuthates, Sorted from Lowest to Highest

	anion dimensionality	band gap (eV)
$(C_6H_{16}N_2)_2CuBiI_8$	2	1.68[72]
$(Cu(CH_3CN)_4)_2Cu_2Bi_2I_{10}$	1	1.80[67]
$(PPh_4)_4Cu_2Bi_2I_{12}$	molecular	1.8[74]
$(Et_4N)_2Cu_2Bi_2I_{10}$	1	1.89[67]
$(PPh_4)_2(MeCN)Cu_2BiI_7$	molecular	1.91[75]
$(Et_4N)_2Ag_2Bi_4I_{16}$	2	1.93[66]
$(C_6H_{16}N_2)_2AgBiI_8$	2	1.93[72]
$(Et_4N)_2Ag_2Bi_2I_{10}$	1	2.05[66]
$(n\text{-}Bu_4N)_2(CH_3CN)_2Cu_2Bi_2I_{10}$	molecular	2.06[67]
$(Et_4N)_4Hg_2Bi_4I_{20}$	molecular	2.08[68]
$(PPh_4)_4Ag_2Bi_2I_{12}$	molecular	2.1[74]
$(n\text{-}Bu_4N)_2HgBi_2I_{10}$	molecular	2.13[68]

Multinary halogenido bismuthates are available with a number of different metal complexes and organic cations as counterions, suggesting that there are no general restrictions in this regard. However, alkylammonium and phenylphosphonium cations appear to be especially versatile. In our experience with both multinary and simple halogenido bismuthates and antimonates, spherical, weakly interacting cations are helpful in allowing stronger reaction control via the stoichiometry and solvent. This makes them well suited when the goal is to prepare extended families of compounds with the same cation because they avoid the thermodynamic sink of having a single, very stable metalate that precipitates or crystallizes from solution independent of any additional reaction parameters.[81] However, this flexibility occasionally, but not inevitably, comes at a price: Crystallization of several different species in one batch can be observed, and reaction outcomes can be sensitive to small, hard-to-control changes like the starting material crystallinity or reaction vessel surface and roughness or crystallization times.[82] Nevertheless, alkyl- and arylammonium and -phosphonium cations present good starting points toward new multinary bismuthates with new anion motifs and element combinations.

To demonstrate this, we have chosen the tetrabenzylphosphonium PBz_4^+ as the templating cation for a new series of compounds. This cation combines the flexibility of alkylammonium cations with the capability of forming π interactions due to the phenyl rings and thus represents a logical candidate and expansion from previous reactions toward multinary bismuthates. A small number of halogenido metalates with PBz_4^+ as a counterion were prepared by Krautscheid in the 2000s, including $(PBz_4)_2Bi_2I_8$, a rare example of a iodido bismuthate with square-pyramidal BiI_5 units,[83] and bromido plumbates $(PBz_4)_2PbBr_4$ and $(PBz_4)_4[Pb_2Br_6][PbBr_4]$ with unusual tetracoordinated metalate motifs.[84] Despite the obvious capability of the PBz_4^+ ion to stabilize unusual halogenido metalate motifs and the easy synthetic access to the starting materials $(PBz_4)Br$ and $(PBz_4)[PF_6]$, no further studies using this counterion have been reported.

Here, we present the first results of our investigation of tetrabenzylphosponium halogenido bismuthates: the bromido compounds $(PBz_4)_3Bi_3Br_{12}$ (**1**) and $(PBz_4)_2(MeCN)_2Cu_2Bi_2Br_{10}$ (**2**), which represents the first example of a Bi−Br−Cu unit in a halogenido bismuthate, and $(PBz_4)Bi_2I_7$ (**3**), $(PBz_4)_2(MeCN)_2Cu_2Bi_2I_{10}$ (**4**), $(PBz_4)_2AgBi_2I_9$ (**5**), and $(PBz_4)_3Bi_3I_{12}\cdot(C_4H_8O)$ (**6**), iodido bismuthates with both known and new anion motifs. The absorption spectra of **1**−**4** and **6** allow us to identify both commonly observed trends and a peculiarity associated with the anion motif found in **4**, suggesting that the connectivity between coordination polyhedra also plays a role in the optical properties of these compounds.

■ EXPERIMENTAL DETAILS

General Procedures. BiI_3 was synthesized from the elements according to literature procedures.[85] Tribenzylphosphine, benzyl bromide, potassium hexafluorophosphate, and silver iodide were used as supplied from commercial sources. $(PBz_4)Br$ and $(PBz_4)PF_6$ were prepared according to literature procedures.[84] CHN analysis was carried out on an Elementar CHN analyzer. Powder patterns were recorded on a STADI MP (STOE Darmstadt) powder diffractometer, with Cu Kα_1 radiation and λ = 1.54056 Å at room temperature in transmission mode. The IR spectra were measured on a Bruker

Tensor 37 Fourier transform infrared spectrometer equipped with an ATR-platinum measuring unit.

Synthesis. Compounds **1**−**4** were synthesized from stoichiometric mixtures of the respective starting compounds in organic solvents. For compounds **5** and **6**, only nonstoichiometric reaction solutions resulted in the desired compounds. As is well documented for halogenido metalates, many factors, such as the reaction stoichiometry and temperature, reagent concentration, and solvent, control the formation of crystals of a specific species in nontrivial ways, and the crystallization of several compounds in one batch is a commonly observed obstacle. Except for compound **2**, all reactions were carried out under aerobic conditions.

*$(PBz_4)_3Bi_3Br_{12}$ (**1**).* $BiBr_3$ (46 mg, 0.1 mmol) and $(PBz_4)Br$ (47 mg. 0.1 mmol) were dissolved in 5 mL of acetonitrile by heating to boiling under magnetic stirring for 30 min. The hot reaction solution was slowly cooled to room temperature and stored for crystallization. Bright-yellow block-shaped crystals precipitated after 1 day at room temperature. The crystals were isolated by filtration. Yield: 34.4 mg, 0.012 mmol, 37% based on the total bismuth content. Anal. Calcd for $C_{84}H_{84}Bi_3Br_{12}P_3$ (M = 2772.31 g mol^{-1}): C, 36.39; H, 3.05. Found: C, 36.51; H, 3.25.

*$(PBz_4)_2(MeCN)_2Cu_2Bi_2Br_{10}$ (**2**).* For obtaining single crystals of **2**, $BiBr_3$ (46 mg, 0.1 mmol), CuBr (15 mg, 0.1 mmol), and $(PBz)_4Br$ (47 mg, 0.1 mmol) were dissolved in 4 mL of dried acetonitrile by heating to boiling under magnetic stirring for 30 min. Working under inert conditions was necessary to prevent the oxidation of Cu(I) to Cu(II). Concentration of the reaction solution to half its volume resulted in a few yellow block-shaped crystals. Microcrystalline powders of **2** were prepared by dissolving the same amounts of starting reagents in 4 mL of acetonitrile. The clear reaction solution was concentrated by evaporation until a yellow powder precipitated, which was washed with pentane. Compared to the single crystals, the microcrystalline powder seems to be less stable, which is indicated by a fast color change from yellow to brown when drying under vacuum, and the observation of extra reflections in the PXRD pattern is shown in Figure S9. Yield: 31.5 mg, 0.028 mmol, 28%. Anal. Calcd for $C_{30}H_{31}BiBr_5CuNP$ (M = 1108.61 g mol^{-1}): C, 32.50; H, 2.82; N, 1.26. Found: C, 32.54; H, 2.84; N, 1.18.

*$(PBz_4)Bi_2I_7$ (**3**).* BiI_3 (120 mg, 0.2 mmol), $(PBz_4)PF_6$ (54.4 mg, 0.1 mmol), and NaI (15 mg, 0.1 mmol) were dissolved in 6 mL of acetonitrile by heating to boiling under magnetic stirring for 30 min. The hot reaction solution was slowly cooled to room temperature. During evaporation of the solvent to half its original volume, dark-red crystals precipitated. Yield: 17.2 mg, 0.01 mmol, 10% based on the total bismuth content. Anal. Calcd for $C_{28}H_{28}Bi_2I_7P$ (M = 1701.80 g mol^{-1}): C, 19.76; H, 1.66. Found: C, 19.76; H, 1.72.

*$(PBz_4)_2(MeCN)_2Cu_2Bi_2I_{10}$ (**4**).* BiI_3 (60 mg, 0.1 mmol), CuI (19 mg, 0.1 mmol), $(PBz_4)PF_6$ (54.4 mg, 0.1 mmol), and NaI (15 mg, 0.1 mmol) were dissolved in 6 mL of acetonitrile by heating to boiling under magnetic stirring for 30 min. The hot reaction solution was slowly cooled to room temperature and stored for crystallization. Dark-red block-shaped crystals precipitated after 1 week at room temperature. Crystals were isolated by filtration. Yield: 43.1 mg, 0.016 mmol, 32% based on the total bismuth content. Anal. Calcd for $C_{60}H_{62}Bi_2Cu_2I_{10}N_2P_2$ (M = 2687.22 g mol^{-1}): C, 26.82; H, 2.33; N, 1.04. Found: C, 26.57; H, 2.44; N, 1.06.

*$(PBz_4)_2AgBi_2I_9$ (**5**) and $(PBz_4)_3Bi_3I_{12}\cdot(C_4H_8O)$ (**6**).* BiI_3 (60 mg, 0.1 mmol), AgI (46 mg, 0.2 mmol), $(PBz_4)PF_6$(54 mg, 0.1 mmol), and NaI (15 mg, 0.1 mmol) were suspended in 6 mL of 2-butanone and heated to boiling under magnetic stirring for 30 min. The hot reaction solution was filtered and stored for crystallization. Dark-red block-shaped crystals were observed after 8 days. Single-crystal diffraction measurements revealed the presence of crystals of **5** and **6**. Because of the close resemblance of the crystals' color and shape, a separation of the two species by hand was not possible.

*Compound **6**.* BiI_3 (120 mg, 0.2 mmol), AgI (24.4 mg, 0.1 mmol), $(PBz_4)PF_6$ (108 mg, 0.2 mmol), and NaI (30 mg, 0.2 mmol) were suspended in 6 mL of 2-butanone and heated to boiling under magnetic stirring for 30 min. The hot reaction solution was filtered and stored for crystallization. Dark-red plank-shaped crystals precipitated after 3 days at room temperature. Crystals were isolated by filtration. Yield: 46.3 mg, 0.014 mmol, 20.3% based on the total bismuth content. Anal. Calcd for $C_{88}H_{92}Bi_3I_{12}OP_3$ (M = 3408.42 g mol^{-1}): C, 31.01; H, 2.72. Found: C, 30.82; H, 2.72.

X-ray Crystallography. Single-crystal X-ray determination was performed on a Bruker Quest D8 diffractometer with microfocus Mo Kα radiation and a Photon 100 (CMOS) detector or on a STOE IPDS-2T diffractometer equipped with an imaging-plate detector system using Mo Kα radiation with graphite monochromatization. The structures were solved using direct methods, refined by full-matrix least-squares techniques, and expanded using Fourier techniques, using the *SHELX* software package[86−88] within the *OLEX2* suite.[89] Pictures of the crystal structures were created using *DIAMOND*.[90] Additional details on the refinement of each structure can be found in the Supporting Information. Structures have been deposited as CCDC 1964160−1964165.

Optical Characterization. Optical absorption spectra were recorded on a Varian Cary 5000 UV/vis/near-IR spectrometer in the range of 200−800 nm in diffuse-reflectance mode employing a Praying Mantis accessory (Harrick). For ease of viewing, raw data were transformed from % reflectance R to absorbance A according to $A = \log(1/R)$, which yields estimates comparable to the widely used Kubelka−Munk relationship.[91]

DISCUSSION

Synthesis. The synthesis of compounds **1**−**4** was accomplished by dissolving stoichiometric ratios of the reactants in hot acetonitrile or 2-butanone. An additional iodide source is necessary for synthesis of the iodido bismuthates **3**−**6**, and NaI was used in all cases. While the synthesis of **1** and **4** leads to phase-pure crystalline samples, the formation of side products can be observed for **2**, **3**, and **5**. In earlier work on a reaction system with the PPh_4^+ cation, we could also observe multiple species, especially binary bismuthates, crystallizing from nonstoichiometric reaction solutions. This can be avoided by tuning the reaction mixtures and carefully controlling the crystallization conditions. Nevertheless, the yields of the respective products remained low, especially for compounds **2**, **3**, and **5**. In the case of compound **2**, a fast oxidation of Cu^+ to Cu^{2+} was observed under ambient conditions, indicated by a color change from a light-yellow to a green solution. This could be avoided by working under an inert atmosphere. Pictures of the crystalline samples are shown in Figure 4.

While crystals of **1** could be obtained after a few hours, concentration of the reaction solution was necessary for obtaining crystals of **2**−**4**. Crystallization of **5** still remains a challenge because we have not yet found a way to suppress the cocrystallization of **6** despite testing a number of different solvents and reaction stoichiometries. Remarkably, efforts to synthesize **5** from stoichiometric reaction solutions resulted in phase-pure samples of **6**. Because AgI shows only poor solubility in 2-butanone and other organic solvents, an excess of AgI seems to be necessary for obtaining **5**. Because of the crystals' close resemblance in color and shape, a manual separation of **5** and **6** was not possible. To take the crystal picture of **5** shown in Figure 4, the crystal had to be identified with single-crystal X-ray diffraction.

Description of the Crystal Structures. All six compounds feature tetrabenzylphosphonium cations. In earlier work, we could successfully integrate tetraphenylphosphonium cations into multinary iodido bismuthates. In comparison to PPh_4^+, PBz_4^+ features an additional CH_2 unit between the central P atom and the phenyl rings, allowing more flexibility because the benzyl groups are less rigid than the phenyl

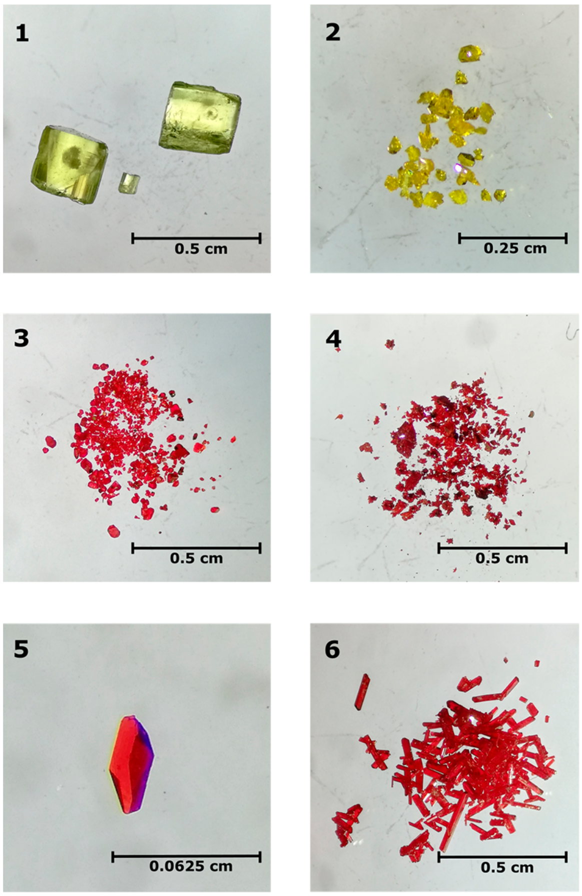

Figure 4. Pictures of the crystalline samples of **1**−**6** from top left to bottom right.

groups. Compounds **1** and **2** show known anion motifs with a new element combination, and **3** and **4** show anion motifs that have already been reported before but with a different cation. Compound **5** shows a previously unknown anion motif. Compound **6** is also comprised of a well-known anion but serves as a good point of comparison for **1**. Generally, metal−halide distances are within the expected ranges for all compounds, so only specific features of interest will be highlighted in the following discussion.

Compound **1** crystallizes in the monoclinic space group $P2_1/c$ as large yellow blocks. It features a trinuclear anion that consists of three trans-face-sharing $\{BiBr_6\}$ octahedra. Two excerpts of the crystal structure are displayed in Figure 5.

While dinuclear bromido bismuthates with $[Bi_2Br_9]^{3-}$ are well-known,[37] the corresponding trinuclear anion has only been reported for the lighter[92] and heavier halides.[93] The interatomic distances in all three anions follow the same trends: The shortest Bi−X distances are obtained for the bonds connecting the Bi atoms with the terminal halogen atoms. The distances from the outer Bi atoms to the bridging halogen atoms are approximately 0.5 Å larger, while the Bi−X distances involving the central Bi atom lie between these two values. This results in a relatively undistorted central octahedral $\{BiX_6\}$ unit. Therefore, the anion structure can be described as a central $\{BiX_6\}$ octahedron, to which two neutral BiX_3 units are added on both sites. The anions are packed in the *ab* plane and oriented ca. ±15° away from the *b* direction.

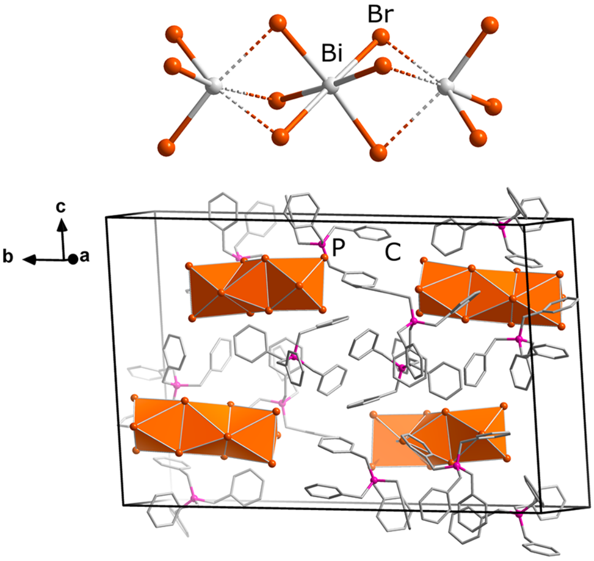

Figure 5. Anion (top) and unit cell (bottom) in **1**.

Compound **2** crystallizes in the triclinic space group *P*-1 as bright-yellow blocks. The compound features the first multinary copper bromido bismuthate anion. The corresponding iodido bismuthate $[(MeCN)_2Cu_2Bi_2I_{10}]^{4-}$ was already described by Chen and co-workers.[67] In **2**, two $\{BiBr_6\}$ octahedra are connected via a common edge, forming a $[Bi_2Br_{10}]^{4-}$ unit. The coordination sphere of the Cu atoms is tetrahedral, with three bromide ligands and one acetonitrile ligand coordinating to the Cu atom. Two of these $\{CuBr_3(MeCN)\}$ tetrahedra are connected to the $[Bi_2Br_{10}]^{4-}$ unit via two common edges on opposite sides, resulting in the anion shown in Figure 6. Ternary bismuthate anions with a nitrile ligand have been observed not only in the $[(MeCN)_2Cu_2Bi_2I_{10}]^{4-}$ anion but also in a series of multinary antimonates and bismuthates featuring a $\{CuI_3(nitrile)\}$ group.[75]

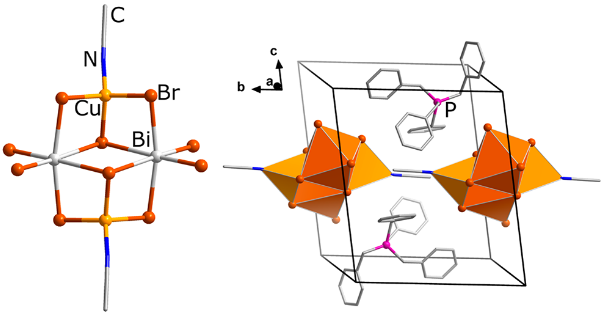

Figure 6. Anion (left) and unit cell (right) in **2**.

To highlight the influence of the $[Cu(MeCN)]^+$ fragment on the structure of the anion, their interatomic distances and angles are compared with the respective values of the binary anion $[Bi_2Br_{10}]^{4-}$, which consists of two edge-sharing $\{BiBr_6\}$ octahedra,[18] because they are also featured in **2**. It becomes clear that the addition of $[Cu(MeCN)]^+$ results in a distortion of the Br−Bi−Br angles adjacent to the Cu atom. In the $[Bi_2Br_{10}]^{4-}$ anion, an almost ideal octahedral coordination of the Bi atom is observed, with all Br−Bi−Br angles approximately 90° and μ-bridging Bi−Br distances slightly elongated compared to terminal Bi−Br distances. With the addition of the $[Cu(MeCN)]^+$ fragment, two former terminal Bi−Br bonds are now bridging the Bi and Cu atoms. This results in a distortion of the respective Br−Bi−Br angles toward only 84° in the direction of the Cu atoms, while the atomic distances remain similar to those found in the $[Bi_2Br_{10}]^{4-}$ anion (Figure 7). Similar to **1**, the copper bromido bismuthate anions are packed in the *ab* plane with the acetonitrile ligands of adjacent anions oriented parallel to each other.

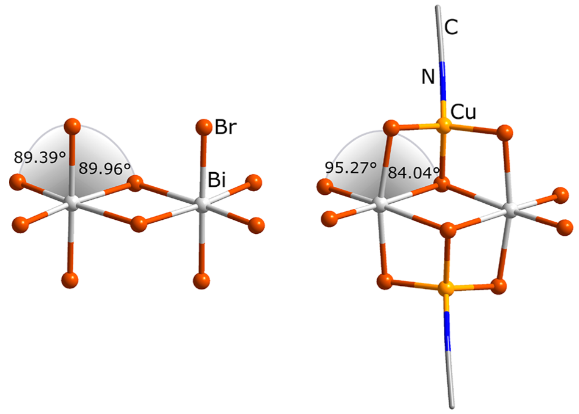

Figure 7. Anions in $(Dim)_2Bi_2Br_{10}$[18] and **2** with the respective angles highlighted.

Compound **3** crystallizes in the triclinic space group *P*-1 as dark-red blocks (Figure 8). It features a chainlike $[Bi_2I_7]^-$ anion with a tetranuclear repetition unit, which has been reported once before in $(CH_2{=}C(C_6H_4\text{-}4\text{-}NO_2)CH_2NMe_3)[Bi_2I_7]$.[94] The anionic chains are running parallel to the *a* direction. Overall, the anion and cation packing in **3** is quite different from that in **1** and **2** because the PBz_4^+ cations form strongly corrugated layers to accommodate the more space-consuming anions. Here, as in the other compounds, the PBz_4^+ cation arrangements show some phenyl rings oriented parallel to each other, suggesting the presence of distinct, directional supramolecular interactions. However, this appears to be largely a packing effect because no particularly short distances between the parallel rings or rings and CH groups are observed.[95−97]

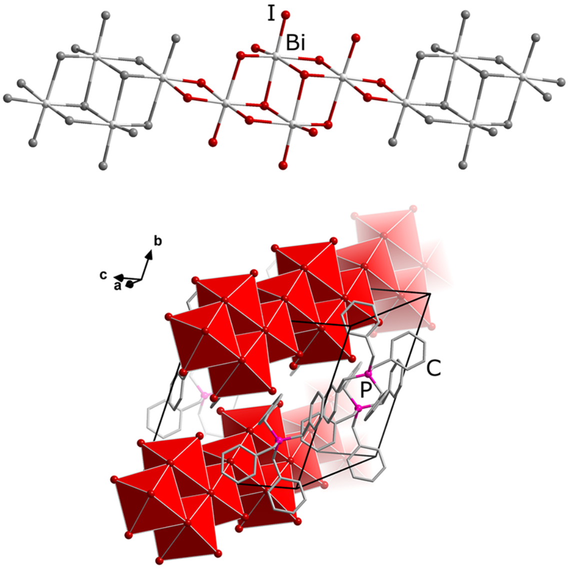

Figure 8. Excerpts of the crystal structures of **3**. The tetranuclear repetition unit is highlighted.

Compound **4** crystallizes in the triclinic space group *P*-1 as dark-red blocks. The compound features the same tetranuclear anion as that in **2**, with I instead of Br atoms. As mentioned above, the anion motif was already described by Chen and co-workers, who successfully crystallized it with NBu_4^+ as a counterion.[67] Two excerpts of the crystal structure of **4** are shown in Figure 9. **2** and **4** feature closely related crystal structures; however, the orientation of the PBz_4^+ cations differs in some details, likely to compensate for the size difference of the anions.

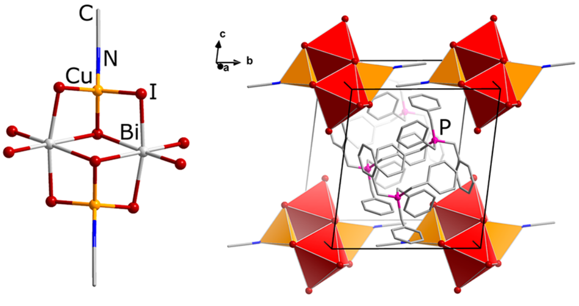

Figure 9. Anion (left) and unit cell (right) in **4**.

Compound **5** crystallizes in the monoclinic space group $P2_1/n$ as red blocks. The compound features a unique strandlike silver iodido bismuthate anion. The 1D anion consists of a trinuclear repetition unit, which can be derived from the simple binary anion $[Bi_2I_9]^{3-}$.[36] In this binary anion, two $\{BiI_6\}$ octahedra are connected via a common face. In **5**, a $\{AgI_4\}$ tetrahedron connects the $[Bi_2I_9]^{3-}$ fragments via common edges. The resulting chain propagates along the crystallographic *b* axis. So far, four silver iodio bismuthates are known. Of these, only the $[Bi_2Ag_2I_{10}]^{2-}$ anions found in $(Et_4N)_2Ag_2Bi_2I_{10}$[66] display edge-sharing polyhedra similar to those in **5**. A comparison of the Ag−I distances in **5** reveals values from 2.84 to 2.86 Å, which is in good agreement with the distances found in the $[Bi_2Ag_2I_{10}]^{2-}$ anion. The PBz_4^+ cations are arranged between the anions, forming a columnar, honeycomb-like network. Excerpts of the crystal structure are shown in Figure 10.

Compound **6** crystallizes in the monoclinic space group $P2_1/c$ as red needles (Figure 11). The anion observed in **6**, a trinuclear $[Bi_3I_{12}]^{3-}$ anion composed of three trans-face-sharing octahedra, is well-known and has been found for several simple iodido bismuthates with ammonium and phosphonium counterions,[98,99] so it is not surprising to observe it for PBz_4^+ as well.

For our work, **6** is helpful insofar as it allows us to draw a direct comparison between the optical properties of **1** and **2** and also **6** and **4**, as shown below. Interestingly, the packing in **6** is quite different from that in **1**, which features the bromido homologue of the $[Bi_3I_{12}]^{3-}$ anion, in order to accommodate the solvate butanone molecule. In the crystal structure of **6**, the anions are oriented along the *bc* plane with two perpendicular

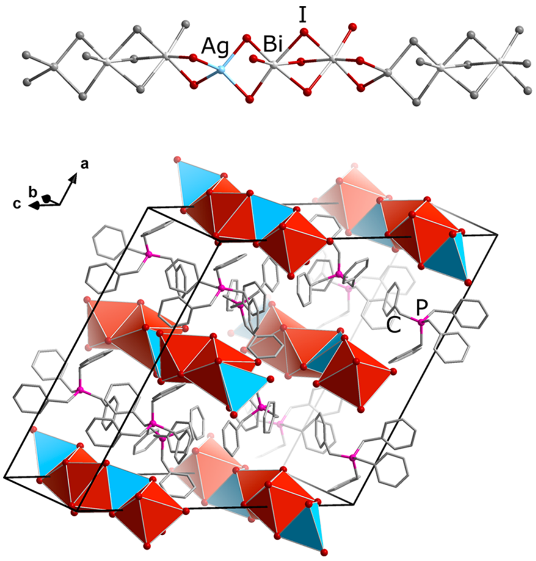

Figure 10. Anion (top) and unit cell (bottom) in **5**, with the trinuclear repetition unit highlighted.

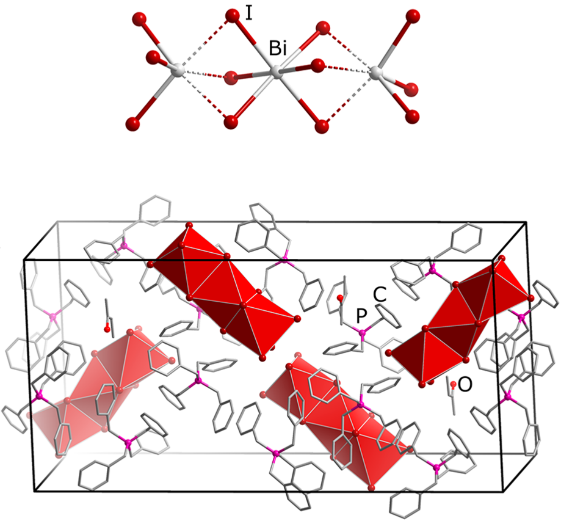

Figure 11. Anion (top) and unit cell (bottom) in **6**.

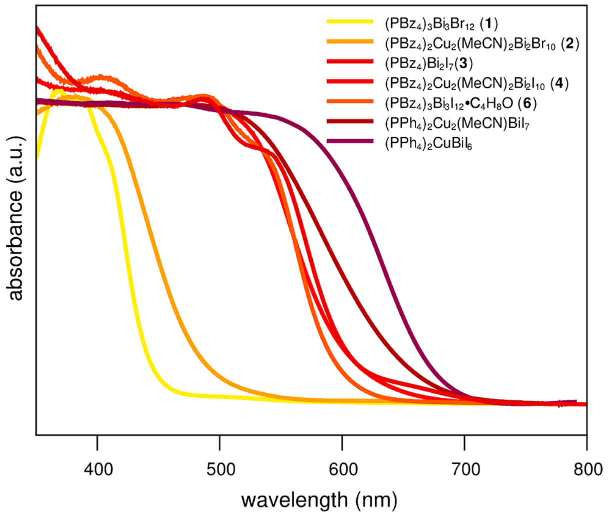

Figure 12. Optical absorption measured in diffuse reflectance for compounds **1**−**4** and **6**. Spectra of the literature-known compounds $(PPh_4)_2(MeCN)Cu_2BiI_7$[75] and $(PPh_4)_4Cu_2Bi_2I_{12}$[74] are included for reference.

Table 2. Onset of Absorption Observed for Compounds 1−4 and 6

	onset of absorption (eV)
$(PBz_4)_3Bi_3Br_{12}$ (**1**)	2.80
$(PBz_4)_2Cu_2(MeCN)_2Bi_2Br_{10}$ (**2**)	2.56
$(PBz_4)Bi_2I_7$ (**3**)	2.05
$(PBz_4)_2Cu_2(MeCN)_2Bi_2I_{10}$ (**4**)	2.06
$(PBz_4)_3Bi_3I_{12}\cdot C_4H_8O$ (**6**)	2.08

orientations and an overall much stronger separation by the cations.

Optical Properties. As shown in Figure 4, the incorporated halide has a striking influence on the crystals' color. While the iodido compounds appear in different shades of red, the bromido compounds show a bright-yellow color, a trend that is well in line with typical observations.[18] We also note that the copper bromido bismuthate **2** is darker in color than the simple bromido bismuthate **1**. The optical absorption spectra, as shown in Figure 12 and summarized in Table 2, confirm this first impression: A red shift of ca. 0.24 eV is seen upon going from **1** to **2**. This indicates that the red shift observed upon going from simple iodido bismuthates to multinary copper iodido bismuthates observed by our group and others[75] translates to the bromido analogues as well. This relationship was previously unknown because **2** is the first reported copper bromido bismuthate. For the iodido compounds **6** and **4**, which feature the same binary and ternary anion motifs as **1** and **2**, a similar trend might be expected. Surprisingly, all three iodido bismuthates **3**, **4**, and **6** show approximately the same optical behavior, with onsets of absorption varying between 2.05 and 2.08 eV. In very good agreement with our results, Chen and co-workers reported an onset of absorption of 2.06 eV for $(NBu_4)_2(MeCN)_2Cu_2Bi_2I_{10}$,[67] which features the same anion as **4**, and Pike and co-workers observed a similar range of onsets for the closely related $(Bu_4N)_2L_nCu_2Bi_2I_{10}$ (n = 1, L = Py; n = 2, L = PPh_3, $P(OPh)_3$) family of compounds.[71] This suggests that the absorption spectrum that we observe for **4** is representative for this anion motif and not a peculiarity of our particular compound. We also included the absorption spectra of two copper iodido bismuthates that we studied in earlier works in Figure 12. $(PPh_4)_2Cu_2(MeCN)BiI_7$ also contains an acetonitrile-coordinated Cu atom, as in **4**, while $(PPh_4)_4Cu_2Bi_2I_{12}$ features a tetranuclear anion (see also Figure 3). Both show an onset of absorption around 1.8 eV, similar to copper iodido bismuthates like $(Et_4N)_2Cu_2Bi_2I_{10}$ (1.9 eV), $(Cu(CH_3CN)_4)_2Cu_2Bi_2I_{10}$ (1.8 eV),[67] and $(C_6H_{16}N_2)_2CuBiI_8$ (1.7 eV).[72] This suggests a more complex relationship between the onset of absorption observed in copper iodido bismuthates than previously anticipated. The examples at hand show that it is not only the nuclearity of molecular anions and the overall anion dimensionality that play a role. It seems plausible that the mode of connection between $\{CuI_4\}$ tetrahedra and $\{BiI_6\}$ octahedra, e.g., face-sharing versus edge-sharing, is also relevant; however, additional examples, also of other multinary bromido bismuthates, as well as quantum-chemical investigations are needed to further elucidate this.

CONCLUSION

Overall, we hope to have shown that multinary halogenido bismuthates beyond the double perovskite motif are an underexplored, but promising class of compounds and to inspire more researchers to join us in our efforts to broaden the scope of these materials. To demonstrate the ready availability of multinary halogenido bismuthates, we employed the equally underexplored tetrabenzylphosphonium cation PBz_4^+ in our synthesis and obtained six new bismuthates, including three multinary examples, the first copper bromido bismuthate, and a compound with a new silver iodido bismuthate anion motif. Our investigations of the compounds' optical properties reveal both expected trends with regard to the overall influence of the halide and the effect of copper in bromido bismuthates but also a comparatively high onset of absorption in a copper iodido bismuthate that hints at a more complicated relationship between the anion composition, nuclearity, and dimensionality involving the connectivity of coordination polyhedra than previously known.

ASSOCIATED CONTENT

Supporting Information

The Supporting Information is available free of charge at https://pubs.acs.org/doi/10.1021/acs.inorgchem.9b03287.

Additional crystallographic details, powder diffraction, and IR spectroscopy (PDF)

Accession Codes

CCDC 1964160–1964165 contain the supplementary crystallographic data for this paper. These data can be obtained free of charge via www.ccdc.cam.ac.uk/data_request/cif, or by emailing data_request@ccdc.cam.ac.uk, or by contacting The Cambridge Crystallographic Data Centre, 12 Union Road, Cambridge CB2 1EZ, UK; fax: +44 1223 336033.

AUTHOR INFORMATION

Corresponding Author

Johanna Heine – *Department of Chemistry and Material Sciences Center, Philipps-Universität Marburg, 35043 Marburg, Germany;* orcid.org/0000-0002-6795-5288; Email: johanna.heine@chemie.uni-marburg.de

Authors

Natalie Dehnhardt – *Department of Chemistry and Material Sciences Center, Philipps-Universität Marburg, 35043 Marburg, Germany;* orcid.org/0000-0001-8239-1268

Hayden Paneth – *Department of Chemistry, Union College, Schenectady, New York 12308, United States*

Nikolas Hecht – *Department of Chemistry, Technische Universität Darmstadt, 64287 Darmstadt, Germany*

Complete contact information is available at: https://pubs.acs.org/10.1021/acs.inorgchem.9b03287

Notes

The authors declare no competing financial interest.

ACKNOWLEDGMENTS

This work is funded by the SFB 1083. J.H. thanks Prof. Stefanie Dehnen for her support. N.D. thanks the Fonds der Chemischen Industrie and the Studienstiftung des Deutschen Volkes for their support. H.P. thanks DAAD/RISE, Union College, and University of Marburg for support of her research internship.

REFERENCES

(1) Dragendorff, G. *Beiträge zur gerichtlichen Chemie einzelner organischer Gifte*; Verlag der Kaiserlichen Hofbuchhandlung Heinrich Schmitzdorff: St. Petersburg, 1872.

(2) Santos, H.; Lima, A. S.; Mazega, A.; Domingos, E.; Thompson, C. J.; Maldaner, A. O.; Filgueiras, P. R.; Vaz, B. G.; Romão, W. Quantification of cocaine and its adulterants (lidocaine and levamisole) using the Dragendorff reagent allied to paper spray ionization mass spectrometry. *Anal. Methods* **2017**, *9*, 3662–3668.

(3) Lamchen, M.; Pugh, W.; Stephen, A. M. Some salts of secondary amines and of their condensation products with carbonyl compounds. *J. Chem. Soc.* **1954**, 4418–4425.

(4) Ahmed, E.; Beck, J.; Daniels, J.; Doert, T.; Eck, S. J.; Heerwig, A.; Isaeva, A.; Lidin, S.; Ruck, M.; Schnelle, W.; Stankowski, A. A Semiconductor or A One-Dimensional Metal and Superconductor through Tellurium π Stacking. *Angew. Chem., Int. Ed.* **2012**, *51*, 8106–8109.

(5) Wells, H. L.; Foote, H. W. On Certain Double Halogen Salts of Cæsium and Rubidium: 1. The Complicated Rubidium-Antimony Chloride. 3. The Cæsium-Bismuth Chlorides and Iodides. *Am. J. Sci.* **1897**, *s4-3*, 461.

(6) Cavalca, L.; Nardelli, M.; Braibanti, A. Relazioni strutturali nei composti di formula $Cs_3R_2X_9$ (con R= As, Sb, Bi e X= Cl, Br, I). *Gazz. Chim. Ital.* **1955**, *85*, 1239–1249.

(7) Lazarini, F. Tetraphenylphosphonium Enneabromodibismuthate(III). *Acta Crystallogr., Sect. B: Struct. Crystallogr. Cryst. Chem.* **1977**, *B33*, 2686–2689.

(8) Aurivillius, B.; Stalhandske, C.; et al. The Crystal structure of a Tetranuclear Bismuth(III) Complex, $(C_5H_5NH)_6Bi_4Cl_{18}$. *Acta Chem. Scand.* **1978**, *32a*, 715–719.

(9) Whealy, R. D.; Scott, J. C. A Study of the Reaction Between Bismuth(II1) Iodide and Amine Hydriodides. *Inorg. Chim. Acta* **1967**, *1*, 479–481.

(10) Whealy, R. D.; Osborne, J. F. A study of the reaction between bismuth bromide and amine hydrobromides. *Inorg. Chim. Acta* **1970**, *4*, 420–422.

(11) Fluorido bismuthates are, of course, an interesting class of compounds as well. However, the small size of the fluoride ion and the greater oxidation power of fluorine produce a structural chemistry that is distinctly different from the heavier halides, featuring coordination numbers greater than 6 and allowing for the synthesis of bismuth(V) metalates. For a representative example, see: Beck, H. P.; Becker, D.; Haberkorn, R. Tribochemical Synthesis and Structure of K_2BiF_5. *Z. Naturforsch., B: J. Chem. Sci.* **2008**, *63b*, 251–254.

(12) Fisher, G. A.; Norman, N. C. The structures of the group 15 element (III) halides and halogenoanions. *Adv. Inorg. Chem.* **1994**, *41*, 233–271.

(13) Wu, L.-M.; Wu, X.-T.; Chen, L. Structural Overview and Structure-Property Relationships of Iodoplumbate and Iodobismuthate. *Coord. Chem. Rev.* **2009**, *253*, 2787–2804.

(14) Mercier, N.; Louvain, N.; Bi, W. Structural Diversity and Retro-Crystal Engineering Analysis of Iodometalate Hybrids. *CrystEngComm* **2009**, *11*, 720–734.

(15) Adonin, S. A.; Sokolov, M. N.; Fedin, V. P. Polynuclear Halide Complexes of Bi(III): From Structural Diversity to the New Properties. *Coord. Chem. Rev.* **2016**, *312*, 1–21.

(16) Mitzi, D. B. Organic- inorganic perovskites containing trivalent metal halide layers: the templating influence of the organic cation layer. *Inorg. Chem.* **2000**, *39*, 6107–6113.

(17) Li, M.-Q.; Hu, Y.-Q.; Bi, L.-Y.; Zhang, H.-L.; Wang, Y.; Zheng, Y.-Z. Structure tunable organic-inorganic bismuth halides for an enhanced two-dimensional lead-free light-harvesting material. *Chem. Mater.* **2017**, *29*, 5463–5467.

(18) García-Fernández, A.; Marcos-Cives, I.; Platas-Iglesias, C.; Castro-García, S.; Vázquez-García, D.; Fernández, A.; Sánchez-Andújar, M. Diimidazolium Halobismuthates $[Dim]_2[Bi_2X_{10}]$ (X = Cl^-, Br^-, or I^-): A New Class of Thermochromic and Photoluminescent Materials. *Inorg. Chem.* **2018**, *57*, 7655−7664.

(19) Gągor, A.; Węcławik, M.; Bondzior, B.; Jakubas, R. Periodic and incommensurately modulated phases in a (2-methylimidazolium)-tetraiodobismuthate(III) thermochromic organic-inorganic hybrid. *CrystEngComm* **2015**, *17*, 3286−3296.

(20) Mercier, N. The Templating Effect and Photochemistry of Viologens in Halometalate Hybrid Crystals. *Eur. J. Inorg. Chem.* **2013**, *2013*, 19−31.

(21) Evans, H. A.; Labram, J. G.; Smock, S. R.; Wu, G.; Chabinyc, M. L.; Seshadri, R.; Wudl, F. Mono- and Mixed-Valence Tetrathiafulvalene Semiconductors $(TTF)BiI_4$ and $(TTF)_4BiI_6$ with 1D and 0D Bismuth-Iodide Networks. *Inorg. Chem.* **2017**, *56*, 395−401.

(22) Jena, A. K.; Kulkarni, A.; Miyasaka, T. Halide Perovskite Photovoltaics: Background, Status, and Future Prospects. *Chem. Rev.* **2019**, *119*, 3036−3103.

(23) Chang, J.-H.; Doert, T.; Ruck, M. Structural Variety of Defect Perovskite Variants $M_3E_2X_9$ (M = Rb, Tl, E = Bi, Sb, X = Br, I). *Z. Anorg. Allg. Chem.* **2016**, *642*, 736−748.

(24) Lehner, A. J.; Fabini, D. H.; Evans, H. A.; Hébert, C.-A.; Smock, S. R.; Hu, J.; Wang, H.; Zwanziger, J. W.; Chabinyc, M. L.; Seshadri, R. Crystal and Electronic Structures of Complex Bismuth Iodides $A_3Bi_2I_9$ (A = K, Rb, Cs) Related to Perovskite: Aiding the Rational Design of Photovoltaics. *Chem. Mater.* **2015**, *27*, 7137−714.

(25) Park, B.-W.; Philippe, B.; Zhang, X.; Rensmo, H.; Boschloo, G.; Johansson, E. M. J. Bismuth Based Hybrid Perovskites $A_3Bi_2I_9$ (A: Methylammonium or Cesium) for Solar Cell Application. *Adv. Mater.* **2015**, *27*, 6806−6813.

(26) Eckhardt, K.; Bon, V.; Getzschmann, J.; Grothe, J.; Wisser, F. M.; Kaskel, S. Crystallographic insights into $(CH_3NH_3)_3(Bi_2I_9)$: a new lead-free hybrid organic-inorganic material as a potential absorber for photovoltaics. *Chem. Commun.* **2016**, *52*, 3058−3060.

(27) Lyu, M.; Yun, J.-H.; Cai, M.; Jiao, Y.; Bernhardt, P. V.; Zhang, M.; Wang, Q.; Du, A.; Wang, H.; Liu, G.; Wang, L. Organic-inorganic bismuth (III)-based material: A lead-free, air-stable and solution-processable light-absorber beyond organolead perovskites. *Nano Res.* **2016**, *9*, 692.

(28) Öz, S.; Hebig, J.-C.; Jung, E.; Singh, T.; Lepcha, A.; Olthof, S.; Flohre, J.; Gao, Y.; German, R.; van Loosdrecht, P. H. M.; Meerholz, K.; Kirchartz, T.; Mathur, S. Zero-dimensional $(CH_3NH_3)_3Bi_2I_9$ perovskite for optoelectronic applications. *Sol. Energy Mater. Sol. Cells* **2016**, *158*, 195−201.

(29) Singh, T.; Kulkarni, A.; Ikegami, M.; Miyasaka, T. Effect of Electron Transporting Layer on Bismuth-Based Lead-Free Perovskite $(CH_3NH_3)_3Bi_2I_9$ for Photovoltaic Applications. *ACS Appl. Mater. Interfaces* **2016**, *8*, 14542−14547.

(30) Jain, S. M.; Phuyal, D.; Davies, M. L.; Li, M.; Philippe, B.; De Castro, C.; Qiu, Z.; Kim, J.; Watson, T.; Tsoi, W. C.; Karis, O.; Rensmo, H.; Boschloo, G.; Edvinsson, T.; Durrant, J. R. An effective approach of vapour assisted morphological tailoring for reducing metal defect sites in lead-free, $(CH_3NH_3)_3Bi_2I_9$ bismuth-based perovskite solar cells for improved performance and long-term stability. *Nano Energy* **2018**, *49*, 614−624.

(31) Zhuang, R.; Wang, X.; Ma, W.; Wu, Y.; Chen, X.; Tang, L.; Zhu, H.; Liu, J.; Wu, L.; Zhou, W.; Liu, X.; Yang, Y. Highly sensitive X-ray detector made of layered perovskite-like $(NH_4)_3Bi_2I_9$ single crystal with anisotropic response. *Nat. Photonics* **2019**, *13*, 602−608.

(32) McCall, K. M.; Liu, Z.; Trimarchi, G.; Stoumpos, C. C.; Lin, W.; He, Y.; Hadar, I.; Kanatzidis, M. G.; Wessels, B. W. α-Particle Detection and Charge Transport Characteristics in the $A_3M_2I_9$ Defect Perovskites (A = Cs, Rb; M = Bi, Sb). *ACS Photonics* **2018**, *5*, 3748−3762.

(33) Yang, B.; Chen, J.; Hong, F.; Mao, X.; Zheng, K.; Yang, S.; Li, Y.; Pullerits, T.; Deng, W.; Han, K. Lead-Free, Air-Stable All-Inorganic Cesium Bismuth Halide Perovskite Nanocrystals. *Angew. Chem., Int. Ed.* **2017**, *56*, 12471−12475.

(34) Guo, Y.; Liu, G.; Li, Z.; Lou, Y.; Chen, J.; Zhao, Y. Stable Lead-Free $(CH_3NH_3)_3Bi_2I_9$ Perovskite for Photocatalytic Hydrogen Generation. *ACS Sustainable Chem. Eng.* **2019**, *7*, 15080−15085.

(35) Jakubas, R.; Piecha, A.; Pietraszko, A.; Bator, G. Structure and ferroelectric properties of $(C_3N_2H_5)_5Bi_2Cl_{11}$. *Phys. Rev. B: Condens. Matter Mater. Phys.* **2005**, *72*, 104107.

(36) Feldmann, C. Crystal structure of tris(tetramethylammonium) dibismuth nonaiodide, $[N(CH_3)_4]_3Bi_2I_9$. *Z. Kristallogr. NCS* **2001**, *216*, 465−466.

(37) Ahmed, I. A.; Blachnik, R.; Kastner, G.; Brockner, W. The Phase Diagram of the System $[Ph_4P]Br/BiBr_3$. Synthesis, Crystal Structure, Thermal Behaviour, and Vibrational Spectra of $[Ph_4P]_3[Bi_2Br_9]\cdot CH_3COCH_3$ and two Modifications of $[Ph_4P]_4[Bi_6Br_{22}]$. *Z. Anorg. Allg. Chem.* **2001**, *627*, 2261−2268.

(38) Owczarek, M.; Szklarz, P.; Jakubas, R.; Miniewicz, A. $[NH_2(C_2H_4)_2O]MX_5$: a new family of morpholinium nonlinear optical materials among halogenoantimonate(iii) and halogenobismuthate(iii) compounds. Structural characterization, dielectric and piezoelectric properties. *Dalton Trans.* **2012**, *41*, 7285−7294.

(39) Goforth, A. M.; Peterson, L., Jr.; Smith, M. D.; Zur Loye, H.-C. Syntheses and crystal structures of several novel alkylammonium iodobismuthate materials containing the 1,3-bis-(4-piperidinium)-propane cation. *J. Solid State Chem.* **2005**, *178*, 3529−3540.

(40) Igbari, F.; Wang, Z.-K.; Liao, L.-S. Progress of Lead-Free Halide Double Perovskites. *Adv. Energy Mater.* **2019**, *9*, 1803150.

(41) Morrs, L. R.; Robinson, W. R. Crystal structure of $Cs_2NaBiCl_6$. *Acta Crystallogr., Sect. B: Struct. Crystallogr. Cryst. Chem.* **1972**, *28*, 653−654.

(42) Volonakis, G.; Filip, M. R.; Haghighirad, A. A.; Sakai, N.; Wenger, B.; Snaith, H. J.; Giustino, F. Lead-Free Halide Double Perovskites via Heterovalent Substitution of Noble Metals. *J. Phys. Chem. Lett.* **2016**, *7*, 1254−1259.

(43) Slavney, A. H.; Hu, T.; Lindenberg, A. M.; Karunadasa, H. I. A Bismuth-Halide Double Perovskite with Long Carrier Recombination Lifetime for Photovoltaic Applications. *J. Am. Chem. Soc.* **2016**, *138*, 2138−2141.

(44) McClure, E. T.; Ball, M. R.; Windl, W.; Woodward, P. M. Cs_2AgBiX_6 (X = Br, Cl): New Visible Light Absorbing, Lead-Free Halide Perovskite Semiconductors. *Chem. Mater.* **2016**, *28*, 1348−1354.

(45) Giustino, F.; Snaith, H. J. Toward Lead-Free Perovskite Solar Cells. *ACS Energy Lett.* **2016**, *1*, 1233−1240.

(46) Wei, F.; Deng, Z.; Sun, S.; Zhang, F.; Evans, D. M.; Kieslich, G.; Tominaka, S.; Carpenter, M. A.; Zhang, J.; Bristowe, P. D.; Cheetham, A. K. Synthesis and Properties of a Lead-Free Hybrid Double Perovskite: $(CH_3NH_3)_2AgBiBr_6$. *Chem. Mater.* **2017**, *29*, 1089−1094.

(47) Slavney, A. H.; Leppert, L.; Bartesaghi, D.; Gold-Parker, A.; Toney, M. F.; Savenije, T. J.; Neaton, J. B.; Karunadasa, H. I. Defect-Induced Band-Edge Reconstruction of a Bismuth-Halide Double Perovskite for Visible-Light Absorption. *J. Am. Chem. Soc.* **2017**, *139*, 5015−5018.

(48) Bartesaghi, D.; Slavney, A. H.; Gélvez-Rueda, M. C.; Connor, B. A.; Grozema, F. C.; Karunadasa, H. I.; Savenije, T. J. Charge Carrier Dynamics in $Cs_2AgBiBr_6$ Double Perovskite. *J. Phys. Chem. C* **2018**, *122*, 4809−4816.

(49) Zelewski, S. J.; Urban, J. M.; Surrente, A.; Maude, D. K.; Kuc, A.; Schade, L.; Johnson, R. D.; Dollmann, M.; Nayak, P. K.; Snaith, H. J.; Radaelli, P.; Kudrawiec, R.; Nicholas, R. J.; Plochocka, P.; Baranowski, M. Revealing the nature of photoluminescence emission in the metal-halide double perovskite $Cs_2AgBiBr_6$. *J. Mater. Chem. C* **2019**, *7*, 8350−8356.

(50) Igbari, F.; Wang, R.; Wang, Z.-K.; Ma, X.-J.; Wang, Q.; Wang, K.-L.; Zhang, Y.; Liao, L.-S.; Yang, Y. Composition Stoichiometry of $Cs_2AgBiBr_6$ Films for Highly Efficient Lead-Free Perovskite Solar Cells. *Nano Lett.* **2019**, *19*, 2066−2073.

(51) Yang, B.; Chen, J.; Yang, S.; Hong, F.; Sun, L.; Han, P.; Pullerits, T.; Deng, W.; Han, K. Lead-Free Silver-Bismuth Halide Double Perovskite Nanocrystals. *Angew. Chem., Int. Ed.* **2018**, *57*, 5359−5363.

(52) Zhang, Z.; Liang, Y.; Huang, H.; Liu, X.; Li, Q.; Chen, L.; Xu, D. Stable and Highly Efficient Photocatalysis with Lead-Free Double-Perovskite of $Cs_2AgBiBr_6$. *Angew. Chem., Int. Ed.* **2019**, *58*, 7263−7267.

(53) Mao, L.; Stoumpos, C. C.; Kanatzidis, M. G. Two-Dimensional Hybrid Halide Perovskites: Principles and Promises. *J. Am. Chem. Soc.* **2019**, *141*, 1171−1190.

(54) Mitzi, D. B. Synthesis, Crystal Structure, and Optical and Thermal Properties of $(C_4H_9NH_3)_2MI_4$ (M = Ge, Sn, Pb). *Chem. Mater.* **1996**, *8*, 791−800.

(55) Connor, B. A.; Leppert, L.; Smith, M. D.; Neaton, J. B.; Karunadasa, H. I. Layered Halide Double Perovskites: Dimensional Reduction of $Cs_2AgBiBr_6$. *J. Am. Chem. Soc.* **2018**, *140*, 5235−5240.

(56) Yuan, W.; Niu, G.; Xian, Y.; Wu, H.; Wang, H.; Yin, H.; Liu, P.; Li, W.; Fan, J. In Situ Regulating the Order-Disorder Phase Transition in $Cs_2AgBiBr_6$ Single Crystal toward the Application in an X-Ray Detector. *Adv. Funct. Mater.* **2019**, *29*, 1900234.

(57) Jana, M. K.; Janke, S. M.; Dirkes, D. J.; Dovletgeldi, S.; Liu, C.; Qin, X.; Gundogdu, K.; You, W.; Blum, V.; Mitzi, D. B. Direct-Bandgap 2D Silver-Bismuth Iodide Double Perovskite: The Structure-Directing Influence of an Oligothiophene Spacer Cation. *J. Am. Chem. Soc.* **2019**, *141*, 7955−7964.

(58) Goldschmidt, V. M. Die Gesetze der Krystallochemie. *Naturwissenschaften* **1926**, *14*, 477−485.

(59) Fu, Y.; Hautzinger, M. P.; Luo, Z.; Wang, F.; Pan, D.; Aristov, M. M.; Guzei, I. A.; Pan, A.; Zhu, X.; Jin, S. Incorporating Large A Cations into Lead Iodide Perovskite Cages: Relaxed Goldschmidt Tolerance Factor and Impact on Exciton-Phonon Interaction. *ACS Cent. Sci.* **2019**, *5*, 1377−1386.

(60) López, C. A.; Martínez-Huerta, M. V.; Alvarez-Galván, M. C.; Kayser, P.; Gant, P.; Castellanos-Gomez, A.; Fernández-Díaz, M. T.; Fauth, F.; Alonso, J. A. Elucidating the Methylammonium (MA) Conformation in $MAPbBr_3$ Perovskite with Application in Solar Cells. *Inorg. Chem.* **2017**, *56*, 14214−14219.

(61) Wei, F.; Deng, Z.; Sun, S.; Zhang, F.; Evans, D. M.; Kieslich, G.; Tominaka, S.; Carpenter, M. A.; Zhang, J.; Bristowe, P. D.; Cheetham, A. K. Synthesis and Properties of a Lead-Free Hybrid Double Perovskite: $(CH_3NH_3)_2AgBiBr_6$. *Chem. Mater.* **2017**, *29*, 1089−1094.

(62) Sharma, M.; Yangui, A.; Whiteside, V. R.; Sellers, I. R.; Han, D.; Chen, S.; Du, M.-H.; Saparov, B. $Rb_4Ag_2BiBr_9$: A Lead-Free Visible Light Absorbing Halide Semiconductor with Improved Stability. *Inorg. Chem.* **2019**, *58*, 4446−4455.

(63) Gerisch, A.; Ruck, M. $(Bi_9)_4[Bi_3Pb_9Br_{47}]$: Probing the limits of the concept "crystal. *Z. Kristallogr. - Cryst. Mater.* **2011**, *226*, 613−618.

(64) Wahl, B.; Erbe, M.; Gerisch, A.; Kloo, L.; Ruck, M. Nobel-Metal Centered Polycations $[Au@Bi_{10}]^{5+}$ or $[Pd@Bi_{10}]^{4+}$ Embedded in Halogenido-Bismuthate(III)-Stannate(II) Frameworks. *Z. Anorg. Allg. Chem.* **2009**, *635*, 743−752.

(65) Feldmann, C. $CuBi_7I_{19}(C_4H_8O_3H)_3(C_4H_8O_3H_2)$, a Novel Complex Bismuth Iodide Containing One-Dimensional $[CuBi_5I_{19}]^{3-}$ Chains. *Inorg. Chem.* **2001**, *40*, 818−819.

(66) Chai, W.-X.; Wu, L.-M.; Li, J.-Q.; Chen, L. Silver Iodobismuthates: Syntheses, Structures, Properties, and Theoretical Studies of $[Bi_2Ag_2I_{10}{}^{2-}]_n$ and $[Bi_4Ag_2I_{16}{}^{2-}]_n$. *Inorg. Chem.* **2007**, *46*, 1042−1044.

(67) Chai, W.-X.; Wu, L.-M.; Li, J.-Q.; Chen, L. A Series of New Copper Iodobismuthates: Structural Relationships, Optical Band Gaps Affected by Dimensionality, and Distinct Thermal Stabilities. *Inorg. Chem.* **2007**, *46*, 8698−8704.

(68) Yuan, M.-W.; Li, L.-H.; Chen, L. Syntheses, Structures, and Theoretical Studies of New Mercury Iodobismuthates: $(Et_4N)_4(Bi_4Hg_2I_{20})$ and $(nBu_4N)_2(Bi_2HgI_{10})$. *Z. Anorg. Allg. Chem.* **2009**, *635*, 1645−1649.

(69) Adonin, S. A.; Sokolov, M. N.; Smolentsev, A. I.; Kozlova, S. G.; Fedin, V. P. $[PtBi_2I_{12}]^{2-}$: the first polyiodobismuthate containing an octahedral heterometallic unit. *Dalton Trans.* **2013**, *42*, 9818−9821.

(70) Wójcik, K.; Preda, A. M.; Mertens, L.; Ecorchard, P.; Rüffer, T.; Lang, H.; Mehring, M. Iron-Bismuth Halido Compounds: Molecules, Clusters, and Polymers. *Inorg. Chem.* **2015**, *54*, 3905−3912.

(71) Kelly, A. W.; Wheaton, A. M.; Nicholas, A. D.; Barnes, F. H.; Patterson, H. H.; Pike, R. D. Iodobismuthate(III) and Iodobismuthate(III)/Iodocuprate(I) Complexes with Organic Ligands. *Eur. J. Inorg. Chem.* **2017**, *2017*, 4990−5000.

(72) Bi, L.-Y.; Hu, Y.-Q.; Li, M.-Q.; Hu, T.-L.; Zhang, H.-L.; Yin, X.-T.; Que, W.-X.; Lassoued, M. S.; Zheng, Y.-Z. Two-dimensional lead-free iodide-based hybrid double perovskites: crystal growth, thin-film preparation and photocurrent responses. *J. Mater. Chem. A* **2019**, *7*, 19662−19667.

(73) Xiao, Z.; Du, K.-Z.; Meng, W.; Mitzi, D. B.; Yan, Y. Chemical Origin of the Stability Difference between Copper(I)- and Silver(I)-Based Halide Double Perovskites. *Angew. Chem., Int. Ed.* **2017**, *56*, 12107−12111.

(74) Dehnhardt, N.; Borkowski, H.; Schepp, J.; Tonner, R.; Heine, J. Ternary Iodido Bismuthates and the Special Role of Copper. *Inorg. Chem.* **2018**, *57*, 633−640.

(75) Dehnhardt, N.; Klement, P.; Chatterjee, S.; Heine, J. Divergent Optical Properties in an Isomorphous Family of Multinary Iodido Pentelates. *Inorg. Chem.* **2019**, *58*, 10983−10990.

(76) Hartl, H.; Mahdjour-Hassan-Abadi, F. $[Cu_5I_7]^{2-}$—An Isopolyanion with Cyclic Face-to-Face Linking of CuI_4 Tetrahedra. *Angew. Chem., Int. Ed. Engl.* **1984**, *23*, 378−379.

(77) Hartl, H. $[\{Co(Cp)_2\}\{CuI_2\}]$ n (n= 3, 4), Cobaltocenium Iodocuprates (I) with Unusual Anion Structures. *Angew. Chem., Int. Ed. Engl.* **1987**, *26*, 927−928.

(78) Hartl, H.; Mahdjour-Hassan-Abadi, F. $[(C_6H_5)_4P][Cu_3I_4]$—The First Compound with a Helical Chain of Face-Sharing Tetrahedra as a Structural Element. *Angew. Chem., Int. Ed. Engl.* **1994**, *33*, 1841−1842.

(79) Jagner, S.; Helgesson, G. On the Coordination Number of the Metal in Crystalline Halogenocuprates(I) and Halogenoargentates(I). *Adv. Inorg. Chem.* **1991**, *37*, 1−45.

(80) Arnby, C. H.; Jagner, S.; Dance, I. Questions for crystal engineering of halocuprate complexes: concepts for a difficult system. *CrystEngComm* **2004**, *6*, 257−275.

(81) Heine, J. A Step Closer to the Binary: The $[Bi_6I_{20}]^{2-}$ Anion. *Dalton Trans.* **2015**, *44*, 10069−10077.

(82) Dehnhardt, N.; Böth, A.; Heine, J. Discoveries on the Way to an Old Compound: Four Transient Iodido Antimonates. *Dalton Trans.* **2019**, *48*, 5222−5229.

(83) Krautscheid, H. $(Bzl_4P)_2[Bi_2I_8]$ - an Iodobismuthate with Penta-coordinated Bi^{3+} Ions. *Z. Anorg. Allg. Chem.* **1999**, *625*, 192−194.

(84) Gröger, H.; Lode, C.; Vollmer, H.; Krautscheid, H.; Lebedkin, S. Bromoplumbate mit kettenförmigen und isolierten Anionen: $(Bzl_4P)_2[Pb_3Br_8]$, $(Bzl_4P)_2[Pb_3Br_8(dmf)_2]$, $(Bzl_4P)[PbBr_3]$, $(Bzl_4P)_2[PbBr_4]$ und $(Bzl_4P)_4[Pb_2Br_6][PbBr_4]$. *Z. Anorg. Allg. Chem.* **2002**, *628*, 57−62.

(85) Ruck, M. Darstellung und Kristallstruktur von fehlordnungsfreiem Bismuttriiodid. *Z. Kristallogr. - Cryst. Mater.* **1995**, *210*, 650−655.

(86) Sheldrick, G. M. A Short History of SHELX. *Acta Crystallogr., Sect. A: Found. Crystallogr.* **2008**, *A64*, 112−122.

(87) Sheldrick, G. M. SHELXT - Integrated Space-Group and Crystal-Structure Determination. *Acta Crystallogr., Sect. A: Found. Adv.* **2015**, *A71*, 3−8.

(88) Sheldrick, G. M. Crystal Structure Refinement with SHELXL. *Acta Crystallogr., Sect. C: Struct. Chem.* **2015**, *C71*, 3−8.

(89) Dolomanov, O. V.; Bourhis, L. J.; Gildea, R. J.; Howard, J. A. K.; Puschmann, H. OLEX2: A Complete Structure Solution, Refinement and Analysis Program. *J. Appl. Crystallogr.* **2009**, *42*, 339−341.

(90) Brandenburg, K. *DIAMOND*; Crystal Impact GbR: Bonn, Germany, 2005.

(91) Boldish, S. I.; White, W. B. Optical Band Gaps of Selected Ternary Sulfide Minerals. *Am. Mineral.* **1998**, *83*, 865−871.

(92) Kushch, N. D.; Dyachenko, A. A.; Gritsenko, V. V.; Cassoux, P.; Faulmann, C.; Kobayashi, A.; Kobayashi, H. Two new cation radical bis(ethylenedithio)tetraselenafulvalene (BETS) salts, α-$(BETS)_6Bi_3Cl_{12}\cdot PhCl$ and $(BETS)_2Bi_2Cl_8$: synthesis, structure and conducting properties. First characterisation of the new trinuclear anion $[Bi_3Cl_{12}]^{3-}$. *J. Chem. Soc., Dalton Trans.* **1998**, 683−688.

(93) Nørby, P.; Jørgensen, M. R. V.; Johnsen, S.; Brummerstedt Iversen, B. Bismuth Iodide Hybrid Organic-Inorganic Crystal Structures and Utilization in Formation of Textured BiI_3 Film. *Eur. J. Inorg. Chem.* **2016**, *2016*, 1389−1394.

(94) Carmalt, C. J.; Farrugia, L. J.; Norman, N. C. Synthesis and X-Ray Crystal Structure of a Polymeric Iodobismuthate Anion. *Z. Naturforsch., B: J. Chem. Sci.* **1995**, *50b*, 1591−1596.

(95) Nishio, M. CH/π hydrogen bonds in crystals. *CrystEngComm* **2004**, *6*, 130−158.

(96) Martinez, C. R.; Iverson, B. L. Rethinking the term "pi-stacking. *Chem. Sci.* **2012**, *3*, 2191−2201.

(97) Wagner, J. P.; Schreiner, P. R. London Dispersion in Molecular Chemistry—Reconsidering Steric Effects. *Angew. Chem., Int. Ed.* **2015**, *54*, 12274−12296.

(98) Geiser, U.; Wade, E.; Wang, H. H.; Williams, J. M. Structure of a new iodobismuthate: tetra(n-butyl)ammonium 1,2;1,2;1,2;2,3;2,3;2,3-hexa-μ-iodo-1,1,1,3,3,3-hexaiodotribismuthate-(III) (3:1). *Acta Crystallogr., Sect. C: Cryst. Struct. Commun.* **1990**, *C46*, 1547−1549.

(99) Carmalt, C. J.; Farrugia, L. J.; Norman, N. C. Structural Studies on some Iodoantimonate and Iodobismuthate Anions. *Z. Anorg. Allg. Chem.* **1995**, *621*, 47−56.

3.5. Enabling tailored 2D materials by introducing 1D organic-inorganic perovskites with supramolecular intra-layer interactions

Philip Klement, Natalie Dehnhardt, Chuan-Ding Dong, Samuel Bayliff, Julius Winkler, Peter J. Klar, Stefan Schumacher, Sangam Chatterjee and Johanna Heine, *Manuskript in Bearbeitung nach Peer-Review und Ablehnung in Nature Chemistry.*

Abstract

Tailored 2D materials offer intriguing possibilities for next-generation device applications. The intentional design of their building blocks promises a modular approach to introducing superior chemical and physical properties. It is commonly assumed that 2D materials require in-plane covalent bonding only, limiting the number of candidates. Here we show that individual single layers of 2D organic-inorganic perovskites with only 1D covalent intralayer-interactions exist. $[BzA]_3[BiCl_5]Cl$ (BzA = benzylammonium) is exfoliated down to single layers and reveals extremely strong dimensional effects evidenced by a 0.4 eV shift of the photoluminescence between bulk and single layers. Such perovskite derivatives go far beyond the current state-of-the-art as we demonstrate that already 1D covalent interactions render truly 2D materials possible. These findings enable a much more general construction principle for identifying and creating tailored 2D materials with custom functionalization. The kit of available compounds is no longer limited to covalently bonded 2D sheets.

Zusammenfassung

In dieser Veröffentlichung wurde ein neues organisch-anorganisches Chloridobismutat auf seine Eigenschaften als neues 2D-Material untersucht. Hierfür wurden Exfoliationsexperimente, sowie quantenchemische Rechnungen zur Stabilität der exfolierten Schichten durchgeführt. Wird Benzylamin zu einer Lösung von Bismut-III-oxid in konzentrierter wässriger Chlorwasserstoffsäure gegeben und anschließend für 30 Minuten erhitzt, können aus der abgekühlten Reaktionslösung nach 24 Stunden farblose Plättchen von $[BzA]_3[BiCl_5]Cl$ erhalten werden. Die Verbindung enthält Benzylammonium-Kationen, sowie strangförmige Chloridobismutat-Anionen. Die Benzylammonium-Kationen ordnen sich hierbei in flachen Schichten an, die durch C-H-π-Wechselwirkungen zwischen den Benzolringen der Kationen begünstigt werden. Die Anordnung der Kationen erzwingt eine ebenso flache Anordnung der $[BiCl_5]^{2-}$-Anionen, die eine lamellare Struktur einnehmen. Die einzelnen anionischen Schichten sind von Benzylammonium-Doppelschichten getrennt, wobei zusätzliche Chloridionen ober- und unterhalb der Schichten zum Ladungsausgleich beitragen. In Abbildung 3.5 a) ist ein Ausschnitt aus der Kristallstruktur von

$[BzA]_3[BiCl_5]Cl$ zu sehen. Eine vereinfachte schematische Darstellung der Schichten und der Wechselwirkungen innerhalb dieser ist in Abbildung 3.5 b) dargestellt.

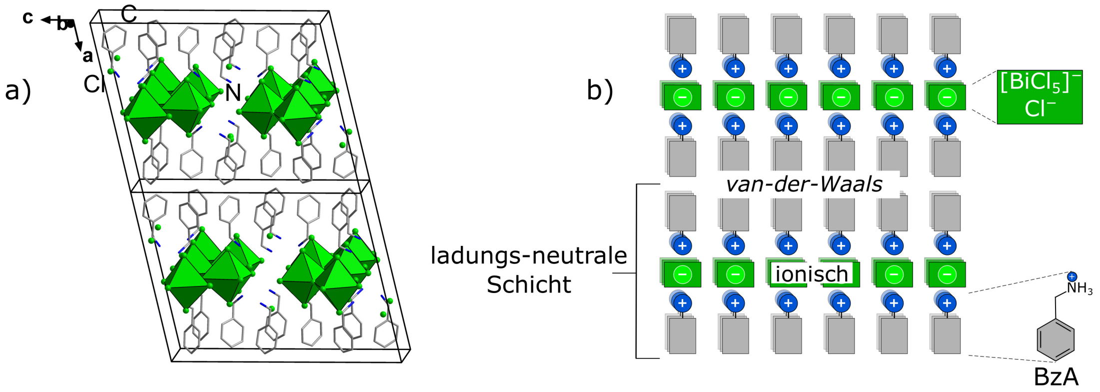

Abbildung 3.5: a) Ausschnitt aus der Kristallastruktur von $[BzA]_3[BiCl_5]Cl$. Zur besseren Übersicht sind die Anionen in Polyeder-Darstellung und die Kationen im Stabmodell abgebildet. Wasserstoffatome werden nicht gezeigt. b) Vereinfachte schematische Darstellung der Wechselwirkungen innerhalb und zwischen den Schichten von $[BzA]_3[BiCl_5]Cl$.

Die Struktur kann darüber hinaus als Perowskit mit geordneten Leerstellen der <100>-Familie betrachtet werden, was eine strukturelle Verwandtschaft mit der Verbindungsklasse der Bleiperowskite belegt. Um zu bestätigen, dass zwischen den einzelnen Schichten in $[BzA]_3[BiCl_5]Cl$ nur schwache Wechselwirkungen vorliegen, wurden quantenchemische Rechnungen mit DFT-Methoden durchgeführt. Sie ergaben, dass die Bindungen entlang der kristallographischen *a*-Achse am schwächsten sind, womit die Spaltrichtung im Kristall senkrecht auf der *b*-*c*-Ebene liegen sollte. Um dies zu überprüfen, wurden mechanische Exfoliationsexperimente an Kristallen von $[BzA]_3[BiCl_5]Cl$ durchgeführt, die dünne Schichten mit einer Dicke von drei bis einigen hundert Nanometern ergaben. Die erhaltenen Schichten wurden mittels Hellfeldmikroskopie und Rasterkraftmikroskopie untersucht.

Absorptionsmessungen ergaben eine Absorptionskante bei 3,1 eV (400 nm), mit einer Exzitonenresonanz bei 3,3 eV (375 nm). Temperaturabhängige Photolumineszenzmessungen zeigten eine breite Weißlichtemmission über den sichtbaren Bereich des elektromagnetischen Spektrums mit einem Maximum bei 2 eV. Weitere Messungen an exfolierten Proben ergaben, dass mit sinkender Probendicke eine Verschiebung zu höheren Emmissionsenergien einhergeht. Die Untersuchungen bestätigten die Eignung von $[BzA]_3[BiCl_5]Cl$ als 2D-Material. Hierdurch konnte gezeigt werden, dass auch Materialen ohne kovalent gebundene Schichtstruktur als 2D-Material geeignet sein können, was die Anzahl der zugänglichen 2D-Materialien erhöht.

Eigener Anteil

Die Synthese von $[BzA]_3[BiCl_5]Cl$ wurde erstmals von *Julius Winkler* unter meiner Anleitung durchgeführt und später von *Samuel Bayliff* im Rahmen eines Forschungspraktikums unter meiner Betreuung optimiert. $[BzA]_3[BiCl_5]Cl$ wurde über Röntgenbeugung am Einkristall und Pulver, UV-Vis-, Infrarot-, Raman- und Photolumineszenz-Spektroskopie, Thermogravimetrie und gekoppelte Differenzkalorimetrie sowie CHN-Elementaranalyse charakterisiert und identifiziert. Die Einkristallmessung sowie Strukturlösung und -verfeinerung wurde von *Dr. Johanna Heine* durchgeführt. Pulverdiffraktogramme, UV-Vis- und Infrarotspektren wurden von mir aufgenommen. Raman-Spektroskopie, Exfoliationsexperimente, optische Mikroskopie, Rasterkraftmikroskopie und Photolumineszenzmessungen wurden in der Arbeitsgruppe von *Prof. Dr. Sangam Chatterjee* von *Philip Klement* durchgeführt und ausgewertet. Thermogravimetrie und gekoppelte Differenzkalorimetrie wurden von *Uwe Justus* durchgeführt. Die CHN-Elementaranalyse wurde von der zentralen Abteilung für Massenspektrometrie und Elementaranalyse der Philipps-Universität Marburg vorgenommen. Quantenchemische Rechnungen wurden von *Chuan-Ding Dong* und *Stefan Schumacher* durchgeführt. Das Erstellen des Manuskripts erfolgt unter Beteiligung aller Co-Autoren.

Enabling tailored 2D materials by introducing 1D organic-inorganic perovskites with supramolecular intra-layer interactions

Philip Klement[1], Natalie Dehnhardt[2], Chuan-Ding Dong[3], Samuel K. Bayliff[4], Julius Winkler[2], Peter J. Klar[1], Stefan Schumacher[3,5], Sangam Chatterjee[1], and Johanna Heine[2]*

1 Institute of Experimental Physics I and Center for Materials Research (ZfM), Justus Liebig University Giessen, Heinrich-Buff-Ring 16, D-35392 Giessen, Germany

2 Department of Chemistry and Material Sciences Center, Philipps-Universität Marburg, Hans-Meerwein-Straße, 35043 Marburg, Germany

3 Department of Physics and Center for Optoelectronics and Photonics Paderborn (CeOPP), Paderborn University, Warburger Strasse 100, D-33098 Paderborn, Germany

4 Department of Chemistry and Biochemistry, University of Oklahoma, 101 Stephenson Parkway, Norman, OK 73019, USA

5 College of Optical Sciences, The University of Arizona, 1630 E. University Blvd., Tucson, AZ 85721-0094, USA

Abstract

Tailored 2D materials offer intriguing possibilities for next-generation device applications. The intentional design of their building blocks promises a modular approach to introducing superior chemical and physical properties. It is commonly assumed that 2D materials require in-plane covalent bonding only, limiting the number of candidates. Here we show that individual single layers of 2D organic-inorganic perovskites with only 1D covalent intralayer-interactions exist. $[BzA]_3[BiCl_5]Cl$ (BzA = benzylammonium) is exfoliated down to single layers and reveals extremely strong dimensional effects evidenced by a 0.4 eV shift of the photoluminescence between bulk and single layers. Such perovskite derivatives go far beyond the current state-of-the-art as we demonstrate that already 1D covalent interactions render truly 2D materials possible. These findings enable a much more general construction principle for identifying and creating tailored 2D materials with custom functionalization. The kit of available compounds is no longer limited to covalently bonded 2D sheets.

The successful preparation and unique properties of graphene[1] have sparked vast research interests in atomically thin 2D materials. Examples of other allotropes include silicene, phosphorene, and tellurene.[2] Binary or multinary compounds that can be prepared as true monolayers span a large array of different materials, from the insulating hexagonal boron nitride[2] to semiconducting or metallic transition metal dichalcogenides.[3] In principle, any layered material with only van der Waals forces acting between its comparatively strong bound layers can be exfoliated.[4] Even charged layers in metal oxides and hydroxides[5] or carbides and nitrides[6] can be isolated via the intercalation of organic ions acting as capping agents. Research interests in these materials spans a wide field of topics, ranging from fundamental physical phenomena such as polaritons,[7] superconductivity[8] or charge density waves[9] to practical applications such as water purification,[10] photovoltaics[11] or sensing.[12] More recent additions to the continuously growing family of 2D materials are 2D covalent organic frameworks (COFs) ,[13] coordination polymers (CP),[14,15] and layered perovskite derivatives.[16-18] These materials pave the way to the intentional design of 2D materials and heterostructures thereof, as the building blocks can be chosen deliberately to create new 2D material candidates with specific properties. The limiting factor in this approach has been the need to control the compounds' dimensionality so that they feature strong, typically covalent bonds in two dimensions only. This is demonstrated by the rather small number of COFs and CPs investigated in the context of 2D materials in stark contrast to their widespread use in other fields and applications.[19] Whilst equipollent 3D interactions need to be avoided so that no strong bonds are to be broken when cleaving the material, strong in-plane interactions are deemed mandatory and typically realized by 2D covalent bonds. Going beyond the current state-of-the-art, we demonstrate that 2D covalent bonds are not as strictly necessary for 2D materials as is often implicitly assumed in the community, and successful control of the dimensionality can be achieved by other means. Here, we employ the principle of using supramolecular architectures to construct highly functional layered structures. The principle is inspired by molecular biology, where supramolecular interactions allow for the formation of lipid bilayer as outer cell membranes. [20]

In this work, we present $[BzA]_3[BiCl_5]Cl$ (**BBC**, BzA = benzylammonium, $C_7H_{10}N^+$), as a principle example of single crystalline organic-inorganic hybrid truly 2D materials that feature only 1D, wire-like covalent interactions within their layers (Figure 1). The ionic and supramolecular interactions present in this compound are strong enough to allow for mechanical exfoliation of bulk crystals down to single layers. We find ultrathin crystals of good quality with extremely strong dimensional effects evidenced by a 0.4 eV shift of the photoluminescence between bulk and single layer. This suggests that single crystalline compounds featuring lamellar supramolecular motifs can be understood as 2D material candidates, leading toward a general construction principle for identifying and creating tailored, custom functional 2D materials even when no 2D covalent interactions are present within the individual layers.

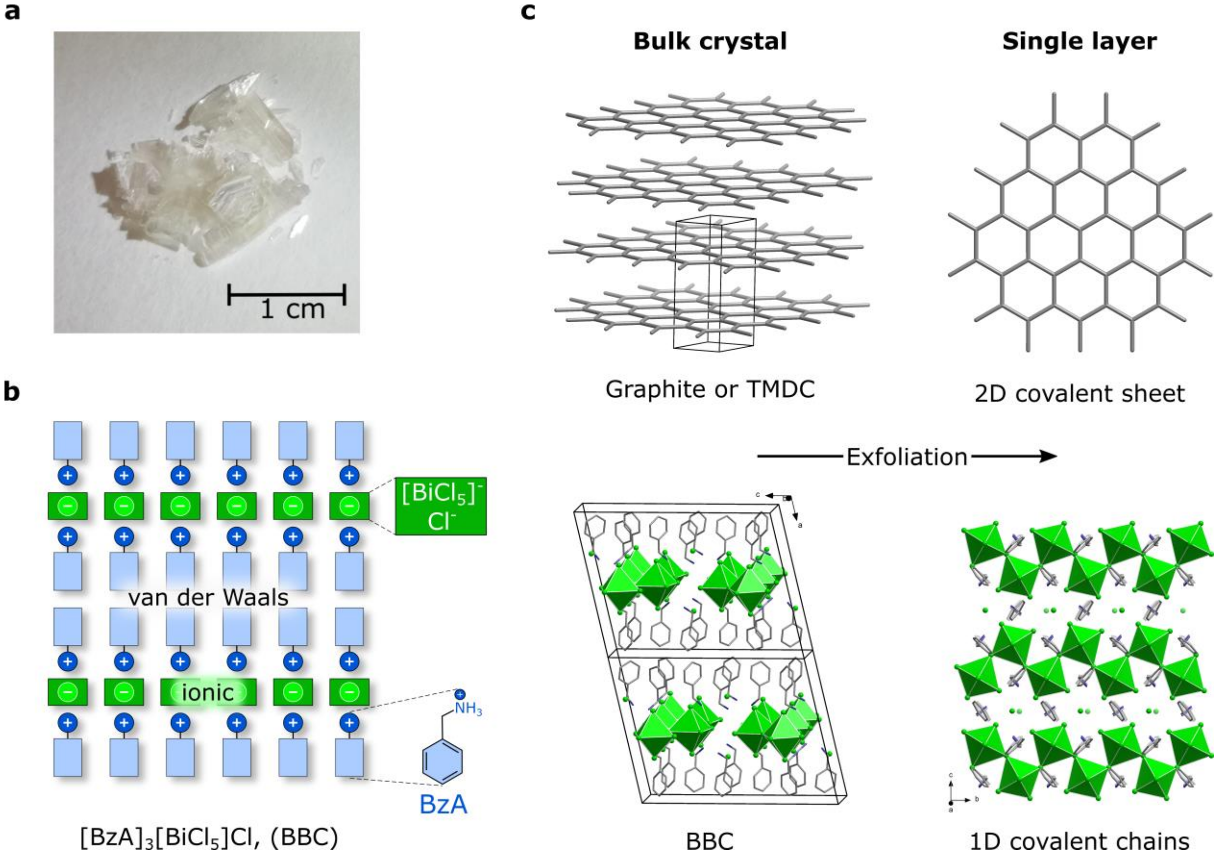

Figure 1 | Schematic representation of interactions in BBC compared to a typical 2D material. a, Photograph of large, colorless bulk BBC crystals. **b**, Schematic illustration of the layered structure of BBC with main interactions marked in the specific layers. **c**, Individual layers in conventional 2D materials are held together by strong 2D covalent bonds, facilitating exfoliation into a single layer (top). In BBC (bottom), ionic and supramolecular interactions allow for exfoliation of single layers assembled from 1D covalent chains.

Results

Synthesis and structural characterization of BBC. The reaction of benzylamine with a solution of Bi_2O_3 in concentrated hydrochloric acid solution yields large, colorless plates of BBC (Figure 1a). The single-crystal structure shows the hybrid nature of the compound: Benzylammonium cations are arranged in flat layers, with C-H···π interactions between the benzene rings. This enforces the equally flat arrangement of the $[BiCl_5]^{2-}$ chloro bismuthate chains, resulting in an overall lamellar structure (Figure 1b, 1c). Additional chloride ions are found above and below the metalate ion plane, completing the compound's charge balance. The motif in BBC is reminiscent of 2D lead halide perovskites such as $(BzA)_2[PbCl_4]$,[21] and is conceptually derived from the cubic perovskite aristotype (Figure 2). BBC is the first example of a group 15 hybrid organic-inorganic halogenido metalate that is described as a vacancy-ordered 2D perovskite of the <100> family.[22, 23] Only one singular example of a hybrid iodido bismuthate of this family exists to date: $(H_2AEQT)M_{2/3}I_4$ (M = Bi or Sb; AEQT = 5,5’’’-bis-(aminoethyl)-2,2’:5’,2’’:5’’,2’’’-quaterthiophene). However, it features statistically disordered vacancies at all metal positions and the use of a diammonium cation prevents direct exfoliation in this case.[24]

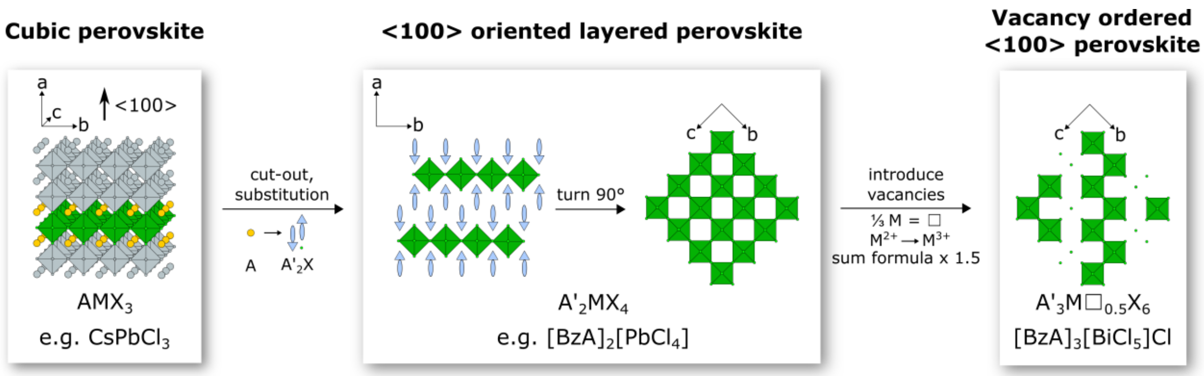

Figure 2 | Schematic derivation of BBC as a cut-out of the perovskite aristotype. Within the cubic perovskite (left), each cation A is replaced by two larger organic cations A’ such as benzylammonium (BzA) and an additional halide ion X^- for overall charge balance. This way, <100> oriented layered perovskites of composition A'_2MX_4 are derived (middle). Next, a third of the metal atoms in each of the <100> layers is removed, and the charge on each metal is increased from 2+ to 3+ to maintain charge neutrality. The result is a vacancy ordered <100> perovskite with *cis*-connected MX_5 chains and additional halide ions completing each individual layer (right) as found in $[BzA]_3[BiCl_5]Cl$.

Exfoliation, morphology and topography of 2D BBC. The conventional belief that 2D covalent interactions are an essential prerequisite for stable 2D materials suggests that the mechanical exfoliation should not be possible with BBC as it was observed in other layered perovskites.[16] Questioning this paradigm, we have investigated the mechanical exfoliation process of BBC by microscopic modelling to evaluate its ability for exfoliation, any possible cleavage plane(s), and compare BBC to well-established 2D materials. The required energy for expansions of the unit cell along the three crystallographic axes is calculated using density functional theory (Figure 3a). This energy is similar for expansions of up to 10 % along all crystallographic axes. Beyond that, the ***a*** axis differs from the others. Its expansion energy saturates at about 2.3 eV for expansions of about 20 %, while the other energies continue to increase. This indicates weaker binding of BBC along the ***a*** axis and determines the cleavage plane to be the ***b***-***c***-plane of the crystal. The calculated crystal structure of the single layer shows only a slight rearrangement of the organic molecules as the unit cell is expanded along the **a** axis. This predicts excellent preservation of the individual layers upon exfoliation

(Figure 3b). In contrast, the robustness of the 2D layered structure is corroborated by the continuously steep rise in required energies for expansions along the ***b*** and ***c*** axes.

Notably, the expansion energies along the ***b** axis* and the ***c*** axis are almost identical although the bonding interactions are very different in nature (Figure 3a): BBC features continuous covalent bonds along the ***b*** axis only and exclusively supramolecular interactions along its ***c*** axis. Examination of the change in the Bi-Cl bond length of the inorganic Bi-Cl-octahedral reveals similar results for expansions along the ***b*** axis and the ***c*** axis (Figure S6). Consequently, the ionic interaction in *c* direction yields a comparably strong binding as the covalent bonds within the octahedral chains along ***b***. This predicts the exfoliation potential of BBC despite it featuring only 1D covalent bonds as stronger 2D interactions are present intralayer while interlayer interactions are weak.

We have verified these predictions by mechanically exfoliating BBC single crystals. This yields ultrathin sheets down to the truly 2D level. The procedure is similar to the technique that is successfully applied to common van-der-Waals-materials such as TMDCs and graphene. Typical ultrathin BBC sheets on SiO_2/Si substrates exhibit lateral dimensions of a few microns - similar to other 2D materials (Figure 3c). Samples of only a few unit cells thickness can be realized this way and feature reduced lateral dimensions (less than 1 µm). The structure appears mechanically brittle, which is common for this class of materials.[16] The comparison of the expansion energies of the 2D sheets of BBC and common 2D materials like graphene and molybdenum disulfide (MoS_2) reveals that significantly less energy is required to expand the 2D sheet of BBC explaining these observations (Figure S7). The ultrathin sheets are reasonably stable in air - at least on the order of days - and long-term stable in vacuum, where they sustain repeated thermal cycling to cryogenic temperatures without damage. Degradation after 15 weeks of storage under ambient conditions becomes apparent by a reduced thickness and a deterioration of the surface topography (Figure S5).

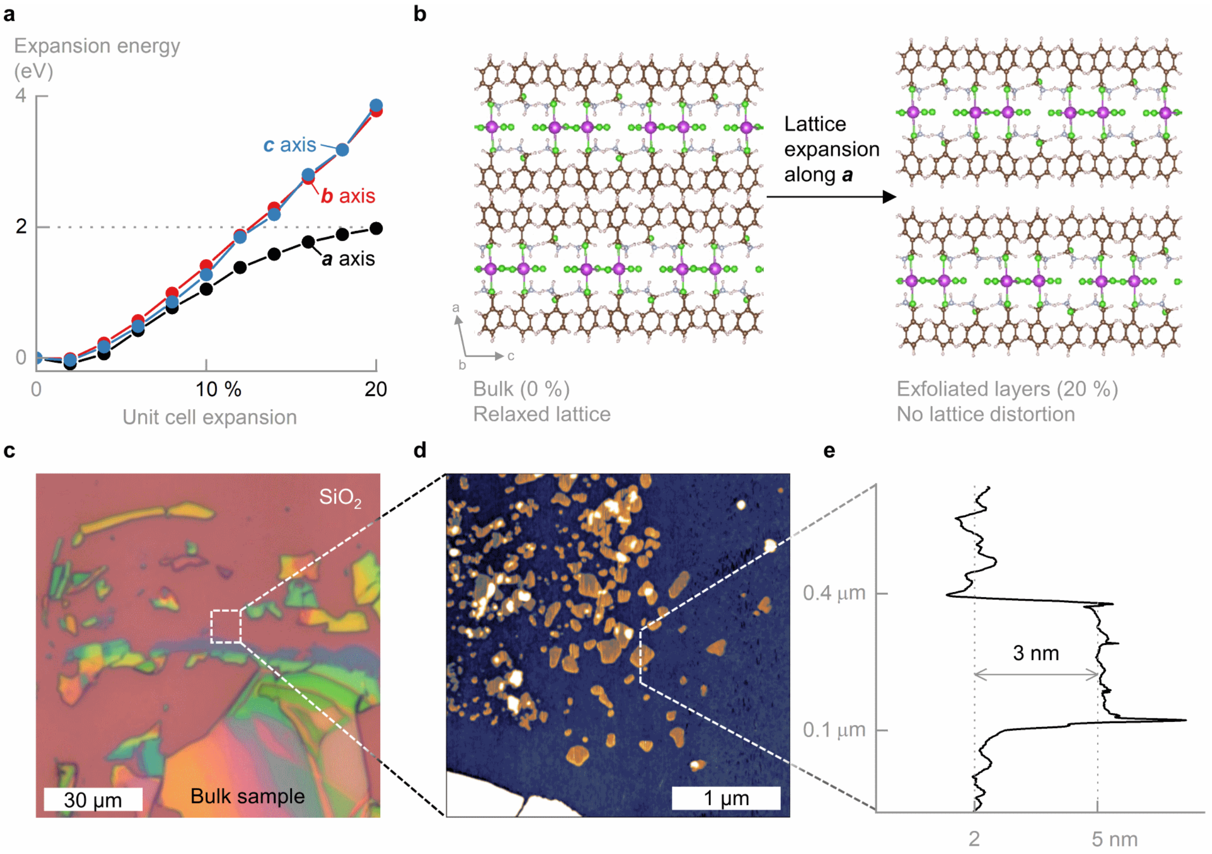

Figure 3 | Exfoliation and topography of ultrathin BBC. a, Required energy for expansion of the unit cell along the three crystallographic axes. **b**, The expansion of the crystal lattice along the ***a*** axis reveals separation of layers but no significant lattice distortion within individual layers. **c**, Typical bright-field microscopy image of mechanically exfoliated ultrathin BBC sheets on a SiO_2/Si substrate. **d**, AFM image of the area highlighted by the white rectangle in **c** showing single layers (orange). **e**, Height profile of a single layer highlighted by the white dashed line in **d**. The thickness is 3 nm.

Optical bright-field microscopy and atomic-force microscopy of ultrathin sheets reveal smooth and uniform surfaces highlighting the good crystal quality (Figure 3d). The thicknesses of the sheets range from several hundreds to only a few nanometers. The thinnest sheets are 3 nm thick (Figure 3e) which corresponds to a single, truly 2D layer of BBC as this is significantly less than twice the corresponding layer spacing along the *a*-axis of the bulk crystal. Apparently, substrate interactions increase the observed thickness of the first attached layer in accordance with findings for other 2D materials.[16,25]

Thickness-dependent optical properties of 2D BBC. The absorption spectrum of BBC (Figure 4a) shows a sharp onset of the absorption at 3.1 eV (400 nm), and a spectroscopic feature typically associated with an exciton resonance at 3.3 eV (375 nm). These are in a similar spectral range as those of other chlorobismuthates, e.g., $[H_3N(CH_2)_6NH_3][BiCl_5]$, which also consists of cis-corner-sharing $[BiCl_5]^{2-}$ chain anions and has an exciton resonance at 3.4 eV (364 nm).[26] It is interesting to note that the onset of absorption as well as the exciton resonance are red-shifted by about 55 meV (50 nm) with respect to the related 2D perovskite $[BzA]_2[PbCl_4]$, which features a layered $[PbCl_4]^{2-}$ anion.[21]

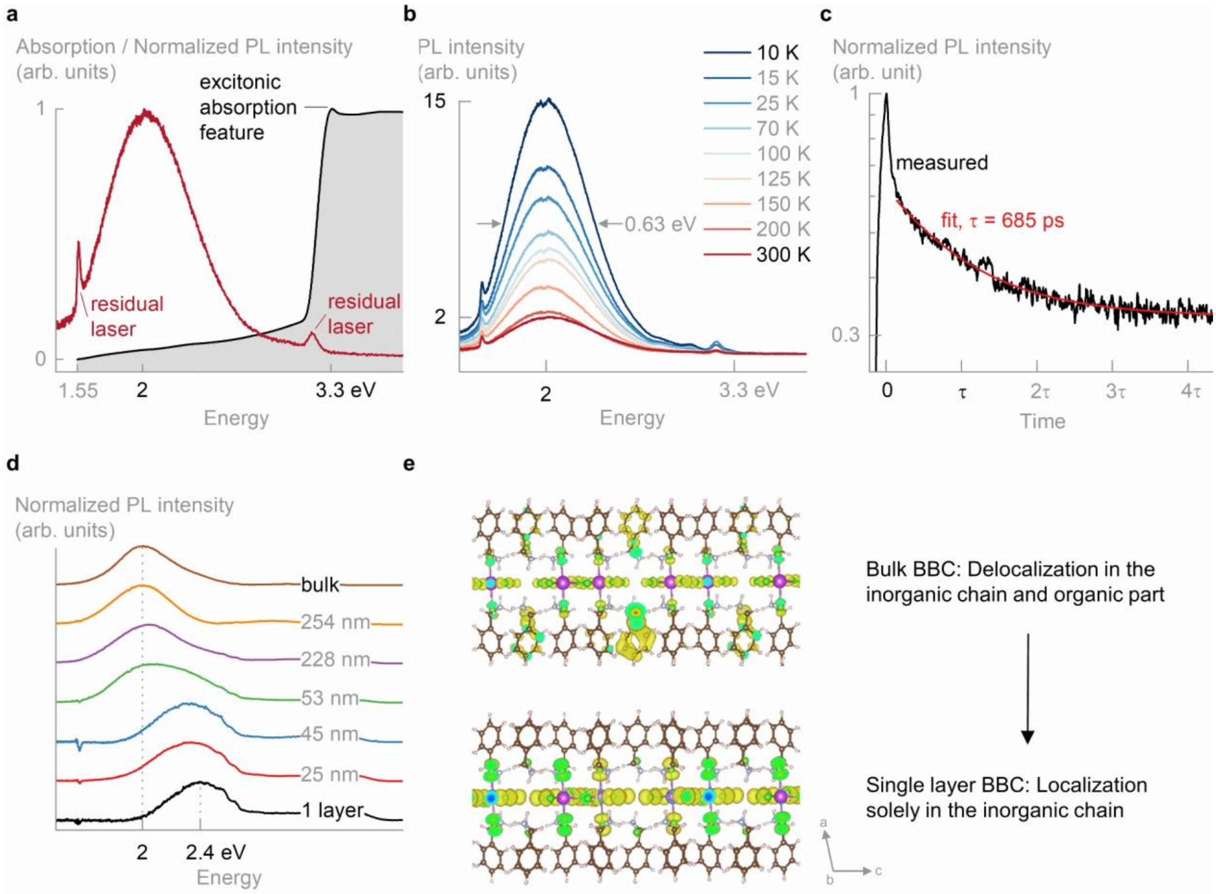

Figure 5 | Thickness-dependent optical properties and calculated valence-band charge distribution in BBC. a, Optical absorption of microcrystalline bulk powder showing a resonance at 3.3 eV, and photoluminescence (PL) of a bulk crystal at 300 K lattice temperature. **b**, PL spectra of a bulk crystal between 10 and 300 K showing bright white-light emission across the visible spectrum. **c**, Time-resolved PL of bulk BBC near 2 eV shows a luminescence lifetime of 685 ps. **d**, PL spectra for an excitation at 4.66 eV of few-layer sheets and a bulk crystal show a shift to higher emission energies when the number of layers (and thickness) decreases. **e**, Calculated valence-band edge charge-distribution in bulk and single layer BBC. In the bulk structure (top), charge carriers experience interlayer delocalization through supramolecular interactions. In the single layer limit (bottom), charge carriers are confined to the inorganic chain**.**

Bulk BBC crystals display a strong, broad white light emission across the visible spectrum centered at 2 eV (Figure 4b). Similar emission profiles have been observed for other halogenido metalates, which are currently discussed as incoherent white light-emitters.[27] The PL emission shows a small blue shift from 2.02 to 2.05 eV accompanied by a broadening from 0.63 to 0.70 eV with increasing lattice temperatures. The internal quantum efficiency (IQE) is estimated to η = 16 %, from the comparison of the integrated PL intensities between 1.6 and 2.6 eV at 300 and 10 K. This value is in the same range as those reported for other layered perovskite derivatives.[16,18] The PL intensity increases linearly with the excitation power in the range investigated (Figure S8), indicating that there is no threshold for the onset of PL due to non-radiative recombination through defects at low excitation powers, and no saturation of the absorption at high excitation powers. The PL lifetime of the emissive state at 2.0 eV is measured by time-resolved PL (Figure 4c). The transient shows an exponential decay after the laser excitation with a lifetime of $\tau_{\mathrm{PL}} = 685\ \mathrm{ps}$, which is comparable to other few-layered Pb-based 2D perovskites,[16,28] but longer than in TMDCs.[29-31] The IQE (η) and luminescence lifetime (τ_{PL}) are macroscopically linked to the radiative (τ_{r}) and non-radiative (τ_{nr}) decay times of the single crystal according to $\tau_{\mathrm{r}} = {}^{\tau_{\mathrm{PL}}}/_{\eta}$ and $\tau_{\mathrm{nr}} = {}^{\tau_{\mathrm{PL}}}/_{1-\eta}$. Accordingly, the radiative and non-radiative decay times are calculated from the measured data, yielding $\tau_{\mathrm{r}} = 4.3\ \mathrm{ns}$ and $\tau_{\mathrm{nr}} = 815\ \mathrm{ps}$, respectively. The radiative decay time is on the shorter end of the reported range for other layered perovskite derivatives,[28,32] and the non-radiative decay time is significantly shorter[32] indicating extremely good light-matter coupling. Furthermore, the homogeneous spectral constriction of the time-resolved PL indicates a single emissive state with negligible inhomogeneous broadening (Figure S9).

Comparison of the PL spectra of the bulk crystal and several ultrathin sheets of different thicknesses reveals an extremely strong dimensional effects in this compound (Figure 5d). All display white-light emission across the visible spectrum; the emission of the bulk crystal is centered at 2.0 eV and blue-shifts to 2.4 eV as the thickness is reduced to the single layer. The large blue-shift of the emission energy is accompanied by a broadening of the emission from 450 (bulk) to 585 meV (single layer). The emission-peak-energy difference of 0.4 eV between single layer and bulk samples is about one order of magnitude larger than that found for lead-based layered 2D perovskites, which typically display PL shifts of 20 to 40 meV.[16,28] This stark contrast indicates strong dimensional effects in BBC: the excitations apparently delocalize significantly in bulk samples through the coupling of the organic groups with the inorganic chains. In single layer samples, however, excitations apparently localize exclusively in the 1D inorganic chains becoming more Frenkel-exciton-like. This general picture is also supported by the structure of the valence-band edge charge-distribution in bulk and single layer BBC (Figure 5e). The band gap increases as single layer samples feature stronger in-plane localization of charge carriers inferring increased confinement energies.

In addition, we examined the evolution of the characteristic lattice vibrations of the bulk crystal and several thin sheets by Raman spectroscopy (Figure S10). The peaks at 225 and 267 cm^{-1} can be assigned to the bridging Bi-Cl and terminal Bi-Cl stretching vibrations (T_2 and A_1) of the $BiCl_6$-octahedron, whereas the broad feature at 157 cm^{-1} arises from the Cl-Bi-Cl bending vibrations (E_1).[33,34] The intensity of the peaks decreases for thinner sheets, and eventually vanishes for ultrathin sheets indicating weak Raman scattering efficiencies.

Expansion towards new 2D materials without 2D covalent interactions. It is highly desirable to be able to choose the components of a hybrid 2D material to enable the tuning of specific functionalities such as luminescence, non-linear optical properties, magnetism, and their combination, e.g., in one single material. The possibility of exfoliating BBC proves that the range of available compounds is no longer limited to covalently bound 2D sheets. Thus, the materials' basis can be expanded to other truly 2D materials composed of 1D covalent chains or even just from molecular units opening a magnitude of new opportunities.

New 2D materials can be readily identified from the Cambridge Structural Database[35] without the need to synthesize and analyze new compounds. Even a simple search for crystal structures containing benzylammonium cations as a substructure yields 24 suitable candidates (Table S12). These 24 compounds already define a new material class with a wide range of chemical and physical properties: Characteristic examples include bioactive decavanadates[36] and luminescent molecular and chain-like tin and lead halide perovskite derivatives.[37,38] The list also encompasses transition-metal complexes with magnetic and catalytic properties.[39] The use of chiral building blocks facilitates the synthesis of non-centrosymmetric compounds,[40] which should exhibit strong second harmonic generation properties and feature ferroelectric properties.[41]

In general, the search for new 2D materials needs not be restricted to the benzylammonium substructure or even ammonium cations. The concept will work similarly well for other amphiphilic components capable of forming a flat, non-interdigitated lamellar arrangement. Such arrangements may also be realized with anionic sulfonates, allowing the use of cationic metal complexes as a component of the 2D material.[42] We note that the synthesis of new hybrid 2D materials without 2D covalent interactions is not without obstacles. For example, $(BzA)_2[SbBr_5]$ shows a non-layered arrangement despite the presence of $SbBr_5$ chains[43] similar to those in BBC. However, the possibility of using, in principle, any desired metalate anion opens vast possibilities of desired materials. Obviously, not every idea may be realized, so that synthetic effort and proof remains of paramount importance. However, several of the readily available benzylammonium derivatives and the significant number of known examples provide ample guidance and show the potential of this approach.

Conclusion

In conclusion, we demonstrate that truly 2D organic-inorganic perovskites with only 1D covalent intralayer-interactions exist by preparing $[BzA]_3[BiCl_5]Cl$, a bismuth-based 2D organic-inorganic perovskite, the first vacancy-ordered 2D perovskite of the <100> family. Single crystals of BBC are mechanically exfoliated down to single layers, thereby defying the common paradigm that 2D materials require covalently bonded 2D sheets. BBC shows extremely large dimensional effects as its strong white light emission blue-shifts by as much as 0.4 eV from the bulk response to the single layer. First-principles based modelling predicts asymmetric binding strength mandatory for mechanical exfoliation as well as reveals that the wave-functions at the valence-band edge localize solely to the 1D inorganic chains. This, in turn, reconfirms the experimental observation as stronger confinement yields higher emission energies. These findings enable a general construction principle for identifying and creating tailored, custom-functionalized 2D materials where specific functionalities are introduced both in the organic and the inorganic parts of the materials. The materials base can be expanded to 2D materials composed of 1D covalent chains or even just molecular units opening a magnitude of new opportunities with materials properties ranging from luminescent, magnetic, and catalytic properties to second-harmonic generation or ferroelectric properties. Future work should focus on identifying robust supramolecular architectures that reliably yield atomically thin layered arrangements with a broad array of counterions, and the integration of BBC with other 2D materials to form heterostructures. Our approach enables interface-controlled device integration of brightly luminescent 1D and 0D hybrid perovskites and offers a promising pathway for the non-covalent functionalization of classical 2D materials through heterostructures.

Methods

Synthesis of BBC. Bi_2O_3 (233 mg, 0.5 mmol) was dissolved in 10 mL of concentrated hydrochloric acid (37%). A stoichiometric amount of benzylamine (0.33 mL, 3 mmol) was added. The solution was stirred and heated to reflux for 30 min, then left to cool to room temperature undisturbed. $[BzA]_3[BiCl_5]Cl$ (193 mg, 0.26 mmol, 52 %) was obtained as large colourless crystals.

CHN Data: Anal. Calcd for $C_{21}H_{30}BiCl_6N_3$, (M = 746.16 $gmol^{-1}$): C, 33.80; H, 4.05; N, 5.63 %. Found: C, 33.83; H, 4.06; N, 5.64 %.

Single crystal X-ray data brief for BBC. Monoclinic, space group $P2_1/c$ (no. 14), a = 17.0182(8) Å, b = 7.6205(4) Å, c = 22.4391(9) Å, β = 102.638(2)°, V = 2839.6(2) $Å^3$, Z = 4, T = 100 K, R_1 = 0.0565 ($I > 2\sigma(I)$), wR_2 = 0.1268 (all data). Additional details on data collection and structure refinement can be found in the Supplementary Information. Structure data has also been deposited in the Cambridge Crystallographic Data Centre under accession code CCDC 1952283.

Mechanical exfoliation and AFM. Ultrathin sheets of $[BzA]_3[BiCl_5]Cl$ were produced by exfoliation of bulk single crystals onto Si substrates with a 275 nm thick wet thermal oxide layer. Thin sheets were identified by optical contrast imaging and confirmed by Atomic Force Microscopy (AFM, AIST-NT SmartSPM 1000). Noncontact tapping mode was used to avoid sample damage.

Optical measurements. Low-temperature PL and time-resolved PL measurements are conducted in a continuous-flow liquid He with the sample in vacuum. The samples are excited with about 100-fs pulses at 266nm (4.1eV) into a 1 µm diameter spot (1.4 µW excitation power). Optical absorption spectra are recorded in diffuse reflectance mode and transformed to Absorbance A according to A = log(1/R).

Modelling. Density functional theory (DFT) calculations were performed using projector-augmented wave (PAW) potentials[44] and plane-wave basis sets, as implemented in the VASP software package.[45,46] The PBE functional[47] and Tkatchenko-Scheffler method[48] were used to describe exchange-correlation and dispersion interaction, respectively. Details are given in the Supplementary Information.

Acknowledgements.

This work is funded by the German Research Foundation (DFG) via the collaborative research center SFB 1083. N.D. thanks the Fonds der Chemischen Industrie and the Studienstiftung des Deutschen Volkes for their support. S.K.B. thanks the DAAD / RISE program and the SFB 1083 for a research internship. S.C. acknowledges financial support by the Heisenberg programme (CH660/2). J.H. thanks Prof. Stefanie Dehnen for her constant support. The Paderborn group acknowledges funding from the Deutsche Forschungsgemeinschaft through project SCHU 1980/13 and through the Heisenberg program (No. 270619725). A grant for computing time at the Paderborn Center for Parallel Computing (PC2) is also gratefully acknowledged.

Author contributions.

S.C. and J.H. conceived and designed the experiments. N.D., S.K.B. and J.W. developed and optimized the synthesis of BBC and performed bulk characterizations. J.H. measured, solved and refined the crystal structure and performed the CCDC database analysis. P.K. prepared the 2D samples and performed the AFM, optical and Raman measurements; P.K. and S.C. performed data analysis with input from P.J.K.. C.-D.D. and S.S. performed the theoretical modelling. P.K., S.C., C.-D.D., S.S., and J.H. wrote the paper. All authors discussed the results and commented on the manuscript.

Competing interests.

The authors declare no competing interests.

References

[1] Novoselov, K. S., Fal'ko, V. I., Colombo, L., Gellert, P. R., Schwab, M. G. & Kim, K. A roadmap for graphene. *Nature* **490**, 192–200 (2012).

[2] Tan, C. et al. Recent Advances in Ultrathin Two-Dimensional Nanomaterials. *Chem. Rev.* **117**, 6225–6331 (2017).

[3] Mak, K. F. & Shan, J. Photonics and optoelectronics of 2D semiconductor transition metal dichalcogenides. *Nat. Photon.* **10**, 216–226 (2016).

[4] Nicolosi, V., Chhowalla, M., Kanatzidis, M. G., Strano, M. S. Coleman, J. N. Liquid Exfoliation of Layered Materials, *Science* **340**, 1226419 (2013).

[5] Wang, Q. & O'Hare, D. Recent Advances in the Synthesis and Application of Layered Double Hydroxide (LDH) Nanosheets. *Chem. Rev.* **112**, 4124-4155 (2012).

[6] Anasori, B., Lukatskaya, M. R. & Gogotsi, Y. 2D metal carbides and nitrides (MXenes) for energy storage. *Nat. Rev. Mater.* **2**, 16098 (2017).

[7] Low, T., Chaves, A., Caldwell, J. D., Kumar, A., Fang, N. X., Avouris, P., Heinz, T. F., Guinea, F., Martin-Moreno, L. & Koppens, F. Polaritons in layered two-dimensional materials. *Nat. Mater.* **16**, 182–194 (2017).

[8] Takada, K., Sakurai, H., Takayama-Muromachi, E., Izumi, F., Dilanian, R. A. & Sasaki, T. Superconductivity in two-dimensional CoO_2 layers. *Nature* **422**, 53-55 (2003).

[9] Xi, X., Zhao, L., Wang, Z., Berger, H., Forró, L., Shan, J. & Mak, K. F. Strongly enhanced charge-density-wave order in monolayer $NbSe_2$. *Nat. Nanotechnol.* **10**, 765-769 (2015).

[10] Dervin, S., Dionysiou, D. D. & Pillai, S. C. 2D nanostructures for water purification: graphene and beyond, *Nanoscale* **8**, 15115–15131 (2016).

[11] Pospischil, A., Furchi, M. M. & Mueller, T. Solar-energy conversion and light emission in an atomic monolayer p–n diode. *Nat. Nanotechnol.* **9**, 257-261 (2014).

[12] Klement, P., Steinke, C., Chatterjee, S., Wehling, T. O. & Eickhoff, M. Effects of the Fermi level energy on the adsorption of O_2 to monolayer MoS_2. *2D Mater.* **5**, 045025 (2018).

[13] Jin, E., Li, J., Geng, K., Jiang, Q., Xu, H., Xu, Q. & Jiang, D. Designed synthesis of stable light-emitting two-dimensional sp^2 carbon-conjugated covalent organic frameworks. *Nat. Comm.* **9**, 4143 (2018).

[14] Rodríguez-San-Miguel, D., Amo-Ochoa, P. & Zamora, F. MasterChem: cooking 2D-polymers. *Chem. Commun.* **52**, 4113-4127 (2016).

[15] López-Cabrelles J., Mañas-Valero, S., Vitórica-Yrezábal, I. J., Bereciartua, P. J., Rodríguez-Velamazá, J. A., Waerenborgh, J. C., Vieira, B. J. C., Davidovikj , D., Steeneken, P. G., van der Zant, H. S. J., Mínguez Espallargas, G. & Coronado, E. Isoreticular two-dimensional magnetic coordination polymers prepared through pre-synthetic ligand functionalization. *Nat. Chem.* **10**, 1001-1007 (2018).

[16] Dou, L., Wong, A. B., Yu, Y., Lai, M., Kornienko, N., Eaton, S. W., Fu, A., Bischak, C. G., Ma, J., Ding, T., Ginsberg, N. S., Wang, L.-W., Alivisatos, A. P., Yang, P. Atomically thin two-dimensional organic-inorganic hybrid perovskites. *Science* **349**, 1518-1521 (2015).

[17] Shi, E., Gao, Y., Finkenauer, B. P., Akriti, Coffey, A. H. & L. Dou, Two-dimensional halide perovskite nanomaterials and heterostructures. *Chem. Soc. Rev.* **47**, 6046-6072 (2018).

[18] Yaffe, O., Chernikov, A., Norman, Z. M., Zhong, Y., Velauthapillai, A., van der Zande, A., Owen, J. S. & Heinz, T. F. Excitons in ultrathin organic-inorganic perovskite crystals. *Phys. Rev. B* **92**, 045414 (2015).

[19] Hendon, C. H., Rieth, A. J., Korzyński, M. D. & Dincă, M. Grand Challenges and Future Opportunities for Metal–Organic Frameworks. *ACS Cent. Sci.* **3**, 554-563 (2017).

[20] van Meer, G., Voelker, D. R. & G. W. Feigenson, Membrane lipids: where they are and how they behave. *Nat. Rev. Mol. Cell Biol.* **9**, 112–124 (2008).

[21] Liao, W.-Q., Zhang, Y., Hu, C.-L., Mao, J.-G., Ye, H.-Y., Li, P.-F., Huang S. D. & Xiong, R.-G. A lead-halide perovskite molecular ferroelectric semiconductor. *Nat. Commun.* **6**, 7338 (2015).

[22] Mao, L., Stoumpos, C. C. & Kanatzidis, M. G. Two-Dimensional Hybrid Halide Perovskites: Principles and Promises. *J. Am. Chem. Soc.* **141**, 1171−1190 (2019).

[23] Saparov, B. & Mitzi, D. B. Organic−Inorganic Perovskites: Structural Versatility for Functional Materials Design. *Chem. Rev.* **116**, 4558−4596 (2016).

[24] Mitzi, D. B. Organic-Inorganic Perovskites Containing Trivalent Metal Halide Layers: The Templating Influence of the Organic Cation Layer. *Inorg. Chem.* **39**, 6107-6113 (2000).

[25] Shearer, C. J., Slattery, A. D., Stapleton, A. J., Shapter, J. G. & Gibson, C. T. Accurate thickness measurement of graphene. *Nanotechnology* **27**, 125704 (2016).

[26] Mousdis, G. A., Papavassiliou, G. C., Terzis, A. & Raptopoulou, C. P. Preparation, Structures and Optical Properties of $[H_3N(CH_2)_6NH_3]BiX_5$(X=I, Cl) and $[H_3N(CH_2)_6NH_3]SbX_5$ (X=I, Br). *Z. Naturforsch.* **53b**, 927-931 (1998).

[27] Smith, M. D. & Karunadasa, H. I. White-Light Emission from Layered Halide Perovskites. *Acc. Chem. Res.* **51**, 619−627 (2018).

[28] Zhang, Q. Chu, L. Zhou, F. Ji, W. & Eda, G. Excitonic Properties of Chemically Synthesized 2D Organic–Inorganic Hybrid Perovskite Nanosheets. *Adv. Mater.* **30**, 1704055 (2018).

[29] Wang, Q. H., Kalantar-Zadeh, K., Kis, A., Coleman, J. & Strano, M. Electronics and optoelectronics of two-dimensional transition metal dichalcogenides. *Nat. Nanotechnol.* **7**, 699-712 (2012).

[30] Wang, G., Bouet, L., Lagarde, D., Vidal, M., Balocchi, A., Amand, T., Marie, X. & Urbaszek, B. Valley dynamics probed through charged and neutral exciton emission in monolayer WSe_2. *Phys. Rev. B* **90**, 075413 (2014).

[31] Lagarde, D., Bouet, L., Marie, X., Zhu, C. R., Liu, B. L. Amand, T., Tan, P. H. & Urbaszek, B. Carrier and Polarization Dynamics in Monolayer MoS_2. *Phys. Rev. Lett.* **112**, 047401 (2014).

[32] Kawano, N. *et al.* Effects of organic moieties on luminescence properties of organic-inorganic layered perovskite-type compounds. *J. Phys. Chem. C* **118**, 9101–9106 (2014).

[33] Bednarska-Bolek, B., Zaleski, J., Bator, G. & Jakubas, R. On structural phase transitions in piperidinium halogenoantimonates(III) and bismuthates(III): X-ray, calorimetric, dilatometric, dielectric and Raman studies. *J. Phys. Chem. Solids* **61**, 1249-1261 (2000).

[34] Rhandour, A., Ouasri, A., Roussel, P. & Mazzah, A. Crystal structure and vibrational studies of butylenediammonium pentachlorobismuthate (III) hydrate $[NH_3(CH_2)_4NH_3]BiCl_5\cdot H_2O$. *J. Mol. Struct.* **990**, 95-101 (2011).

[35] Groom, C. R., Bruno, I. J., Lightfoot M. P. & Ward, S. C. The Cambridge Structural Database. *Acta Cryst.* **B72**, 171-179 (2016).

[36] Yraola, F., García-Vicente, S., Marti, L., Albericio, F., Zorzano, A. & Royo, M. Understanding the Mechanism of Action of the Novel SSAO Substrate $(C_7NH_{10})_6(V_{10}O_{28})\cdot 2H_2O$, a Prodrug of Peroxovanadate Insulin Mimetics. *Chem. Biol. Drug Des.* **69**, 423-428 (2007).

[37] Billing, D. G. & Lemmerer, A. Synthesis and crystal structures of inorganic–organic hybrids incorporating an aromatic amine with a chiral functional group. *CrystEngComm* **8**, 686-695 (2006).

[38] Quan, L. N., Rand, B. P., Friend, R. H., Mhaisalkar, S. G., Lee, T.-W., Sargent, E. H. Perovskites for Next-Generation Optical Sources. *Chem. Rev.* **119**, 7444-7477 (2019).

[39] Kammoun, O., Bataille, T., Lucas, A., Dorcet, V., Marlart, I., Rekik, W., Naïli, H. & Mhiri, T. A Supramolecular Double Sulfate Salt with a Lamellar Type: Crystal Structure and Thermal Behavior. *Inorg. Chem.* **53**, 2619-2627 (2014).

[40] Srinivasan, B. R., Naik, A. R., Näther, C. & Bensch, W. Synthesis, Spectroscopy and Crystal Structures of Chiral Organic Ammonium Tetrathiometalates Showing N-H···S and C-H···S Interactions. *Z. allg. anorg. Chem.* **633**, 582-588 (2007).

[41] Li, P.-F., Liao, W.-Q., Tang, Y.-Y., Qiao, W., Zhao, D., Ai, Y., Yao, Y.-F. & Xiong, R.-G. Organic enantiomeric high-Tc ferroelectrics. *PNAS* **116**, 5878–5885 (2019).

[42] Qiu, R., Xu, X., Li, Y., Zhang, G., Shao, L., An, D. & Yin, S. Synthesis and structure of air-stable Lewis acidic binuclear complex of zirconocene pentafluorophenylsulfonate and its catalytic application in the allylation of carbonyl compounds with tetraallyltin. *Chem. Commun.* **2009**, 1679–1681 (2009).

[43] Anyfantis, G. C., Ganotopoulos, N.-M., Savvidou, A., Raptopoulou, C. P., Psycharis V. & Mousdis, G. A. Synthesis and characterization of new organic–inorganic hybrid compounds based on Sb, with a perovskite like structure. *Polyhedron* **151**, 299–305 (2018).

[44] Kresse, G. & Joubert, D. From ultrasoft pseudopotentials to the projector augmented-wave method. *Phys. Rev. B* **59**, 1758 (1999).

[45] Kresse, G. & Hafner, J. Ab initio molecular dynamics for liquid metals. *Phys. Rev. B* **47**, 558 (1993).

[46] Kresse, G. & Hafner, J. Ab initio molecular-dynamics simulation of the liquid-metal–amorphous-semiconductor transition in germanium. *Phys. Rev. B* **49**, 14251 (1994).

[47] Perdew, J., Burke, K. & Ernzerhof, M. Generalized gradient approximation made simple. *Phys. Rev. Lett.* **77**, 3865 (1996)**.**

[48] Tkatchenko, A. & Scheffler, M. Accurate molecular van der Waals interactions from ground-state electron density and free-atom reference data. *Phys. Rev. Lett.* **102**, 073005 (2009).

3.6. Band Gap-Tunable, Chiral Hybrid Metal Halides Displaying Second-Harmonic Generation

Natalie Dehnhardt, Marleen Axt, Jonas Zimmermann, Meng Yang, Gerson Mette, Johanna Heine, *Chemistry of Materials* **2020**, *32*, 4801-4807, DOI: 10.1021/acs.chemmater.0c01605.

Abstract

The introduction of chirality in lead halide perovskites and related metal halide materials allows for an expansion of their unique and useful properties towards nonlinear optics. However, when synthesizing materials based on the less toxic metals antimony and bismuth, the large variability in the crystal structures of their metalates and their tendency to form molecular or chain-like anion motifs can be a challenge when creating tunable, multifunctional materials. Here we show that, using a chiral amine template, we can synthesize an isomorphous family of compounds $[(R)\text{-1-(4-F)PEA}]_4[E_2X_{10}]$ ((R)-1-(4-F)PEA = (R)-1-(4-fluoro)phenyl-ethylammonium; E = Sb, Bi; X = Cl, Br, I) that combines multiple functionalities: The compounds are not only chiral, but also feature a trilayered arrangement of cations and anions that allows for facile cleavage and exfoliation. The different combinations of E and X allow for a variation of the onset of absorption between 3.35 eV and 2.09 eV. Using femtosecond laser spectroscopy, we show that our materials allow for efficient second-harmonic generation (SHG). Together with a simple synthesis and good stabilities, this makes these materials promising candidates for linear and nonlinear optical devices.

Zusammenfassung

In dieser Publikation wird über sechs neue Halogenidoantimonate und -bismutate berichtet, die auf ihre Eigenschaften zur optischen Frequenzverdopplung untersucht wurden. Ziel der Untersuchungen war die Ergebnisse aus der unter Abschnitt 3.5. beschriebenen Veröffentlichung zu erweitern, indem durch Substitution am Benzylammoniumkation eine neue Funktionalität in die Halogenidometallate eingebracht wird. Alle sechs Verbindungen sind isostrukturell und enthalten $[E_2X_{10}]^{4-}$-Anionen und (R)-1-(4-F)-Phenethylammonium-Kationen ((R)-1-(4-F)PEA). Die Anionen ordnen sich hierbei entlang der kristallographischen *a*-*b*-Ebene zu Schichten an, welche von (R)-1-(4-F)PEA-Doppelschichten getrennt werden. Die Kationen orientieren sich mit ihrer polaren Kopfgruppe zu den Anionen, während die Fluorosubstituenten am Benzylgerüst zueinander angeordnet sind. Folglich treten nur schwache Wechselwirkungen zwischen den einzelnen ladungsneutralen Schichten auf, sodass die Kristalle leicht an der *a*-*b*-Ebene gespalten werden können. In Abbildung 3.6 a) ist ein Ausschnitt aus der Kristallstruktur zu sehen. Eine vereinfachte schematische

Darstellung der Schichten und der Wechselwirkungen innerhalb dieser ist in Abbildung 3.6 b) dargestellt.

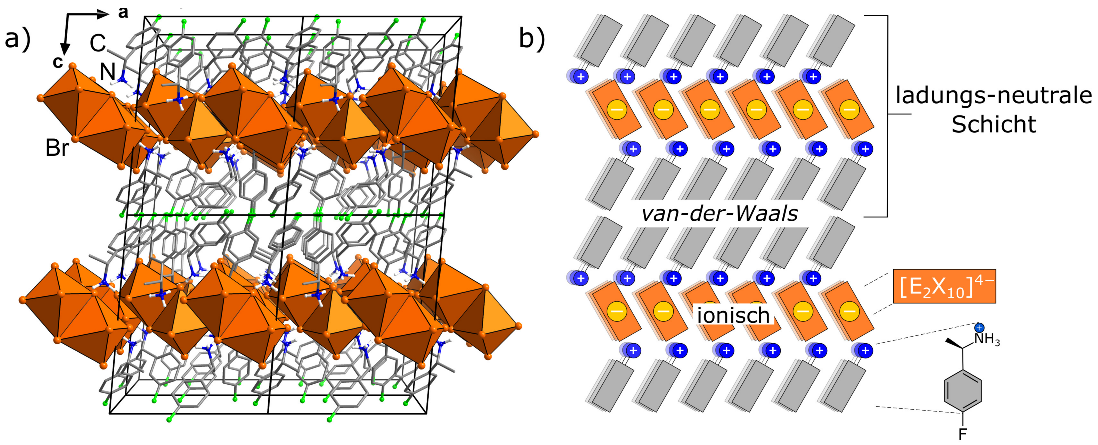

Abbildung 3.6: a) Ausschnitt aus der Kristallastruktur der $[(R)\text{-}1\text{-}(4\text{-}F)PEA]_4[E_2X_{10}]$-Metallate entlang der kristallographischen *b*-Achse. Zur besseren Übersicht sind die Anionen in Polyeder-Darstellung und die Kationen im Stabmodell abgebildet. Wasserstoffatome werden nicht gezeigt. b) Vereinfachte schematische Darstellung der Wechselwirkungen innerhalb und zwischen den Schichten der $[(R)\text{-}1\text{-}(4\text{-}F)PEA]_4[E_2X_{10}]$-Metallate.

Wird Antimon-III-oxid bzw. Bismut-III-oxid (Bi_2O_3) in konzentrierten Halogenwasserstoffsäuren (HCl_{aq}, HBr_{aq}, HI_{aq}) gelöst und mit stöchiometrischen Mengen (*R*)-1-(4-F)Phenethylamin versetzt, können beim Abkühlen der Lösungen Kristalle von **1** bis **6** erhalten werden. Die Verbindungen kristallisieren sehr schnell und weisen entsprechend ihrer Elementkombination intensive Farben auf. Um geeignete Einkristalle für die Untersuchung der optischen Eigenschaften zu erhalten, musste daher in stark verdünnter Lösung gearbeitet werden. Hierbei war gerade bei der Synthese von Verbindung **1** das Arbeiten in konzentrierter Chlorwasserstoffsäure essenziell, da ansonsten ein Hydrolyse zu $Sb_4Cl_2O_5$ beobachtet wird. Die Verbindungen sind an Luft mehrere Wochen stabil und zersetzen sich ab 190 °C, wobei die Bismutate eine größere thermische Stabilität als die Antimonate aufweisen.

Die Absorptionsspektren spiegeln die Farben der Verbindungen wieder, die Iodidometallate absorbieren bei höheren Wellenlängen als die entsprechenden Bromido- und Chloridometallate. Da die Verbindungen in der nicht-zentrosymmetrischen Raumgruppe $P2_1$ kristallisieren, wurden sie auf die Möglichkeit zur Frequenzverdopplung (*second harmonic generation* = SHG) untersucht. Bei einer Anregung mit 800 nm zeigen alle Verbindungen SHG, wobei das emittierte 400 nm SHG-Licht eine quadratische Abhängigkeit von der Laserleistung zeigt.

Rotationsanisotropie-Experimente zeigen für die Chlorido- und Bromidometallate Ergebnisse, die mit den erwarteten Werten für die Raumgruppe $P2_1$ übereinstimmen. Für die

Iodidometallate weichen die Werte stark ab, was von einer Inhomogenität im Kristall verursacht sein könnte. Bei einer Schichtdicke von 125 ± 20 μm zeigen die Verbindungen schwächere SHG als Quartz. Eine signifikant dickere Probe von **1** (700 μm) lieferte ein stärkeres SHG-Signal, was in gutem Einklang mit einer quadratischen Abhängigkeit des SHG-Signals von der Probendicke steht. Die guten SHG-Eigenschaften sowie die Stabilität und die Vielfältigkeit der Verbindungen machen sie besonders interessant.

Eigener Anteil

Als erste Verbindung der Serie wurde **4** von mir auf solvothermalem Weg dargestellt. Unter meiner Anleitung wurde von *Meng Yang* eine Syntheseroute in Lösung entwickelt, wodurch die Verbindungen **2**, **3**, **5** und **6** erhalten werden konnten. Um ausreichend große Einkristalle zu erhalten wurden die Reaktionsbedingungen von mir optimiert sowie eine Synthese von **1** entwickelt, dessen Darstellung am meisten Hindernisse barg. Alle Verbindungen wurden über Röntgenbeugung an Einkristallen und Pulvern, UV-Vis- und Infrarot-Spektroskopie, Thermogravimetrie und gekoppelte Differenzkalorimetrie sowie CHN-Elementaranalyse charakterisiert und identifiziert. Alle Ergebnisse wurden von mir ausgewertet und für die Publikation aufbereitet. Einkristallmessungen sowie Strukturlösung und -verfeinerung wurden von *Dr. Johanna Heine* durchgeführt. Pulverdiffraktogramme, UV-Vis-Spektren und Infrarotspektren wurden von mir aufgenommen. Thermogravimetrie und gekoppelte Differenzkalorimetrie wurden von *Uwe Justus* durchgeführt. Die CHN-Elementaranalyse wurde von der zentralen Abteilung für Massenspektrometrie und Elementaranalyse der Philipps-Universität Marburg durchgeführt. Die nicht-linearen optischen Eigenschaften wurden von *Marleen Axt* und *Jonas Zimmermann* in der Arbeitsgruppe von *Dr. Gerson Mette* charakterisiert. An der Erstellung des Manuskripts wirkten alle Co-Autoren mit.

cm CHEMISTRY OF MATERIALS

pubs.acs.org/cm Article

Band Gap-Tunable, Chiral Hybrid Metal Halides Displaying Second-Harmonic Generation

Natalie Dehnhardt, Marleen Axt, Jonas Zimmermann, Meng Yang, Gerson Mette,* and Johanna Heine*

Cite This: *Chem. Mater.* 2020, 32, 4801−4807 Read Online

ABSTRACT: The introduction of chirality in lead halide perovskites and related metal halide materials allows for an expansion of their unique and useful properties toward nonlinear optics. However, when synthesizing materials based on less toxic metals antimony and bismuth, the large variability in the crystal structures of their metalates and their tendency to form molecular or chain-like anion motifs can be a challenge when creating tunable materials. Here, we show that using a chiral amine template, we can synthesize an isomorphous family of compounds $[(R)\text{-}1\text{-}(4\text{-F})\text{PEA}]_4[E_2X_{10}]$ ((*R*)-1-(4-F)PEA = (*R*)-1-(4-fluoro)-phenylethylammonium; E = Sb and Bi; X = Cl, Br, and I) that combines multiple aspects: the compounds are not only chiral but also feature a trilayered arrangement of cations and anions that allows for facile cleavage and exfoliation. The different combinations of E and X allow for a variation of the onset of absorption between 3.35 and 2.09 eV. Using femtosecond laser spectroscopy, we show that our materials allow for efficient second-harmonic generation. Together with a simple synthesis and good stability, this makes these materials promising candidates for linear and nonlinear optical devices.

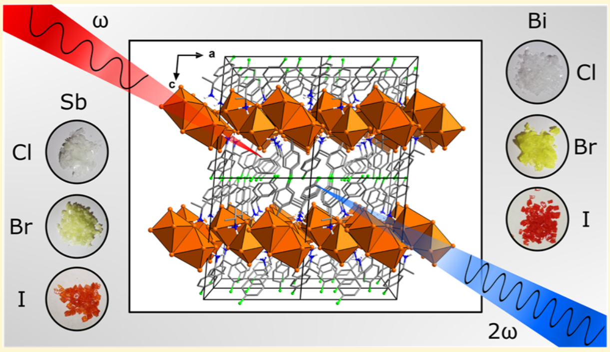

■ INTRODUCTION

The recent surge in interest in metal halide perovskites AMX_3 (A = Cs and CH_3NH_3; M = Sn and Pb; X = Cl, Br, and I)[1] and their successful use in photovoltaics[2] has sparked additional research into a number of related materials. Among these are layered main group halogenido metalates: inspired by works on perovskite-derived layered transition metal halides,[3] the first in-depth studies of these materials were performed in the 1980s and 1990s.[4−7] Compounds such as $(C_6H_5CH_2CH_2NH_3)_2SnI_4$ showed interesting optoelectronic properties and controllable, “natural quantum-well”[8] structures tested in LEDs[9] and FETs.[10]

Currently, investigations of such layered perovskite materials have been greatly expanded[11,12] and also include multinary compounds such as double perovskites.[13,14] A number of examples show that these materials can possess luminescence properties that vary from sharp lines to broad white light emission.[15] They can also be used in applications such as solar cells[16] and lasers[17] and show greater stability against moisture than their AMX_3 parent compounds.[18] Additionally, they provide great opportunities for material design, as new functionalities can be introduced via the organic cations[19−21] without rigid size requirements governing AMX_3 perovskites.[22,23] Their anisotropic nature also allows for integration with 2D materials such as graphene or MoS_2 monolayers.[24] One possible functionality of 2D perovskites that has recently come into focus is chirality: by using chiral amines, it is possible to create chiral materials by design.[25,26] These can be used for the detection[27] and generation of circularly polarized light,[28] as ferroelectrics[29] and in spintronics.[30]

We are interested in halogenido metalates of antimony and bismuth, as these compounds avoid the toxicity[31] and instability[32] issues associated with lead-based and tin-based metalates, respectively.[33] Because of an increase in the charge of metals from 2+ to 3+, halogenido antimonates and bismuthates show a related, yet distinctly different structural chemistry compared to group 14 metalates.[34−36] In consequence, halogenido pentelates rarely form layered anions, especially when larger organic cations are used.[37−44]

In this work, we demonstrate a new approach toward halogenido metalates with similar properties as layered perovskite materials: we use organic cations that template a layered arrangement of the molecular halogenido pentelate anions. This way, we create an isomorphous family of compounds $[(R)\text{-}1\text{-}(4\text{-F})\text{PEA}]_4[E_2X_{10}]$ ((*R*)-1-(4-F)PEA = (*R*)-1-(4-fluoro)phenylethylammonium; E = Sb and Bi; X =

Received: April 15, 2020
Revised: May 7, 2020
Published: May 8, 2020

https://dx.doi.org/10.1021/acs.chemmater.0c01605
Chem. Mater. 2020, 32, 4801−4807

Cl, Br, and I). This allows us to tune the onset of absorption from 400 to 600 nm and, by using an enantiopure amine, enforce a noncentrosymmetric crystal structure showing very efficient optical second-harmonic generation (SHG) under femtosecond laser excitation.

■ METHODS

General. All reagents were used as received from commercial sources. (*R*)-1-(4-Fluoro)phenylethylamine with 98% ee was obtained from Alfa Aesar. CHN analysis was carried out on an Elementar CHN-analyzer. Powder patterns were recorded on a STADI MP (STOE Darmstadt) powder diffractometer, with Cu Kα_1 radiation with λ = 1.54056 Å at room temperature in transmission mode (see Figures S7−S12). IR spectra were measured on a Bruker Tensor 37 FT-IR spectrometer equipped with an ATR-Platinum measuring unit (see Figures S13−18). Thermal analysis was carried out by simultaneous DTA/TG on a NETZSCH STA 409 C/CD in the temperature range of 25−1000 °C at a heating rate of 10 °C min^{-1} in a constant flow of 80 mL min^{-1} Ar (see Figures S19−S24). Optical absorption spectra were recorded on a Varian Cary 5000 UV/vis/NIR spectrometer in the range of 300−800 nm in diffuse reflectance mode employing a Praying Mantis accessory (Harrick). For the ease of viewing, raw data were transformed from % reflectance *R* to absorbance *A* according to $A = \log(1/R)$ which yields estimates comparable to the widely used Kubelka−Munk relation (see Figure S25).[45]

Synthesis. Sb_2O_3 or Bi_2O_3 was dissolved in the respective concentrated hydrohalic acid and an excess of (*R*)-1-(4-fluoro)-phenylethylamine was added directly. The solution was stirred and heated to reflux for 30 min, then left undisturbed to cool to room temperature. After 24 h, a crystalline product formed and was isolated by filtration. The product was washed with pentane and dried under vacuum. See Table S1 for individual amounts. Yields are given with respect to E_2O_3 as the limiting reagent.

[(R)-1-(4-F)PEA]$_4$[Sb$_2$Cl$_{10}$] ***(1)***. Colorless crystals. Yield: 24%. CHN Data for **1**: Anal. Calcd for $C_{32}H_{44}Sb_2Cl_{10}F_4N_4$, ($M$ = 1158.71 gmol^{-1}): C, 33.17; H, 3.83; N, 4.84%. Found: C, 33.47; H, 3.87; N, 4.91%.

[(R)-1-(4-F)PEA]$_4$[Sb$_2$Br$_{10}$] ***(2)***. Very light yellow crystals. Yield: 23%. CHN data for **2**: Anal. Calcd for $C_{32}H_{44}Sb_2Br_{10}F_4N_4$, ($M$ = 1603.31 g mol^{-1}): C, 23.97; H, 2.77; N, 3.49%. Found: C, 24.15; H, 2.72; N, 3.54%.

[(R)-1-(4-F)PEA]$_4$[Sb$_2$I$_{10}$] ***(3)***. Orange crystals. Yield: 28%. CHN data for **3**: Anal. Calcd for $C_{32}H_{44}Sb_2I_{10}F_4N_4$, ($M$ = 2073.21 g mol^{-1}): C, 18.54; H, 2.14; N, 2.70%. Found: C, 18.71; H, 2.18; N, 2.76%.

[(R)-1-(4-F)PEA]$_4$[Bi$_2$Cl$_{10}$] ***(4)***. Colorless crystals. Yield: 40%. CHN data for **4**: Anal. Calcd for $C_{32}H_{44}Bi_2Cl_{10}F_4N_4$, ($M$ = 1333.17 g mol^{-1}): C, 28.83; H, 3.33; N, 4.20%. Found: C, 29.00; H, 3.45; N, 4.19%.

[(R)-1-(4-F)PEA]$_4$[Bi$_2$Br$_{10}$] ***(5)***. Yellow crystals. Yield: 58%. CHN data for **5**: Anal. Calcd for $C_{32}H_{44}Bi_2Br_{10}F_4N_4$, ($M$ = 1777.77g mol^{-1}): C, 21.62; H, 2.49; N, 3.15%. Found: C, 21.80; H, 2.65; N, 3.17%.

[(R)-1-(4-F)PEA]$_4$[Bi$_2$I$_{10}$] ***(6)***. Red crystals. Yield: 12%. CHN data for **6**: Anal. Calcd for $C_{32}H_{44}Bi_2I_{10}F_4N_4$, ($M$ = 2247.67g mol^{-1}): C, 17.10; H, 1.97; N, 2.49%. Found: C, 17.31; H, 1.97; N, 2.56%.

X-ray Crystallography. Single-crystal X-ray determination was performed at 100 K on a Bruker D8 Quest diffractometer with microfocus Mo Kα radiation and a Photon 100 (CMOS) detector. The structures were solved using direct methods, refined by full-matrix least-squares techniques, and expanded using Fourier techniques, using the SHELX software package[46−48] within the OLEX2 suite.[49] All nonhydrogen atoms were refined anisotropically unless otherwise indicated. Hydrogen atoms were assigned to idealized geometric positions and included in structure factor calculations. Pictures of the crystal structures were created using DIAMOND.[50] Additional details on individual refinements are reported in the Supporting Information, Tables S2−S7 and Figures S1−S6. The data for compounds **1**−**6** are deposited as CCDC 1995570−1995575.

SHG Setup. The SHG measurements were performed under ambient conditions using 10 fs laser pulses generated by a Ti:Sapphire oscillator operating at 800 nm at a repetition rate of 82 MHz. The generated second-harmonic (SH) light at frequency 2ω was observed in transmission for different combinations of input and output polarizations. Further details on the optical setup can be found in the Supporting Information.

■ RESULTS AND DISCUSSION

Synthesis. Compounds **1**−**6** can be obtained via a simple solution-based method. Sb_2O_3 or Bi_2O_3 is dissolved in an aqueous HX solution. (*R*)-4-Fluoro-α-methylbenzylamine is added and the solution is heated to reflux for 30 min. As the hot solution cools down, crystals of **1**−**6** are deposited which can be isolated by filtration. Photographs of the isolated compounds are shown in Figure 1. In the case of compound **1**, the use of concentrated HCl solution is strictly necessary to suppress the formation of $Sb_4Cl_2O_5$,[51] underlining the fact that the tendency toward hydrolysis is greater in chlorides and antimonates.

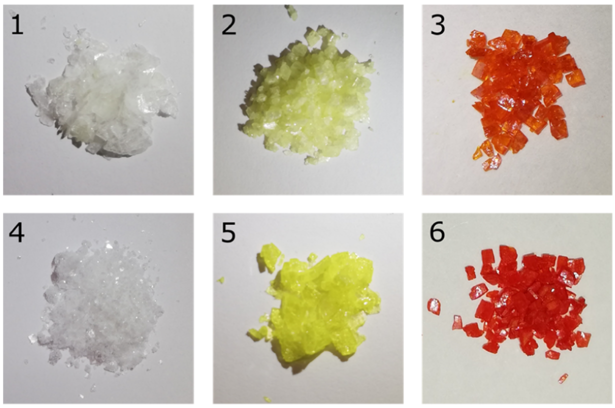

Figure 1. Crystalline samples of compounds **1**−**6**; the side length of photographs is about 1 cm.

X-ray Crystallography. Compounds **1**−**6** crystallize in the monoclinic Sohncke space group $P2_1$ with very low Flack parameters, as expected from the use of an enantiopure amine reagent. The specific crystal habit observed is dependent on the exact reaction conditions such as concentrations and cooling rates, allowing for the isolation of nontwinned blocks or planks. Typically, a fraction of the product crystallizes at the air−water interface as thin flakes, indicating that few-layered crystals may be available this way.[52] In block-like crystals, the (001) crystal face is easily identified, and it is possible to mechanically cleave the crystals perpendicular to (001) using Scotch Tape.

The compounds' crystal structure is composed of anionic $[E_2X_{10}]^{4-}$ building blocks and $[(R)\text{-}1\text{-}(4\text{-}F)PEA]^+$ ammonium units (Figure 2). $[E_2X_{10}]^{4-}$ anions are a well-known anion type in the chemistry of halogenido pentelates, and examples are known for each E−X combination discussed here.[53−56] The motif of an edge-sharing dinuclear anion appears to be especially prominent in compounds obtained from hydrohalic acid. Bond lengths are within expected ranges (see Table S7), with chlorides and antimonates showing a greater tendency toward more distorted octahedral environments around the

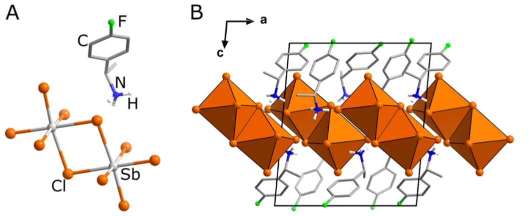

Figure 2. Excerpt of the crystal structure of **1** shown as an example for the whole isostructural series. All hydrogen atoms not belonging to the ammonium group are omitted for clarity. (A) The anion and the cation in **1**. (B) A unit cell with coordination polyhedra shown as closed octahedra.

metal atom and greater differences between the longer bridging and shorter terminal E−X bond lengths.

A comparison of the cell parameters along the isomorphous series shows the expected trends (see Table S7). The parameters *a* and *b* as well as cell volumes increase going from Cl → Br → I. The difference between antimonates and bismuthates is less clear-cut because of the larger range of the Sb−X bond length. Interestingly, the parameter *c* in **1** is the largest across the series, likely because of small differences in the arrangement of ammonium cations.

The significant feature of compounds **1**−**6** is their crystal packing (Figure 3). The $[E_2X_{10}]^{4-}$ anions are arranged in a layer in the *a*−*b* plane and the NH_3 groups of the organic ammonium cations are oriented toward this plane. This results in an overall charge-neutral trilayer, with only van der Waals forces between the opposite 4-fluorophenyl groups. This pseudo-layered type of arrangement is unusual for halogenido pentelates featuring molecular anions. Typically, when using ammonium cations that enable layered arrangements in halogenido tetrelates such as *n*-butylammonium[57] or 1,6-diammoniohexane,[58] the supramolecular interactions are not strong enough to overcome the tendency toward a more even charge distribution in the pentelates,[59−61] where the additional driving force for the formation of a layered anion is missing.

A number of secondary interactions can be considered in **1**−**6**. The ionic interactions between the anions and cations are accompanied by N−H···X interactions[62] that provide more directionality to the overall arrangement and link the individual anions into a layer (see Figure S7). X···X interactions below the sum of the van der Waals radii provide further interconnection between anions within the *ab* plane (see Figure S8).[63] Overall, it appears that it is the sum of small interactions that enables this particular packing motif, not just the presence of a benzylammonium (BzA)-derived building block, as illustrated by the examples $[BzA]_2[SbBr_5]$ and $[BzA]_3[Sb_2I_9]$, where an overall nonplanar packing is observed.[64] Ok and group has recently shown that [(*R*/*S*)-PEA]$_4$[Bi$_2$Br$_{10}$] (PEA = phenylethylammonium), a compound that is very similar to those presented here, can be obtained,[65] but their investigations were limited to single E−X combinations.

The use of chiral amines to produce chiral halogenido metalates of group 14 and 15 has remained rare despite the great interest in these materials and the ready availability of the starting materials from chemical suppliers,[66−68] with a growing number of examples prepared in the last year.[69−72] Nonetheless, these examples as well as our family of compounds show that the introduction of chirality by this route and the design of specific material properties is quite straightforward. The additional feature of a pseudo-layered arrangement in **1**−**6** provides the possibility to exfoliate the compounds and more easily integrate them into device architectures in controlled orientation.

Optical Properties. Absorption spectra of **1**−**6**, measured in diffuse reflection mode, are shown in Figure 4. The onset of absorption follows expected trends with regard to the influence of the halide, displaying red-shifts going from Cl to Br and I.[56] For chlorides and bromides, no large difference is observed going from Sb to Bi, with the bismuthates showing a steeper

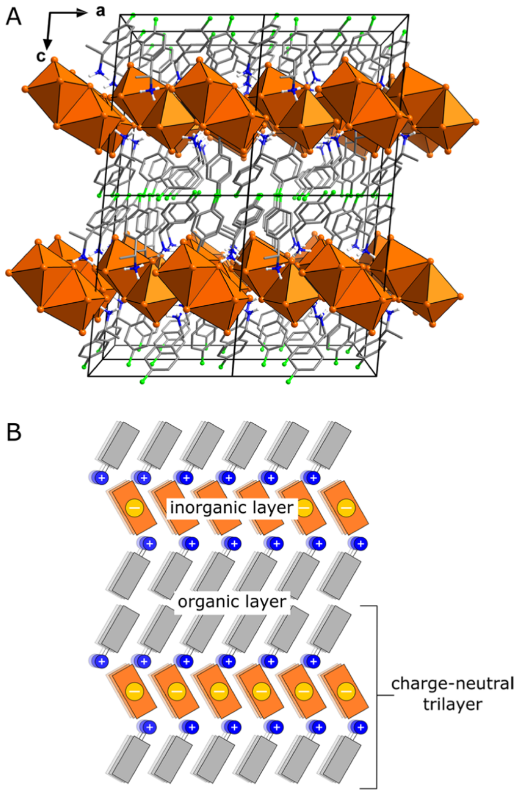

Figure 3. (A) Excerpt of the crystal structure of **1** in central projection with $Sb_2Cl_{10}^{4-}$ anions shown as closed polyhedra. (B) Conceptual sketch of the quantum-well-like nature of **1**−**6**, with separate organic and inorganic layers and cleavable, charge-neutral trilayers.

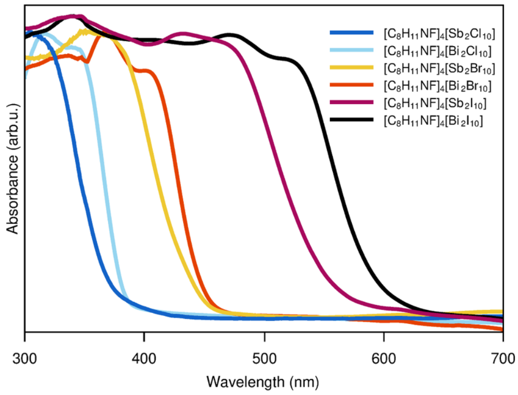

Figure 4. UV−vis spectra of **1**−**6** measured in diffuse reflectance mode on ground single crystals.

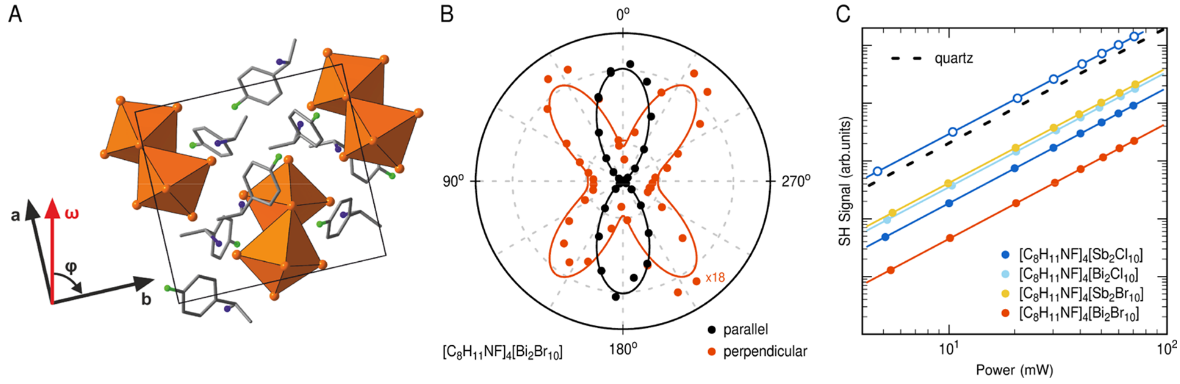

Figure 5. (A) Top view of the crystal structure of **1** for the *ab*-plane perpendicular to the *c*-axis. The rotation angle $\varphi = 0°$ corresponds to an orientation where the vertical s-polarization of the 800 nm fundamental (ω, red arrow) is parallel to the *b*-direction. (B) Polar plot of the SH intensity of material **5** as a function of the crystal's azimuth angle φ. The SH radiation components parallel (black) and perpendicular (red) to the polarization of the fundamental field are shown. Symbols and solid lines represent the experimental data and the corresponding theoretical fits, respectively. (C) SH signal vs applied laser power for compounds **1**, **2**, **4**, and **5** in comparison to a quartz reference. Linear fits (lines) reveal the quadratic power dependence of the measured SH response from a set of thin samples of different materials (filled dots). A much thicker sample of compound **1** exhibits a significantly stronger SH signal (blue circles).

onset. In contrast, there is a more significant red-shift going from Sb to Bi for the iodido metalates **3** and **6** in line with a large difference in band gaps of the parent halides SbI_3 (2.2 eV)[73] and BiI_3 (1.7 eV).[74] Overall, this series provides the first data on the absorption properties of an isomorphous family of halogenido antimonates and bismuthates that do not feature a counterion with large influence on absorption, similar to the recently reported series of tropylium compounds.[75] While the trends we observe here may not be so surprising, we want to highlight that despite the great recent interest in iodido bismuthates like $(CH_3NH_3)_3[Bi_2I_9]$, data on optical properties of these materials remain conflicting,[40,76] and a series of compounds prepared and measured under the same conditions allow for an easy comparison and provide a solid reference point for future work. Overall, the onset of absorption in this family of compounds can be varied between 3.35 eV for **1** and 2.09 eV for **6** (see also Table S9) allowing for facile adaptation to potential applications.

Stability. All six compounds are stable against air and moisture. After several weeks in air, the crystals' surfaces change from clear and smooth to more brittle, indicating degradation on the surface level. They decompose completely over a two-step thermal degradation process, starting between 190 and 250 °C, with the bismuthates being more stable than the antimonates (see Figure S19−S24 for details). The lack of residual mass in TGA measurements suggests a concomitant sublimation of EX_3 and [(*R*)-1-(4-F)PEA]X and the possibility to deposit the compounds, for example, via pulsed laser deposition in future experiments, similar to methods applied in 2D lead halide perovskite materials.[77] The compounds are also quite stable against laser damage, as we show below, with the exception of **6**, which displayed oscillating SHG signals under continuous laser irradiation, indicating at least some surface level damage.

Nonlinear Optical Properties. Second-order nonlinear processes such as SHG originate from a noncentrosymmetric crystal structure.[78] Because the compounds **1**−**6** share a monoclinic space group ($P2_1$), their nonlinear optical properties are investigated for 800 nm femtosecond laser excitation. All compounds **1**−**6** show efficient SHG with the expected quadratic dependence of the emitted 400 nm SH light on the applied laser power. The rotational anisotropy of the SH intensity is measured by rotating the sample around the *c*-axis, as characterized by the azimuthal angle φ for selected input and output polarizations (cf. Figure 5A). As shown in Figure 5B, the strongest SH response is observed for s-polarized input and s-polarized output polarization ("parallel", black data points) at 0° azimuth angle. See Supporting Information for additional data and more details on the optical setup.

The polarization-dependent rotational anisotropy of compounds **1**, **2**, **4**, and **5** agree quite well with the expected anisotropies for $P2_1$ space group materials, as illustrated in Figure 5B for compound **5**. Materials **3** and **6**, however, deviate considerably from the expected anisotropies, probably because of inhomogeneity within these crystals or instability caused by laser damage, as observed for **6**. Therefore, it is not possible to determine the SH response of **3** and **6** at a defined azimuth angle for direct comparison of the SHG efficiency of different compounds. Figure 5C shows the SH signal of compounds **1**, **2**, **4**, and **5** relative to each other and with respect to the quartz (α-SiO_2) reference depending on the applied laser power. A set of samples with a respective crystal thickness of 125 ± 20 μm (filled colored dots) exhibits a 5−45 times smaller SH signal compared to the quartz reference with the strongest signal obtained from material **2** followed by materials **4**, **1**, and **5**. Because compound **2** shows a pronounced absorption peak around 400 nm in the UV−vis spectra, the SH response could be affected by resonant enhancement. Additionally, absorption of SH light in some of the crystals has to be considered (see Figure 4).

A much higher SH intensity is observed for a comparatively thick sample (700 ± 50 μm) of compound **1** (see the empty blue circles in Figure 5A). As it turns out, this sample yields a 15 times larger signal than the respective thin sample of compound **1**. This is in reasonable agreement with a quadratic dependence of the SH intensity on the crystal length for the case of perfect phase-matching in the undepleted-pump approximation.[78] Systematic measurements in dependence of the thickness of different crystals are necessary to explore this correlation in more detail. In addition, spectroscopic SHG measurements would be desirable, in particular, at longer excitation wavelengths, to investigate the possible effects of resonant enhancement as well as absorption of SH light in different compounds. Overall, the nonlinear optical properties of the presented halogenido metalates are in the range of (and can even exceed) the nonlinear properties of crystalline quartz, which makes this material class with its large variability particularly interesting for application in nonlinear optical devices.

■ CONCLUSIONS

Using a suitable chiral amine template, it is possible to create an isomorphous family of organic−inorganic metal halide materials. The aspect of chirality in the materials is combined with a pseudo-layered arrangement allowing for well-defined crystal cleavage and exfoliation. Through the variation of metal and halides, a wide range of onsets of absorption can be achieved. The materials' SHG capabilities compare well with established materials like quartz. Overall, the ease of synthesis, high stability, and high variability will allow a facile integration of linear and nonlinear optical devices in future work.

■ ASSOCIATED CONTENT

Supporting Information

The Supporting Information is available free of charge at https://pubs.acs.org/doi/10.1021/acs.chemmater.0c01605.

Powder patterns, FTIR spectra, thermal analysis data, UV−vis spectra, details on the SHG setup and SHG data (PDF)
Single crystal data of compound **1** (CIF)
Single crystal data of compound **2** (CIF)
Single crystal data of compound **3** (CIF)
Single crystal data of compound **4** (CIF)
Single crystal data of compound **5** (CIF)
Single crystal data of compound **6** (CIF)

Accession Codes

CCDC 1995570−1995575 contain the supplementary crystallographic data for this paper. These data can be obtained free of charge via www.ccdc.cam.ac.uk/data_request/cif, or by emailing data_request@ccdc.cam.ac.uk, or by contacting The Cambridge Crystallographic Data Centre, 12 Union Road, Cambridge CB2 1EZ, UK; fax: +44 1223 336033.

■ AUTHOR INFORMATION

Corresponding Authors

Johanna Heine − *Department of Chemistry and Material Sciences Center, Philipps-Universität Marburg, 35043 Marburg, Germany*; orcid.org/0000-0002-6795-5288; Email: johanna.heine@chemie.uni-marburg.de

Gerson Mette − *Department of Physics and Material Sciences Center, Philipps-Universität Marburg, 35032 Marburg, Germany*; orcid.org/0000-0001-7561-3264; Email: gerson.mette@physik.uni-marburg.de

Authors

Natalie Dehnhardt − *Department of Chemistry and Material Sciences Center, Philipps-Universität Marburg, 35043 Marburg, Germany*

Marleen Axt − *Department of Physics and Material Sciences Center, Philipps-Universität Marburg, 35032 Marburg, Germany*

Jonas Zimmermann − *Department of Physics and Material Sciences Center, Philipps-Universität Marburg, 35032 Marburg, Germany*

Meng Yang − *Department of Chemistry and Material Sciences Center, Philipps-Universität Marburg, 35043 Marburg, Germany*

Complete contact information is available at: https://pubs.acs.org/10.1021/acs.chemmater.0c01605

Author Contributions

The manuscript was written through contributions of all authors. All authors have given approval to the final version of the manuscript.

Notes

The authors declare no competing financial interest.

■ ACKNOWLEDGMENTS

We gratefully acknowledge funding by the Deutsche Forschungsgemeinschaft through the SFB 1083. J.H. thanks Prof. Stefanie Dehnen for her support. G.M. thanks Prof. Ulrich Höfer and Dr. Jens Güdde for their support. N.D. thanks the Fonds der Chemischen Industrie and the Studienstiftung des Deutschen Volkes for their support.

■ REFERENCES

(1) Stoumpos, C. C.; Kanatzidis, M. G. Halide Perovskites: Poor Man's High-Performance Semiconductors. *Adv. Mater.* **2016**, *28*, 5778−5793.

(2) Jena, A. K.; Kulkarni, A.; Miyasaka, T. Halide Perovskite Photovoltaics: Background, Status, and Future Prospects. *Chem. Rev.* **2019**, *119*, 3036−3103.

(3) Arend, H.; Huber, W.; Mischgofsky, F. H.; Richter-Van Leeuwen, G. K. Layer Perovskites of the $(C_nH_{2n+1}NH_3)_2MX_4$ and $NH_3(CH_2)_mNH_3MX_4$ Families with M = Cd, Cu, Fe, Mn or Pd and X = Cl or Br: Importance, Solubilities and Simple Growth Techniques. *J. Cryst. Growth* **1978**, *43*, 213−223.

(4) Nagapetyan, S. S.; Dolzhenko, Y. I.; Arakelova, E. R.; Koshkin, V. M.; Struchkov, Y. T.; Shklover, V. E. 33. Preparation, structure and properties of nonylammonium tetraiodoplumbate(II). *Zh. Neorg. Khim.* **1988**, *33*, 2806−2812.

(5) Calabrese, J.; Jones, N. L.; Harlow, R. L.; Herron, N.; Thorn, D. L.; Wang, Y. Preparation and Characterization of Layered Lead Halide Compounds. *J. Am. Chem. Soc.* **1991**, *113*, 2328−2330.

(6) Hong, X.; Ishihara, T.; Nurmikko, A. V. Dielectric Confinement Effect on Excitons in PbI_4-Based Layered Semiconductors. *Phys. Rev. B* **1992**, *45*, 6961−6964.

(7) Mitzi, D. B.; Feild, C. A.; Harrison, W. T. A.; Guloy, A. M. Conducting Tin Halides with a Layered Organic-Based Perovskite Structure. *Nature* **1994**, *369*, 467−469.

(8) Papavassiliou, G. C.; Koutselas, I. B.; Terzis, A.; Whangbo, M.-H. Structural and Electronic Properties of the Natural Quantum-Well System $(C_6H_5CH_2CH_2NH_3)_2SnI_4$. *Solid State Commun.* **1994**, *91*, 695−698.

(9) Era, M.; Morimoto, S.; Tsutsui, T.; Saito, S. Organicinorganic Heterostructure Electroluminescent Device Using a Layered Perovskite Semiconductor $(C_6H_5C_2H_4NH_3)_2PbI_4$. *Appl. Phys. Lett.* **1994**, *65*, 676−678.

(10) Kagan, C. R.; Mitzi, D. B.; Dimitrakopoulos, C. D. Organic-Inorganic Hybrid Materials as Semiconducting Channels in Thin-Film Field-Effect Transistors. *Science* **1999**, *286*, 945−947.

(11) Mao, L.; Stoumpos, C. C.; Kanatzidis, M. G. Two-Dimensional Hybrid Halide Perovskites: Principles and Promises. *J. Am. Chem. Soc.* **2019**, *141*, 1171−1190.

(12) Katan, C.; Mercier, N.; Even, J. Quantum and Dielectric Confinement Effects in Lower-Dimensional Hybrid Perovskite Semiconductors. *Chem. Rev.* **2019**, *119*, 3140−3192.

(13) Connor, B. A.; Leppert, L.; Smith, M. D.; Neaton, J. B.; Karunadasa, H. I. Layered Halide Double Perovskites: Dimensional Reduction of $Cs_2AgBiBr_6$. *J. Am. Chem. Soc.* **2018**, *140*, 5235−5240.

(14) Jana, M. K.; Janke, S. M.; Dirkes, D. J.; Dovletgeldi, S.; Liu, C.; Qin, X.; Gundogdu, K.; You, W.; Blum, V.; Mitzi, D. B. A Direct-Bandgap 2D Silver-Bismuth Iodide Double Perovskite: The Structure-Directing Influence of an Oligothiophene Spacer Cation. *J. Am. Chem. Soc.* **2019**, *141*, 7955−7964.

(15) Smith, M. D.; Karunadasa, H. I. White-Light Emission from Layered Halide Perovskites. *Acc. Chem. Res.* **2018**, *51*, 619−627.

(16) Cohen, B.-E.; Li, Y.; Meng, Q.; Etgar, L. Dion−Jacobson Two-Dimensional Perovskite Solar Cells Based on Benzene Dimethanammonium Cation. *Nano Lett.* **2019**, *19*, 2588−2597.

(17) Raghavan, C. M.; Chen, T.-P.; Li, S.-S.; Chen, W.-L.; Lo, C.-Y.; Liao, Y.-M.; Haider, G.; Lin, C.-C.; Chen, C.-C.; Sankar, R.; Chang, Y.-M.; Chou, F.-C.; Chen, C.-W. Low-Threshold Lasing from 2D Homologous Organic−Inorganic Hybrid Ruddlesden−Popper Perovskite Single Crystals. *Nano Lett.* **2018**, *18*, 3221−3228.

(18) Spanopoulos, I.; Hadar, I.; Ke, W.; Tu, Q.; Chen, M.; Tsai, H.; He, Y.; Shekhawat, G.; Dravid, V. P.; Wasielewski, M. R.; Mohite, A. D.; Stoumpos, C. C.; Kanatzidis, M. G. Uniaxial Expansion of the 2D Ruddlesden−Popper Perovskite Family for Improved Environmental Stability. *J. Am. Chem. Soc.* **2019**, *141*, 5518−5534.

(19) Smith, I. C.; Smith, M. D.; Jaffe, A.; Lin, Y.; Karunadasa, H. I. Between the Sheets: Postsynthetic Transformations in Hybrid Perovskites. *Chem. Mater.* **2017**, *29*, 1868−1884.

(20) Yang, S.; Wu, D.; Gong, W.; Huang, Q.; Zhen, H.; Ling, Q.; Lin, Z. Highly Efficient Room-Temperature Phosphorescence and Afterglow Luminescence from Common Organic fluorophores in 2D Hybrid Perovskites. *Chem. Sci.* **2018**, *9*, 8975−8981.

(21) Li, T.; Dunlap-Shohl, W. A.; Reinheimer, E. W.; Le Magueres, P.; Mitzi, D. B. Melting Temperature Suppression of Layered Hybrid Lead Halide Perovskites via Organic Ammonium Cation Branching. *Chem. Sci.* **2019**, *10*, 1168−1175.

(22) Goldschmidt, V. M. Die Gesetze der Krystallochemie. *Naturwissenschaften* **1926**, *14*, 477−485.

(23) Kieslich, G.; Sun, S.; Cheetham, A. K. Solid-state principles applied to organic−inorganic perovskites: new tricks for an old dog. *Chem. Sci.* **2014**, *5*, 4712−4715.

(24) Shi, E.; Gao, Y.; Finkenauer, B. P.; Akriti, A.; Coffey, A. H.; Dou, L. Two-dimensional halide perovskite nanomaterials and heterostructures. *Chem. Soc. Rev.* **2018**, *47*, 6046−6072.

(25) Dong, Y.; Zhang, Y.; Li, X.; Feng, Y.; Zhang, H.; Xu, J. Chiral Perovskites: Promising Materials toward Next-Generation Optoelectronics. *Small* **2019**, *15*, 1902237.

(26) Long, G.; Sabatini, R.; Saidaminov, M. I.; Lakhwani, G.; Rasmita, A.; Liu, X.; Sargent, E. H.; Gao, W. Chiral-perovskite optoelectronics. *Nat. Rev. Mater.* **2020**, DOI: 10.1038/s41578-020-0181-5.

(27) Chen, C.; Gao, L.; Gao, W.; Ge, C.; Du, X.; Li, Z.; Yang, Y.; Niu, G.; Tang, J. Circularly polarized light detection using chiral hybrid perovskite. *Nat. Commun.* **2019**, *10*, 1927.

(28) Ma, J.; Fang, C.; Chen, C.; Jin, L.; Wang, J.; Wang, S.; Tang, J.; Li, D. Chiral 2D Perovskites with a High Degree of Circularly Polarized Photoluminescence. *ACS Nano* **2019**, *13*, 3659−3665.

(29) Yang, C. K.; Chen, W. N.; Ding, Y. T.; Wang, J.; Rao, Y.; Liao, W. Q.; Tang, Y. Y.; Li, P. F.; Wang, Z. X.; Xiong, R. G. The First 2D Homochiral Lead Iodide Perovskite Ferroelectrics: [R- and S-1-(4-Chlorophenyl)ethylammonium]$_2$PbI$_4$. *Adv. Mater.* **2019**, *31*, 1808088.

(30) Long, G.; Jiang, C.; Sabatini, R.; Yang, Z.; Wei, M.; Quan, L. N.; Liang, Q.; Rasmita, A.; Askerka, M.; Walters, G.; Gong, X.; Xing, J.; Wen, X.; Quintero-Bermudez, R.; Yuan, H.; Xing, G.; Wang, X. R.; Song, D.; Voznyy, O.; Zhang, M.; Hoogland, S.; Gao, W.; Xiong, Q.; Sargent, E. H. Spin control in reduced-dimensional chiral perovskites. *Nat. Photon.* **2018**, *12*, 528−533.

(31) Babayigit, A.; Boyen, H.-G.; Conings, B. Environment versus sustainable energy: The case of lead halide perovskite-based solar cells. *MRS Energy Sustain.* **2018**, *5*, E1.

(32) Noel, N. K.; Stranks, S. D.; Abate, A.; Wehrenfennig, C.; Guarnera, S.; Haghighirad, A.-A.; Sadhanala, A.; Eperon, G. E.; Pathak, S. K.; Johnston, M. B.; Petrozza, A.; Herz, L. M.; Snaith, H. J. Lead-Free Organic−Inorganic Tin Halide Perovskites for Photovoltaic Applications. *Energy Environ. Sci.* **2014**, *7*, 3061−3068.

(33) Yang, N.; Sun, H. Biocoordination chemistry of bismuth: Recent advances. *Coord. Chem. Rev.* **2007**, *251*, 2354−2366.

(34) Mercier, N.; Louvain, N.; Bi, W. Structural Diversity and Retro-Crystal Engineering Analysis of Iodometalate Hybrids. *CrystEngComm* **2009**, *11*, 720−734.

(35) Wu, L.-M.; Wu, X.-T.; Chen, L. Structural Overview and Structure−Property Relationships of Iodoplumbate and Iodobismuthate. *Coord. Chem. Rev.* **2009**, *253*, 2787−2804.

(36) Adonin, S. A.; Sokolov, M. N.; Fedin, V. P. Polynuclear Halide Complexes of Bi(III): From Structural Diversity to the New Properties. *Coord. Chem. Rev.* **2016**, *312*, 1−21.

(37) Mitzi, D. B. Organic-Inorganic Perovskites Containing Trivalent Metal Halide Layers: The Templating Influence of the Organic Cation Layer. *Inorg. Chem.* **2000**, *39*, 6107−6113.

(38) Lehner, A. J.; Fabini, D. H.; Evans, H. A.; Hébert, C.-A.; Smock, S. R.; Hu, J.; Wang, H.; Zwanziger, J. W.; Chabinyc, M. L.; Seshadri, R. Crystal and Electronic Structures of Complex Bismuth Iodides $A_3Bi_2I_9$ (A = K, Rb, Cs) Related to Perovskite: Aiding the Rational Design of Photovoltaics. *Chem. Mater.* **2015**, *27*, 7137−7148.

(39) Chang, J.-H.; Doert, T.; Ruck, M. Structural Variety of Defect Perovskite Variants $M_3E_2X_9$ (M = Rb, Tl, E = Bi, Sb, X = Br, I). *Z. Anorg. Allg. Chem.* **2016**, *642*, 736−748.

(40) McCall, K. M.; Stoumpos, C. C.; Kostina, S. S.; Kanatzidis, M. G.; Wessels, B. W. Strong Electron−Phonon Coupling and Self-Trapped Excitons in the Defect Halide Perovskites $A_3M_2I_9$ (A = Cs, Rb; M = Bi, Sb). *Chem. Mater.* **2017**, *29*, 4129−4145.

(41) Wojciechowska, M.; Gągor, A.; Piecha-Bisiorek, A.; Jakubas, R.; Ciżman, A.; Zaręba, J. K.; Nyk, M.; Zieliński, P.; Medycki, W.; Bil, A. Ferroelectricity and Ferroelasticity in Organic Inorganic Hybrid (Pyrrolidinium)$_3$[Sb$_2$Cl$_9$]. *Chem. Mater.* **2018**, *30*, 4597−4608.

(42) Leng, M.; Chen, Z.; Yang, Y.; Li, Z.; Zeng, K.; Li, K.; Niu, G.; He, Y.; Zhou, Q.; Tang, J. Lead-Free, Blue Emitting Bismuth Halide Perovskite Quantum Dots. *Angew. Chem., Int. Ed.* **2016**, *55*, 15012−15016.

(43) Li, M.-Q.; Hu, Y.-Q.; Bi, L.-Y.; Zhang, H.-L.; Wang, Y.; Zheng, Y.-Z. Structure Tunable Organic−Inorganic Bismuth Halides for an Enhanced Two-Dimensional Lead-Free Light-Harvesting Material. *Chem. Mater.* **2017**, *29*, 5463−5467.

(44) Dehnhardt, N.; Luy, J.-N.; Szabo, M.; Wende, M.; Tonner, R.; Heine, J. Synthesis of a two-dimensional organic−inorganic bismuth iodide metalate through in situ formation of iminium cations. *Chem. Commun.* **2019**, *55*, 14725−14728.

(45) Boldish, S. I.; White, W. B. Optical band gaps of selected ternary sulfide minerals. *Am. Mineral.* **1998**, *83*, 865−871.

(46) Sheldrick, G. M. Short History of SHELX. *Acta Crystallogr., Sect. A: Found. Crystallogr.* **2008**, *64*, 112−122.

(47) Sheldrick, G. M. SHELXT − Integrated Space-Group and Crystal-Structure Determination. *Acta Crystallogr., Sect. A: Found. Adv.* **2015**, *71*, 3−8.

(48) Sheldrick, G. M. Crystal Structure Refinement with SHELXL. *Acta Crystallogr., Sect. C: Struct. Chem.* **2015**, *71*, 3−8.

(49) Dolomanov, O. V.; Bourhis, L. J.; Gildea, R. J.; Howard, J. A. K.; Puschmann, H. OLEX2: A Complete Structure Solution, Refinement and Analysis Program. *J. Appl. Crystallogr.* **2009**, *42*, 339−341.

(50) Brandenburg, K. *Diamond*; Crystal Impact GbR: Bonn, Germany, 2005.

(51) Särnstrand, C. The Crystal Structure of Antimony(III) Chloride Oxide $Sb_4O_5Cl_2$. *Acta Crystallogr., Sect. B: Struct. Crystallogr. Cryst. Chem.* **1978**, *34*, 2402−2407.

(52) Wang, K.; Wu, C.; Yang, D.; Jiang, Y.; Priya, S. Quasi-Two-Dimensional Halide Perovskite Single Crystal Photodetector. *ACS Nano* **2018**, *12*, 4919−4929.

(53) Zarychta, B.; Bujak, M.; Zaleski, J. Distortions of $[Sb_2Cl_{10}]^{4-}$ Bioctahedra and Phase Transitions in the Chloroantimonate(III) $(C_3H_5NH_3)_2[SbCl_5] \cdot (C_3H_5NH_3)Cl$. *Z. Naturforsch., B: Chem. Sci.* **2007**, *62*, 44−50.

(54) Terao, H.; Ninomiya, S.; Hashimoto, M.; Eda, K. ^{81}Br NQR and crystal structure of 4-bromopyridinium pentabromoantimonate(III); 3c−4e bonding and NQR trans influence. *J. Mol. Struct.* **2010**, *965*, 68−73.

(55) Bukvetskii, B. V.; Storozhuk, T. V.; Mirochnik, A. G.; Petrochenkova, N. V.; Karasev, V. E. Synthesis, Crystal Structure, and Luminescent Properties of Antimony(III) Halide Complexes with 6-Methylquinoline. *Russ. J. Inorg. Chem.* **2004**, *49*, 43−50.

(56) García-Fernández, A.; Marcos-Cives, I.; Platas-Iglesias, C.; Castro-García, S.; Vázquez-García, D.; Fernández, A.; Sánchez-Andújar, M. Diimidazolium Halobismuthates $[Dim]_2[Bi_2X_{10}]$ (X = Cl^-, Br^-, or I^-): A New Class of Thermochromic and Photoluminescent Materials. *Inorg. Chem.* **2018**, *57*, 7655−7664.

(57) Mitzi, D. B. Synthesis, Crystal Structure, and Optical and Thermal Properties of $(C_4H_9NH_3)_2MI_4$ (M = Ge, Sn, Pb). *Chem. Mater.* **1996**, *8*, 791−800.

(58) Mousdis, G. A.; Papavassiliou, G. C.; Raptopoulou, C. P.; Terzis, A. Preparation and characterization of $[H_3N(CH_2)_6NH_3]PbI_4$ and similar compounds with a layered perovskite structure. *J. Mater. Chem.* **2000**, *10*, 515−518.

(59) Zarychta, B.; Zaleski, J. Phase Transitions Mechanism and Distortion of $SbCl_6^{3-}$ Octahedra in Bis(n-butylammonium) Pentachloroantimonate(III) $(C_4H_9NH_3)_2[SbCl_5]$. *Z. Naturforsch., B: Chem. Sci.* **2006**, *61*, 1101−1109.

(60) Jha, N. K.; Rizvi, S. S. A. Some studies on bromoantimonate(III) complexes. *J. Inorg. Nucl. Chem.* **1974**, *36*, 1479−1489.

(61) Mousdis, G. A.; Papavassiliou, G. C.; Terzis, A.; Raptopoulou, C. P. Preparation, Structures and Optical Properties of $[H_3N(CH_2)_6NH_3]BiX_5$ (X=I, Cl) and $[H_3N(CH_2)_6NH_3]SbX_5$ (X=I, Br). *Z. Naturforsch., B: Chem. Sci.* **1998**, *53*, 927−932.

(62) Steiner, T. Hydrogen-Bond Distances to Halide Ions in Organic and Organometallic Crystal Structures: Up-to-date Database Study. *Acta Crystallogr., Sect. B: Struct. Sci.* **1998**, *54*, 456−463.

(63) Alvarez, S. A cartography of the van der Waals territories. *Dalton Trans.* **2013**, *42*, 8617−8636.

(64) Anyfantis, G. C.; Ganotopoulos, N.-M.; Savvidou, A.; Raptopoulou, C. P.; Psycharis, V.; Mousdis, G. A. Synthesis and characterization of new organic−inorganic hybrid compounds based on Sb, with a perovskite like structure. *Polyhedron* **2018**, *151*, 299−305.

(65) Moon, T. H.; Oh, S.-J.; Ok, K. M. $[((R)\text{-}C_8H_{12}N)_4][Bi_2Br_{10}]$ and $[((S)\text{-}C_8H_{12}N)_4][Bi_2Br_{10}]$: Chiral Hybrid Bismuth Bromides Templated by Chiral Organic Cations. *ACS Omega* **2018**, *3*, 17895−17903.

(66) Billing, D. G.; Lemmerer, A. Synthesis and crystal structures of inorganic−organic hybrids incorporating an aromatic amine with a chiral functional group. *CrystEngComm* **2006**, *8*, 686−695.

(67) Mercier, N.; Barres, A.-L.; Giffard, M.; Rau, I.; Kajzar, F.; Sahraoui, B. Conglomerate- to- true- racemate reversible solid- state transition in crystals of an organic disulfide- based iodoplumbate. *Angew. Chem., Int. Ed.* **2006**, *45*, 2100−2103.

(68) Bi, W.; Mercier, N. Reversible dynamic isomerism change in the solid state, from Bi_4I_{16} clusters to BiI_4 1D chains in L-cystine based hybrids: templating effect of cations in iodobismuthate network formation. *Chem. Commun.* **2008**, 5743−5745.

(69) Peng, Y.; Yao, Y.; Li, L.; Wu, Z.; Wang, S.; Luo, J. White-light emission in a chiral one-dimensional organic−inorganic hybrid perovskite. *J. Mater. Chem. C* **2018**, *6*, 6033−6037.

(70) Zhu, L.-L.; Huang, Y.-E.; Lin, Y.-P.; Huang, X.-Y.; Liu, H.-Q.; Mitzi, D. B.; Du, K.-Z. Stereochemically active lead chloride enantiomers mediated by homochiral organic cation. *Polyhedron* **2019**, *158*, 445−448.

(71) Salah, M. B. H.; Mercier, N.; Allain, M.; Zouari, N.; Botta, C. Dual phosphorescence from the organic andinorganic moieties of 1D hybrid perovskites of the $Pb_{n'}Br_{4n'+2}$ series (n'=2,3,4,5). *J. Mater. Chem. C* **2019**, *7*, 4424−4433.

(72) Wang, L.; Xue, Y.; Cui, M.; Huang, Y.; Xu, H.; Qin, C.; Yang, J.; Dai, H.; Yuan, M. A Chiral Reduced-Dimension Perovskite for an Efficient Flexible Circularly Polarized Light Photodetector. *Angew. Chem., Int. Ed.* **2020**, *59*, 6442−6450.

(73) Mady, K. A.; Eid, A. H.; Soliman, W. Z. Optical Properties and Interband Transitions in the Layered Compounds SbI_3. *Czech J. Phys.* **1979**, *29*, 907−912.

(74) Podraza, N. J.; Qiu, W.; Hinojosa, B. B.; Motyka, M. A.; Phillpot, S. R.; Baciak, J. E.; Trolier-McKinstry, S.; Nino, J. C.; Nino, J. C. Band gap and structure of single crystal BiI_3: Resolving discrepancies in literature. *J. Appl. Phys.* **2013**, *114*, 033110.

(75) Oswald, I. W. H.; Mozur, E. M.; Moseley, I. P.; Ahn, H.; Neilson, J. R. Hybrid Charge-Transfer Semiconductors: $(C_7H_7)SbI_4$, $(C_7H_7)BiI_4$, and Their Halide Congeners. *Inorg. Chem.* **2019**, *58*, 5818−5826.

(76) Abulikemu, M.; Ould-Chikh, S.; Miao, X.; Alarousu, E.; Murali, B.; Ngongang Ndjawa, G. O.; Barbé, J.; El Labban, A.; Amassian, A.; Del Gobbo, S. Optoelectronic and photovoltaic properties of the air-stable organohalide semiconductor $(CH_3NH_3)_3Bi_2I_9$. *J. Mater. Chem. A* **2016**, *4*, 12504−12515.

(77) Dunlap-Shohl, W. A.; Zhou, Y.; Padture, N. P.; Mitzi, D. B. Synthetic Approaches for Halide Perovskite Thin Films. *Chem. Rev.* **2019**, *119*, 3193−3295.

(78) Shen, Y. R. *The Principles of Nonlinear Optics*; Wiley & Sons: New Jersey, 2003.

Zusammenfassung 4

4.1. Zusammenfassung in deutscher Sprache

Im Rahmen dieser Doktorarbeit habe ich mich mit der Synthese neuer Halogenidometallate der Elemente Antimon und Bismut beschäftigt. Neben der grundlegenden Erforschung der Verbindungsklasse im Bezug auf Strukturvielfalt und Synthesemethoden untersuchte ich, welche Faktoren die optoelektronischen Eigenschaften beeinflussen. Des Weiteren entwickelte ich ein Konzept um Halogenidoantimonate und -bismutate als 2D-Materialien zugänglich zu machen. Hierbei gliederten sich die Untersuchungen in zwei Teilprojekte.

Im ersten Teilprojekt wurde der Einfluss von Übergangsmetallkationen auf die optoelektronischen Eigenschaften von Halogenidopentelaten untersucht. Da zu Beginn der Untersuchungen nur wenige ternäre Verbindungen bekannt waren, war ein weiteres Ziel die Erweiterung der Substanzklasse. Für diese Untersuchungen wurden große und gering geladene organische Kationen gewählt, deren positive Ladung durch die sterisch anspruchsvollen organischen Reste gut abgeschirmt ist. Durch Umsetzungen in organischen Lösungsmitteln konnten auf diesem Weg die Verbindungen der unter Abschnitt 3.1 bis 3.4 diskutierten Veröffentlichungen erhalten werden.

Die Umsetzung von Antimontriiodid und Kupfer-(I)-iodid in Acetonitril lieferte anders als erwartet keine ternäre Verbindung vom Typ $[Cu(MeCN)_4]_2[E_2Cu_2I_{10}]$, wie von *Chen* für E = Bi beobachtet wurde, sonder vier transiente Iodidoantimonate, jedes davon mit einem neuen Anionenmotiv. Die Ergebnisse zeigen, dass auch die binären Metallate noch nicht erschöpfend untersucht wurden und unterstreichen die Bedeutung der Kristallisationszeit auf die Bildung verschiedener Spezies.

Unter Zugabe von Phosphoniumsalzen konnte eine Reihe neuer Verbindungen erhalten werden, darunter das erste Iodidoantimonat und das erste Bromidobismutat mit einem ternären Anion. Ich konnte zeigen, dass das Einführen von Cuprat-Einheiten in Iodidobismutaten eine Veränderung der Absorptionseigenschaften hervorruft. Es kommt zu einer Rotverschiebung der Absorptionskante, welche auch für die leichteren Bromidobismutate beobachtet werden kann. Ersetzt man in der Synthese Bismuttriiodid durch Antimontriiodid kann allerdings keine Rotverschiebung der Absorptionseigenschaften beobachtet werden. Es wurden auch Synthesen mit Metallen der Platingruppe durchgeführt. Diese resultierten jedoch lediglich in der Darstellung binärer Palladate und Platinate.

Durch Umsetzung von Bismuttriiodid und Dimethylammoniumiodid in Aceton konnte ein Iodidobismutat mit einem seltenen neuen Anion mit Schichtstruktur erhalten werden. Hierbei kam es zu einer *in-situ* Kondensation des Ammoniumkations mit dem Lösungsmittel Aceton, wodurch Iminiumkationen gebildet wurden. Die Kationen ordnen sich zwischen den anorganischen Schichten an, wobei zwischen den Schichten sehr kurze Iod−Iod-Wechselwirkungen unter 4 Å zu finden sind. Über quantenchemische Rechnungen konnte gezeigt werden, dass diese kurzen Iod−Iod-Abstände zu einer Rotverschiebung der Absorptionseigenschaften und somit zu einer ungewöhnlich kleinen Bandlücke von 1,87 eV führen. Die Verbindung sublimiert bei 260 °C und ist stabil gegenüber Wasser und Sauerstoff. Die Kombination dieser Eigenschaften liefert die Grundlage für eine potentielle Anwendung als neues Halbleitermaterial.

Im zweiten Teilprojekt habe ich die Eignung von Halogenidopentelaten als neue 2D-Materialien untersucht. Um eine Anwendung in der Halbleitertechnik zu ermöglichen, ist es notwendig die Verbindungen als Dünnfilme oder exfolierbare Nanosheets darzustellen. Klassische 2D-Materialien wie Graphit weisen Schichtstrukturen mit kovalenten Bindungen in einer Ebene auf. Solche Strukturmotive sind, wie oben erwähnt, nur sehr selten in Halogenidopentelaten zu finden.

Um trotzdem exfolierbare Materialien darzustellen, habe ich eine Syntheseroute entwickelt, die eine Darstellung exfolierbarer Halogenidopentelate ohne kovalent gebundene Schichtstruktur ermöglichte. Hierfür kamen verschiedene Benzylamin-Derivate zum Einsatz. Durch Umsetzung in Halogenwasserstoffsäuren werden *in-situ* Benzylammoniumkationen gebildet, die sich auf Grund ihres amphiphilen Charakters entlang einer Ebene anordnen können. Hierbei ordnen sich die polaren Ammoniumkopfgruppen in Richtung der anorganischen Anionen, welche meist ein- oder zweikernig sind, aus und zwingen diese ebenfalls zu einer Anordnung entlang dieser Ebene. Es werden ladungsneutrale Schichten erhalten, die auf Grund der schwachen *Van-der-Waals*-Wechselwirkungen untereinander gespalten werden können.

Erfolgreiche Exfoliationsexperimente an dem Chloridobismutat $[BzA]_3[BiCl_5]Cl$ zeigten, dass die Verbindung trotz fehlender kovalenter Wechselwirkungen innerhalb der Schichten spaltbar ist, und bestätigten die Eignung der Verbindungsklasse als 2D-Material.

Ausgehend von diesen Ergebnissen modifizierte ich das Reaktionssystem, um eine zusätzliche Funktionalität in die Hybridverbindungen einzubringen. Hierfür wurden eine Reihe chiraler Amine getestet, von denen sich (R)-(1)-(4-F)PEA als besonders geeignet herausstellte. Die erhaltenen Halogenidopentelate können ebenfalls entlang einer Ebene gespalten werden, zeigen je nach Elementkombination Absorptionskanten zwischen 3,35 eV und 2,09 eV und, induziert durch das chirale Kation, Frequenzverdopplung. Kombiniert mit einer guten Stabilität sind sie besonders im Hinblick auf eine Anwendung in der nichtlinearen Optik interessant. Die erhaltenen Ergebnisse sind in Abbildung 4.1 nochmals grafisch zusammengefasst.

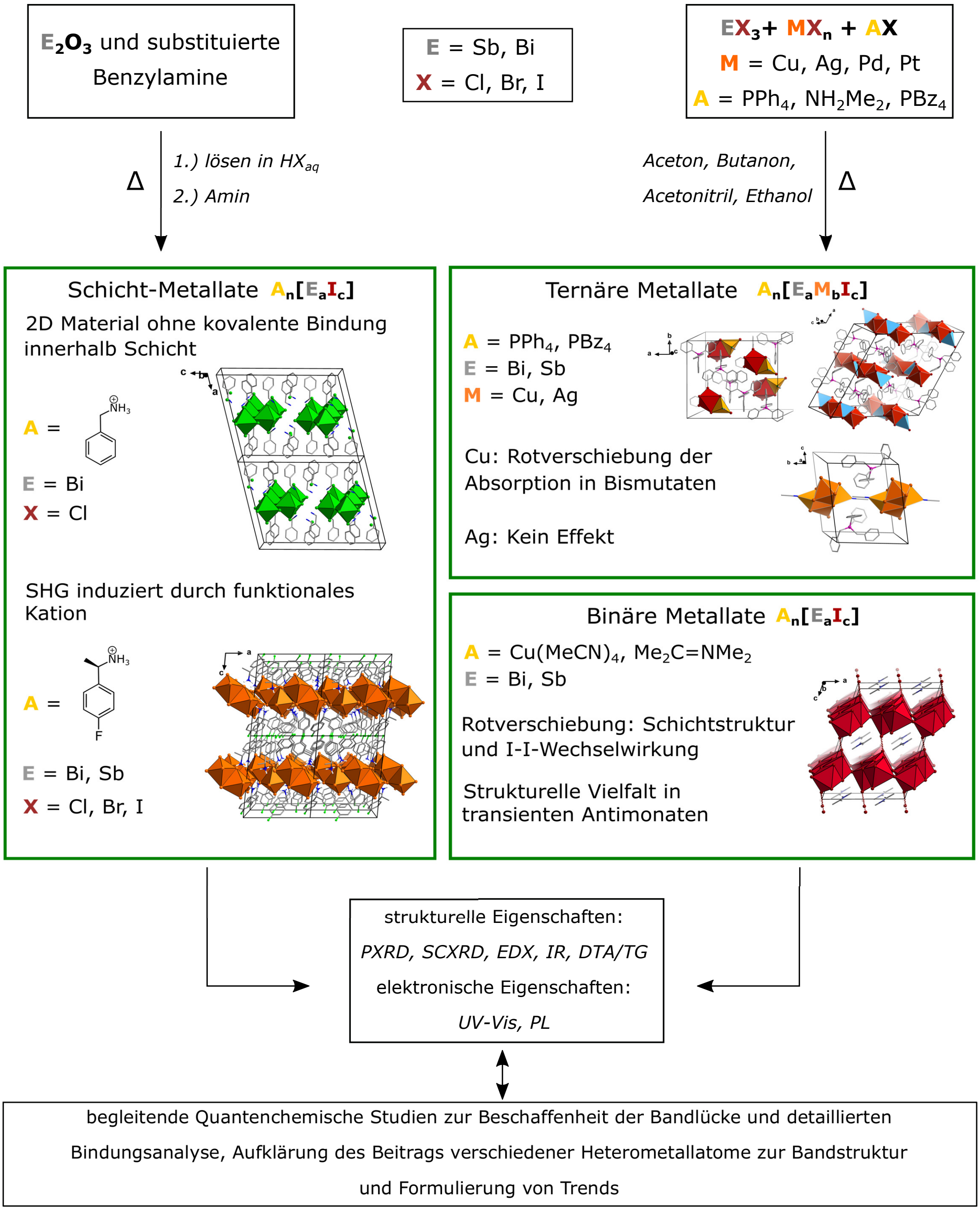

Abbildung 4.1: Übersicht der in dieser Arbeit durchgeführten Experimente und ihrer Ergebnisse.

4.2. English Summary

In this doctoral thesis I investigated the synthesis of new halogenidometalates of the elements antimony and bismuth. In addition to the basic research of the compound class in terms of structural diversity and synthetic methods, I tried to elucidate the factors influencing the optoelectronic properties. Furthermore, I developed a concept to make halogenidoantimonates and -bismuthates accessible as 2D-materials. The investigations were divided into two subprojects.

In the first subproject, the influence of transition metal cations on the optoelectronic properties of halogenido antimonates was investigated. Since only a few ternary compounds were known at the beginning of the investigations, a further aim was to produce additional members of the substance class. For these investigations large organic cations were chosen, whose positive charge is well shielded by sterically demanding organic residues. In this way, the compounds of the publications discussed in sections 3.1 to 3.4 could be obtained by reactions in organic solvents. The reaction of antimony triiodide and copper-(I)-iodide in acetonitrile did not yield a ternary compound of the type $[Cu(MeCN)_4]_2[E_2Cu_2I_{10}]$ as observed by *Chen* for E = Bi, but four transient iodidoantimonates, each of them with a new anion motif. The results show that the binary metalates have not been exhaustively investigated and underline the importance of the crystallization time for the formation of different species.

With the addition of phosphonium salts, a number of new compounds could be obtained, including the first iodidoantimonate and the first bromidobismuthate with a ternary anion. I was able to show that the introduction of cuprate units in iodidobismutates results in a change of the absoption properties. A red shift of the onset of absorption is observed. These results are also found for the lighter bromidobismuthates. However, if bismuth triiodide is replaced by antimony triiodide in the synthesis, no redshift of the absorption properties can be observed. Syntheses with metals of the platinum group were also carried out. However, these only resulted in the crystallization of binary palladates and platinates.

By dissolving bismuth triiodide and dimethylammonium iodide in acetone an iodidobismutate with a rare new anion with a layered structure could be obtained. This resulted from an *in-situ* condensation of the ammonium cation with the solvent acetone, forming iminium cations. The cations arrange themselves between the inorganic layers, with very short iodine−iodine interactions between the layers under 4 Å. Quantum chemical calculations have shown that these short iodine−iodine distances lead to a red shift in the absorption properties and thus to an unusually low band gap of 1.87 eV. The compound sublimates at 260 °C and is stable against water and oxygen. The combination of these properties provides the basis for a potential application as a new semiconductor material.

In the second subproject I investigated the suitability of halogenido penetelates as new 2D materials. To enable an application in semiconductor technology it is necessary to obtain the compounds as thin films or exfoliable nanosheets. Classical 2D-materials like graphite show layered structures with covalent bonds in one plane. Such structural motifs are, as mentioned above, only rarely found in halogenido penetelates. In order to obtain exfoliable materials nevertheless, I have developed a synthesis route which allows the synthesis of exfoliable halogenido pentelates without covalently bonded layered structure. Various benzylamine derivatives were used for this purpose. By reaction in hydrohalic acids *in-situ* benzylammonium cations are formed, which are arranged along a plane due to their amphiphilic character. Here, the polar ammonium head groups arrange themselves in the direction of the inorganic anions, which are usually mono- or binuclear, and also force them to arrange themselves along this plane. Charge-neutral layers are obtained, which can be split due to the weak *Van-der-Waals* interactions.

Successful exfoliation experiments on a chlorido bismuthate, $[\mathrm{BzA}]_3[\mathrm{BiCl}_5]\mathrm{Cl}$, showed that the compound is cleavable despite the lack of covalent interactions within the layers and confirmed the suitability of the compound class as a 2D material.

Based on these results, I modified the reaction system to introduce additional functionality into the hybrid compounds. For this purpose a number of chiral amines were tested, of which (*R*)-(1)-(4-F)PEA proved to be particularly suitable. The obtained halogenido penetelates can also be cleaved along a plane, show absorption edges between 3.35 eV and 2.09 eV depending on the element combination and, induced by the chiral cation, frequency doubling. Combined with a good stability, they are interesting for an application in nonlinear optics. The obtained results are again graphically summarized in Figure 4.2.

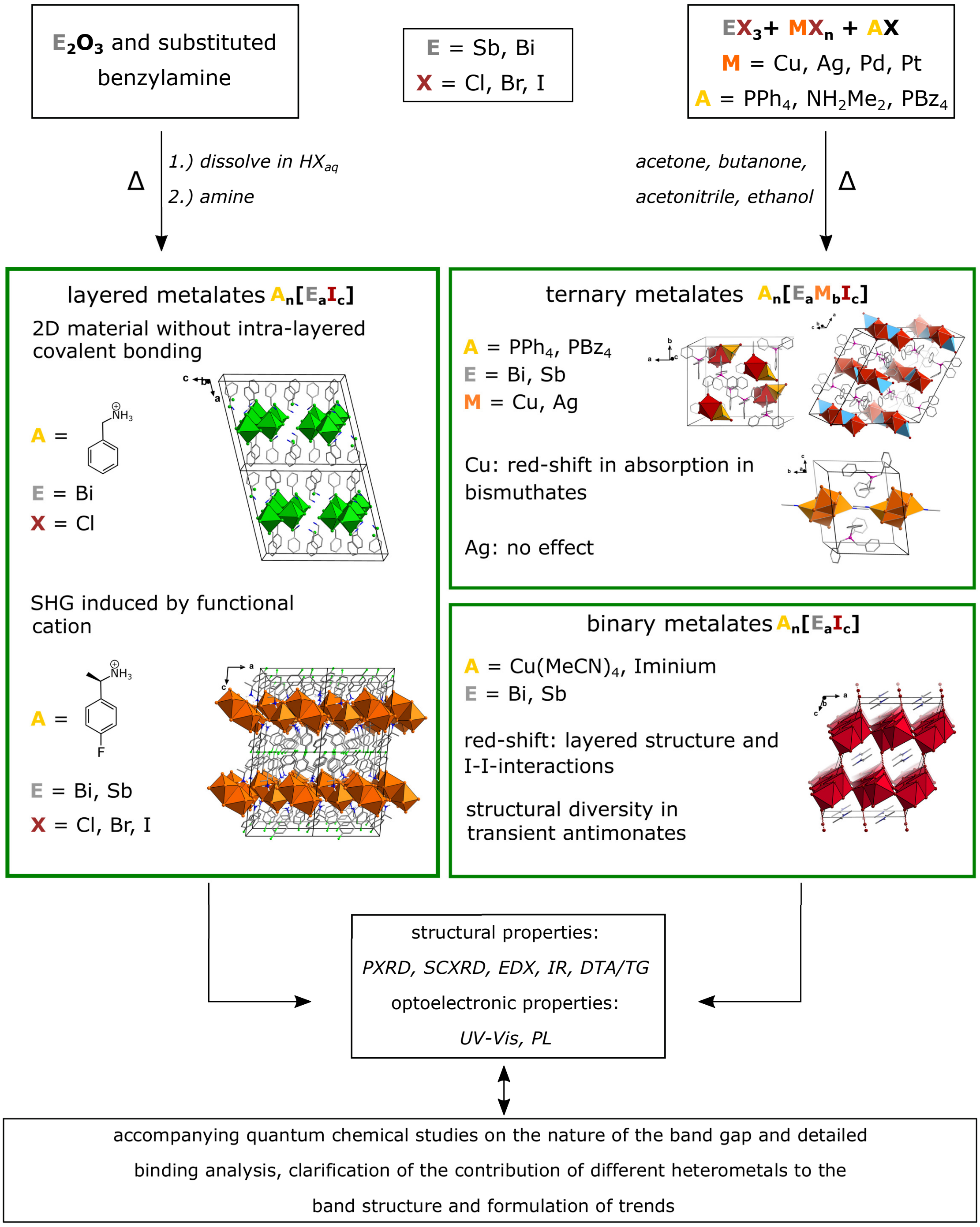

Abbildung 4.2: Overview of the different investigations and results of this thesis.

Literaturverzeichnis 5

[1] G. Hodes, *Science* **2013**, *342*, 317–318.

[2] M. A. Green, E. D. Dunlop, J. Hohl-Ebinger, M. Yoshita, N. Kopidakis, A. W. Ho-Baillie, *Progress in Photovoltaics: Research and Applications* **2020**, *28*(1), 3–15.

[3] A. Kojima, K. Teshima, Y. Shirai, T. Miyasaka, *Journal of the American Chemical Society* **2009**, *131*, 6050–6051.

[4] M. M. Lee, J. Teuscher, T. Miyasaka, T. N. Musakami, H. J. Snaith, *Science* **2012**, *338*, 643 – 647.

[5] Z. Shi, J. Guo, Y. Chen, Q. Li, Y. Pan, H. Zhang, Y. Xia, W. Huang, *Advanced Materials* **2017**, *29*.

[6] A. R. Chakhmouradian, P. M. Woodward, *Physics and Chemistry of Minerals* **2014**, *41*(6), 387–391.

[7] A. K. Jena, A. Kulkarni, T. Miyasaka, *Chemical Reviews* **2019**, *119*(5), 3036–3103.

[8] H. L. Wells, *Zeitschrift für anorganische Chemie* **1893**, *3*(1), 195–210.

[9] D. Weber, *Zeitschrift für Naturforschung* **1978**, *33b*, 1443–1445.

[10] C. K. Møller, *Nature* **1958**, *182*, 1436.

[11] U. Müller, *Anorganische Strukturchemie*, Bd. 6. Auflage, Vieweg + Teubner, **2008**.

[12] T. Barth, E. Posnjak, *Zeitschrift für Kristallographie* **1934**, *88*, 265–270.

[13] A. Hoffmann, *Zeitschrift für Physikalische Chemie* **1935**, *28B*(1), 65 – 77.

[14] Y. Takeda, F. Kanamura, M. Shimada, M. Koizumi, *Acta Crystallographica Section B* **1976**, *32*(8), 2464–2466.

[15] Q. A. Akkerman, L. Manna, *ACS Energy Letters* **2020**, *5*(2), 604–610.

[16] M. E. Kamminga, H. H. Fang, M. R. Filip, F. Giustino, J. Baas, G. R. Blake, M. A. Loi, T. T. Palstra, *Chemistry of Materials* **2016**, *28*(13), 4554–4562.

[17] J. M. Hoffman, X. Che, S. Sidhik, X. Li, I. Hadar, J. C. Blancon, H. Yamaguchi, M. Kepenekian, C. Katan, J. Even, C. C. Stoumpos, A. D. Mohite, M. G. Kanatzidis, *Journal of the American Chemical Society* **2019**, *141*(27), 10661–10676.

[18] N. Mercier, *Angewandte Chemie - International Edition* **2019**, *58*(50), 17912–17917.

[19] S. Geller, *The Journal of Chemical Physics* **1956**, *24*(6), 1236–1239.

[20] L. R. Moras, *Journal of Inorganic and Nuclear Chemistry* **1974**, *36*(12), 3876 – 3878.

[21] N. Sakai, A. A. Haghighirad, M. R. Filip, P. K. Nayak, S. Nayak, A. Ramadan, Z. Wang, F. Giustino, H. J. Snaith, *Journal of the American Chemical Society* **2017**, *139*(17), 6030–6033.

[22] D. Ho, W. C. Riley, R. A. Jacobson, *Crystal Structure Communications* **1978**, *7*, 111–114.

[23] M. Dion, M. Ganne, M. Tournoux, *Materials Research Bulletin* **1981**, *16*(11), 1429–1435.

[24] R. E. Schaak, T. E. Mallouk, *Chemistry of Materials* **2002**, *14*(4), 1455–1471.

[25] S. N. Ruddlesden, P. Popper, *Acta Crystallographica* **1958**, *11*(1), 54–55.

[26] J. Choi, X. Zhang, J. B. Wiley, *Inorganic Chemistry* **2009**, *48*(11), 4811–4816.

[27] X. Gu, G. Zhou, K. Gao, J. Peng, W. Wang, F. Zhang, X. Wu, *Journal of the American Ceramic Society* **2016**, *99*(6), 2024–2028.

[28] D. B. Mitzi, *Journal of the Chemical Society, Dalton Transactions* **2001**, (1), 1–12.

[29] D. B. Mitzi, *Chemical Reviews* **2019**, *119*(5), 3033–3035.

[30] P. Judeinstein, C. Sanchez, *Journal of Materials Chemistry* **1996**, *6*(4), 511–525.

[31] B. Saparov, D. B. Mitzi, *Chemical Reviews* **2016**, *116*(7), 4558–4596.

[32] G. Xu, G. C. Guo, M. S. Wang, Z. J. Zhang, W. T. Chen, J. S. Huang, *Angewandte Chemie - International Edition* **2007**, *46*(18), 3249–3251.

[33] R. G. Lin, G. Xu, G. Lu, M. S. Wang, P. X. Li, G. C. Guo, *Inorganic Chemistry* **2014**, *53*(11), 5538–5545.

[34] W. Shockley, H. J. Queisser, *Journal of Applied Physics* **1961**, *32*(3), 510–519.

[35] A. M. Ganose, C. N. Savory, D. O. Scanlon, *Chemical Communications* **2017**, *53*(1), 20–44.

[36] W. J. Yin, T. Shi, Y. Yan, *Journal of Physical Chemistry C* **2015**, *119*(10), 5253–5264.

[37] B. Suarez, V. Gonzalez-Pedro, T. S. Ripolles, R. S. Sanchez, L. Otero, I. Mora-Sero, *Journal of Physical Chemistry Letters* **2014**, *5*(10), 1628–1635.

[38] H. Zhu, Y. Fu, F. Meng, X. Wu, Z. Gong, Q. Ding, M. V. Gustafsson, M. T. Trinh, S. Jin, X. Y. Zhu, *Nature Materials* **2015**, *14*(6), 636–642.

[39] X. Wang, K. Li, H. Xu, N. Ali, Y. Wang, Q. Shen, H. Wu, *Chemical Communications* **2020**, *56*, 7917–7920.

[40] M. V. Kovalenko, L. Protesescu, M. I. Bodnarchuk, *Science* **2017**, *358*(6364), 745–750.

[41] H. Wei, Y. Fang, P. Mulligan, W. Chuirazzi, H. H. Fang, C. Wang, B. R. Ecker, Y. Gao, M. A. Loi, L. Cao, J. Huang, *Nature Photonics* **2016**, *10*(5), 333–339.

[42] M. Xia, J. H. Yuan, G. Niu, X. Du, L. Yin, W. Pan, J. Luo, Z. Li, H. Zhao, K. H. Xue, X. Miao, J. Tang, *Advanced Functional Materials* **2020**, *30*(24), 2–9.

[43] A. M. Leguy, Y. Hu, M. Campoy-Quiles, M. I. Alonso, O. J. Weber, P. Azarhoosh, M. Van Schilfgaarde, M. T. Weller, T. Bein, J. Nelson, P. Docampo, P. R. Barnes, *Chemistry of Materials* **2015**, *27*(9), 3397–3407.

[44] N. Aristidou, I. Sanchez-Molina, T. Chotchuangchutchaval, M. Brown, L. Martinez, T. Rath, S. A. Haque, *Angewandte Chemie - International Edition* **2015**, *54*(28), 8208–8212.

[45] World Health Organization, „Preventing Disease Through Healthy Environments“ Technischer Bericht, **2010**.

[46] World Health Organization, „Exposure to Lead: A major public health concern (2019 revision)“ Technischer Bericht, **2019**.

[47] B. Hailegnaw, S. Kirmayer, E. Edri, G. Hodes, D. Cahen, *Journal of Physical Chemistry Letters* **2015**, *6*(9), 1543–1547.

[48] F. Giustino, H. J. Snaith, *ACS Energy Letters* **2016**, *1*(6), 1233–1240.

[49] S. F. Hoefler, G. Trimmel, T. Rath, *Monatshefte fur Chemie* **2017**, *148*, 795–826.

[50] N. K. Noel, S. D. Stranks, A. Abate, C. Wehrenfennig, S. Guarnera, A.-A. Haghighirad, A. Sadhanala, G. E. Eperon, S. K. Pathak, M. B. Johnston, A. Petrozza, L. M. Herz, H. J. Snaith, *Energy Environmental Science* **2014**, *7*, 3061–3068.

[51] T. Baikie, Y. Fang, J. M. Kadro, M. Schreyer, F. Wei, S. G. Mhaisalkar, M. Graetzel, T. J. White, *Journal of Materials Chemistry A* **2013**, *1*, 5628–5641.

[52] F. Hao, C. C. Stoumpos, D. H. Cao, R. P. H. Chang, M. G. Kanatzidis, *Nature Photonics* **2014**, *8*, 489.

[53] L. Dou, A. B. Wong, Y. Yu, M. Lai, N. Kornienko, S. W. Eaton, A. Fu, C. G. Bischak, J. Ma, T. Ding, N. S. Ginsberg, L. W. Wang, A. P. Alivisatos, P. Yang, *Science* **2015**, *349*(6255), 1518–1521.

[54] D. H. Cao, C. C. Stoumpos, T. Yokoyama, J. L. Logsdon, T. B. Song, O. K. Farha, M. R. Wasielewski, J. T. Hupp, M. G. Kanatzidis, *ACS Energy Letters* **2017**, *2*(5), 982–990.

[55] S. Sun, S. Tominaka, J. H. Lee, F. Xie, P. D. Bristowe, A. K. Cheetham, *APL Materials* **2016**, *4*(3).

[56] D. H. Fabini, J. G. Labram, A. J. Lehner, J. S. Bechtel, H. A. Evans, A. Van Der Ven, F. Wudl, M. L. Chabinyc, R. Seshadri, *Inorganic Chemistry* **2017**, *56*, 11–25.

[57] B.-W. Park, B. Philippe, X. Zhang, H. Rensmo, G. Boschloo, E. M. J. Johansson, *Advanced Materials* **2015**, *27*, 6806–6813.

[58] S. M. Jain, D. Phuyal, M. L. Davies, M. Li, B. Philippe, C. De Castro, Z. Qiu, J. Kim, T. Watson, W. C. Tsoi, O. Karis, H. Rensmo, G. Boschloo, T. Edvinsson, J. R. Durrant, *Nano Energy* **2018**, *49*, 614 – 624.

[59] M. Scholz, O. Flender, K. Oum, T. Lenzer, *Journal of Physical Chemistry C* **2017**, *121*, 12110–12116.

[60] F. Wei, Z. Deng, S. Sun, F. Zhang, D. M. Evans, G. Kieslich, S. Tominaka, M. A. Carpenter, J. Zhang, P. D. Bristowe, A. K. Cheetham, *Chemistry of Materials* **2017**, *29*, 1089–1094.

[61] B. A. Connor, L. Leppert, M. D. Smith, J. B. Neaton, H. I. Karunadasa, *Journal of the American Chemical Society* **2018**, *140*(15), 5235–5240.

[62] M. K. Jana, S. M. Janke, D. J. Dirkes, S. Dovletgeldi, C. Liu, X. Qin, K. Gundogdu, W. You, V. Blum, D. B. Mitzi, *Journal of the American Chemical Society* **2019**, *141*(19), 7955–7964.

[63] L. Y. Bi, Y. Q. Hu, M. Q. Li, T. L. Hu, H. L. Zhang, X. T. Yin, W. X. Que, M. S. Lassoued, Y. Z. Zheng, *Journal of Materials Chemistry A* **2019**, *7*(34), 19662–19667.

[64] T. Baikie, N. S. Barrow, Y. Fang, P. J. Keenan, P. R. Slater, R. O. Piltz, M. Gutmann, S. G. Mhaisalkar, T. J. White, *Journal of Materials Chemistry A* **2015**, *3*, 9298–9307.

[65] E. Greul, M. L. Petrus, A. Binek, P. Docampo, T. Bein, *Journal of Materials Chemistry A* **2017**, *5*, 19972–19981.

[66] G. Volonakis, M. R. Filip, A. A. Haghighirad, N. Sakai, B. Wenger, H. J. Snaith, F. Giustino, *Journal of Physical Chemistry Letters* **2016**, *7*, 1254–1259.

[67] Z. Xiao, K. Z. Du, W. Meng, D. B. Mitzi, Y. Yan, *Angewandte Chemie - International Edition* **2017**, *56*(40), 12107–12111.

[68] P. C. Harikesh, H. K. Mulmudi, B. Ghosh, T. W. Goh, Y. T. Teng, K. Thirumal, M. Lockrey, K. Weber, T. M. Koh, S. Li, S. Mhaisalkar, N. Mathews, *Chemistry of Materials* **2016**, *28*(20), 7496–7504.

[69] B. Saparov, F. Hong, J. P. Sun, H. S. Duan, W. Meng, S. Cameron, I. G. Hill, Y. Yan, D. B. Mitzi, *Chemistry of Materials* **2015**, *27*(16), 5622–5632.

[70] J. C. Hebig, I. Kühn, J. Flohre, T. Kirchartz, *ACS Energy Letters* **2016**, *1*(1), 309–314.

[71] B. W. Park, B. Philippe, X. Zhang, H. Rensmo, G. Boschloo, E. M. Johansson, *Advanced Materials* **2015**, *27*(43), 6806–6813.

[72] A. H. Slavney, L. Leppert, D. Bartesaghi, A. Gold-Parker, M. F. Toney, T. J. Savenije, J. B. Neaton, H. I. Karunadasa, *Journal of the American Chemical Society* **2017**, *139*, 5015–5018.

[73] K. Z. Du, W. Meng, X. Wang, Y. Yan, D. B. Mitzi, *Angewandte Chemie - International Edition* **2017**, *56*, 8158–8162.

[74] W. Bi, N. Leblanc, N. Mercier, P. Auban-Senzier, C. Pasquier, *Chemistry of Materials* **2009**, *21*, 4099–4101.

[75] D. B. Mitzi, *Chemistry of Materials* **2001**, *13*, 3283–3298.

[76] S. A. Veldhuis, P. P. Boix, N. Yantara, M. Li, T. C. Sum, N. Mathews, S. G. Mhaisalkar, *Advanced Materials* **2016**, *28*, 6804–6834.

[77] N. Mercier, N. Louvain, W. Bi, *CrystEngComm* **2009**, *11*, 720–734.

[78] A. F. Hollemann, N. Wiberg, *Lehrbuch der Anorganischen Chemie*, Bd. 102. Auflage, de Gruyter, **2007**, S. 314f, 323.

[79] S. Pohl, D. Haase, R. Lotz, W. Saak, *Zeitschrift für Naturforschung* **1988**, *43b*, 1033–1037.

[80] S. Pohl, R. Lotz, W. Saak, D. Haase, *Angewandte Chemie* **1989**, *101*(3), 355–357.

[81] S. Pohl, M. Peters, D. Haase, W. Saak, *Zeitschrift für Naturforschung* **1994**, *49b*, 741–746.

[82] G. A. Fisher, N. C. Norman, *Advances in Inorganic Chemistry* **1994**, *41*, 233.

[83] C. R. Groom, I. J. Bruno, M. P. Lightfoot, S. C. Ward, *Acta Crystallographica Section B* **2016**, *72*(2), 171–179.

[84] A. Piecha, G. Bator, R. Jakubas, *Journal of Physics: Condensed Matter* **2005**, *17*(41), L411–L417.

[85] F. Li, H.-D. Yin, J. Zhai, D.-Q. Wang, *Acta Crystallographica Section E* **2006**, *62*(6), m1387–m1389.

[86] A. Villinger, A. Schulz, *Angewandte Chemie International Edition* **2010**, *49*(43), 8017–8020.

[87] N. W. Alcock, M. Ravindran, G. R. Willey, *Journal of the Chemical Society, Chemical Communications* **1989**, 1063–1065.

[88] M. Owczarek, P. Szklarz, R. Jakubas, A. Miniewicz, *Dalton Transactions* **2012**, *41*(24), 7285–7294.

[89] S. Pohl, R. Lotz, D. Haase, W. Saak, *Zeitschrift für Naturforschung B* **1988**, *43*(9), 1144 – 1150.

[90] S. Pohl, R. Lotz, W. Saak, D. Haase, *Angewandte Chemie* **1989**, *101*(3), 355–357.

[91] N. Dehnhardt, H. Borkowski, J. Schepp, R. Tonner, J. Heine, *Inorganic Chemistry* **2018**, *57*(2).

[92] S. A. Adonin, M. N. Sokolov, A. I. Smolentsev, S. G. Kozlova, V. P. Fedin, *Journal of the Chemical Society. Dalton Transactions* **2013**, *42*(27), 9818–9821.

[93] M. W. Yuan, L. H. Li, L. Chen, *Zeitschrift fur Anorganische und Allgemeine Chemie* **2009**, *635*(11), 1645–1649.

[94] W.-X. Chai, L.-M. Wu, J.-Q. Li, L. Chen, *Inorganic Chemistry* **2007**, *46*, 8698–8704.

[95] O.-d. C. I. Chains, C. Feldmann, *Science* **2001**, (14), 818–819.

[96] W.-X. Chai, L.-M. Wu, J.-Q. Li, L. Chen, *Inorganic Chemistry* **2007**, *46*, 1042–1044.

[97] C. Feldmann, *Inorganic Chemistry* **2001**, *40*, 818–819.

[98] W. Bi, N. Mercier, *Chemical communications* **2008**, (44), 5743–5745.

[99] G. C. Papavassiliou, I. B. Koutselas, A. Terzis, C. P. Raptopoulou, *Zeitschrift für Naturforschung B* **1995**, *50*(10), 1566 – 1569.

Publikationsliste A

9. Philip Klement, Natalie Dehnhardt, Chuan-Ding Dong, Samuel Bayliff, Julius Winkler, Peter J. Klar, Stefan Schumacher, Sangam Chatterjee, and Johanna Heine „Enabling tailored 2D materials by introducing 1D organic-inorganic perovskites with supramolecular intra-layer interactions“, *Manuskript in Bearbeitung nach Peer-Review und Ablehnung in Nature Chemistry.**

8. Natalie Dehnhardt, Marleen Axt, Jonas Zimmermann, Meng Yang, Gerson Mette and Johanna Heine „Enforcing Non-Centrosymmetric, Layered Arrangements in Organic-Inorganic Metal Halide Materials“, *Chemistry of Materials* **2020**, *32*, 4801-4807.*

7. Natalie Dehnhardt, Chantsalmaa Berthold, Kevin Dollberg, Johanna Heine „Synthesis and crystal structures of two layered Cu(I) and Ag(I) iodidometalates“, *Zeitschrift für Kristallographie - Crystalline Materials* **2020**, *Manuskript angenommen.*

6. Natalie Dehnhardt, Hayden Paneth, Nikolas Hecht, Johanna Heine „Multinary Halogenido Bismuthates Beyond the Double Perovskite Motif“, *Inorganic Chemistry* **2020**, *59*, 6, 3394-3405.*

5. Natalie Dehnhardt, Jan-Niclas Luy, Marvin Szabo, Mirco Wende, Ralf Tonner, Johanna Heine „Synthesis of a two-dimensional organic–inorganic bismuth iodide metalate through in situ formation of iminium cations“, *Chemical Communications* **2019**, *55*, 14725-14728.*

4. Natalie Dehnhardt, Philip Klement, Sangam Chatterjee, Johanna Heine „Divergent Optical Properties in an Isomorphous Family of Multinary Iodido Pentelates“, *Inorganic Chemistry* **2019**, *58*, 10983-10990.*

3. Natalie Dehnhardt, André Böth, Johanna Heine „Discoveries on the Way to an Old Compound: Four Transient Iodido Antimonates“, *Dalton Transactions* **2019**, *48*, 5222-5229.*

2. Natalie Dehnhardt, Hendrik Borkowski, Johanna Schepp, Ralf Tonner, Johanna Heine „Ternary Iodido Bismuthates and the Special Role of Copper“, *Inorganic Chemistry* **2018**, *57*, 633-640.

1. Bettina Wagner, Natalie Dehnhardt, Martin Schmid, Benedikt P. Klein, Lukas Ruppenthal, Philipp Müller, Malte Zugermeier, J. Michael Gottfried, Sina Lippert, Marc-Uwe Halbich, Arash Rahimi-Iman, Johanna Heine „Color Change Effect in an Organic-Inorganic Hybrid Material Based on a Porphyrin Diacid“, *The Journal of Chemical Physics C* **2016**, *120*, 28363–28373.

Mit * gekennzeichnete Publikationen sind Teil dieser Dissertationsschrift.

B Lebenslauf

Zum Schutz personenbezogener Daten wurde der Lebenslauf aus der öffentlich zugänglichen Version dieser Dissertationsschrift entfernt.

The CV has been removed from the publically available version of this document for the protection of personal data.

Permissions for reprints of publications C

The publications which are part of this dissertation are presented in their original form. Permissions for reprint of the already published articles have been obtained from the publisher. For Chapter 3.5. and 3.6. special permission was not required.

Chapter 3.1.: Reproduced from:

Natalie Dehnhardt, André Böth, Johanna Heine „Discoveries on the Way to an Old Compound: Four Transient Iodido Antimonates“, *Dalton Transactions* **2019**, *48*, 5222-5229, DOI: 10.1039/C9DT00575G

with permission from the Royal Society of Chemistry.

Chapter 3.2.: Reprinted with permission from:

Natalie Dehnhardt, Philip Klement, Sangam Chatterjee, Johanna Heine „Divergent Optical Properties in an Isomorphous Family of Multinary Iodido Pentelates“, *Inorganic Chemistry* **2019**, *58*, 10983-10990, DOI: 10.1021/acs.inorgchem.9b01466.

Copyright 2019 American Chemical Society.

Chapter 3.3.: Reproduced from:

Natalie Dehnhardt, Jan-Niclas Luy, Marvin Szabo, Mirco Wende, Ralf Tonner, Johanna Heine „Synthesis of a two-dimensional organic–inorganic bismuth iodide metalate through in situ formation of iminium cations“, *Chemical Communications* **2019**, *55*, 14725-14728, DOI: 10.1039/c9cc06625j

with permission from the Royal Society of Chemistry.

Chapter 3.4.: Reprinted with permission from:

Natalie Dehnhardt, Hayden Paneth, Nikolas Hecht, Johanna Heine „Multinary Halogenido Bismuthates Beyond the Double Perovskite Motif“, *Inorganic Chemistry* **2020**, *59*, 6, 3394-3405, DOI: 10.1021/acs.inorgchem.9b03287.

Copyright 2020 American Chemical Society.

D Elektronische Zusatzinformationen zu den Publikationen

D.1. Surprising Discoveries on the Way to an Old Compound: Four Transient Iodido Antimonates

Electronic Supplementary Information on

Surprising Discoveries on the Way to an Old Compound: Four Transient Iodido Antimonates

*Natalie Dehnhardt, André Böth, Johanna Heine**

Department of Chemistry and Material Sciences Center, Philipps-Universität Marburg, Hans-Meerwein-Straße, 35043 Marburg, Germany.

Crystallographic Details

Details of Crystal Structure Refinement

Compound **1** crystallizes in the form of elongated, highly sensitive rectangular prisms that lose acetonitrile immediately upon removal from the mother liquor, even when stored under silicon oil. This is evidenced by an independent motion of the crystals when viewed under an optical microscope, ostensibly as solvent molecules found in channels along the *c* axis are expelled. Solvate acetonitrile molecules disordered about these channels can be identified during crystal structure refinement, as shown in Figure S1, but could not be modelled in a completely satisfactory manner and their electron density was thus described with a solvent mask to stabilize the refinement. Additionally, a number of ISOR restraints on carbon atoms had to be used to obtain reasonable anisotropic displacement parameters.

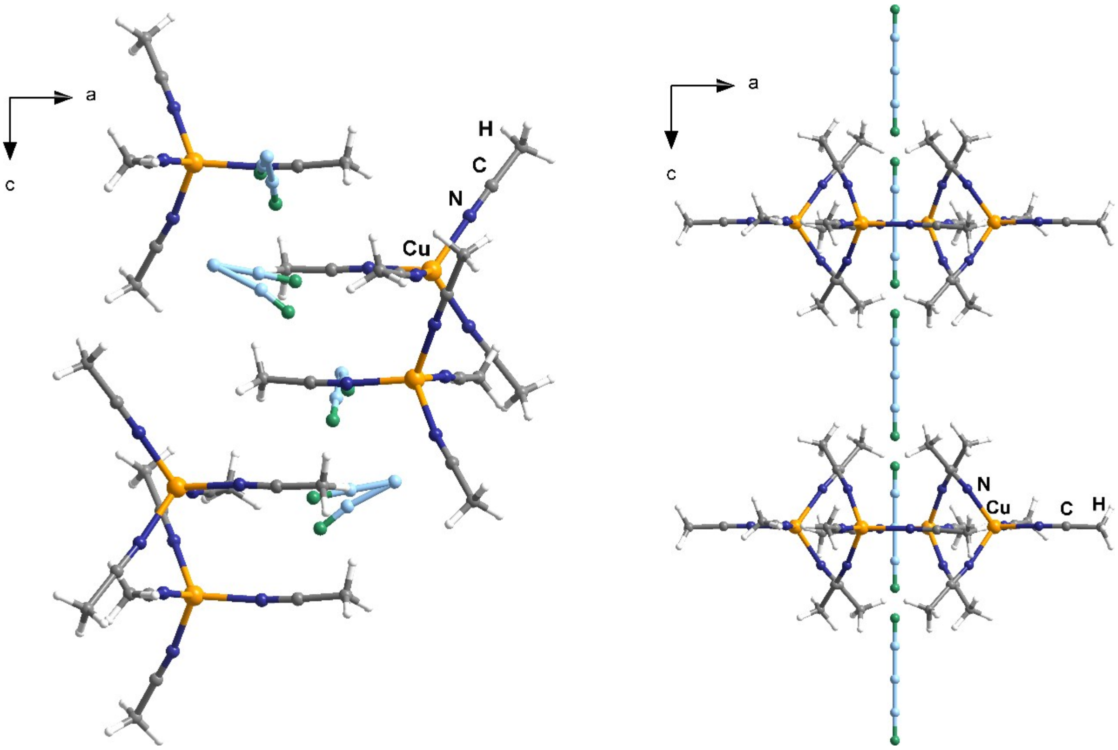

Figure S1: Excerpt of the crystal structure of **1**, with disordered acetonitrile molecules in channels along the *c* axis shown in pale green and light blue. As can be seen, the molecules located directly along the axis cannot be fully modelled within the given crystallographic symmetry.

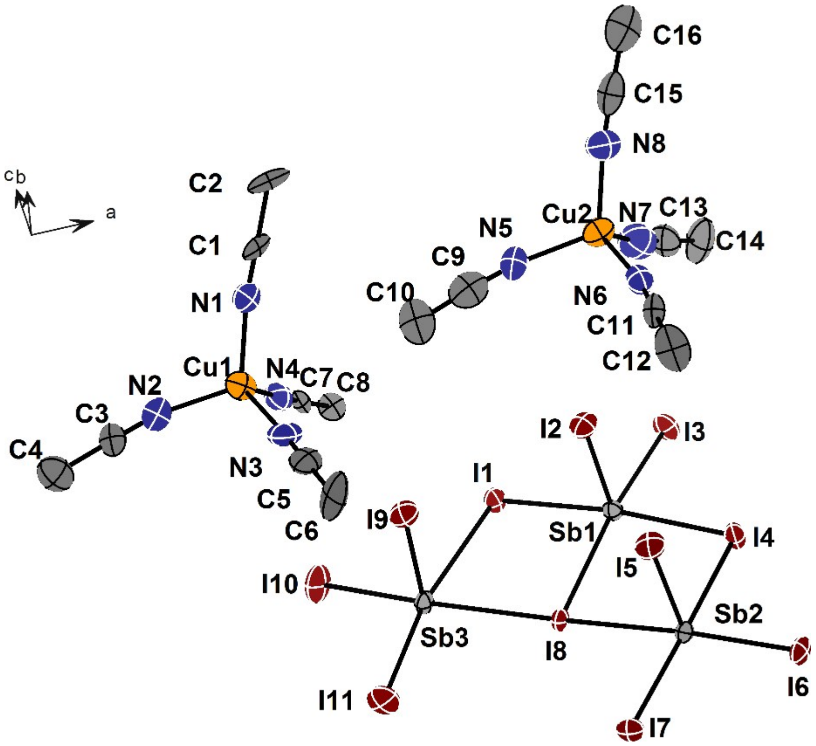

Figure S2: Asymmetric unit of **1**, ellipsoids at 80% probability.

Compound **2** crystallizes in the form of thin planks that also rapidly lose acetonitrile upon removal from the mother liquor. In this case the solvate molecules could be modelled. The compound crystallizes in the non-centrosymmetric space group $P2_1$ (No. 4) and was refined as an inversion twin with BASF 0.38956 and a Flack parameter of 0.39(8). A number of ISOR restraints on carbon and nitrogen atoms had to be used to obtain reasonable anisotropic displacement parameters.

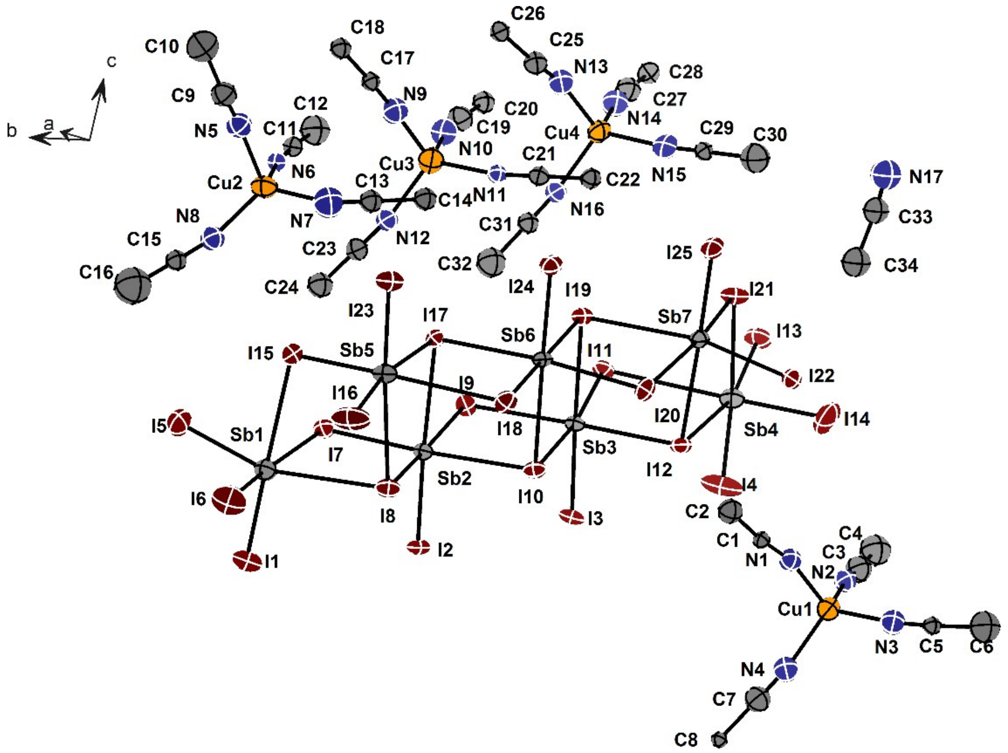

Figure S3: Asymmetric unit of **2**, ellipsoids at 80% probability.

Compound **3** crystallizes in the form of red blocks. The compound crystallizes in the non-centrosymmetric space group P1 (No. 1) and was refined as an inversion twin with BASF 0.23340 and a Flack parameter of 0.23(5). A number of ISOR and DFIX restraints on carbon and nitrogen atoms had to be used to obtain reasonable anisotropic displacement parameters and bond length. The crystal structure can also be solved and refined in the more common space group P$\overline{1}$ (No. 2), yet this leads to a disordered arrangement of the acetonitrile ligands that cannot be accurately modelled while keeping the inversion symmetry, as also shown in Figure 8 in the main manuscript.

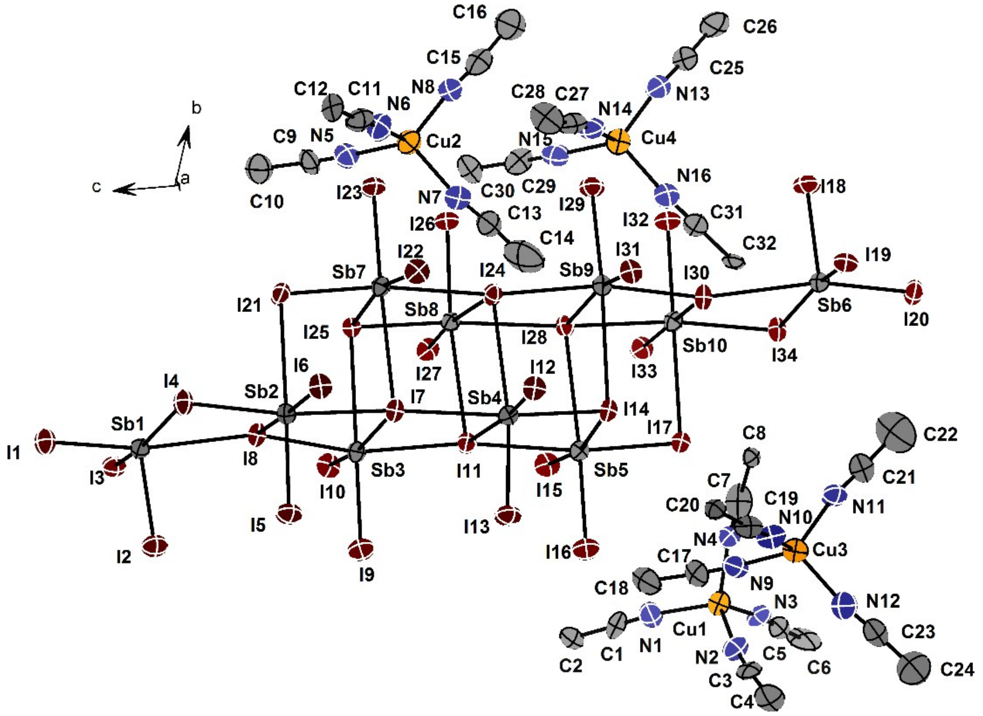

Figure S4: Asymmetric unit of **3**, ellipsoids at 80% probability.

Compound **4** crystallizes in the form of heavily intergrown red rods.

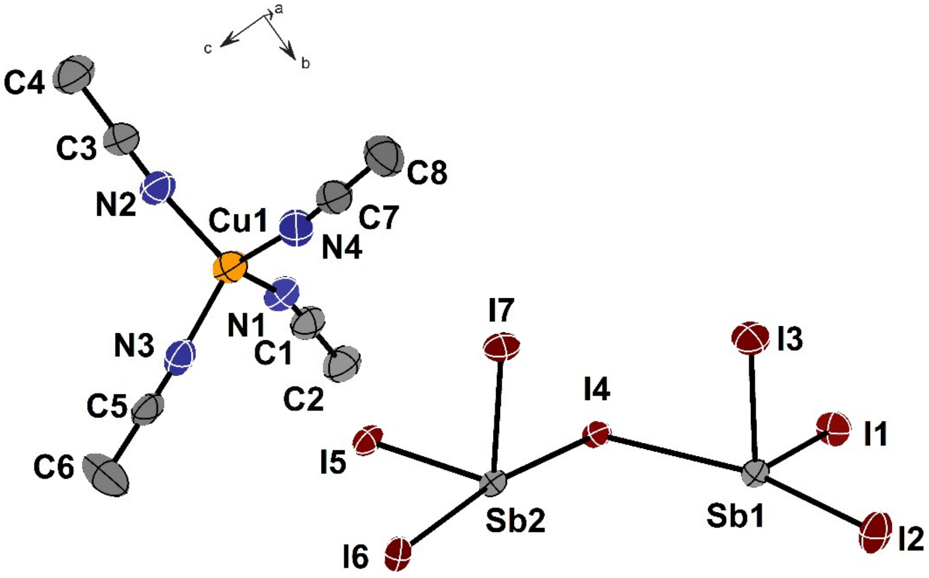

Figure S5: Asymmetric unit of **4**, ellipsoids at 80% probability.

Details of Crystal Structure Analysis

Table S1: Bond length and angles in compounds **1**-**4** and $[Cu(MeCN)_4]_4[Sb_3I_{11}]_2$,[1] all distances in Å, all angles in °.

	1	**2**	**3**	**4**	$[Cu(MeCN)_4]_4[Sb_3I_{11}]_2$
Sb-I$_{terminal}$	2.774-2.870	2.743-2.837	2.738-2.797	2.758-2.811	2.782
Sb-Iμ$_2$	2.844-3.455	2.823-3.549	2.798-3.496	2.849-3.460	3.207
Sb-Iμ$_3$	-	3.024-3.456	2.885-3.523	3.002-3.437	3.356
Sb-Iμ$_4$	3.217-3.395	-	3.102-3.466	-	-
Cu-N	1.965-2.011	1.937-2.045	1.939-2.009	1.982-1.996	1.985-2.080
***cis*-I-Sb-I**	82-97	78-99	82-98	79-99	86-96
N-Cu-N	103-117	104-116	98-117	105-113	106-113

As shown in Table S1, a wide range is observed for the length of Sb-Iμ$_2$ bonds in **1**-**4**. This can be explained by a strong trans-effect,[2] where Sb-Iμ$_2$ distances are longer when trans to a shorter bond, e.g. Sb-I$_{terminal}$ and shorter when trans to a longer bond, e.g. Sb-Iμ$_4$. A similar effect is also observed for Sb-Iμ$_3$ bonds, especially in **3**, where all four types of Sb-I bonds are present. Additionally, the need to accommodate fairly condensed motifs featuring μ$_3$ or μ$_4$ bridging iodine atoms enhances these structural distortions and also results in deviations from the ideal cis-I-Sb-I angle of 90°.

While Cu-N distances are fairly uniform, N-Cu-N angles show some deviation from the ideal angle of 109.5° to accommodate the interlocked packing of the $[Cu(MeCN)_4]^+$ units.

Bond length and angles are similar in the literature reference compound $[Cu(MeCN)_4]_4[Sb_3I_{11}]_2$, although, due to the high symmetry of the crystal structure, only a single distance is observed for each category of Sb-I bonds.

References.

[1] S. Pohl, R. Lotz, W. Saak, D. Haase. *Angew. Chem. Int. Ed. Engl.,* 1989, **28**, 344.

[2] H.-L. Sheu, J. Laane. *Inorg. Chem.,* 2013, **52**, 4244.

D.2. Divergent Optical Properties in an Isomorphous Family of Multinary Iodido Pentelates

Supporting Information on

Divergent Optical Properties in an Isomorphous Family of Multinary Iodido Pentelates

*Natalie Dehnhardt†, Philip Klement‡, Sangam Chatterjee‡, Johanna Heine†**

† Department of Chemistry and Material Sciences Center, Philipps-Universität Marburg, Hans-Meerwein-Straße, 35043 Marburg, Germany.

‡ Institute of Experimental Physics I and Center for Materials Research (ZfM), Justus Liebig University Giessen, Giessen, Germany

* E-Mail: johanna.heine@chemie.uni-marburg.de

Crystallographic Details

Single crystal X-ray determination was performed on a STOE IPDS2 diffractometer equipped with an imaging plate detector system using MoKα radiation with graphite monochromatization (**1**, **4**) or on a Bruker Quest D8 diffractometer with microfocus MoKα radiation and a Photon 100 (CMOS) detector (**2**, **3**).

Table S1: Crystallographic data for $[PPh_4]_2[SbCu_2I_7(CH_3CN)]$ (**1**).

Empirical formula	$C_{50}H_{43}Cu_2I_7NP_2Sb$
Formula weight	1856.92
Temperature/K	100.0
Crystal system	monoclinic
Space group	*Cc*
a/Å	19.5958(8)
b/Å	17.2708(5)
c/Å	16.7887(8)
α/°	90
β/°	103.833(3)
γ/°	90
Volume/Å^3	5517.1(4)
Z	4
ρ_{calc}g/cm^3	2.236
μ/mm^{-1}	5.259
F(000)	3440.0
Crystal size/mm^3	0.22 × 0.182 × 0.118
Absorption correction (T_{min}/T_{max})	analytical (0.2290/0.4637)
2Θ range for data collection/°	3.718 to 63.854
Index ranges	$-28 \leq h \leq 28$, $-25 \leq k \leq 25$, $-21 \leq l \leq 24$
Reflections collected	35374
Independent reflections	16822 [$R_{int} = 0.0512$, $R_{sigma} = 0.0740$]
Data/restraints/parameters	16822/2/579
Goodness-of-fit on F^2	0.840
Final R indexes [I>=2σ (I)]	$R_1 = 0.0311$, $wR_2 = 0.0638$
Final R indexes [all data]	$R_1 = 0.0416$, $wR_2 = 0.0653$
Largest diff. peak/hole / e Å^{-3}	1.66/-1.33
Flack parameter	-0.02(2)

Details of crystal structure refinement: All non-hydrogen atoms were refined anisotropically. Hydrogen atoms were assigned to idealized geometric positions and included in structure factors calculations. One copper atom was disordered over two positions with occupancies 0.3 and 0.7 for Cu1A and Cu1B, respectively. Occupancies were first refined freely, then set to an appropriate value to stabilize the refinement.

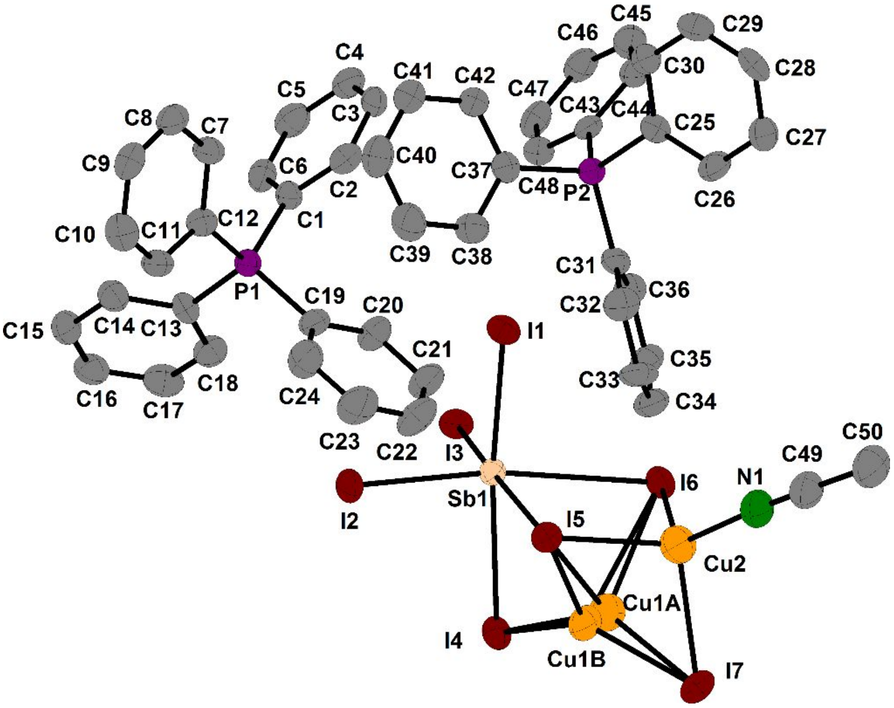

Figure S1: Asymmetric unit of **1**, ellipsoids at 80% probability.

Table S2: Crystallographic data for $[PPh_4]_2[SbCu_2I_7(CH_3CH_2CN)]$ (**2**).

Empirical formula	$C_{51}H_{45}Cu_2I_7NP_2Sb$
Formula weight	1870.95
Temperature/K	105.01
Crystal system	monoclinic
Space group	*Cc*
a/Å	19.7444(8)
b/Å	17.4660(7)
c/Å	16.9029(7)
α/°	90
β/°	104.0120(10)
γ/°	90
Volume/Å^3	5655.6(4)
Z	4
ρ_{calc}g/cm^3	2.197
μ/mm^{-1}	5.131
F(000)	3472.0
Crystal size/mm^3	0.236 × 0.185 × 0.06
Absorption correction (T_{min}/T_{max})	multi-scan (0.5851/0.7452)
2Θ range for data collection/°	4.252 to 50.636
Index ranges	$-23 \leq h \leq 23$, $-20 \leq k \leq 19$, $-20 \leq l \leq 20$
Reflections collected	82962
Independent reflections	10288 [$R_{int} = 0.0389$, $R_{sigma} = 0.0207$]
Data/restraints/parameters	10288/2/575
Goodness-of-fit on F^2	1.075
Final R indexes [I>=2σ (I)]	$R_1 = 0.0149$, $wR_2 = 0.0291$
Final R indexes [all data]	$R_1 = 0.0164$, $wR_2 = 0.0295$
Largest diff. peak/hole / e Å^{-3}	0.67/-0.85
Flack parameter	0.000(6)

Details of crystal structure refinement: All non-hydrogen atoms were refined anisotropically with the exception of a disordered copper atom and the propionitrile ligand. Hydrogen atoms were assigned to idealized geometric positions and included in structure factors calculations. Occupancies in the disordered parts of the structure were first refined freely, then set to an appropriate value to stabilize the refinement. Despite their proximity, the disorder in the copper atom and proprionitrile ligand occurs independent of each other, as indicated by different occupancies (0.15 and 0.85 for Cu1A and Cu1B, and 0.7 and 0.3 for N1A, etc. and N1B, etc., respectively).

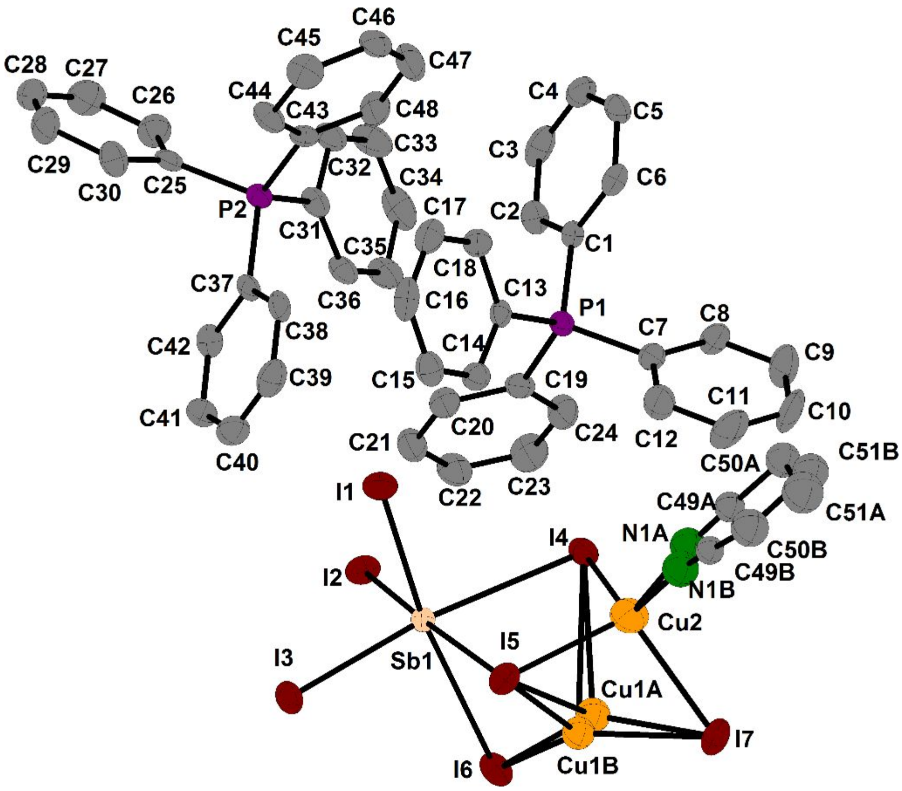

Figure S2: Asymmetric unit of **2**, ellipsoids at 80% probability.

Table S3: Crystallographic data for $[PPh_4]_2[BiCu_2I_7(CH_3CN)]$ (**3**).

Empirical formula	$C_{50}H_{43}BiCu_2I_7NP_2$
Formula weight	1944.26
Temperature/K	100.01
Crystal system	monoclinic
Space group	*Cc*
a/Å	19.6722(9)
b/Å	17.3553(8)
c/Å	16.8568(8)
α/°	90
β/°	103.836(2)
γ/°	90
Volume/Å^3	5588.2(5)
Z	4
ρ_{calc}g/cm^3	2.311
μ/mm^{-1}	7.853
F(000)	3568.0
Crystal size/mm^3	0.304 × 0.22 × 0.088
Absorption correction (T_{min}/T_{max})	multi-scan (0.4737/ 0.7452)
2Θ range for data collection/°	4.264 to 50.65
Index ranges	$-23 \leq h \leq 23$, $-20 \leq k \leq 20$, $-20 \leq l \leq 20$
Reflections collected	79340
Independent reflections	9832 [$R_{int} = 0.0349$, $R_{sigma} = 0.0328$]
Data/restraints/parameters	9832/2/579
Goodness-of-fit on F^2	0.918
Final R indexes [I>=2σ (I)]	$R_1 = 0.0142$, $wR_2 = 0.0313$
Final R indexes [all data]	$R_1 = 0.0148$, $wR_2 = 0.0315$
Largest diff. peak/hole / e Å^{-3}	0.49/-0.71
Flack parameter	0.0136(16)

Details of crystal structure refinement: All non-hydrogen atoms were refined anisotropically. Hydrogen atoms were assigned to idealized geometric positions and included in structure factors calculations. One copper atom was disordered over two positions with occupancies 0.25 and 0.75 for Cu1A and Cu1B, respectively. Occupancies were first refined freely, then set to an appropriate value to stabilize the refinement.

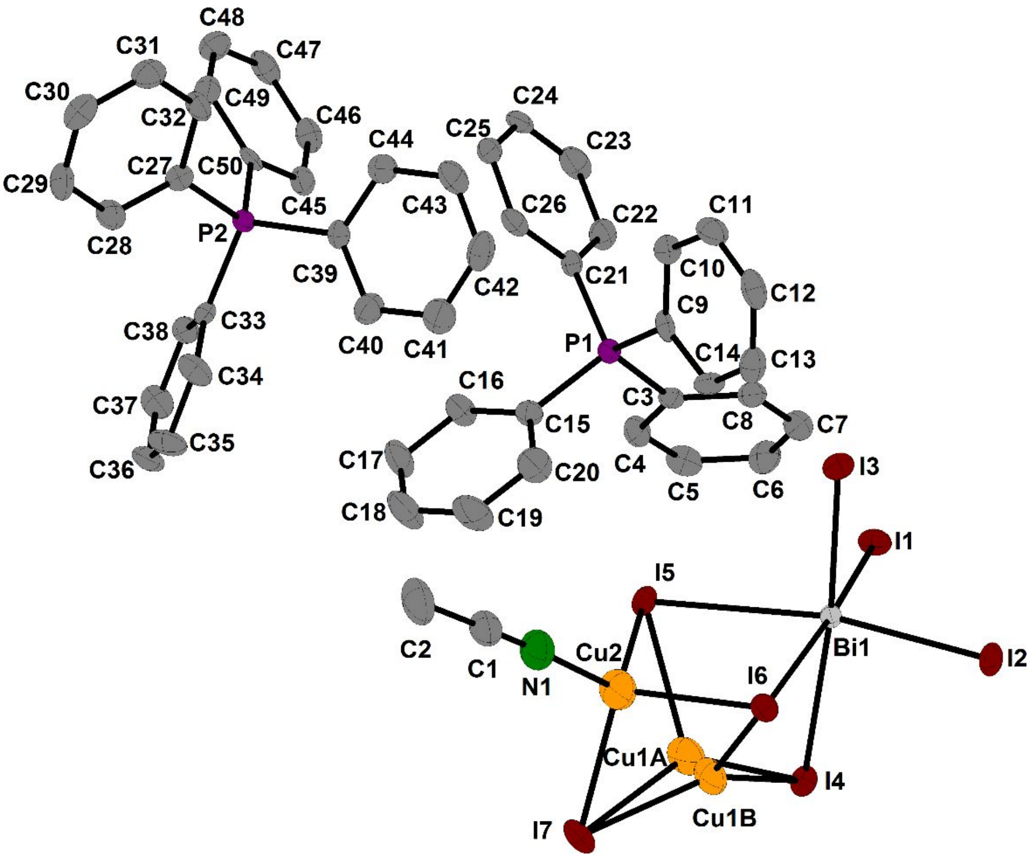

Figure S3: Asymmetric unit of **3**, ellipsoids at 80% probability.

Table S4: Crystallographic data for $[PPh_4]_2[BiCu_2I_7(CH_3CH_2CN)]$ (**4**).

Empirical formula	$C_{51}H_{45}BiCu_2I_7NP_2$
Formula weight	1958.18
Temperature/K	100.0
Crystal system	monoclinic
Space group	*Cc*
a/Å	19.6427(7)
b/Å	17.5050(4)
c/Å	16.8610(5)
α/°	90
β/°	104.022(3)
γ/°	90
Volume/Å^3	5624.8(3)
Z	4
ρ_{calc}g/cm^3	2.312
μ/mm^{-1}	7.803
F(000)	3600.0
Crystal size/mm^3	0.578 × 0.471 × 0.222
Absorption correction (T_{min}/T_{max})	analytical (0.0476/ 0.2312)
2Θ range for data collection/°	3.688 to 63.814
Index ranges	$-29 \leq h \leq 29$, $-25 \leq k \leq 26$, $-23 \leq l \leq 25$
Reflections collected	66513
Independent reflections	18208 [R_{int} = 0.0415, R_{sigma} = 0.0354]
Data/restraints/parameters	18208/2/579
Goodness-of-fit on F^2	1.017
Final R indexes [I>=2σ (I)]	R_1 = 0.0310, wR_2 = 0.0742
Final R indexes [all data]	R_1 = 0.0344, wR_2 = 0.0751
Largest diff. peak/hole / e Å^{-3}	3.60/-1.65
Flack parameter	-0.024(3)

Details of crystal structure refinement: All non-hydrogen atoms were refined anisotropically. Hydrogen atoms were assigned to idealized geometric positions and included in structure factors calculations.

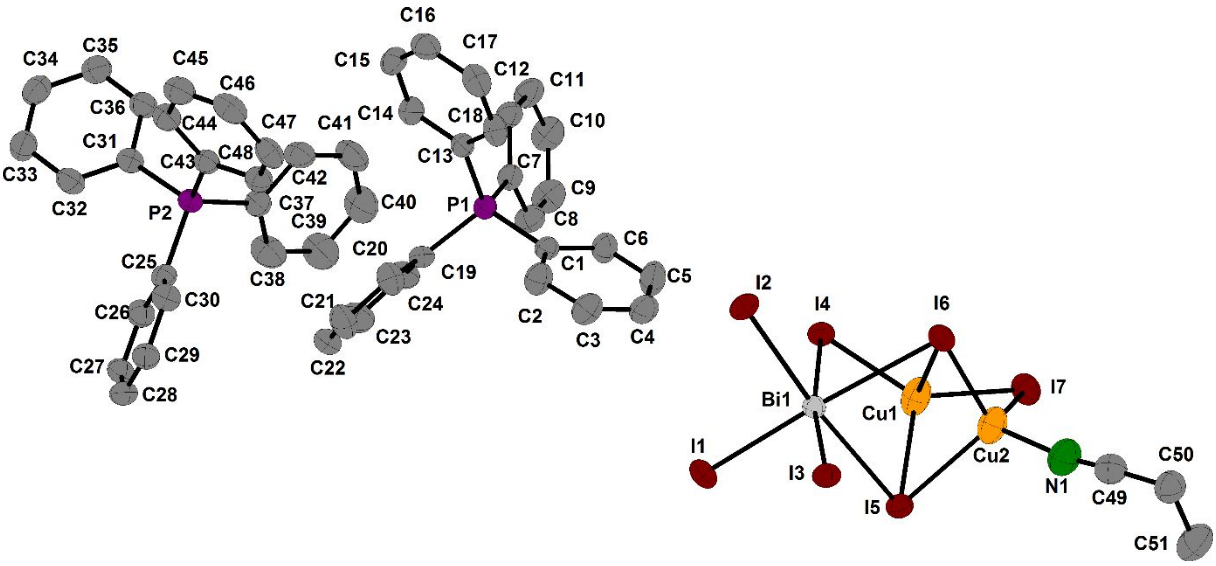

Figure S4: Asymmetric unit of **4**, ellipsoids at 80% probability.

Additional Crystallographic Figures

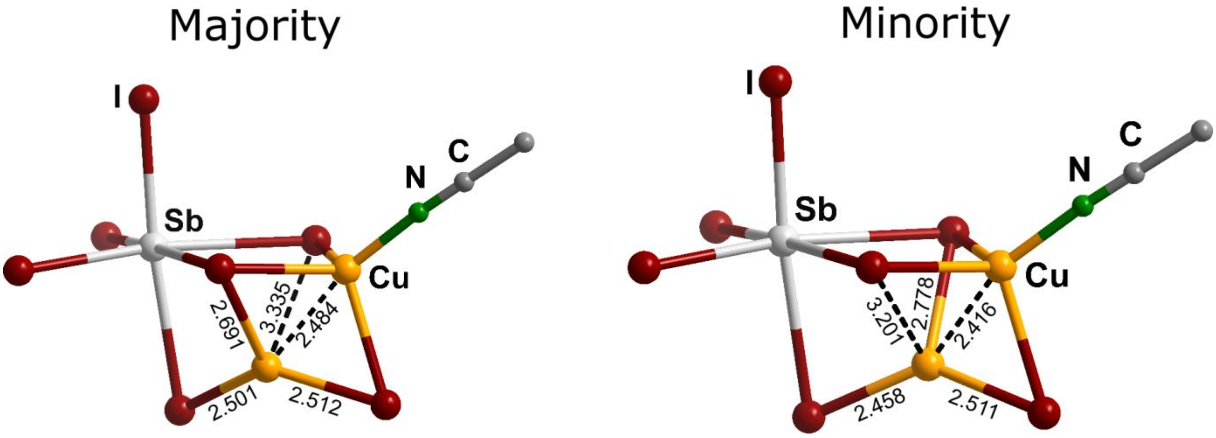

Figure S5: Bond and contact length in Å about the disordered Cu atom positions in $[PPh_4]_2[SbCu_2I_7(CH_3CN)]$ (**1**) for the majority and minority component.

Thermal analysis

The thermal behavior of $[PPh_4]_2[SbCu_2I_7(CH_3CN)]$ (**1**) (12.5 mg), was studied on a Netzsch STA 409 CD from 25 to 1200 °C with a heating rate of 10 °C min^{-1} in a constant flow of 150 mL min^{-1} Ar.

A mass loss of 2 %, corresponding to the loss of the acetonitrile ligand, can be observed starting at 167 °C, followed by a mass loss of 71 % starting at 310 °C. A third mass loss of 11 % can be observed starting at 750 °C.

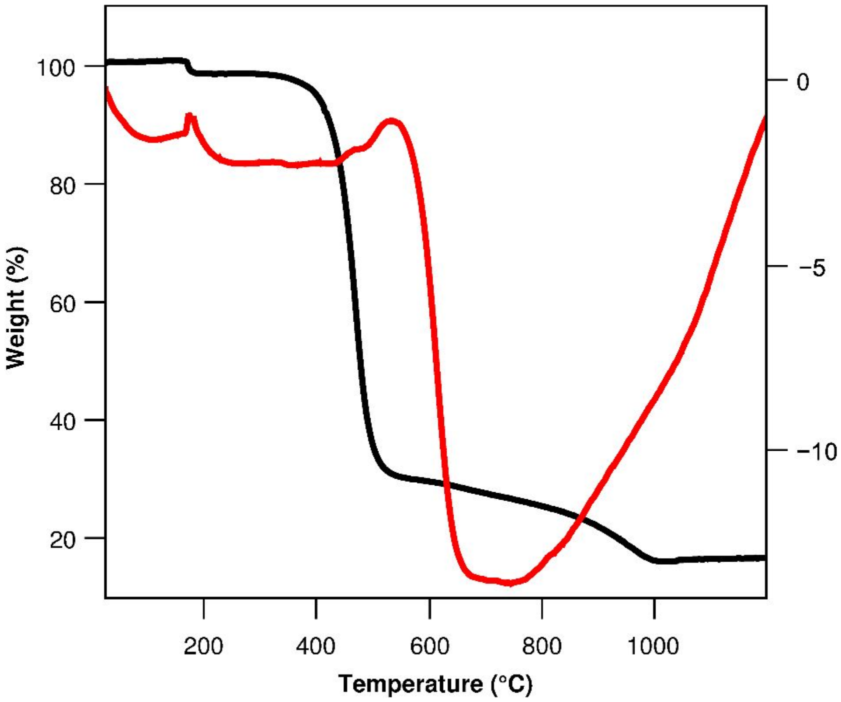

Figure S6. TGA and DSC of $[PPh_4]_2[SbCu_2I_7(CH_3CN)]$ (**1**).

The thermal behavior of $[PPh_4]_2[SbCu_2I_7(CH_3CH_2\,CN)]$ (**2**) (13.1 mg), was studied on a Netzsch STA 409 CD from 25 to 1200 °C with a heating rate of 10 °C min^{-1} in a constant flow of 150 mL min^{-1} Ar.

A mass loss of 3 %, corresponding to the loss of the propionitrile ligand, can be observed starting at 160 °C, followed by a mass loss of 71 % starting at 310 °C. A third mass loss of 14 % can be observed starting at 750 °C.

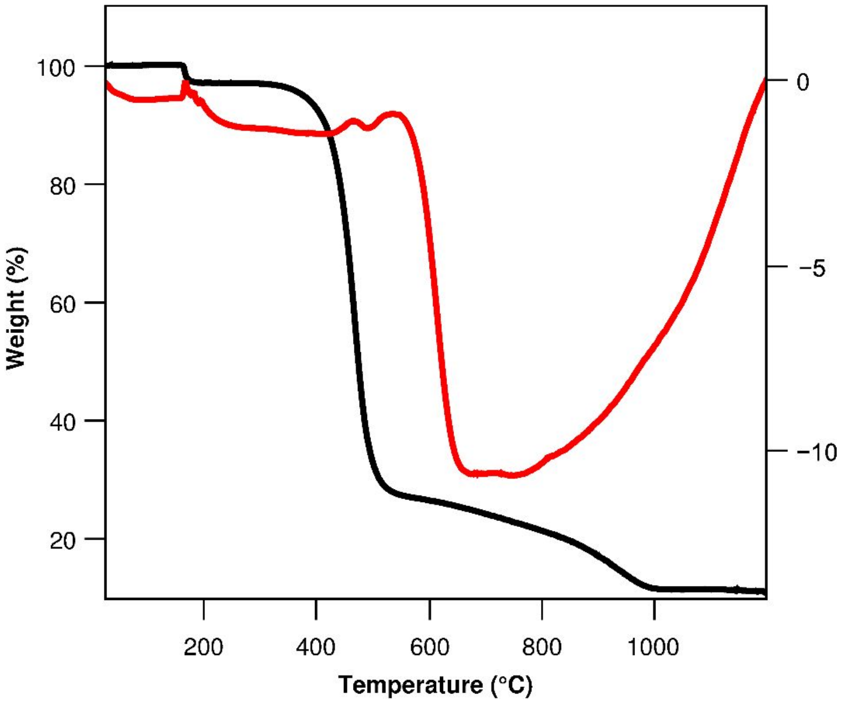

Figure S7. TGA and DSC of $[PPh_4]_2[SbCu_2I_7(CH_3CH_2CN)]$ (**2**).

The thermal behavior of $[PPh_4]_2[BiCu_2I_7(CH_3CN)]$ (**3**) (12.0 mg), was studied by TGA on a Netzsch STA 409 CD from 25 to 1200 °C with a heating rate of 10 °C min^{-1} in a constant flow of 150 mL min^{-1} Ar.

A mass loss of 2 %, corresponding to the loss of the acetonitrile ligand, can be observed starting at 175 °C, followed by a mass loss of 71 % starting at 380 °C. A third mass loss of 12 % can be observed starting at 750 °C.

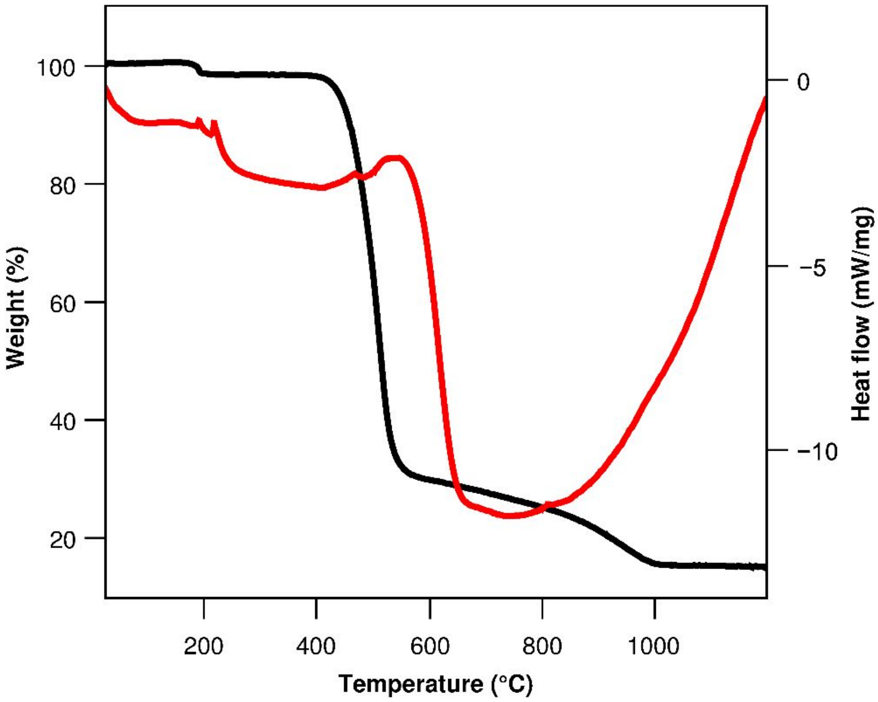

Figure S8. TGA and DSC of $[PPh_4]_2[BiCu_2I_7(CH_3CN)]$ (**3**).

The thermal behavior of $[PPh_4]_2[BiCu_2I_7(CH_3CH_2CN)]$ (**4**) (11.4 mg), was studied by TGA on a Netzsch STA 409 CD from 25 to 1200 °C with a heating rate of 10 °C min^{-1} in a constant flow of 150 mL min^{-1} Ar.

A mass loss of 3 %, corresponding to the loss of the propionitrile ligand, can be observed starting at 170 °C, followed by a mass loss of 72 % starting at 380 °C. A third mass loss of 10 % can be observed starting at 750 °C.

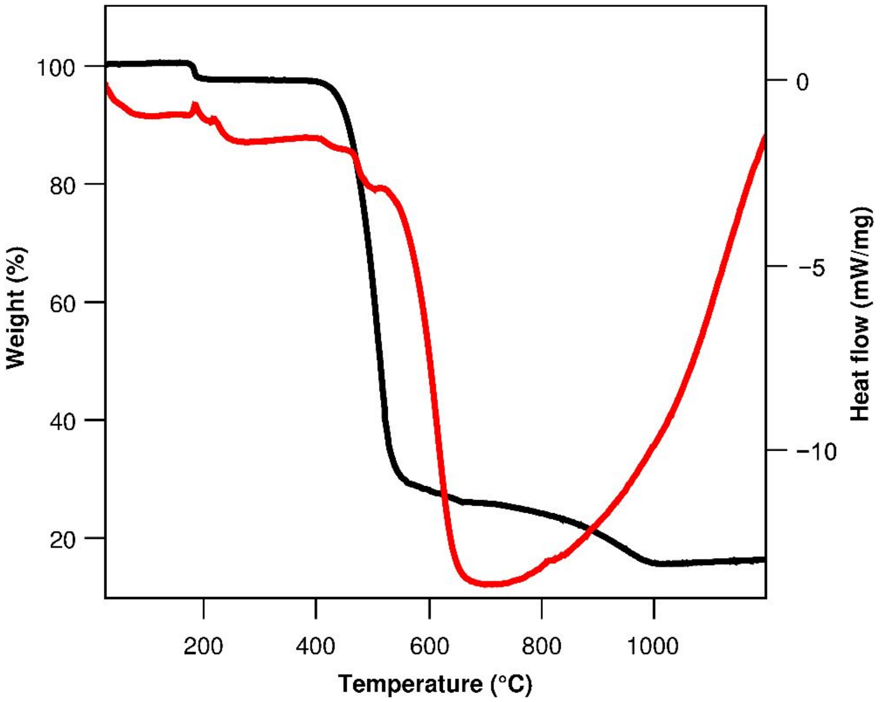

Figure S9. TGA and DSC of $[PPh_4]_2[BiCu_2I_7(CH_3CH_2CN)]$ (**4**).

Powder diffraction

Powder patterns were recorded on a *STADI MP* (*STOE* Darmstadt) powder diffractometer, with CuK$_{\alpha1}$ radiation with λ= 1.54056 Å at room temperature in transmission mode. The patterns confirm the presence of the respective phase determined by SCXRD measurements and the absence of any major crystalline by-products.

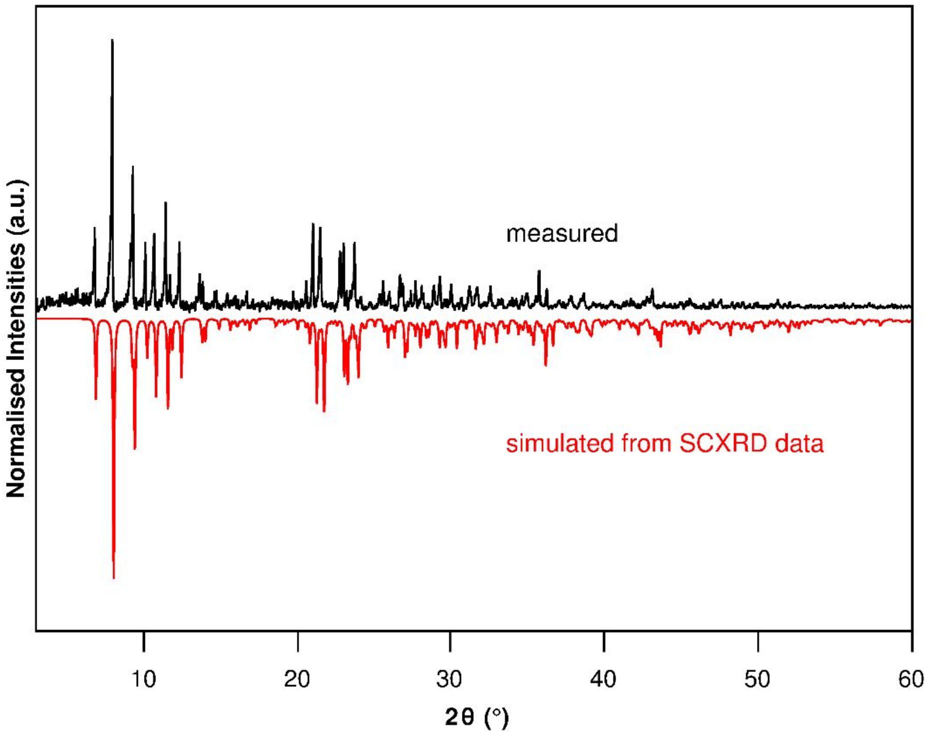

Figure S10. Powder diffraction pattern of $[PPh_4]_2[SbCu_2I_7(CH_3CN)]$ (**1**).

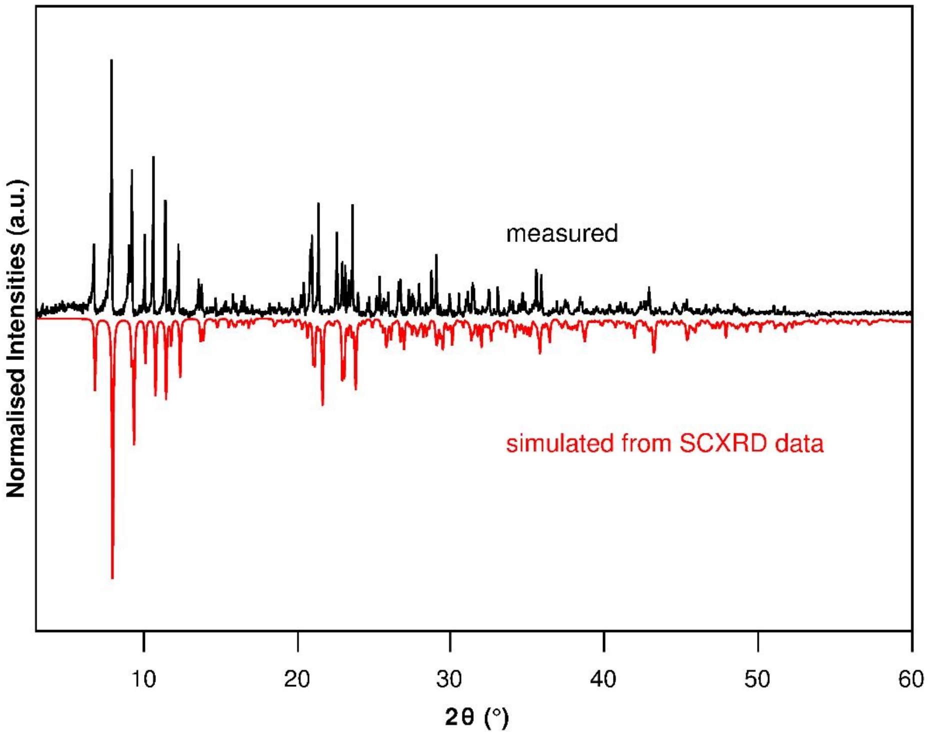

Figure S11. Powder diffraction pattern of $[PPh_4]_2[SbCu_2I_7(CH_3CH_2CN)]$ (**2**).

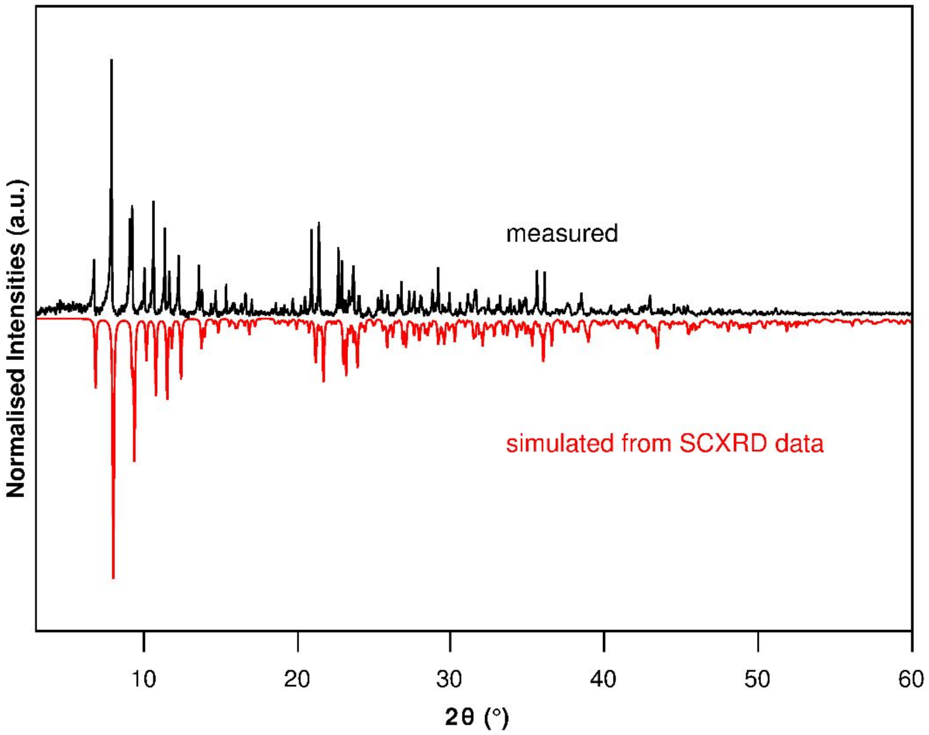

Figure S12. Powder diffraction pattern of $[PPh_4]_2[BiCu_2I_7(CH_3CN)]$ (**3**).

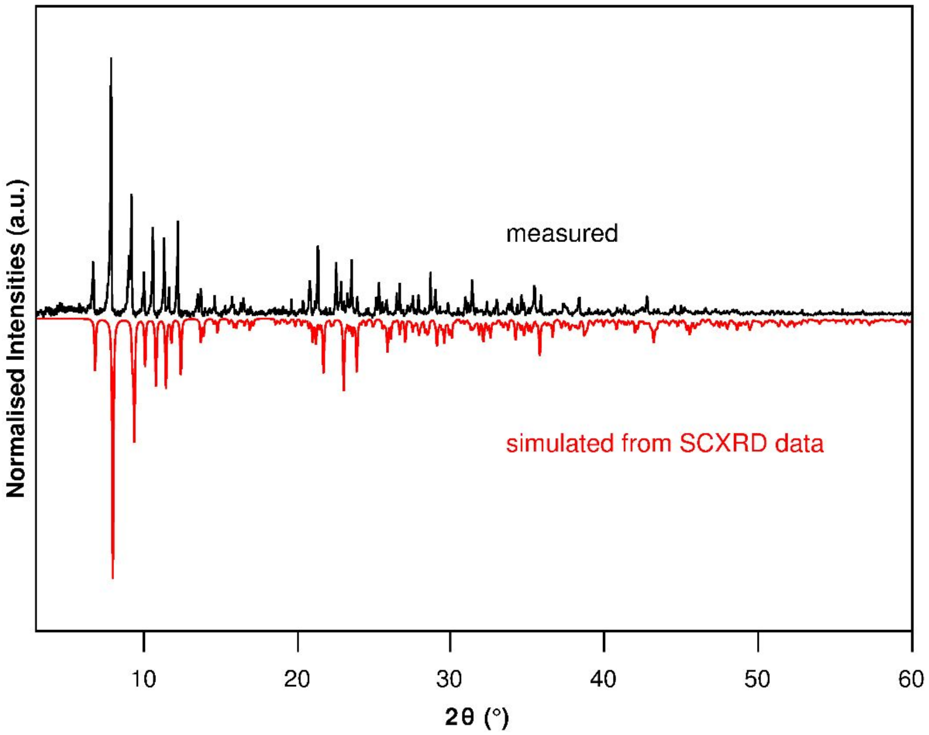

Figure S13. Powder diffraction pattern of $[PPh_4]_2[BiCu_2I_7(CH_3CH_2CN)]$ (**4**).

IR spectroscopy

IR spectra were recorded on a *Bruker Tensor 37* FT-IR spectrometer equipped with an ATR-Platinum measuring unit. The typical peak pattern of the $[PPh_4]^+$ moiety can be identified between 500 and 1500 cm^{-1}.[1]

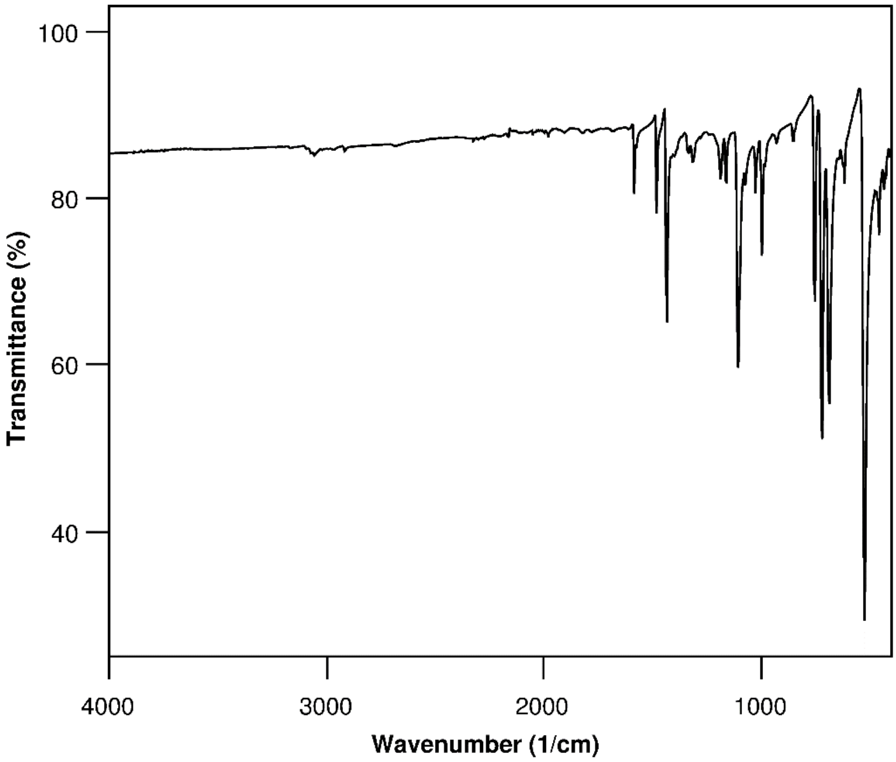

Figure S14. IR spectrum of $[PPh_4]_2[SbCu_2I_7(CH_3CN)]$ (**1**).

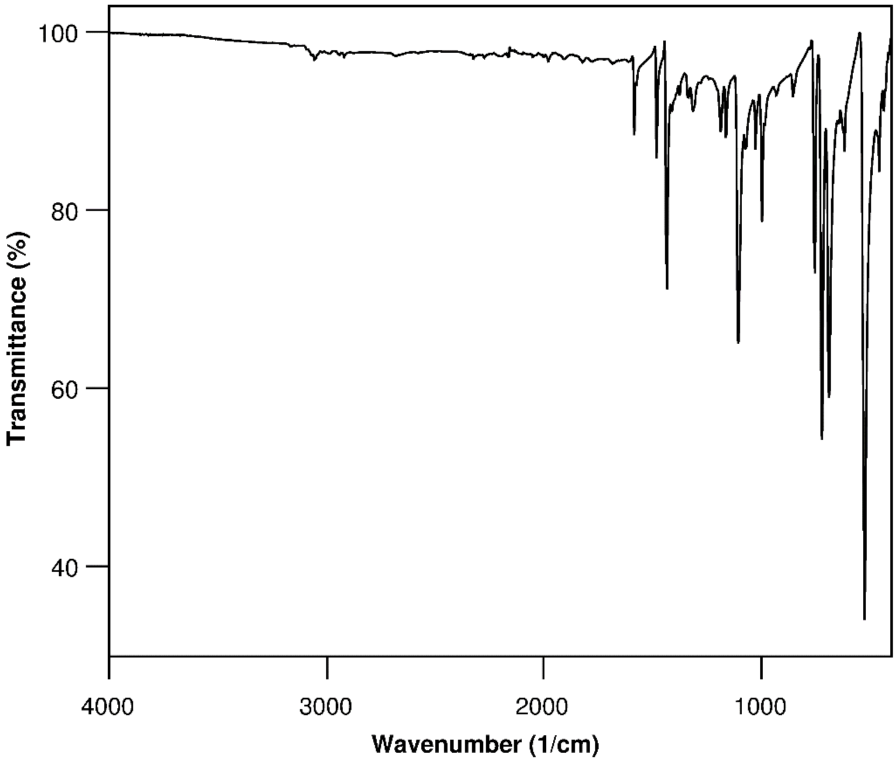

Figure S15. IR spectrum of $[PPh_4]_2[SbCu_2I_7(CH_3CH_2CN)]$ (**2**).

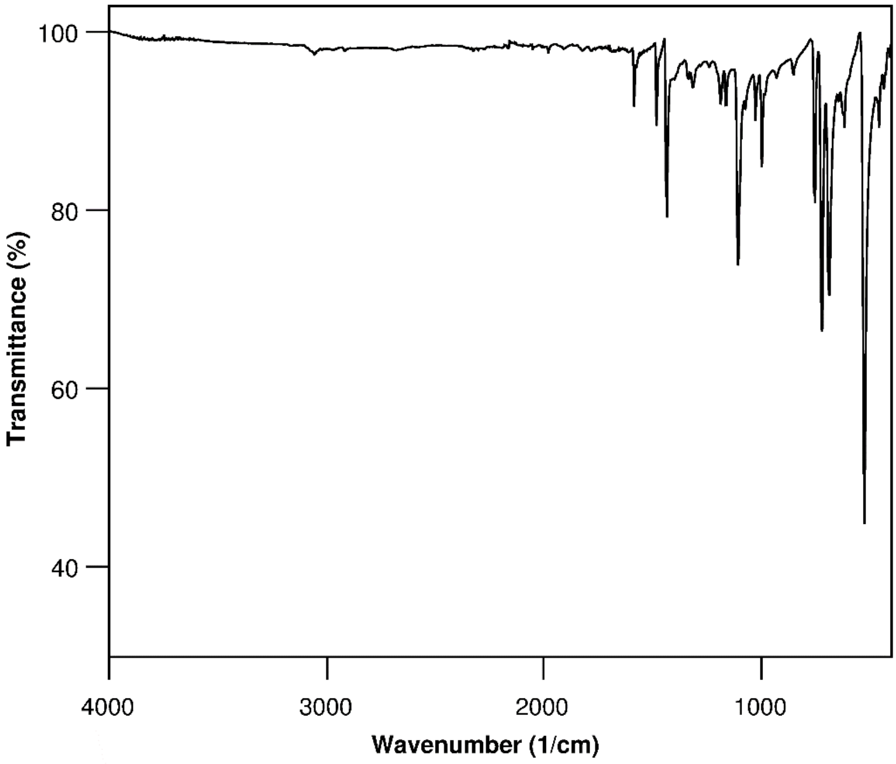

Figure S16. IR spectrum of $[PPh_4]_2[BiCu_2I_7(CH_3CN)]$ (**3**).

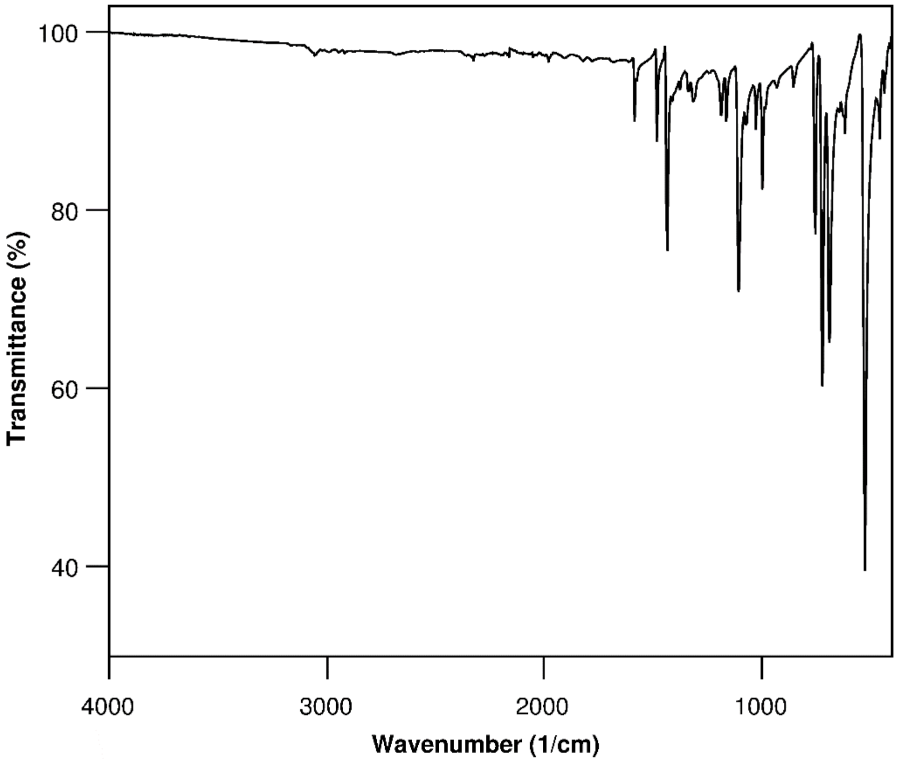

Figure S17. IR spectrum of $[PPh_4]_2[BiCu_2I_7(CH_3CH_2CN)]$ (**4**).

Synthesis and Characterization of Reference Compounds $[NH_2Me_2]_3[EI_6]$

$[NH_2Me_2]_3[EI_6]$ reference compounds were synthesized from stoichiometric amounts of $[NH_2Me_2]I$ and EI_3 in dry acetonitrile and identified from their PXRD patterns. The single crystal structure of $[NH_2Me_2]_3[SbI_6]$ has not been determined yet, but the recorded pattern shows that the compound is isomorphous to $[NH_2Me_2]_3[BiI_6]$.[2]

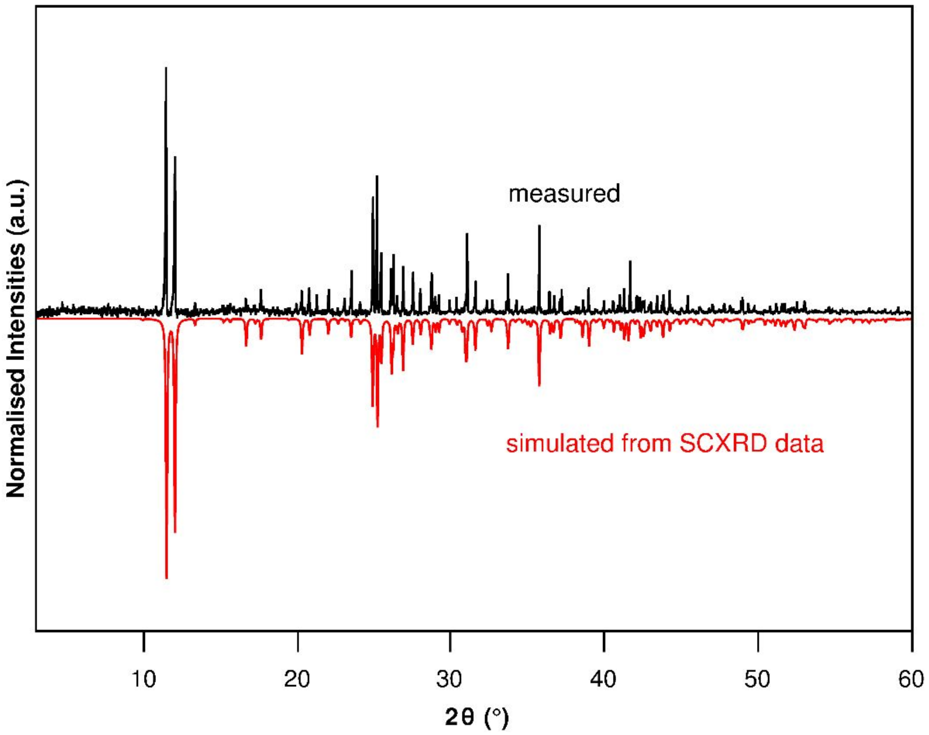

Figure S18. Powder diffraction pattern of $[NH_2Me_2]_3[SbI_6]$ and reference pattern from the literature.[2]

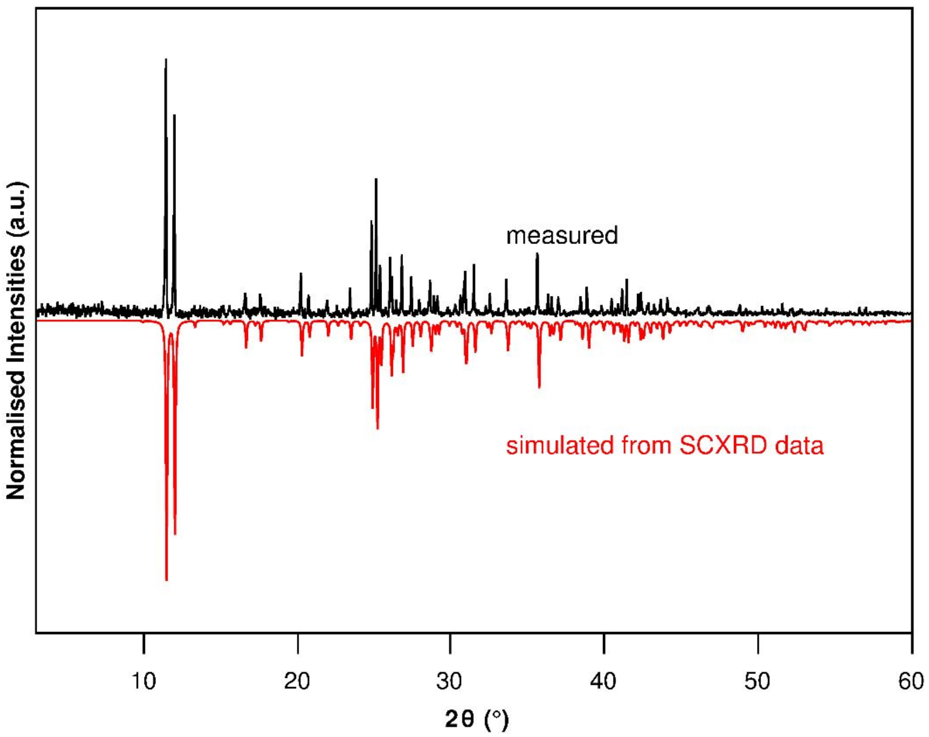

Figure S19. Powder diffraction pattern of $[NH_2Me_2]_3[BiI_6]$ and reference pattern from the literature.[2]

Mechanochemical Reactions

The liquid assisted grinding process for $[PPh_4]_2[SbCu_2I_7(CH_3CN)]$ (**1**) is detailed below, **2**-**4** can be obtained in an identical fashion.

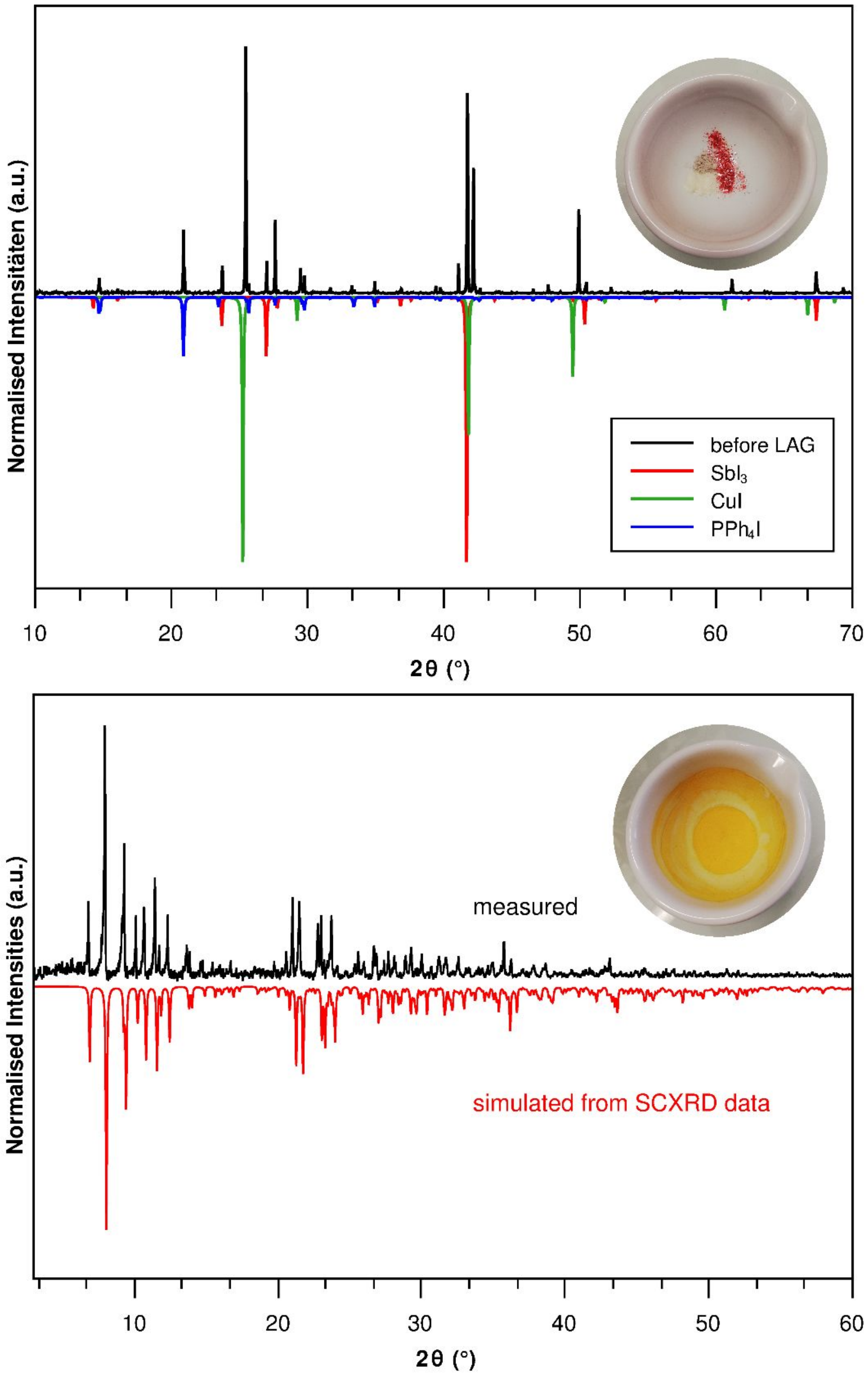

Figure S20. PXRD patterns before and after liquid assisted grinding of the reaction mixture for compound **1** with photographs of the reaction shown as insets.

Photoluminescence spectroscopy

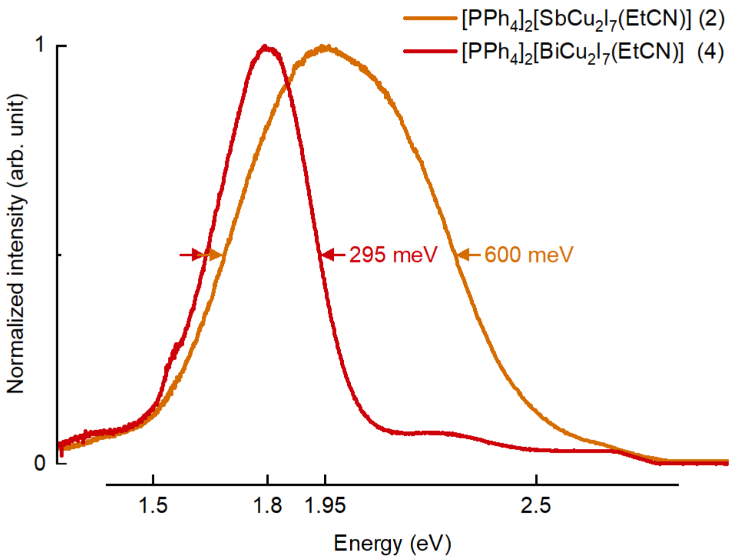

Figure S21. Normalized low temperature photoluminescence spectra of the antimonate **2** and bismuthate **4** (orange and red lines) at 10 K.

References

[1] Wittig, G.; Benz, E. Über das Verhalten von Dehydrobenzol gegenüber nucleophilen und elektrophilen Reagenzien. *Chem. Ber.* **1959**, *92*, 1999-2013.

[2] Lindsjö, M.; Fischer, A.; Kloo, L. Anionic Diversity in Iodobismuthate Chemistry. *Z. Anorg. Allg. Chem.* **2005**, *631*, 1497-1501.

D.3. Synthesis of a two-dimensional organic–inorganic bismuth iodide metalate through in situ formation of iminium cations

Electronic Supplementary Information on

Synthesis of a two-dimensional organic-inorganic bismuth iodide metalate through *in situ* formation of iminium cations

Natalie Dehnhardt, Jan-Niclas Luy, Marvin Szabo, Mirco Wende, Ralf Tonner and Johanna Heine**

Department of Chemistry and Material Sciences Center, Philipps-Universität Marburg, Hans-Meerwein-Straße, 35043 Marburg, Germany.

*E-mail: tonner@chemie.uni-marburg.de
johanna.heine@chemie.uni-marburg.de

Synthetic Details

General. BiI_3 was synthesized from the elements according to literature procedures.[1] Dimethylamine (40 % solution in water) and HI (57 % solution in water, stabilizer: 0.75 % H_3PO_2) were used as supplied from commercial sources. Pentane, ethanol and pyridine were flash-distilled prior to use. Acetone was dried by standing over activated 3 Å molecular sieve. $(Me_2NH_2)I$ was prepared from aqueous solutions of dimethylamine and HI. The reference compound $(Hpy)BiI_4$ (HPy^+ = pyridinium, $C_5H_5NH^+$) was prepared by mixing stoichiometric ratios of BiI_3 and (HPy)I (prepared from pyridine and HI solution) in ethanol for 24 hours at room temperature.[2] A single crystal of $(Hpy)BiI_4$ was identified from its SCXRD cell parameters at 100 K. We note that there is likely a phase transition between 100 K and room temperature, as the PXRD pattern of the crushed single crystal recorded at room temperature did not completely match the simulation. CHN analysis was carried out on an Elementar CHN-analyzer. Details on additional analysis methods can be found in the respective sections below.

$(Me_2C{=}NMe_2)Bi_2I_7$ (1). Under inert conditions, BiI_3 (119 mg, 0.2 mmol) and $(Me_2NH_2)I$ (18 mg, 0.1 mmol) were suspended in 5 mL dry acetone and heated to reflux for 1.5 hours. While cooling down to room temperature, the solid product precipitated. It was washed with pentane and dried under vacuum. $(Me_2C{=}NMe_2)Bi_2I_7$ (**1**) was obtained as dark red microcrystalline powder.

(Yield: 86.7 mg, 0.062 mmol, 62 %). Data for **1**: Anal. Calcd for $C_5H_{12}Bi_2I_7N$, (M = 1392.39 g mol^{-1}): C, 4.31; H, 0.87; N, 1.01 %. Found: C, 4.66; H, 0.87; N, 1.07 %.

Single crystals of **1** were grown by suspending BiI_3 (119 mg, 0.2 mmol) and Me_2NH_2I (18 mg, 0.1 mmol) in 10 mL of dried acetone under inert conditions. The suspension was heated to reflux for 1.5 hours, transferred to a second Schlenk tube and cooled down slowly. Very small dark red crystals of **1** were obtained after 24 hours.

Crystallographic Details

Table S1: Crystallographic data for **1**.

	1
Empirical formula	$C_5H_{12}Bi_2I_7N$
Formula weight /g·mol^{-1}	1392.42
Crystal color and shape	dark red block
Crystal size	0.078 × 0.049 × 0.04
Crystal system	monoclinic
Space group	$P2/n$
a /Å	14.4647(8)
b /Å	7.5084(4)
c /Å	20.9965(11)
α /°	90
β /°	108.165(2)
γ /°	90
V /Å^3	2166.7(2)
Z	4
ρ_{calc} /g·cm^{-3}	4.269
$\mu(Mo_{K\alpha})$ /mm^{-1}	26.177
measurement temp. /K	100
Absorption correction type	multi-scan
Min/max transmission	0.2865/0.3311
2Θ range /°	5.426-50.644
No. of measured reflections	83909
No. of independent reflections	3936
R(int)	0.0623
No. of indep. reflections ($I > 2\sigma(I)$)	3402
No. of parameters	142
R_1 ($I > 2\sigma(I)$)	0.0222
wR_2 (all data)	0.0367
S (all data)	1.111
$\Delta\rho_{max}$, $\Delta\rho_{min}$ /e· Å^{-3}	0.91/-1.26

Details of crystal structure measurement and refinement: Single crystal X-ray determination was performed at 100 K on a Bruker Quest D8 diffractometer with microfocus MoKα radiation and a Photon 100 (CMOS) detector. The structure was solved using direct methods, refined by full-matrix least-squares techniques and expanded using Fourier techniques, using the ShelX software package[3] within the OLEX2 suite.[4] All non-hydrogen atoms were refined anisotropically. Hydrogen atoms were assigned to idealized geometric positions and included in structure factors calculations. Pictures of the crystal structures were created using DIAMOND.[5] Data was deposited as CCDC 1939881.

The carbon and nitrogen atoms in the iminium cation's central C=N bond were found to be occupationally disordered and modelled accordingly. C/N occupancies were refined with a common free variable, allowing preferred occupancies (C=N vs. N=C) to manifest, but keeping the overall model chemically sensible. Nonetheless, occupancies refined close to 0.5. In line with common practice for modelling occupational disorder, EXYZ and EADP constraints were used on both positions.

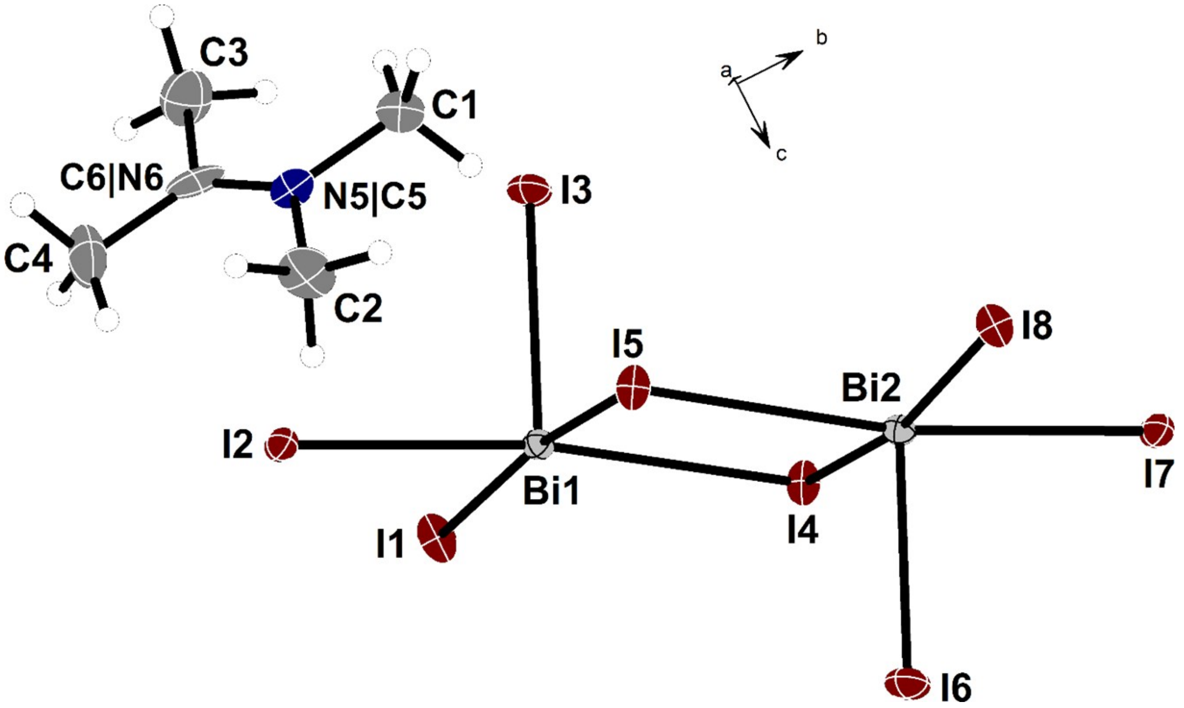

Figure S1: Asymmetric unit of **1**, ellipsoids at 70% probability, majority (0.53) position of disordered atoms in the C=N bond shown.

Table S2: Selected interatomic distances (in Å) and angles (in °) in **1**.

Symmetry operation: I +X,1+Y,+Z, II +X,-1+Y,+Z, III 1/2-X,+Y,3/2-Z, IV 3/2-X,+Y,3/2-Z

Bi2 I8	3.0966(3)	I8 Bi2 I2^{I}	83.846(9)	I5 Bi1 I1	171.991(11)
Bi2 I4	3.0626(5)	I8 Bi2 I5	88.478(12)	I5 Bi1 I7^{II}	85.957(11)
Bi2 I2^{I}	3.3375(4)	I4 Bi2 I8	169.250(11)	I1 Bi1 I4	89.578(12)
Bi2 I5	3.1577(4)	I4 Bi2 I2^{I}	85.409(11)	I1 Bi1 I7^{II}	86.160(10)
Bi2 I7	2.9875(4)	I4 Bi2 I5	90.971(11)	I3 Bi1 I4	94.928(12)
Bi2 I6	2.8907(4)	I5 Bi2 I2^{I}	85.318(11)	I3 Bi1 I2	92.237(12)
Bi1 I4	3.1522(4)	I7 Bi2 I8	86.535(12)	I3 Bi1 I5	91.383(12)
Bi1 I2	2.9896(4)	I7 Bi2 I4	92.634(12)	I3 Bi1 I1	96.476(11)
Bi1 I5	3.0512(5)	I7 Bi2 I2^{I}	87.250(11)	I3 Bi1 I7^{II}	77.186(13)
Bi1 I1	3.1001(4)	I7 Bi2 I5	171.454(12)	Bi2^{III} I8 Bi2	125.283(18)
Bi1 I7^{II}	3.3513(4)	I6 Bi2 I8	97.917(11)	Bi2 I4 Bi1	88.816(12)
Bi1 I3	2.8885(4)	I6 Bi2 I4	92.825(12)	Bi1 I2 Bi2^{II}	93.009(11)
I8 Bi2^{III}	3.0966(3)	I6 Bi2 I2^{I}	178.182(13)	Bi1 I5 Bi2	88.916(12)
I2 Bi2^{II}	3.3377(4)	I6 Bi2 I5	95.157(13)	Bi1 I1 Bi1^{IV}	125.151(19)
I1 Bi1^{IV}	3.1001(3)	I6 Bi2 I7	92.402(12)	Bi2 I7 Bi1^{I}	92.773(11)
I7 Bi1^{I}	3.3513(4)	I4 Bi1 I7^{II}	86.057(11)	C6 N5 C1	122.2(5)
N5 C6	1.283(7)	I2 Bi1 I4	171.855(12)	C6 N5 C2	122.8(5)
N5 C1	1.489(8)	I2 Bi1 I5	92.408(12)	C2 N5 C1	114.9(5)
N5 C2	1.486(8)	I2 Bi1 I1	85.764(12)	N5 C6 C4	123.0(6)
C6 C4	1.481(8)	I2 Bi1 I7^{II}	86.966(11)	N5 C6 C3	121.3(5)
C6 C3	1.510(8)	I5 Bi1 I4	91.288(11)	C4 C6 C3	115.7(5)

Table S3: Comparison of bond length in Angstroms in the cation of **1** with literature references

	1	**$(Me_2C{=}NMe_2)ClO_4$**[a]	**$(Me_2C{=}NMe_2)BPh_4$**[a]
C=N	1.283(7)	1.30	1.291(8)
C-C, C-N	1.481(8)-1.510(8)	1.51	1.505(7)-1.515(7)

[a] Bond length according to [6] and [7], measured at room temperature. In both cases the cation is disordered about a mirror plane.

Table S4: Comparison of bond length in Angstroms in the anion of **1** with literature references

	1	**$(NMe_2H_2)_3[BiI_6]$**[a]	**$(dmes)_2[BiI_5]$**	**$(dim)_2[Bi_2I_{10}]$**[c]
Bi-$I_{terminal}$	2.8885(4) - 2.8907(4)	3.0342(8)-3.0881(8)	2.9484(7)-3.0775(6)	2.9821(6)-3.1176(6)
Bi-$I_{corner\text{-}sharing}$	3.0966(3) - 3.1001(4)	-	3.2078(7)-3.2405(7)	-
Bi-$I_{edge\text{-}sharing}$	2.9875(4) - 3.3513(4)	-	-	3.1757(5)-3.2574(5)

[a] Bond length according to [8], measured at room temperature.

[b] dmes = dimethyl(2-ethylammonium)sulfonium; bond length in the corner-sharing zig-zag-chain according to [9], measured at room temperature.

[c] dim = diimidazolium $(C_9H_{14}N_4)^{2+}$; bond length in the edge-sharing dinuclear unit according to [10], measured at room temperature.

A fairly broad range of Bi-$I_{edge\text{-}sharing}$ bond length is observed in **1**, in line with the well-documented trans-effect in halogenido pentelates, e.g. Bi-$I_{edge\text{-}sharing}$ bonds trans to Bi-$I_{terminal}$ bonds are significantly longer than those trans to other Bi-$I_{edge\text{-}sharing}$ bonds. [11]

Thermal analysis

The thermal behavior of **1** (17.4 mg), was studied by TGA/DSC on a NETSCH STA 409 C/CD from 25 °C to 1000 °C with a heating rate of 10 °C $\mathrm{min^{-1}}$ in a constant flow of 100 ml $\mathrm{min^{-1}}$ N_2. A mass loss of 98.4 % starts at 290 °C. The DSC shows an endothermic peak at 258 °C. During visual inspection of a sample during heating, no melting of the sample at this temperature was observed, indicating a solid-solid phase transition.

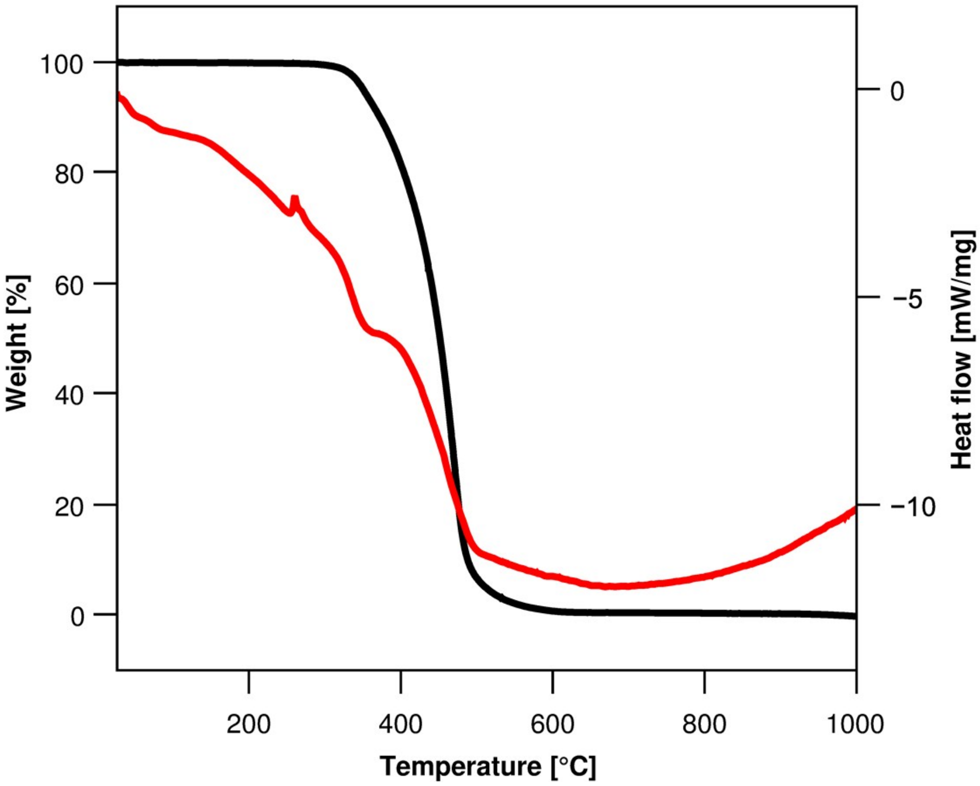

Figure S2. TGA and DSC of **1**.

Powder diffraction

Powder patterns were recorded on a *STADI MP* (*STOE* Darmstadt) powder diffractometer, with CuK$_{\alpha1}$ radiation with λ= 1.54056 Å at room temperature in transmission mode from 3 to 80° in 2θ. The pattern of **1** confirms the presence of the phase determined by SCXRD measurement and the absence of any major crystalline by-products. A study of the hydrolysis sensitivity of **1** was performed by first measuring a freshly prepared powder sample, followed by measuring a sample that was exposed to humidity. To provide a well-defined water-saturated atmosphere a Schlenk tube filled was filled with 10 mL of water. A sample of **1** was suspended above the surface of the water on a piece of scotch tape. The closed tube was kept at room temperature and the sample was removed and measured after 24 h. The pattern shows that **1** remains stable under these high humidity conditions. A study of the long term stability was also conducted, aging a sample in air for 5 months. The corresponding powder pattern shows that no significant decomposition takes place during this timeframe.

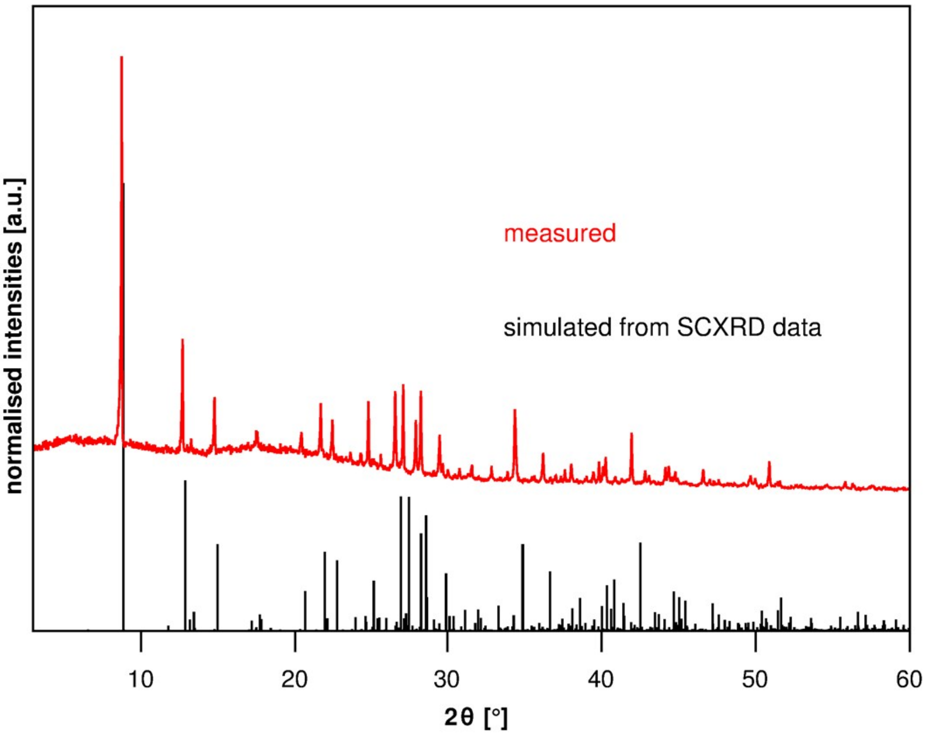

Figure S3. Powder diffraction pattern of **1**.

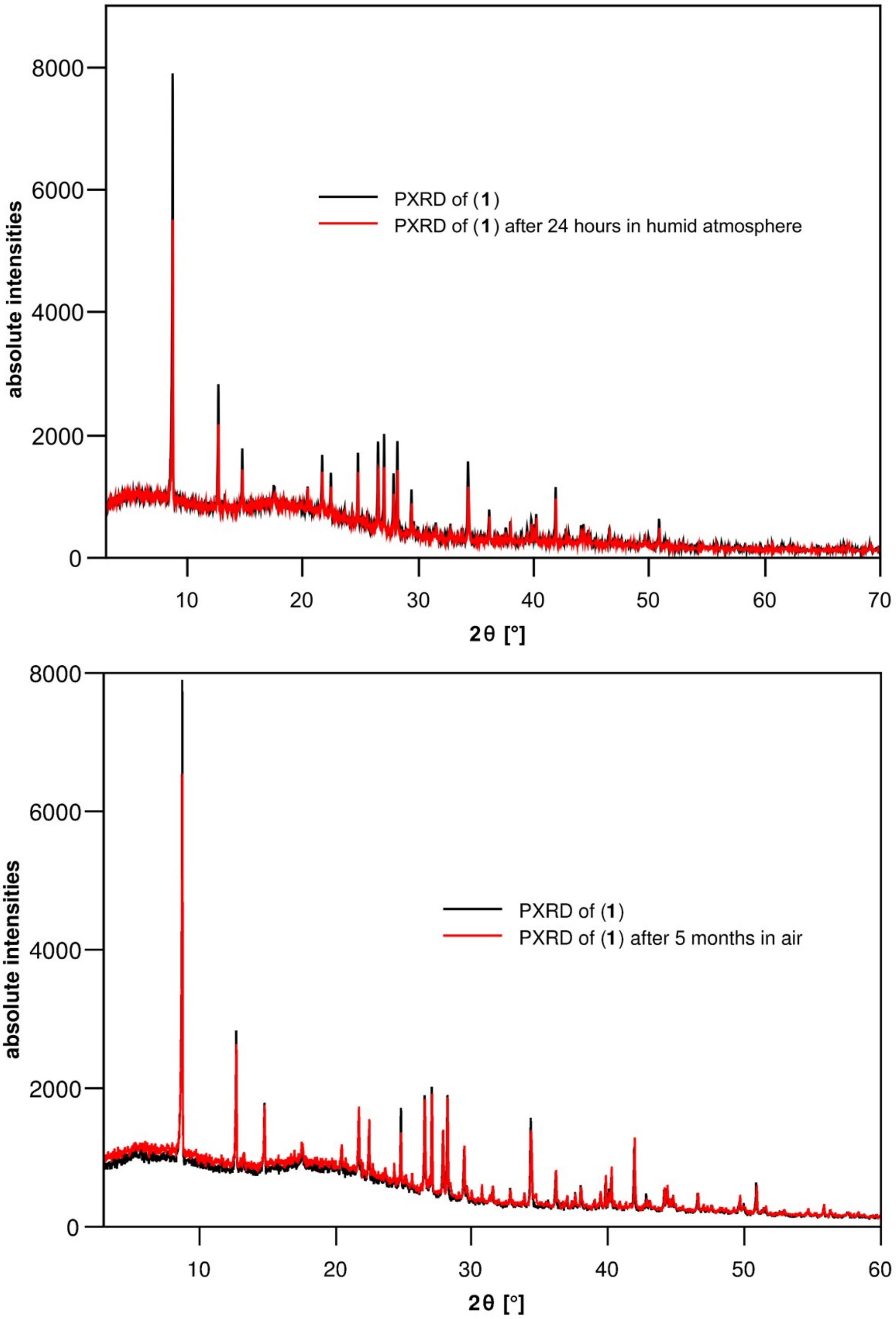

Figure S4. Powder diffraction patterns of a fresh sample of **1** in comparison with a sample stored in a water saturated atmosphere for 24h (top) and aged in air for 5 months (bottom). Data is not normalized or background-corrected to show that no increase in amorphous background below 30° in 2θ is observed between the two compared measurements. The difference in absolute intensities can likely be attributed to small differences in sample preparation such as the exact amount of substance or placement on the scotch tape and sample holder.

IR spectroscopy

An IR spectrum of **1** was recorded on a *Bruker Tensor 37* FT-IR spectrometer equipped with an ATR-Platinum measuring unit. The sample showed significant overall absorption in the measurement range. The characteristic band of the C=N group can be observed at 1666 cm^{-1}, close to values reported for $(Me_2N{=}CMe_2)Ag_2I_3$ (1680 cm^{-1})[12] and $(Me_2N{=}CMe_2)ClO_4$ (1687 cm^{-1}).[13]

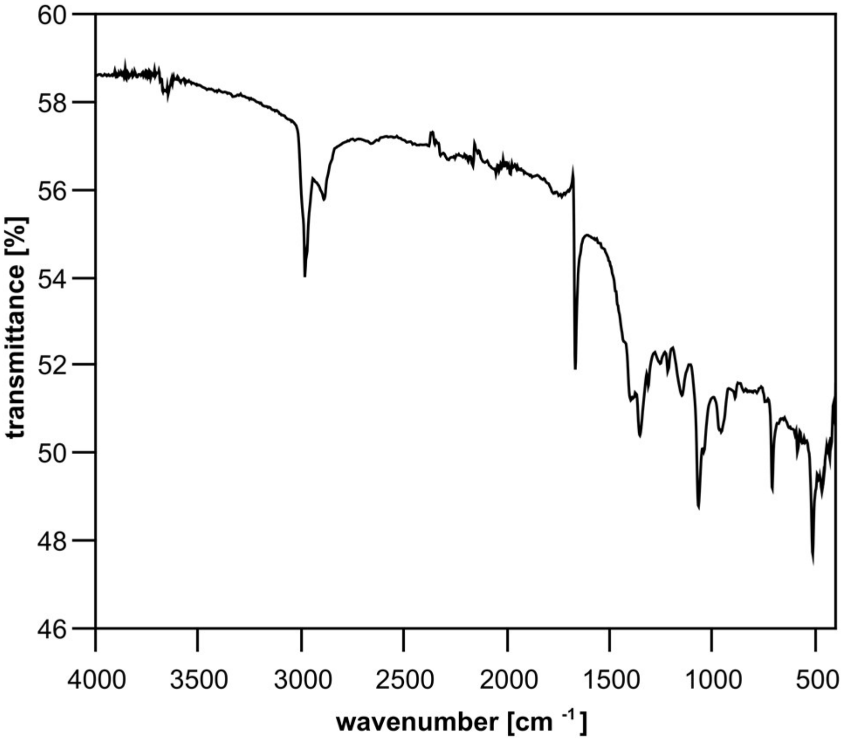

Figure S5. IR spectrum of **1**.

Raman Spectroscopy

A Raman spectrum of **1** was recorded on a confocal Raman microscope (*Monovista CRS+, S&I*) with 633 nm laser excitation. Strong bands are observed at 140, 110 and 65 cm^{-1}, which can be tentatively assigned to Bi-I$_{terminal}$ and Bi-I$_{bridging}$ stretching modes[14] and I-Bi-I scissoring modes,[15] respectively.

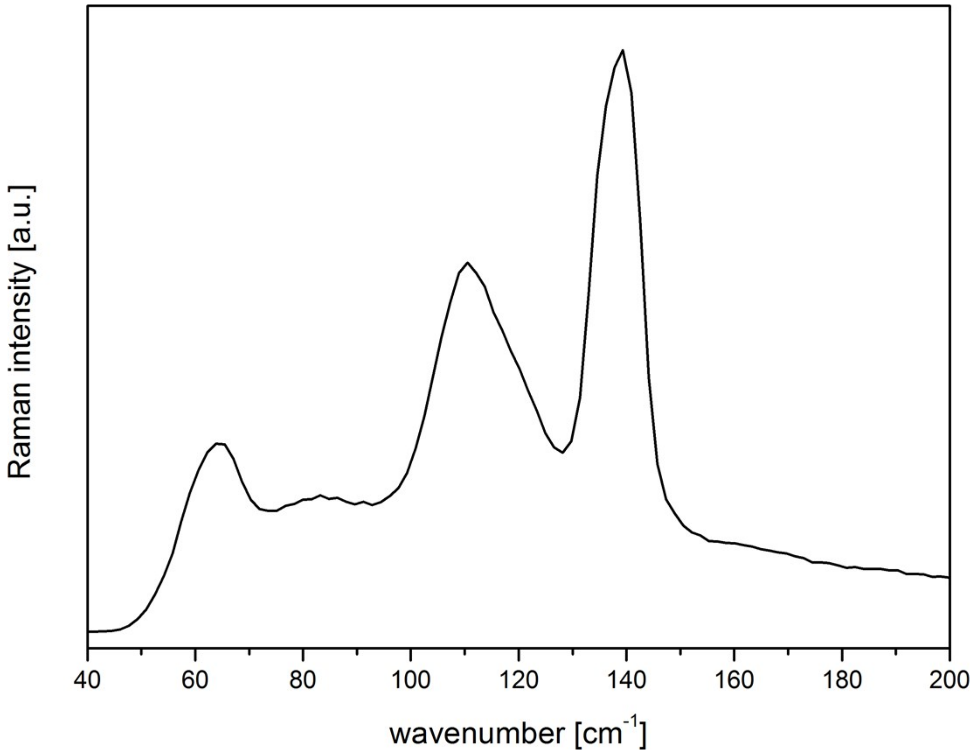

Figure S6. Raman spectrum of **1**.

Optical properties

Optical absorption spectra were recorded on a *Varian Cary 5000* UV/Vis/NIR spectrometer in the range of 200-800 nm in diffuse reflectance mode employing a Praying Mantis accessory (*Harrick*). An onset of absorption can be observed at 671.5 nm (1.8 eV). For ease of viewing, raw data was transformed from %Reflectance R to Absorbance A according to A = log (1/R).[16]

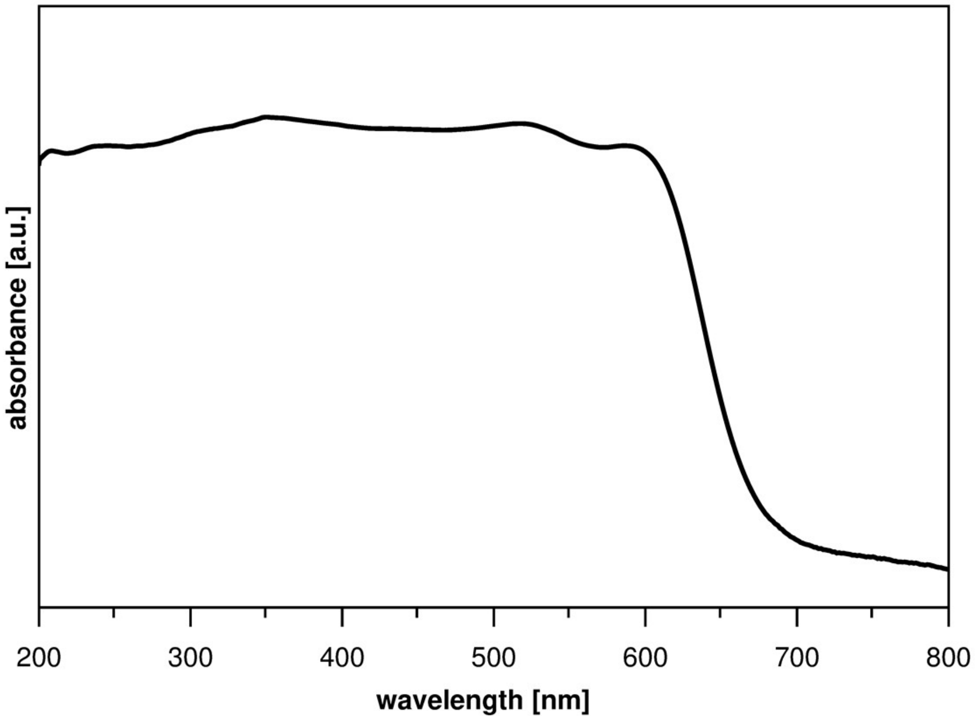

Figure S7. Optical absorption spectrum of **1**, measured in diffuse reflectance.

Details of Computational Studies

Density functional theory (DFT) calculations were performed with the Vienna Ab initio Simulation Package (VASP 5.4.4).[17-19] The projector-augmented wave (PAW) method was used in conjunction with the "standard" pseudo potentials for all atoms (version PBE5.4).[20] Dispersion interactions were captured with the DFT-D3 scheme using the Becke-Johnson-type damping function.[21],[22] The precision tag was set to "accurate", a total energy difference of at most 10^{-5} eV was used for SCF convergence while setting the plane wave energy cutoff to 400 eV. All calculations were done with a Γ-centered 1×2×1 k-mesh. The mesh containing twice as many k-points is more favorable in total energy by only 6 kJ/mol indicating very good convergence. For structure optimization, the generalized gradient approximation (GGA) based exchange-correlation functional proposed by Perdew, Burke and Ernzerhof (PBE)[23] was used without spin-orbit coupling (SOC).[24] The force convergence criterion was 10^{-2} eV/Å. Further electronic structure analysis calculations do include SOC except Crystal Orbital Hamilton Population (COHP). HSE06 and TB09 calculations were carried out on the optimized PBE structure. All convergence criteria were kept identical and SOC was included.

Periodic energy decomposition analysis (pEDA)[25] and QTAIM[26],[27] were calculated with the Amsterdam Modeling Suite (AMS-BAND 18.105)[28-31] while sampling k-space at the Γ-point. Again, the PBE-D3(BJ) functional was used in conjunction with the atom centered DZP[32-34] basis set and a 'large' frozen core. Numerical quality was set to 'Good'. Scalar relativistic effects were included.

Raw data is available at the NOMAD repository. DOI:
http://dx.doi.org/10.17172/NOMAD/2019.06.27-1

Atomic structure:

Table S5: Crystallographic data for **1** compared to calculation.

	Experiment	Theory	Δ%
a / Å	14.4647	14.2472	-1.5
b / Å	7.5084	7.4070	-1.4
c / Å	20.9965	20.8340	-0.8
α / °	90	90.015	0.0
β / °	108.165	108.603	0.4
γ / °	90	89.987	0.0
V / Å^3	2166.7	2083.7	-3.8
d(Bi-Bi) / Å	4.349	4.277	-1.7
d(I-I) / Å	3.839	3.692	-3.8

The structural optimization starting from the experimentally derived structure leads to good agreement with deviations of <1.5% in lattice vectors and a slightly too short (<3.8%) interlayer I-I distances resulting in an underestimation in cell volume (<4%, Table S5). Starting from this structure, the band gap was derived from the density of states (DOS) with different density functionals. As shown in Table S6, the GGA-type functional PBE gives surprisingly good agreement with the experimentally derived band gap ($\Delta\Delta E_{gap}$ <0.2 eV), although this functional class is known to often underestimate the gap due to the self-interaction error.[35]

Consequently, the HSE06 functional including Hartree-Fock type exchange – which usually corrects this underestimation – now gives a too large band gap. The best agreement to experiment is found for the TB09 functional, which contains one additional parameter fitted to semiconductor band gaps and has been found to perform very well for other materials in the past by us and others.[36],[37] This lends confidence to choosing the more computationally efficient PBE functional for further investigations of the electronic structure.

Table S6. Band gap (ΔE_{gap}) from density of states calculations including spin-orbit coupling effects with different density functionals.

Method	ΔE_{gap} in eV
Experiment (this study)	1.8
PBE [23]	1.64
HSE06 [39]	2.23
TB09 [36]	1.87

Table S7. Results from AIM bond critical point analysis for iodine-iodine contacts. The electron density is given in $e{*}a0^{-3}$.

	Interlayer I-I	Intralayer I-I
ρ	0.0128	0.0072
$\nabla^2\rho$	0.0281	0.0160

Table S8. Results of energy decomposition analysis for extended systems (pEDA) for 1. Fragments are outlined in Figure S8a.

ΔE_{int}	-598
$\Delta E_{\text{int}}(\text{disp})^{a}$	-317 (53%)
$\Delta E_{\text{int}}(\text{elec})^{a}$	-281 (47%)
ΔE_{Pauli}	509
$\Delta E_{\text{elstat}}{}^{b}$	-445 (56%)
$\Delta E_{\text{orb}}{}^{b}$	-344 (44%)
$\Delta E_{\text{orb}}(\text{I-I})^{c}$	-146 (42%)

[a] Percentage values give the relative contributions of dispersion and electronic effects to ΔE_{int}; [b] percentage values give the relative contributions to the attractive pEDA terms ΔE_{elstat} and ΔE_{orb}; [c] percentage values give the relative contributions to ΔE_{orb} from the NOCV scheme. All energies are given in kJ mol^{-1}.

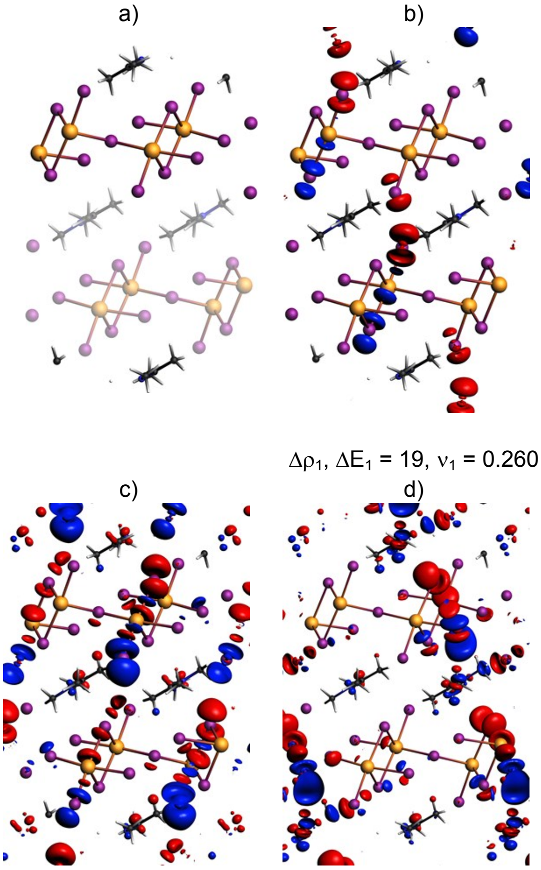

$\Delta\rho_1$, $\Delta E_1 = 19$, $\nu_1 = 0.260$

$\Delta\rho_5$, $\Delta E_5 = 10$, $\nu_5 = 0.185$ $\Delta\rho_{10}$, $\Delta E_{10} = 8$, $\nu_{10} = 0.148$

Figure S8. a) Fragments used for pEDA. b-d) deformation densities (Δρ) showing the charge accumulation (blue) and depletion (red) in the iodine layers. Every Δρ is fourfold degenerate (only one example shown) and slightly different isovalues have been used for visual clarity (b: $3*10^{-5}$, c: $5*10^{-6}$, d: $3*10^{-6}$).

We can identify 12 deformation densities that clearly show charge flow between non-bonding electron pairs of the iodine atoms, three of them are shown in Figure S8.The largest charge shift is seen here toward the edge-sharing iodine atoms ($\Delta\rho_{1-4}$; Fig. S8b) which contributes 74 kJ mol^{-1} (21%) to the orbital stabilization term and leads to slightly larger negative charge at these atoms (q(AIM) = -0.41 e; corner-sharing and terminal I-atoms q(AIM) = -0.37/-0.39 e).

The polarization of iodine atoms thus makes up 42% of the stabilizing orbital interactions and is the major contribution here. The remaining deformation densities are numerous and very small and do not allow further interpretation. But the total deformation density (as sum of all individual densities) is in very good agreement with the commonly used charge density difference and confirms that the iodine-iodine charge shift is the major contribution (Figure S9).

Comparison of charge density difference plot and deformation density from intermediate to final wavefunction in pEDA:

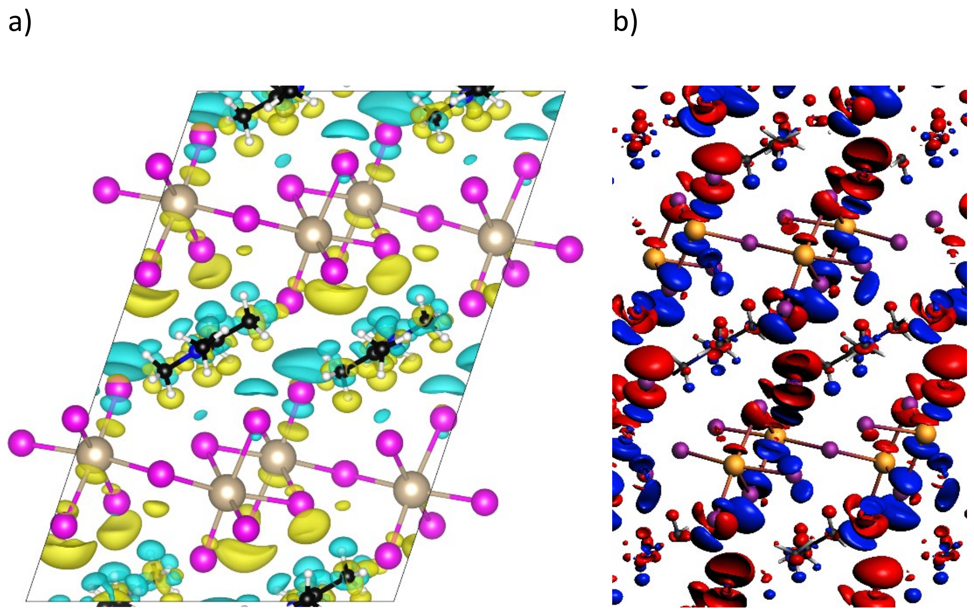

Figure S9: a) Charge density difference plot. Yellow: accumulation of charge density. Cyan: depletion of charge density. Electron density is mainly redistributed within the $[Bi_2I_7]^-$ layer due to its larger polarizability compared to the organic layer. b) Deformation density. Blue: accumulation of charge density. Red: depletion of charge density. The resulting picture is rather similar but the shape of the orbitals where density either flows to or from is more clearly visible. Also, the polarization of the organic layer is already considered so the deformation density is more concentrated in the relevant parts of the structure.

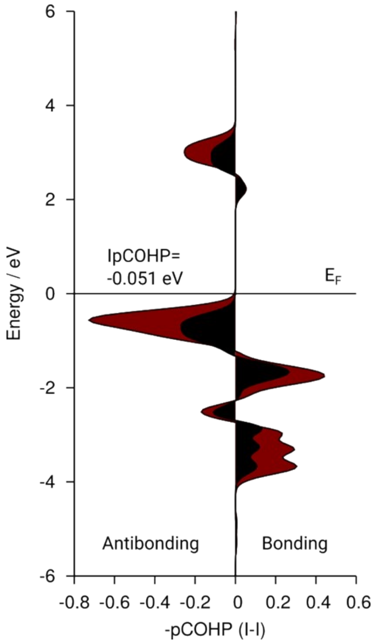

Figure S10. Negative of the pCOHP values of the interlayer I-I bond elongated by 9.6% (shaded black) in comparison to the pCOHP of the optimized structure (red areas).

References

[1] M. Ruck, *Z. Kristallogr.,* 1995, **210**, 650-655.

[2] T. Li, Y. Hu, C. A. Morrison, W. Wu, H. Han and N. Robertson, *Sustainable Energy Fuels,* 2017, **1**, 308-316.

[3] a) G. M. Sheldrick, *Acta Cryst.,* 2008, **A64**, 112-122; b) G. M. Sheldrick, *Acta Cryst.,* 2015, **A71**, 3-8; c) G. M. Sheldrick, *Acta Cryst.,* 2015, **C71**, 3-8.

[4] O. V. Dolomanov, L. J. Bourhis, R. J. Gildea, J. A. K. Howard and H. Puschmann, *J. Appl. Crystallogr.,* 2009, **42**, 339-341.

[5] K. Brandenburg, Diamond, Crystal Impact GbR: Bonn, Germany, 2005.

[6] L. M. Trefonas, R. L. Flurry Jr., R. Majeste, E. A. Meyers and R. F. Copeland, *J. Am. Chem. Soc.,* 1966, **88**, 2145-2149.

[7] O. Knop, T. S. Cameron, P. K. Bakshi, W. Kwiatkowski, S. C. Choi and D. Adhikesavalu, *Can. J. Chem.,* 1993, **71**, 1495-1523.

[8] M. Lindsjö, A. Fischer and L. Kloo, *Z. Anorg. Allg. Chem.,* 2005, **631**, 1497-1501.

[9] N. Louvain, N. Mercier and F. Boucher, *Inorg. Chem.,* 2009, **48**, 879-888.

[10] A. García-Fernández, I. Marcos-Cives, C. Platas-Iglesias, S. Castro-García, D. Vázquez-García, A. Fernández and M. Sánchez-Andújar, *Inorg. Chem.,* 2018, **57**, 7655−7664.

[11] H.-L. Sheu and J. Laane, *Inorg. Chem.,* 2013, **52**, 4244−4249.

[12] R. Kuhn and H. Schretzmann, *Chem. Ber.,* 1957, **90**, 557-564.

[13] N. J. Leonard and J. V. Paukstelis, *J. Org. Chem.,* 1963, **28**, 3021-3024.

[14] J. Laane and P. W. Jagodzinski, *Inorg. Chem.,* 1980, **19**, 44-49.

[15] S. Öz, J.-C. Hebig, E. Jung, T. Singh, A. Lepcha, S. Olthof, J. Flohre, Y. Gao, R. German, P. H. M. van Loosdrecht, K. Meerholz, T. Kirchartz and S. Mathur, *Sol. Energ. Mat. Sol. Cells,* 2016, **158**, 195-201.

[16] S. I. Boldish and W. B. White, *Am. Mineral.,* 1998, **83**, 865-871.

[17] G. Kresse and J. Hafner, *Phys. Rev. B,* 1993, **47**, 558.

[18] G. Kresse and J. Furthmüller, *Comput. Mater. Sci.,* 1996, **6**, 15-50.

[19] G. Kresse and J. Furthmüller, *Phys. Rev. B,* 1996, **54**, 11169.

[20] G. Kresse and D. Joubert, *Phys. Rev. B,* 1999, **59**, 1758.

[21] S. Grimme, J. Anthony, S. Ehrlich and H. Krieg, *J. Chem. Phys.,* 2010, **132**, 154104.

[22] S. Grimme, S. Ehrlich and L. Goerigk, *J. Comput. Chem.,* 2011, **32**, 1456-1465.

[23] J. P. Perdew, K. Burke and M. Ernzerhof, *Phys. Rev. Lett.,* 1996, **77**, 3865.

[24] S. Steiner, S. i Khmelevskyi, M. Marsmann and G. Kresse, *Phys. Rev. B,* 2016, **93**, 224425.

[25] M. Raupach and R. Tonner, *J. Chem. Phys.,* 2015, **142**, 194105.

[26] J. I. Rodriguez, A. M. Köster, P. W. Ayers, A. Santos-Valle, A. Vela, G. Merino, *J. Comput. Chem.,* 2009, **30**, 1082-1092.

[27] J. I. Rodriguez, R. F. W. Bader, P. W. Ayers, C. Michel, A. W. Gotz and C. Bo, *Chem. Phys. Lett.,* 2009, **472**, 149-152.

[28] a) G. te Velde and E. J. Baerends, *Phys. Rev. B,* 1991, **44**, 7888; b) G. Wiesenekker and E. J. Baerends, *J. Phys. Condens. Matter,* 1991, **3**, 6721.

[29] M. Franchini, P. H. T. Philipsen and L. Visscher, *J. Comput. Chem.,* 2013, ***34***, 1819-1827.

[30] M. Franchini, P.H.T. Philipsen, E. van Lenthe and L. Visscher, *J. Chem. Theory Comput.,* 2014, **10**, 1994-2004.

[31] BAND2018, SCM, Theoretical Chemistry, Vrije Universiteit, Amsterdam, The Netherlands, http://www.scm.com.

[32] E. van Lenthe and E. J. Baerends, *J. Comput. Chem.,* 2003, **24**, 1142-1156.

[33] D. P. Chong, E. van Lenthe, S. J. A. van Gisbergen and E. J. Baerends, *J. Comput. Chem.,* 2004, **25**, 1030-1036.

[34] D. P. Chong, *Mol. Phys.,* 2005, **103**, 749-761.

[35] J. P. Perdew, *Int. J. Quantum Chem.,* 1985, **28**, 497-523.

[36] F. Tran and P. Blaha, *Phys. Rev. Lett.,* 2009, **102**, 226401.

[37] P. Rosenow, L. C. Bannow, E. W. Fischer, W. Stolz, K. Volz, S. W. Koch and R. Tonner, *Phys. Rev. B,* 2018, **97**, 075201.

[38] A. V. Krukau, O. A. Vydrov, A. F. Izmaylov and G. E. Scuseria, *J. Chem. Phys*., 2006, **125**, 224106.

D.4. Multinary Halogenido Bismuthates Beyond the Double Perovskite Motif

Supporting Information on

Multinary Halogenido Bismuthates Beyond the Double Perovskite Motif

Natalie Dehnhardt,[†] *Hayden Paneth,*[‡] *Nikolas Hecht,*[§] *Johanna Heine*,*[†]

† Department of Chemistry and Material Sciences Center, Philipps-Universität Marburg, Hans-Meerwein-Straße, 35043 Marburg, Germany.

‡ Department of Chemistry, Union College, Schenectady, New York 12308, USA.

§ Department of Chemistry, Technische Universität Darmstadt, 64287 Darmstadt, Germany.

*Email: johanna.heine@chemie.uni-marburg.de

Crystallographic Details

Single crystal X-ray determination was performed on a Bruker Quest D8 diffractometer with microfocus MoKα radiation and a Photon 100 (CMOS) detector (**1, 2**, **3, 4, 5**) or an a STOE IPDS-2T diffractometer equipped with an imaging plate detector system using MoKα radiation with graphite monochromatization (**6**). All measurements were performed at 100 K.

Table S1: Crystallographic data for $(PBz_4)_3Bi_3Br_{12}$ (**1**), CCDC 1964160.

Empirical formula	$C_{84}H_{84}Bi_3Br_{12}P_3$
Formula weight	2772.28
Crystal system	monoclinic
Space group	$P2_1/c$
a/Å	12.3041(4)
b/Å	32.8540(12)
c/Å	22.3547(8)
β/°	102.4080(10)
Volume/Å^3	8825.6(5)
Z	4
ρ_{calc}g/cm^3	2.086
μ/mm^{-1}	11.496
F(000)	5208.0
Crystal size/mm^3	0.13 × 0.065 × 0.059
Absorption correction (T_{min}/T_{max})	multi-scan (0.0607/0.0915)
2Θ range for data collection/°	4.16 to 50.608
Index ranges	$-14 \leq h \leq 14$, $-39 \leq k \leq 39$, $-25 \leq l \leq 26$
Reflections collected	147837
Independent reflections	16065 [$R_{int} = 0.1158$, $R_{sigma} = 0.0560$]
Data/restraints/parameters	16065/0/919
Goodness-of-fit on F^2	1.018
Final R indexes [I>=2σ (I)]	$R_1 = 0.0342$, $wR_2 = 0.0450$
Final R indexes [all data]	$R_1 = 0.0625$, $wR_2 = 0.0500$
Largest diff. peak/hole / e Å^{-3}	1.17/-0.88

Details of crystal structure refinement: All non-hydrogen atoms were refined anisotropically. Hydrogen atoms were assigned to idealized geometric positions and included in structure factors calculations.

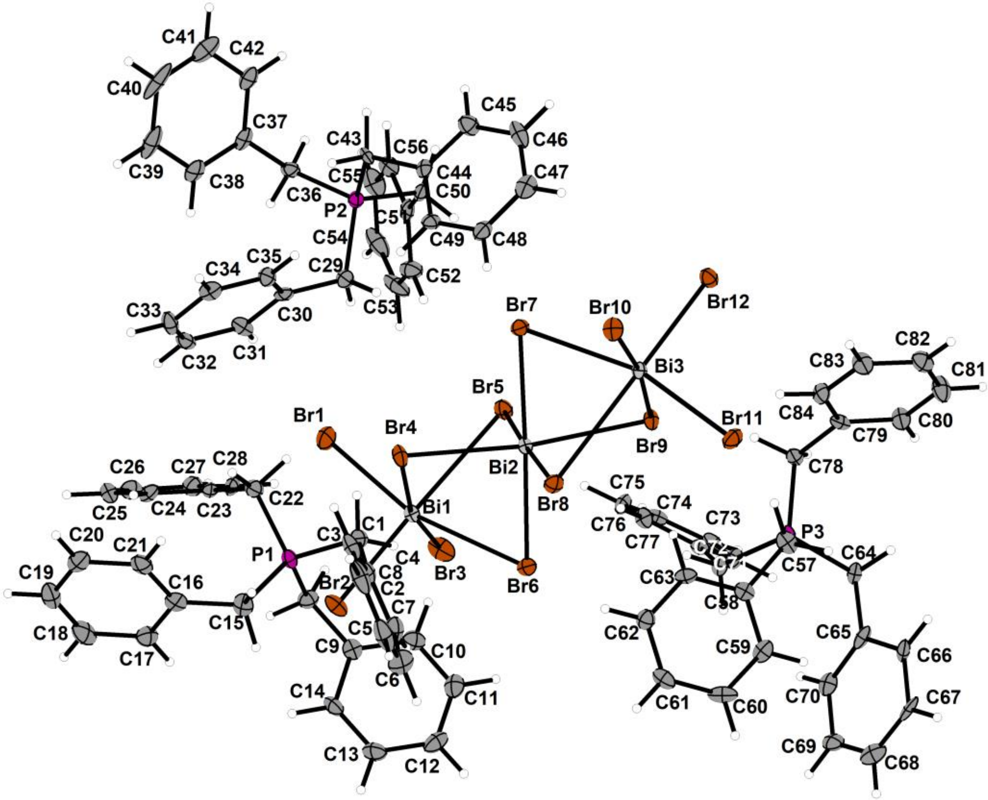

Figure S1: Asymmetric unit of **1**, ellipsoids at 50% probability.

Table S2: Crystallographic data for $(PBz_4)_2(MeCN)_2Cu_2Bi_2Br_{10}$ (**2**), CCDC 1964163.

Empirical formula	$C_{60}H_{62}Bi_2Br_{10}Cu_2N_2P_2$
Formula weight	1108.60
Crystal system	triclinic
Space group	*P*-1
a/Å	11.0504(5)
b/Å	12.1103(5)
c/Å	13.8748(6)
α/°	81.6230(10)
β/°	74.4050(10)
γ/°	70.2340(10)
Volume/Å^3	1679.98(13)
Z	1
ρ_{calc}g/cm^3	2.192
μ/mm^{-1}	11.878
F(000)	1040.0
Crystal size/mm^3	0.328 × 0.224 × 0.188
Absorption correction (T_{min}/T_{max})	multi-scan (0.0076/0.0264)
2Θ range for data collection/°	4.446 to 50.656
Index ranges	$-13 \leq h \leq 13$, $-14 \leq k \leq 14$, $-16 \leq l \leq 16$
Reflections collected	28264
Independent reflections	6123 [R_{int} = 0.0538, R_{sigma} = 0.0401]
Data/restraints/parameters	6123/0/353
Goodness-of-fit on F^2	1.081
Final R indexes [I>=2σ (I)]	R_1 = 0.0213, wR_2 = 0.0510
Final R indexes [all data]	R_1 = 0.0235, wR_2 = 0.0519
Largest diff. peak/hole / e Å^{-3}	0.63/-0.94

Details of crystal structure refinement: All non-hydrogen atoms were refined anisotropically. Hydrogen atoms were assigned to idealized geometric positions and included in structure factors calculations.

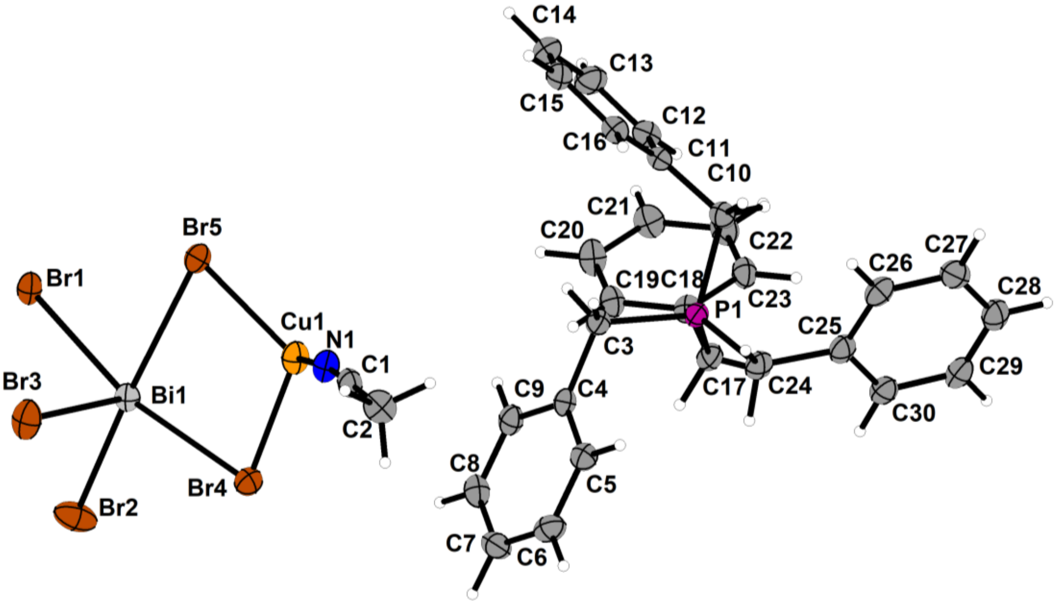

Figure S2: Asymmetric unit of **2**, ellipsoids at 50% probability.

Table S3: Crystallographic data for $(PBz_4)Bi_2I_7$ (**3**), CCDC 1964161.

Empirical formula	$C_{28}H_{28}Bi_2I_7P$
Formula weight	1701.73
Crystal system	triclinic
Space group	P-1
a/Å	11.8654(6)
b/Å	12.9943(6)
c/Å	13.2031(6)
α/°	109.1820(10)
β/°	91.763(2)
γ/°	96.687(2)
Volume/Å^3	1904.41(16)
Z	2
ρ_{calc}g/cm^3	2.968
μ/mm^{-1}	14.961
F(000)	1496.0
Crystal size/mm^3	0.419 × 0.411 × 0.2
Absorption correction (T_{min}/T_{max})	numerical (0.03282/0.17705)
2Θ range for data collection/°	4.486 to 50.638
Index ranges	$-14 \leq h \leq 14$, $-15 \leq k \leq 15$, $-15 \leq l \leq 15$
Reflections collected	29850
Independent reflections	6939 [R_{int} = 0.0617, R_{sigma} = 0.0498]
Data/restraints/parameters	6939/42/343
Goodness-of-fit on F^2	1.102
Final R indexes [I>=2σ (I)]	R_1 = 0.0422, wR_2 = 0.1064
Final R indexes [all data]	R_1 = 0.0447, wR_2 = 0.1082
Largest diff. peak/hole / e Å^{-3}	2.21/-5.91

Details of crystal structure refinement: All non-hydrogen atoms were refined anisotropically. Hydrogen atoms were assigned to idealized geometric positions and included in structure factors calculations. A number of ISOR restraints had to be used to obtain reasonable displacement parameters for some of the carbon atoms. The minimum residual density is comparatively high. We ascribe this to the fairly large crystal specimen that was chosen for measurement.

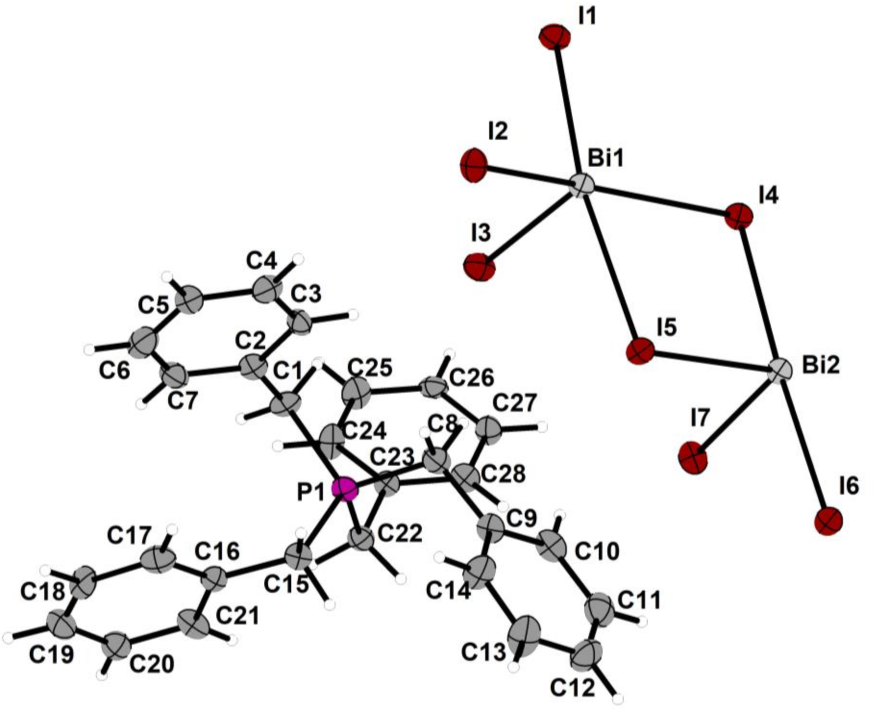

Figure S3: Asymmetric unit of **3**, ellipsoids at 50% probability.

Table S4: Crystallographic data for $(PBz_4)_2(MeCN)_2Cu_2Bi_2I_{10}$ (**4**), CCDC 1964162.

Empirical formula	$C_{60}H_{62}Bi_2Cu_2I_{10}N_2P_2$
Formula weight	2687.09
Crystal system	triclinic
Space group	P-1
a/Å	10.7763(5)
b/Å	12.5033(5)
c/Å	14.8812(7)
α/°	80.5280(10)
β/°	76.0830(10)
γ/°	70.2750(10)
Volume/Å^3	1824.38(14)
Z	1
ρ_{calc}g/cm^3	2.446
μ/mm^{-1}	9.694
F(000)	1220.0
Crystal size/mm^3	0.28 × 0.125 × 0.073
Absorption correction (T_{min}/T_{max})	multi-scan (0.0448/0.0915)
2Θ range for data collection/°	4.278 to 50.624
Index ranges	$-12 \le h \le 12$, $-15 \le k \le 15$, $-17 \le l \le 17$
Reflections collected	30276
Independent reflections	6639 [R_{int} = 0.0294, R_{sigma} = 0.0230]
Data/restraints/parameters	6639/0/353
Goodness-of-fit on F^2	1.140
Final R indexes [I>=2σ (I)]	R_1 = 0.0167, wR_2 = 0.0369
Final R indexes [all data]	R_1 = 0.0192, wR_2 = 0.0377
Largest diff. peak/hole / e Å^{-3}	0.43/-1.10

Details of crystal structure refinement: All non-hydrogen atoms were refined anisotropically. Hydrogen atoms were assigned to idealized geometric positions and included in structure factors calculations.

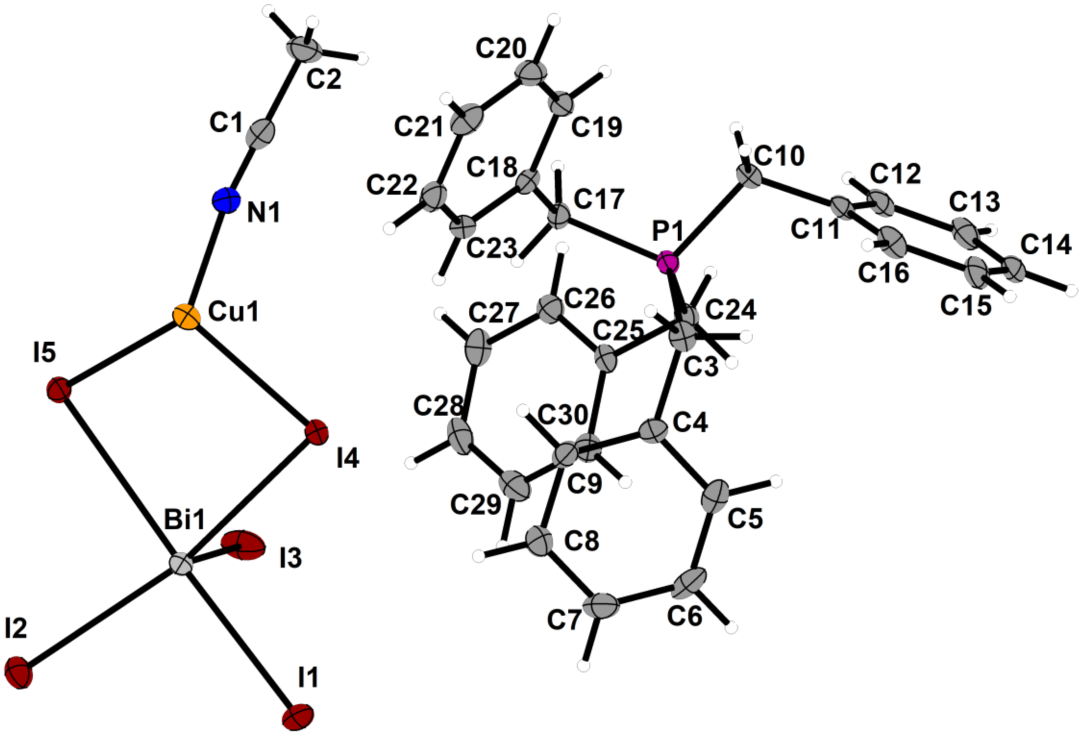

Figure S4: Asymmetric unit of **4**, ellipsoids at 50% probability.

Table S5: Crystallographic data for $(PBz_4)_2AgBi_2I_9$ (**5**), CCDC 1964165.

Empirical formula	$C_{56}H_{56}AgBi_2I_9P_2$
Formula weight	2458.87
Crystal system	monoclinic
Space group	$P2_1/n$
a/Å	24.2571(8)
b/Å	11.5623(4)
c/Å	25.4550(9)
β/°	116.1780(10)
Volume/Å^3	6407.0(4)
Z	4
ρ_{calc}g/cm^3	2.549
μ/mm^{-1}	10.203
F(000)	4448.0
Crystal size/mm^3	0.082 × 0.08 × 0.068
Absorption correction (T_{min}/T_{max})	multi-scan (0.6424/0.7452)
2Θ range for data collection/°	4.694 to 50.594
Index ranges	$-29 \leq h \leq 29$, $-13 \leq k \leq 13$, $-30 \leq l \leq 30$
Reflections collected	105076
Independent reflections	11644 [R_{int} = 0.0474, R_{sigma} = 0.0226]
Data/restraints/parameters	11644/0/631
Goodness-of-fit on F^2	1.066
Final R indexes [I>=2σ (I)]	R_1 = 0.0190, wR_2 = 0.0320
Final R indexes [all data]	R_1 = 0.0254, wR_2 = 0.0331
Largest diff. peak/hole / e Å^{-3}	0.82/-0.73

Details of crystal structure refinement: All non-hydrogen atoms were refined anisotropically. Hydrogen atoms were assigned to idealized geometric positions and included in structure factors calculations.

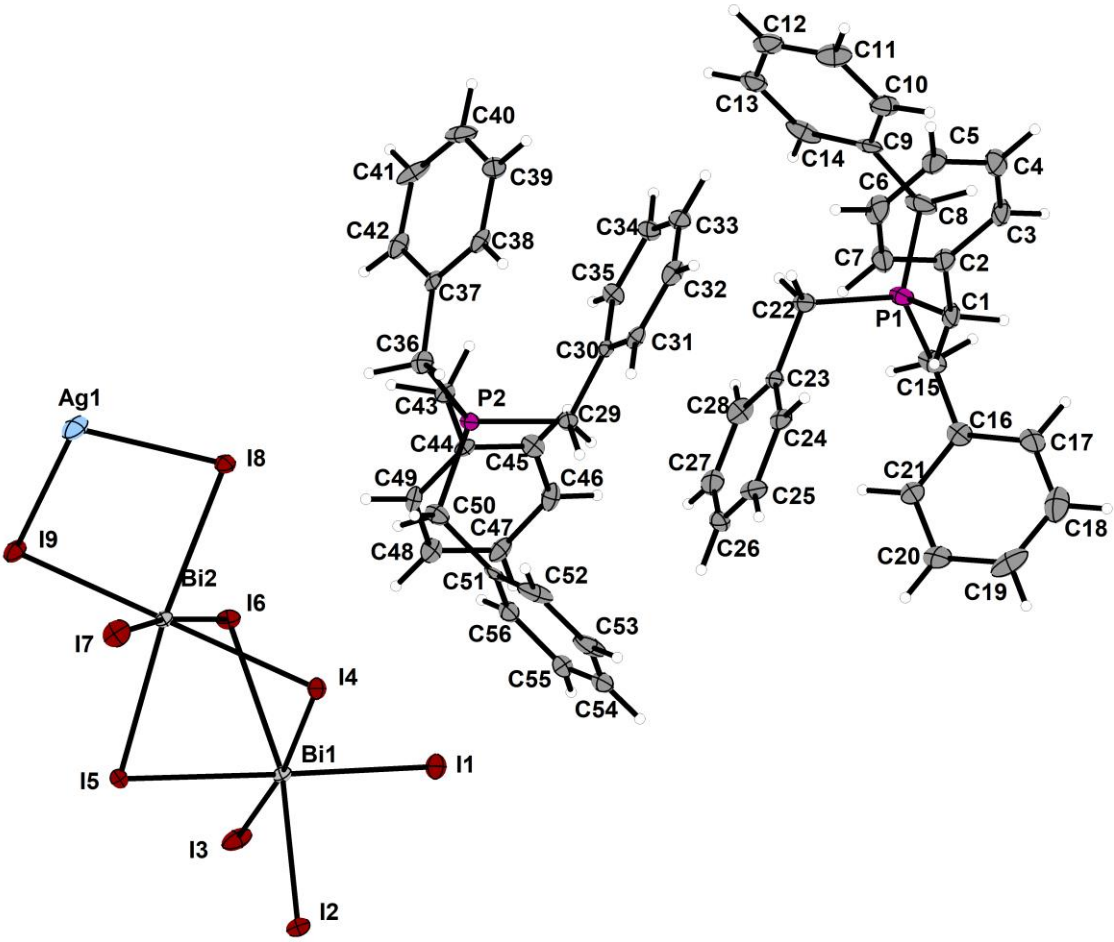

Figure S5: Asymmetric unit of **5**, ellipsoids at 50% probability.

Table S6: Crystallographic data for $(PBz_4)_3Bi_3I_{12}·C_4H_8O$ (**6**), CCDC 1964164.

Empirical formula	$C_{88}H_{92}Bi_3I_{12}OP_3$
Formula weight	3408.26
Crystal system	monoclinic
Space group	$P2_1/c$
a/Å	13.895(3)
b/Å	18.860(3)
c/Å	38.082(9)
β/°	90.588(19)
Volume/Å^3	9979(4)
Z	4
ρ_{calc}g/cm^3	2.269
μ/mm^{-1}	9.079
F(000)	6232.0
Crystal size/mm^3	0.017 × 0.0029 × 0.0026
Absorption correction (T_{min}/T_{max})	numerical (0.1976/0.2998)
2Θ range for data collection/°	3.612 to 49.998
Index ranges	$-16 \leq h \leq 16$, $-20 \leq k \leq 22$, $-45 \leq l \leq 45$
Reflections collected	46220
Independent reflections	17133 [R_{int} = 0.0535, R_{sigma} = 0.0483]
Data/restraints/parameters	17133/0/966
Goodness-of-fit on F^2	0.965
Final R indexes [I>=2σ (I)]	R_1 = 0.0291, wR_2 = 0.0611
Final R indexes [all data]	R_1 = 0.0440, wR_2 = 0.0647
Largest diff. peak/hole / e Å^{-3}	2.16/-1.62

Details of crystal structure refinement: All non-hydrogen atoms were refined anisotropically. Hydrogen atoms were assigned to idealized geometric positions and included in structure factors calculations.

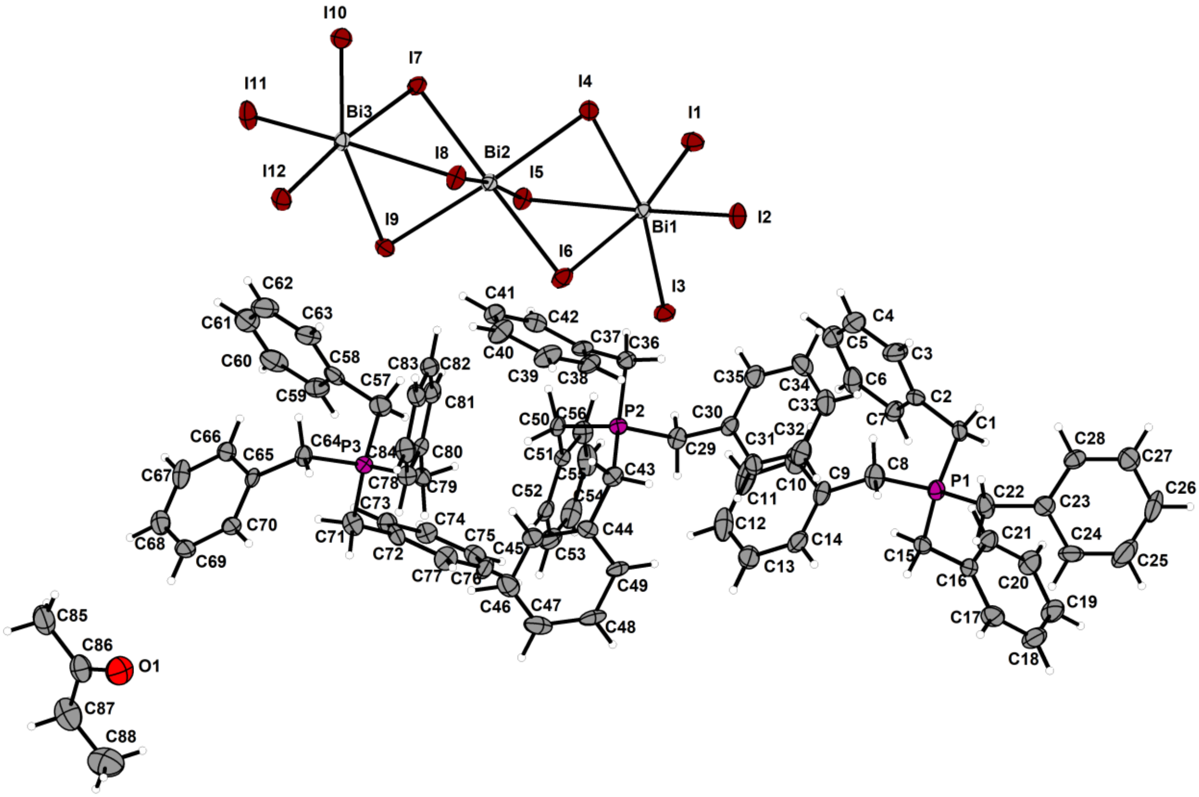

Figure S6: Asymmetric unit of **6**, ellipsoids at 50% probability.

Powder Diffraction

Powder patterns were recorded on a *STADI MP* (*STOE* Darmstadt) powder diffractometer, with $CuK_{\alpha1}$ radiation with λ= 1.54056 Å at room temperature in transmission mode. The patterns confirm the presence of the respective phase determined by SCXRD measurements and the absence of any major crystalline by-products unless otherwise indicated.

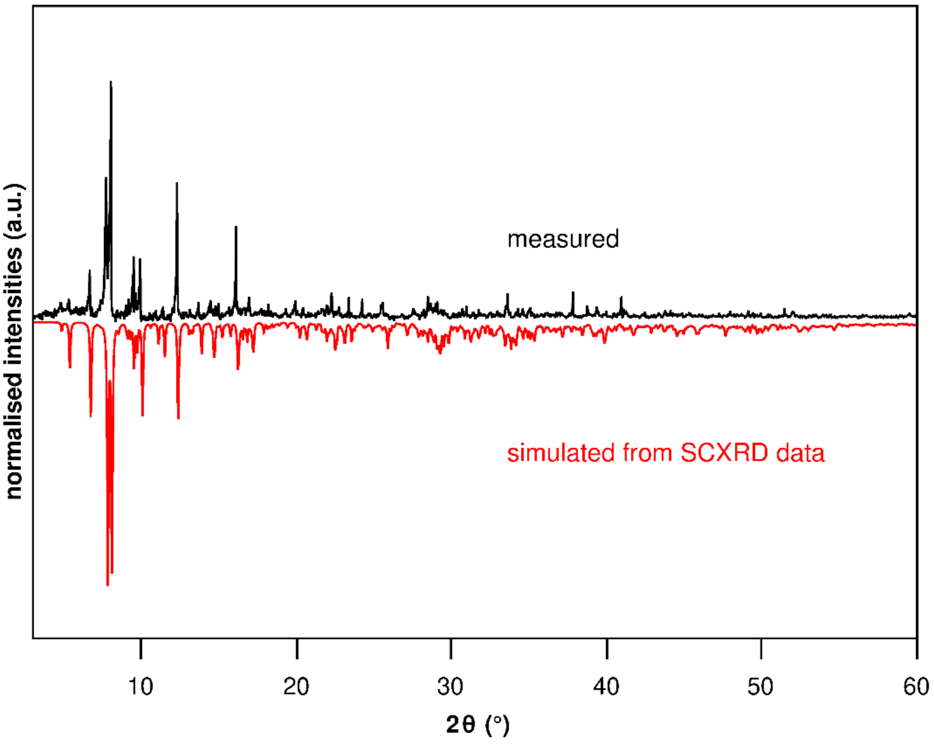

Figure S7. Powder diffraction pattern of $(PBz_4)_3Bi_3Br_{12}$ (**1**).

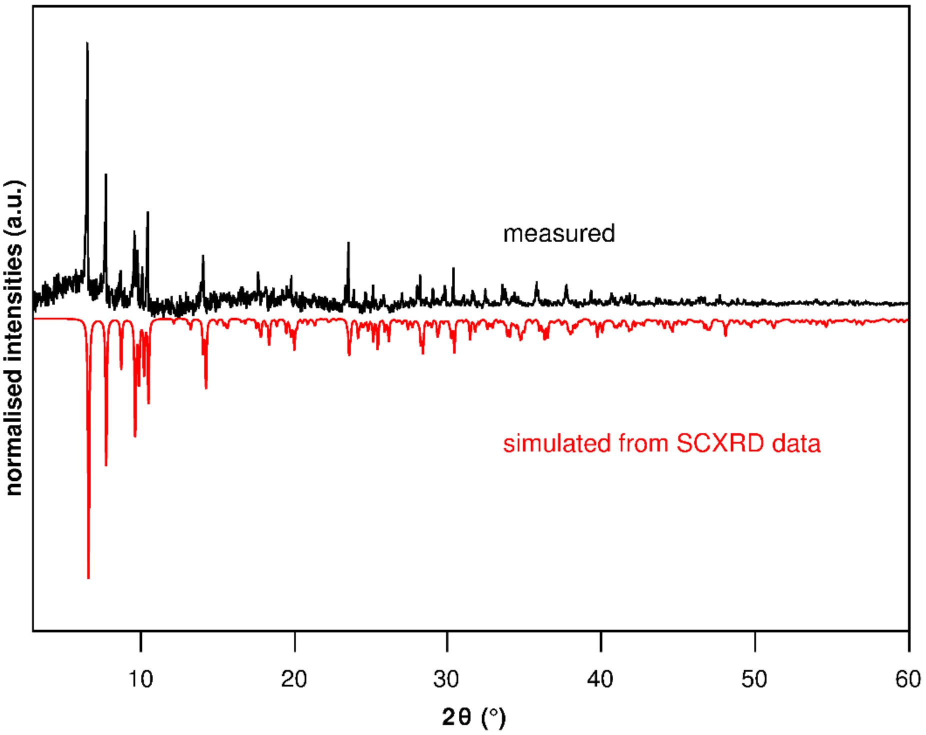

Figure S8. Powder diffraction pattern of $(PBz_4)_2(MeCN)_2Cu_2Bi_2Br_{10}$ (**2**), prepared from single crystals.

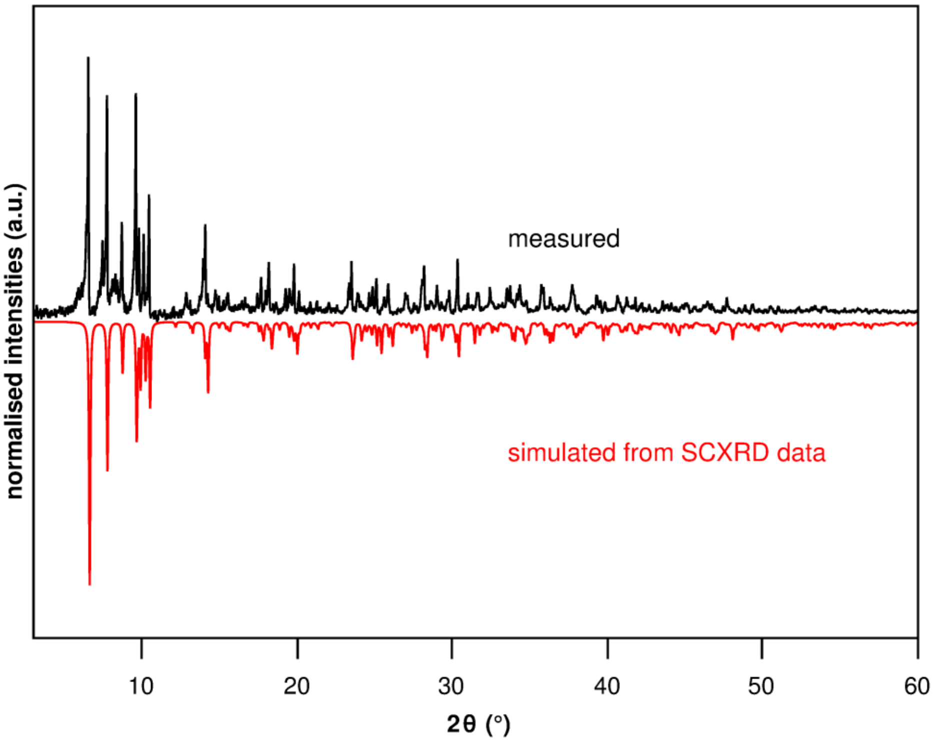

Figure S9. Powder diffraction pattern of microcrystalline powders of **2** obtained from direct synthesis showing additional reflections of a small amount of a side phase below 10°.

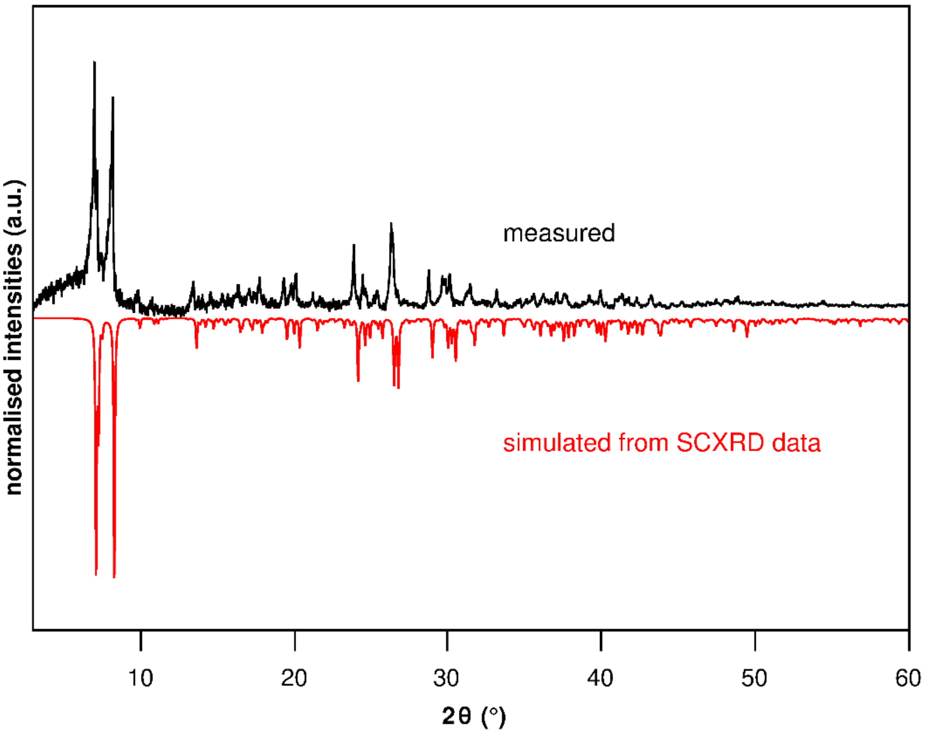

Figure S10. Powder diffraction pattern of $(PBz_4)Bi_2I_7$ (**3**).

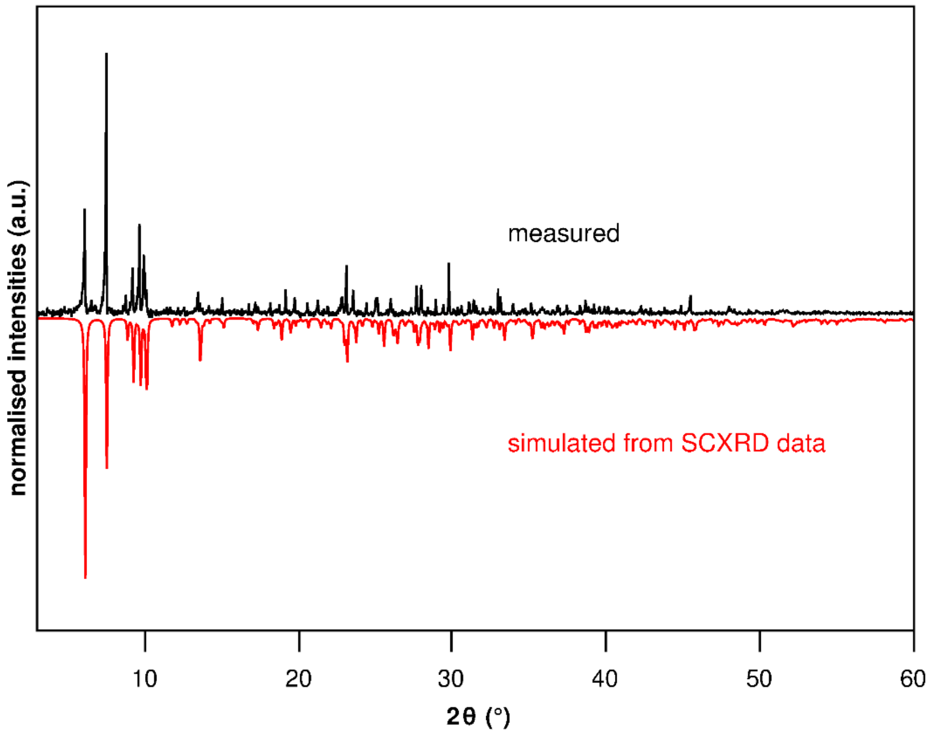

Figure S11. Powder diffraction pattern of $(PBz_4)_2(MeCN)_2Cu_2Bi_2I_{10}$ (**4**).

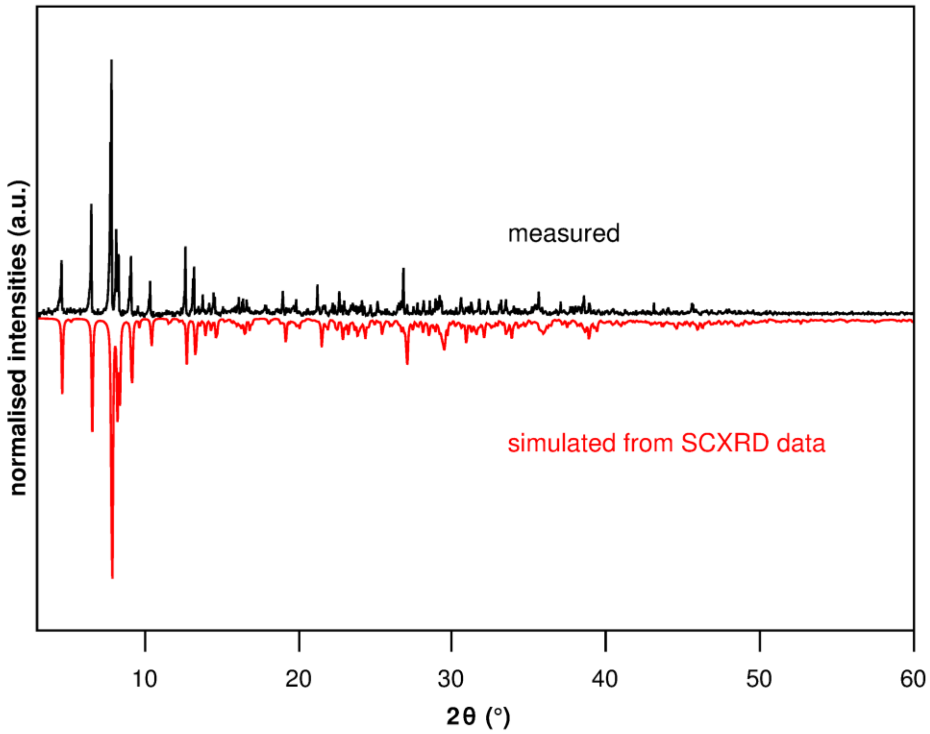

Figure S12. Powder diffraction pattern of $(PBz_4)_3Bi_3I_{12}\cdot(C_4H_8O)$ (**6**).

IR spectroscopy

IR spectra were recorded on a *Bruker Tensor 37* FT-IR spectrometer equipped with an ATR-Platinum measuring unit. All spectra show the characteristic bands of the tetrabenzylphosphonium cation. In Figure S17 the IR-spectrum of PBz_4Br is shown as a reference. In some cases, the characteristic bands of H_2O (3200 cm^{-1}) and CO_2 (2350 cm^{-1}) are visible. Additionally, the band of the CN group (2270 - 2400 cm^{-1}) is visible with variable intensity in the spectra of **2** and **4** and the band of the CO group (1710 cm^{-1}) is present in the spectrum of **6**.

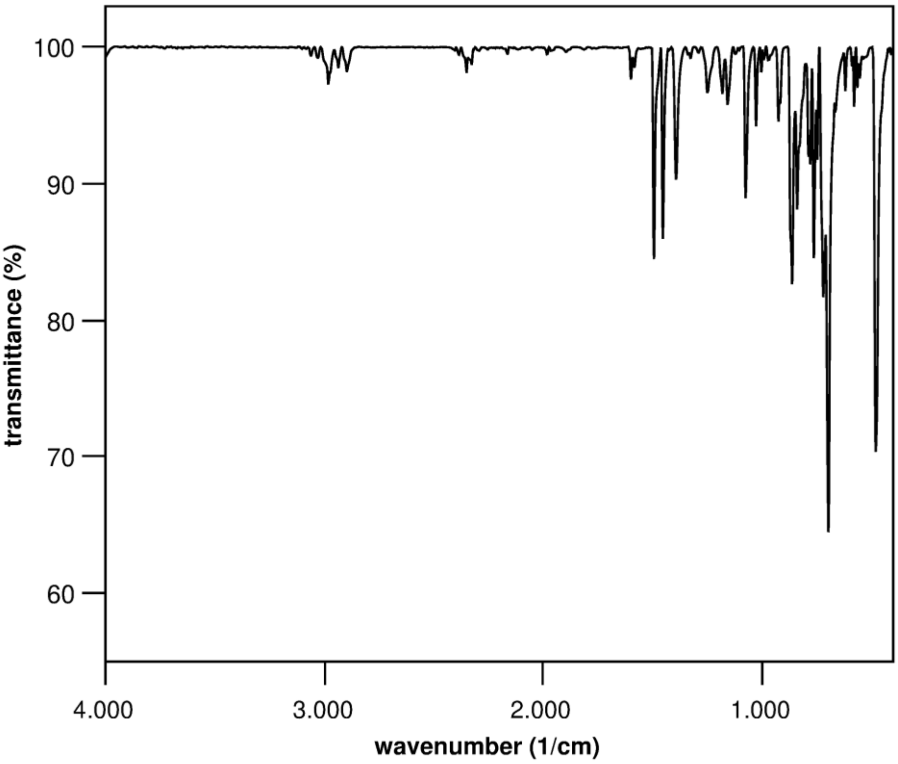

Figure S13. IR spectrum of $(PBz_4)_3Bi_3Br_{12}$ (**1**).

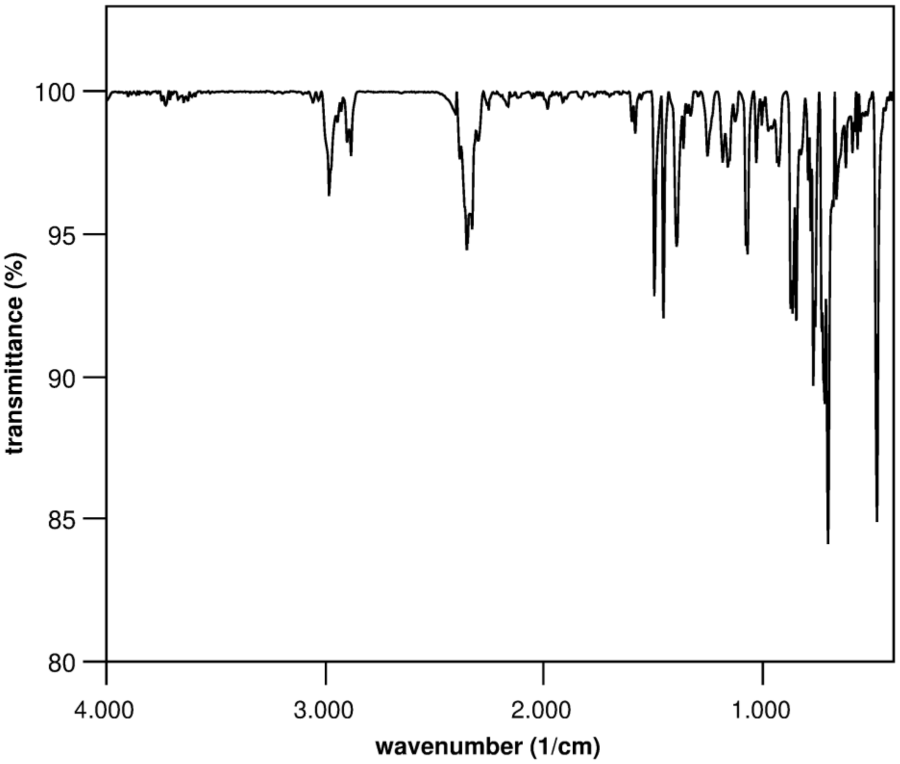

Figure S14. IR spectrum of $(PBz_4)_2(MeCN)_2Cu_2Bi_2Br_{10}$ (**2**).

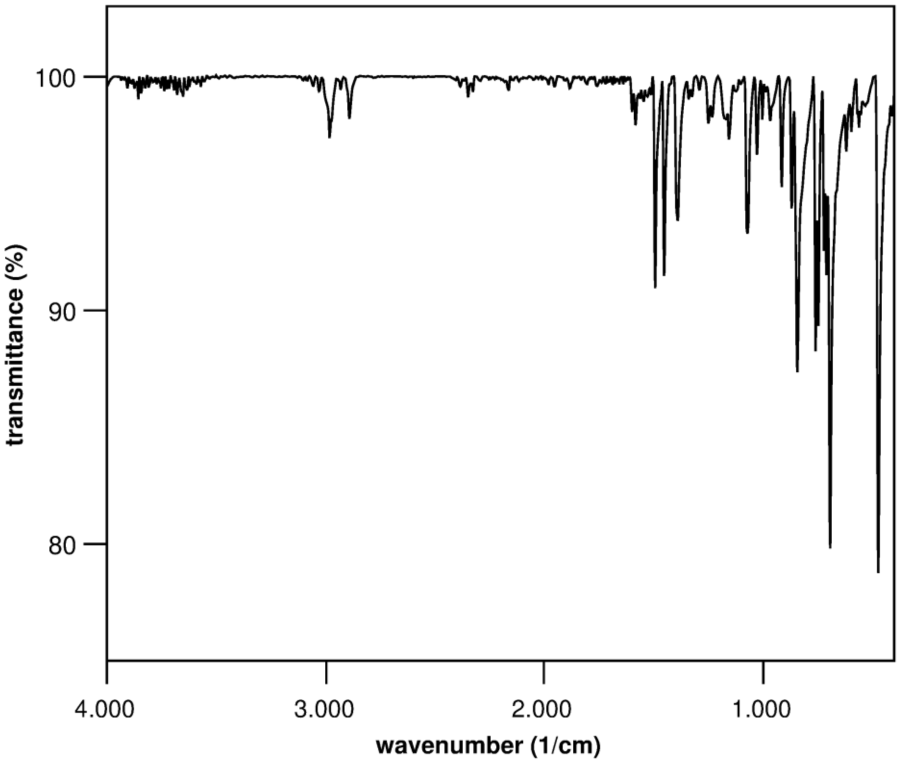

Figure S15. IR spectrum of $(PBz_4)Bi_2I_7$ (**3**).

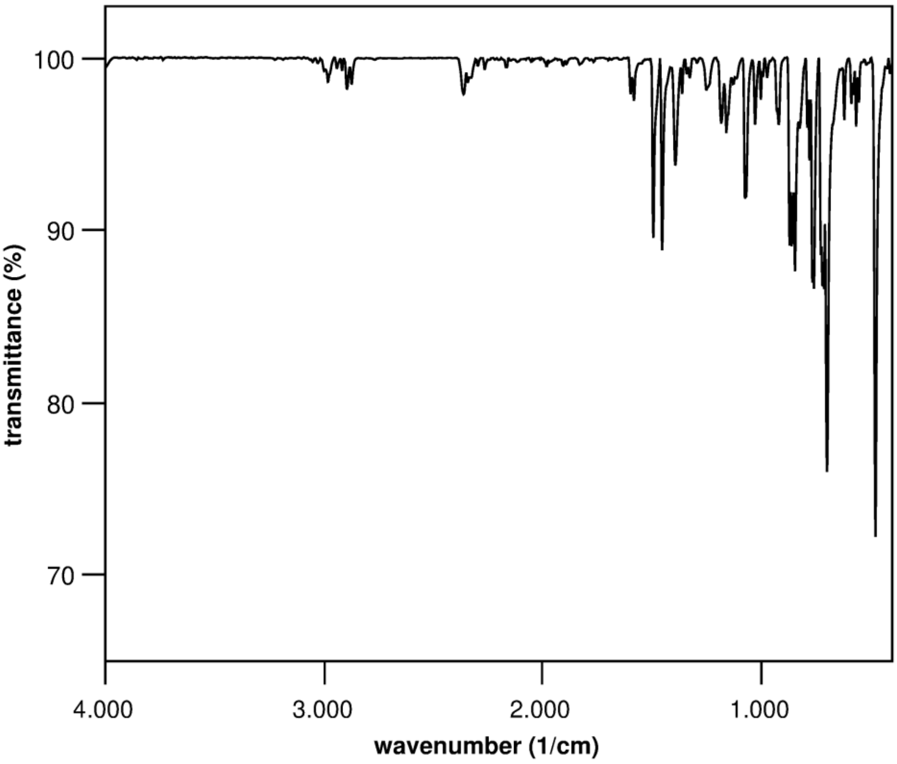

Figure S16. IR spectrum of $(PBz_4)_2(MeCN)_2Cu_2Bi_2I_{10}$ (**4**).

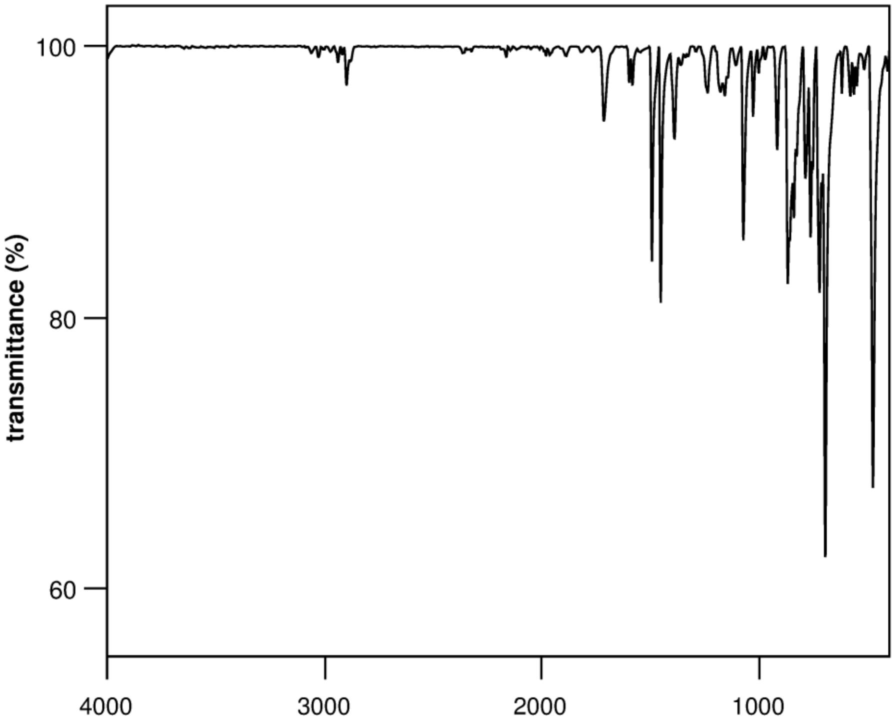

Figure S17. IR spectrum of $(PBz_4)_3Bi_3I_{12}\cdot(C_4H_8O)$ (**6**).

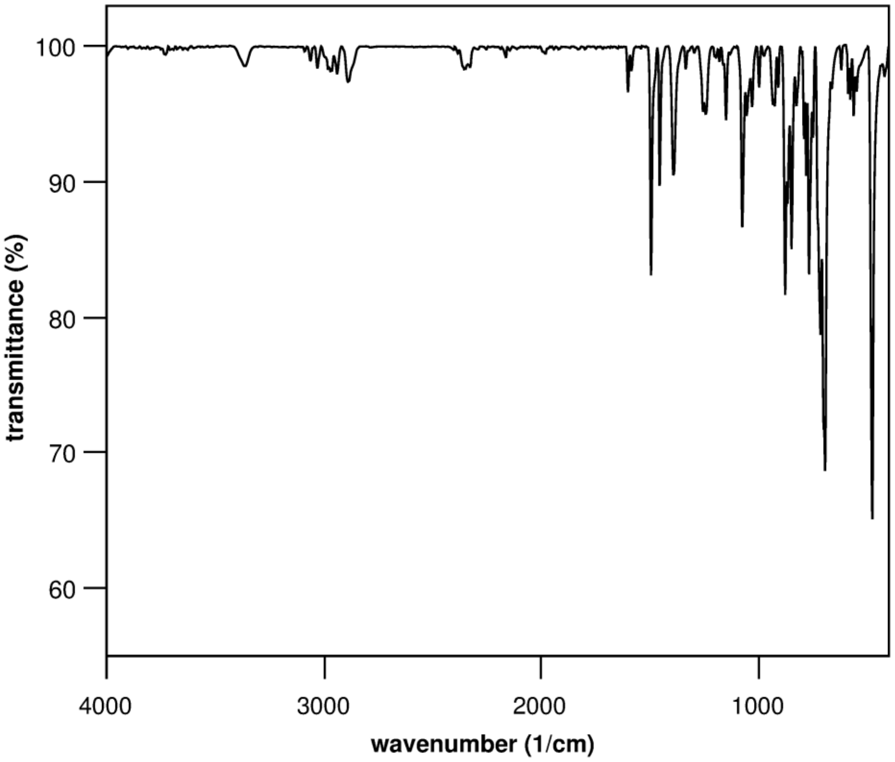

Figure S18. IR spectrum of (PBz_4)Br.

D.5. Enabling tailored 2D materials by introducing 1D organic-inorganic perovskites with supramolecular intra-layer interactions

Supplementary Information on

Enabling tailored 2D materials by introducing 1D organic-inorganic perovskites with supramolecular intra-layer interactions

Philip Klement[1], Natalie Dehnhardt[2], Chuan-Ding Dong[3], Samuel K. Bayliff[4], Julius Winkler[2], Peter J. Klar[1], Stefan Schumacher[3,5], Sangam Chatterjee[1] and Johanna Heine[2]*

1 Institute of Experimental Physics I and Center for Materials Research (ZfM), Justus Liebig University Giessen, Heinrich-Buff-Ring 16, D-35392 Giessen, Germany

2 Department of Chemistry and Material Sciences Center, Philipps-Universität Marburg, Hans-Meerwein-Straße, 35043 Marburg, Germany

3 Department of Physics and Center for Optoelectronics and Photonics Paderborn (CeOPP), Paderborn University, Warburger Strasse 100, D-33098 Paderborn, Germany

4 Department of Chemistry and Biochemistry, University of Oklahoma, 101 Stephenson Parkway, Norman, OK 73019, USA

5 College of Optical Sciences, The University of Arizona, 1630 E. University Blvd., Tucson, AZ 85721-0094, USA

Methods

Optical measurements. Low-temperature PL and time-resolved PL measurements were conducted in a continuous-flow liquid He cold finger cryostat cooled to 10 K with the sample in vacuum. A Ti:sapphire laser emitting 120-fs pulses at a repetition rate of 78 MHz at 800 nm (1.55 eV) was frequency-doubled (400 nm, 3.1 eV) and frequency tripled for excitation (266 nm, 4.66 eV). The excitation light was focused into a 1 µm diameter spot (1.4 µW excitation power) using a confocal beam path with all-reflective optics. The PL signal was spectrally filtered through a 1/4 m monochromator (Oriel MS260i) and detected on a Si charge-coupled device camera (Andor DU440). The time-resolved data was recorded by a streak camera equipped with a S20 cathode yielding time resolution better than 1 ps (Hamamatsu C10910 and Orca Flash). Optical absorption spectra were recorded on a Varian Cary 5000 UV/ Vis/NIR spectrometer in the range of 200−800 nm in diffuse reflectance mode employing a Praying Mantis accessory (Harrick). For ease of viewing, raw data was transformed from %Reflectance R to Absorbance A according to A = log(1/R).

Modelling. Density functional theory (DFT) calculations were performed using projector-augmented wave (PAW) potentials[1] and plane-wave basis sets, as implemented in the VASP software package.[2,3] The PBE functional[4] and Tkatchenko-Scheffler method[5] were used to describe exchange-correlation and dispersion interaction, respectively. The crystallographic unit cell (Table S1) was used as the starting point for the lattice expansion calculations. The lattice constants (*a*, *b*, and *c*) were expanded individually up to 20 % in steps of 2 %. At each point the geometry was optimized for fixed lattice constants by using the conjugated gradient method. Given the large unit cell, a 2*4*2 k-point lattice was adopted to sample the Brillouin zone, and a plane-wave basis set with energy cut off of 550 eV was used. Spin-orbit coupling was included for the calculation of the band-decomposed charge density shown in Figure 6. The bulk calculation is also based on the crystallographic unit cell (Table S1) and 2*4*2 k-point lattice. For the calculation of the single BBC layer, the lattice constant *a* was increased to 30 Å to introduce sufficient interlayer vacuum space, and a 1*4*4 k-point lattice was used.

Crystallographic Details

Table S1: Crystallographic data of $[BzA]_3[BiCl_5]Cl$ (**BBC**, BzA = benzylammonium, $C_7H_{10}N^+$)

	BBC (CCDC 1952283)
Empirical formula	$C_{21}H_{30}BiCl_6N_3$
Formula weight /g·mol^{-1}	746.16
Crystal color and shape	Colorless plate
Crystal size	0.315 × 0.271 × 0.092
Crystal system	monoclinic
Space group	$P2_1/c$
a /Å	17.0182(8)
b /Å	7.6205(4)
c /Å	22.4391(9)
α /°	90
β /°	102.638(2)
γ /°	90
V /Å^3	2839.6(2)
Z	4
ρ_{calc} /g·cm^{-3}	1.745
$\mu(Mo_{K\alpha})$ /mm^{-1}	6.788
measurement temp. /K	100
Absorption correction type	multi-scan
Min/max transmission	0.384/0.745
2Θ range /°	4.884-50.562
No. of measured reflections	24482
No. of independent reflections	5098
R(int)	0.0917
No. of indep. reflections ($I > 2\sigma(I)$)	4354
No. of parameters	246
R_1 ($I > 2\sigma(I)$)	0.0565
wR_2 (all data)	0.1268
S (all data)	1.065
$\Delta\rho_{max}$, $\Delta\rho_{min}$ /e· Å^{-3}	2.59/-2.67

Single crystal X-ray determination was performed on a Bruker Quest D8 diffractometer with microfocus MoKα radiation and a Photon 100 (CMOS) detector. Data collection and processing including the twin integration was performed with the Bruker APEX software package.[6]

The structure was solved using direct methods, refined by full-matrix least-squares techniques and expanded using Fourier techniques, using the Shelx software package[7-9] within the OLEX2 suite.[10] All non-disordered, non-hydrogen atoms were refined anisotropically. Hydrogen atoms were assigned to idealized geometric positions and included in structure factors calculations. Pictures of the crystal structure were created using DIAMOND.[11]

Due to the layered nature of the compound twinning was observed and accounted for by integration of two separate domains. This also necessitated the use of ISOR, SADI and RIGU restraints on the organic part of the crystal structure during refinement to obtain reasonable displacement parameters.

The free chloride ion in the crystal structure is found to be disordered over two positions. Occupancies were first refined freely, then constrained to the appropriate values (0.55 and 0.45) to stabilize the refinement. The disordered atoms were refined isotropically.

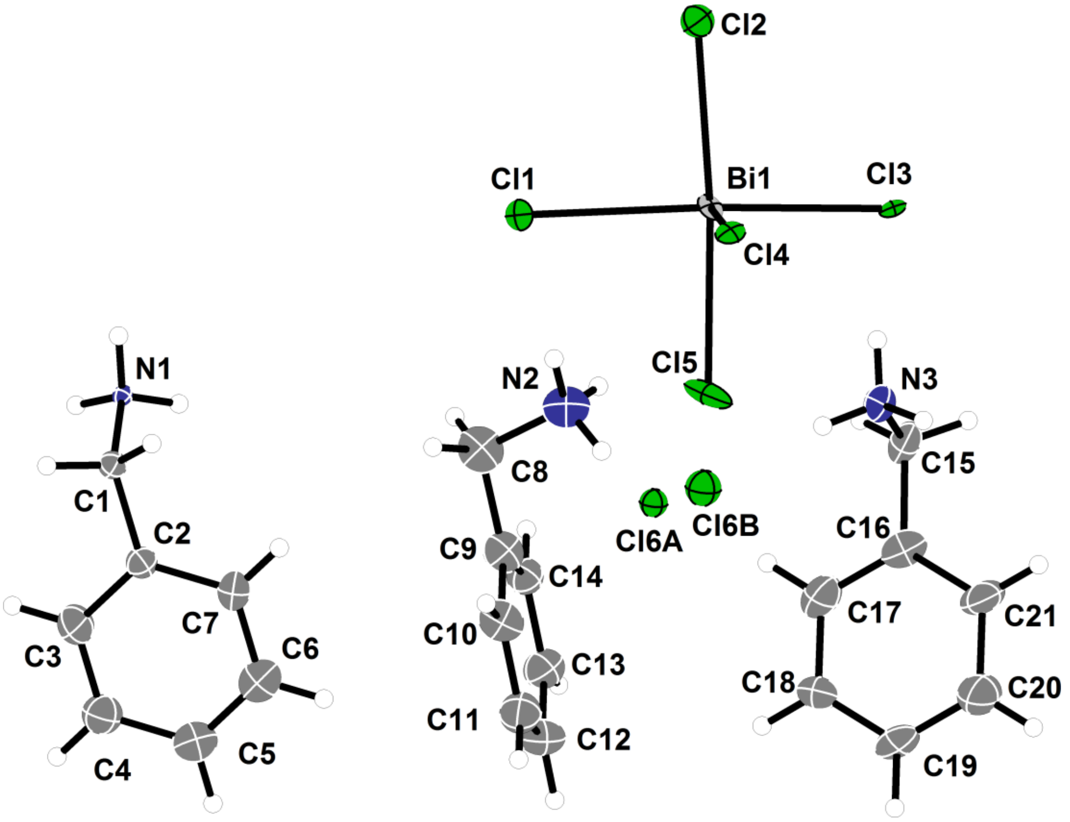

Figure S2 | Asymmetric unit. Asymmetric unit of the single crystal structure of BBC, ellipsoids shown at 70%. Bi-Cl bond length range from 2.587 to 2.869 Å, typical for chloro bismuthates.[12]

Powder diffraction

Powder patterns were recorded on a STADI MP (STOE Darmstadt) powder diffractometer, with CuKα1 radiation with λ = 1.54056 Å at room temperature in transmission mode. The patterns confirm the presence of the phase determined by SCXRD measurements and the absence of any major crystalline by-products. Patterns were simulated from single crystal data using Mercury.[13]

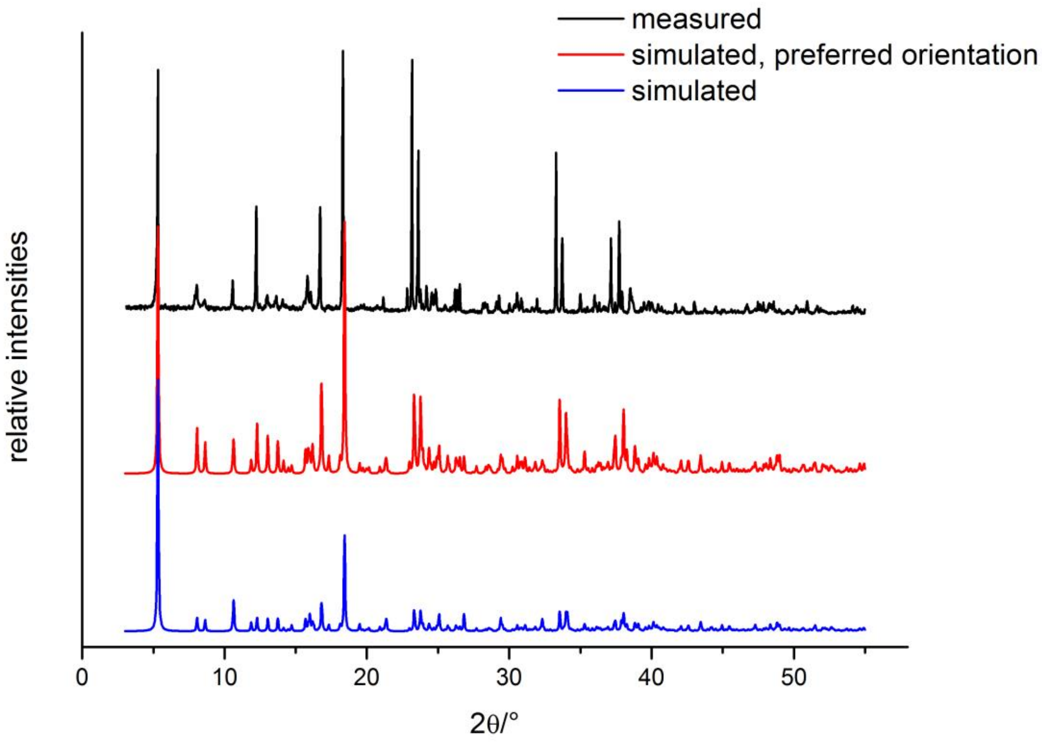

Figure S3 | Powder pattern. Measured and simulated powder patterns of BBC. The diffractogram shows signs of texture effects, which can be demonstrated by simulating a diffractogram with a (100) preferred orientation, as can be expected from the layered crystal structure and plate-like crystal habit.

Thermal analysis

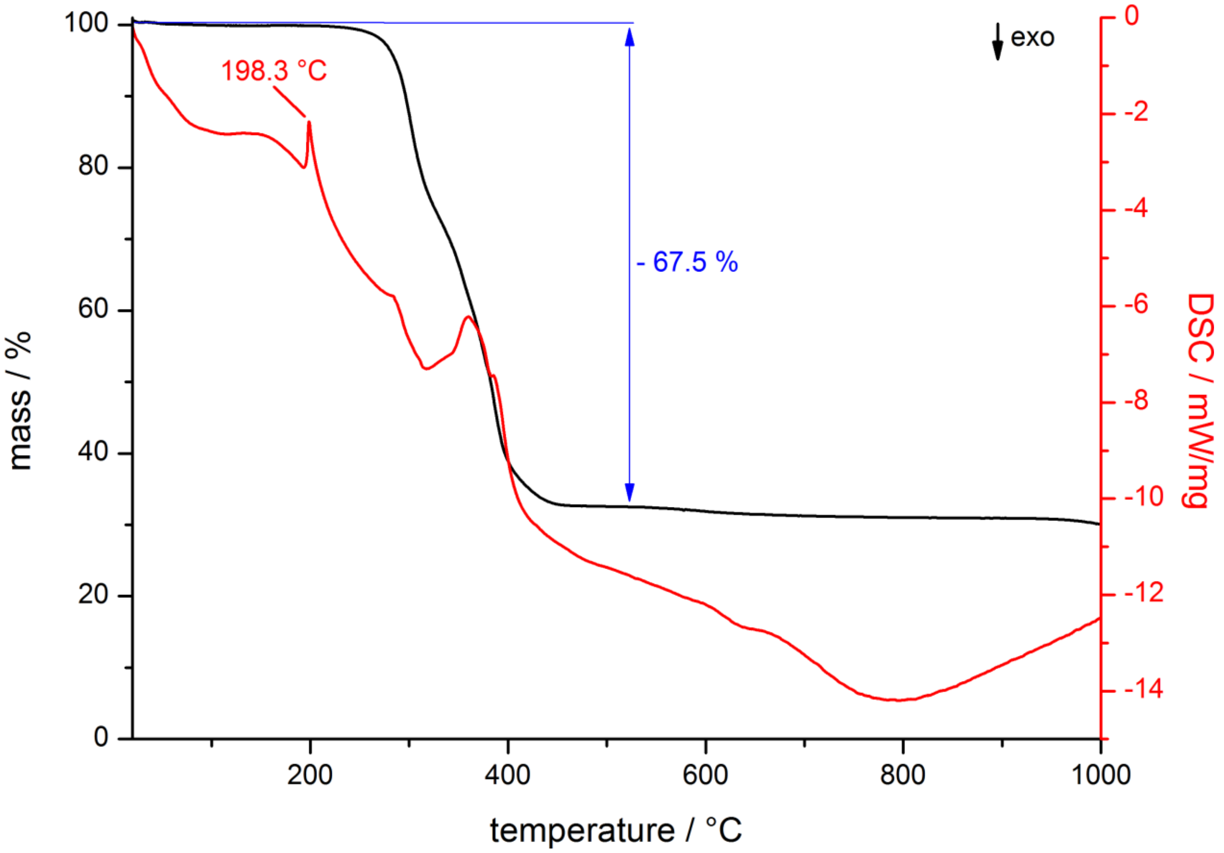

Figure S4 | Thermal analysis. The thermal behavior of BBC (16.8 mg), was studied by simultaneous DTA/TG on a NETZSCH STA 409 C/CD from 25 °C to 800 °C with a heating rate of 10 °C min^{-1} in a constant flow of 80 ml min^{-1} Ar. A melting point or solid-solid phase transition can be observed at 198.3 °C and the onset of decomposition (1 % mass loss) at 257.1 °C.

Stability and long-term storage in air

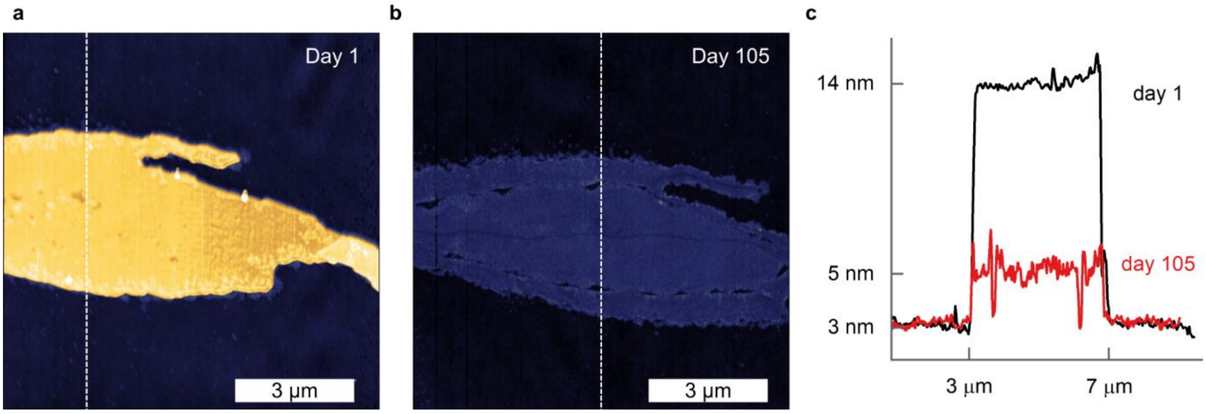

Figure S5 | Topological changes of ultrathin BBC under long-term storage in air. a, AFM image of a typical sample on day of production. **b**, AFM image of the same sample after 105 days of storage in air showing changes in surface topography. **c**, Height profiles of the dashed lines in **a** and **b** showing a thickness decrease from 11 to 2 nm and roughening of the surface.

Bi-Cl bond length upon expansion of the lattice constants

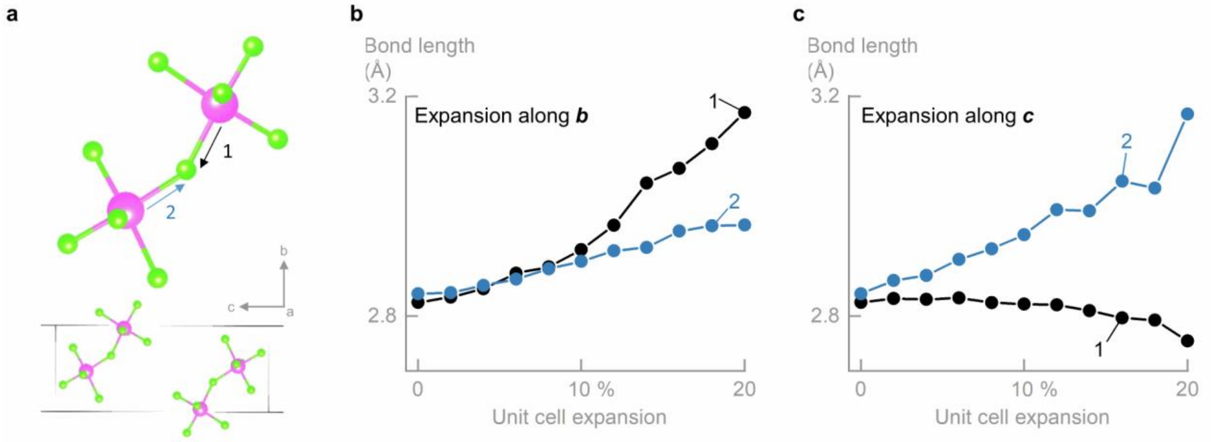

Figure S6 | Bi-Cl bond length upon expansion of the lattice constants. **a**, Excerpt of the crystal structure with individual Bi-Cl bonds marked. The green (pink) spheres represent Cl (Bi) atoms. **b**, Change of the bond length as a function of the expansion of the unit cell along the ***b*** axis. **c**, Change of the bond length as a function of the expansion of the unit cell along the ***c*** axis. The similarity of results indicates a comparably strong binding along both crystallographic axes ***b*** and ***c***.

Examination of the change in the Bi-Cl bond length of the inorganic Bi-Cl-octahedral reveals similar results for expansions along the ***b*** axis and the ***c*** axis (Figure S6). Consequently, the bridging between the organic BzA molecules yields a comparably strong binding as the covalent bonds within the octahedral chains. This fundamentally explains the exfoliation potential of BBC despite it featuring only 1D covalent bonds.

Comparison of the 2D sheet binding strength of BBC and other 2D materials

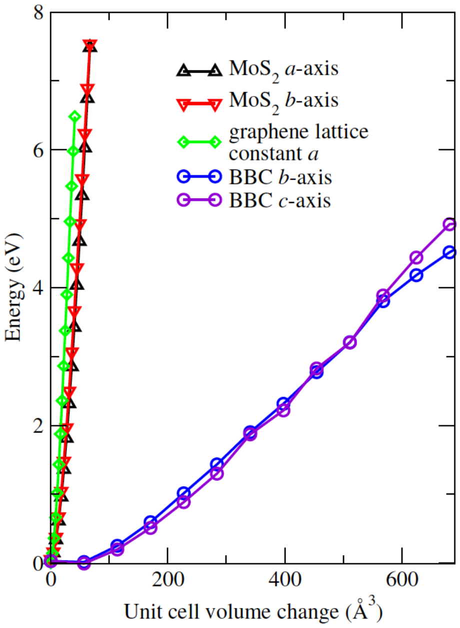

Figure S7 |Comparison of the 2D sheet binding strength of BBC and other 2D materials. Required energy for expansion of the unit cells along the crystallographic axes of the 2D sheets of BBC, graphene and MoS$_2$. The expansions are performed along the in-plane lattice constants ***b*** and ***c*** for BBC, ***a*** and ***b*** for MoS$_2$, and ***a*** for graphene. Significantly less energy is required to expand the 2D sheet of BBC mirroring the mechanically brittle structure of ultrathin BBC sheets observed in the mechanical exfoliation.

Excitation power dependence of the PL

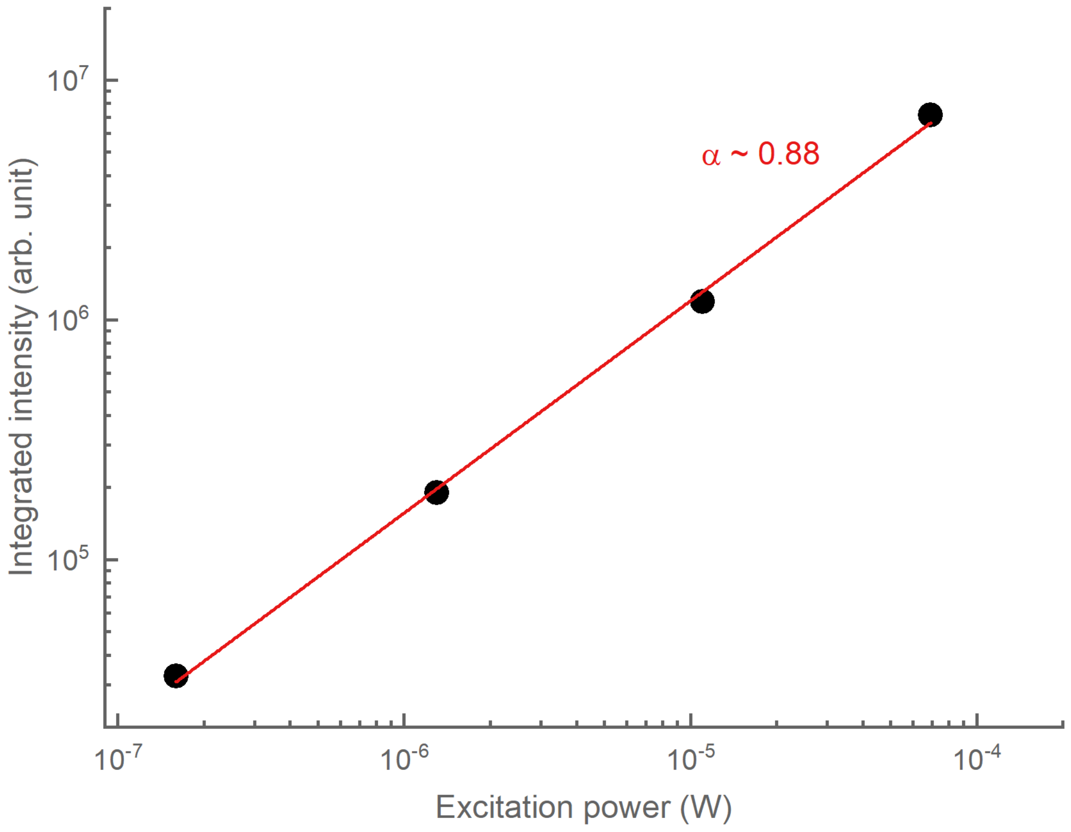

Figure S8 | Excitation power dependence of the PL intensity of BBC. The PL intensity increases linearly (α = 0.88) with the excitation power, indicating that there is no threshold for the onset of PL due to non-radiative recombination through defects at low excitation powers, and no saturation of the absorption at high excitation powers.

Time-resolved photoluminescence spectra

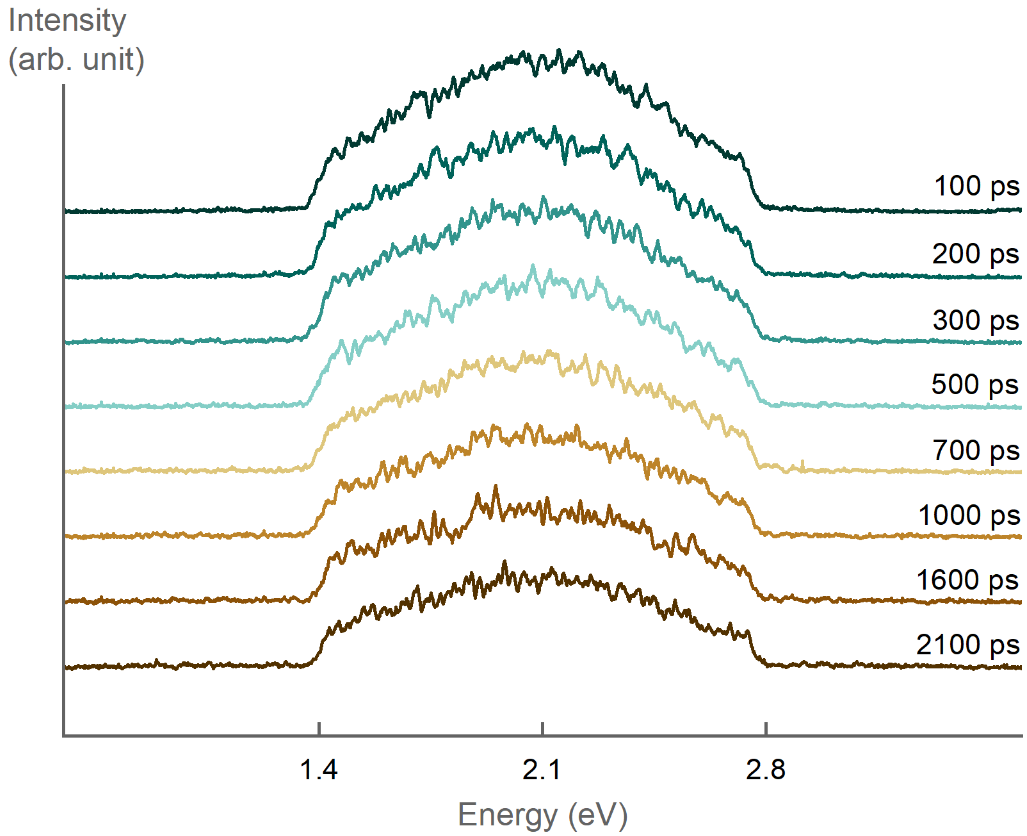

Figure S9 | Time-resolved photoluminescence spectra of bulk BBC. The homogeneous spectral constriction in time indicates a single emissive state with negligible inhomogeneous broadening.

Vibrational properties

A Renishaw inVia Raman microscope with a 785 nm (1.6 eV) laser diode was used for μ-Raman measurements. The beam was focused through a 50X objective achieving a spot size of s ~ 2 μm at 2.16 mW excitation power. Signal was collected by the same objective, dispersed on a diffraction grating (1800 lines cm^{-1}, blazed in the visible region) and collected by a CCD camera. The spectral resolution was 1.8 cm^{-1}, and the Si Raman mode at 520 cm^{-1} was used for frequency calibration.

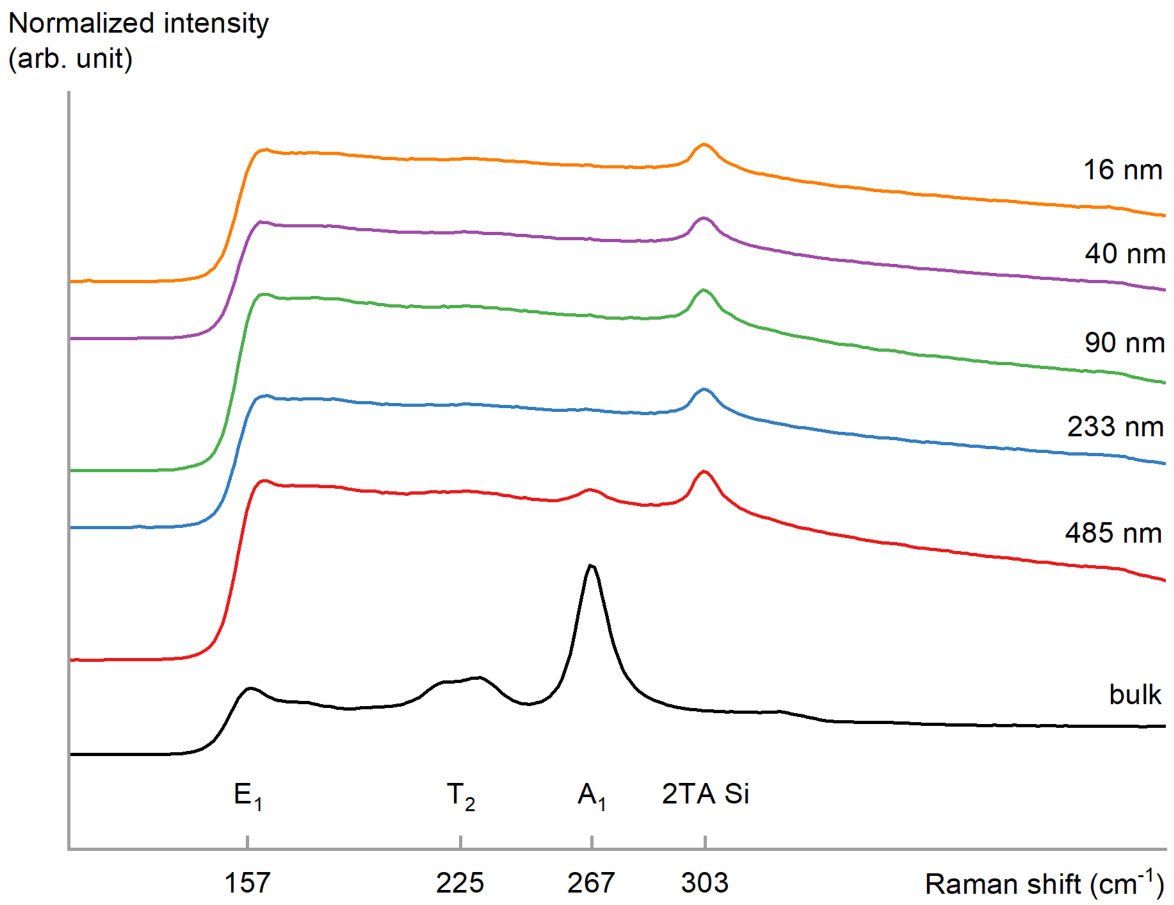

Figure S10 | Thickness-dependent Raman spectra of [BzA]$_3$[BiCl$_5$]Cl. Characteristic Bi-Cl stretching vibrations appear in the low frequency range between 150 and 400 cm^{-1}.

The peaks at 225 and 267 cm^{-1} can be assigned to the bridging Bi-Cl and terminal Bi-Cl stretching vibrations (T_2 and A_1) of the Bi-Cl$_5$-octahedron, whereas the broad feature at 157 cm^{-1} arises from the Cl-Bi-Cl bending vibrations (E_1). The peak at 303 cm^{-1} was assigned to the second order acoustic phonon in silicon.[14] This is supported by the evolution of the peak as it disappears for very thick sheets. The onset of the signal around 140 cm^{-1} originates in the laser line filter.

IR spectroscopy

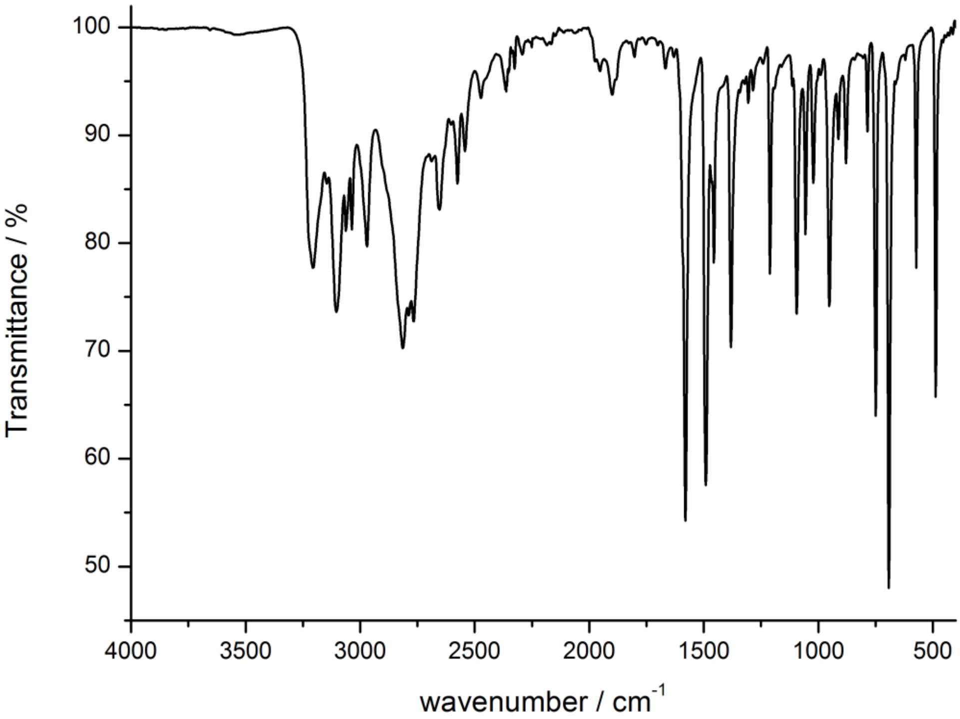

Figure S11 | IR spectrum of BBC. An IR spectrum of BBC was recorded on a Bruker Tensor 37 FT-IR spectrometer equipped with an ATR-Platinum measuring unit. The typical pattern of the benzylammonium moiety is observed.[15]

CSD Analysis[16]

Database Version: Conquest Version 2.0.1, Build 235316; CSD Version 5.40 (February 2019)

Basic Search Criteria: Benzylammonium substructure, organometallic

Advanced criteria: No 3D or 2D covalent interactions, no diammonium cations, no crown ethers, non-interdigitated phenyl groups, no large multinuclear anionic clusters, no significant disorder, benzylammonium fragment not acting as a ligand, crystallographic coordinates available, only one stereoisomers listed

Structure pictures: Carbon shown in dark grey, Nitrogen in blue, Oxygen in red, Sulfur in yellow, Fluorine in blue-green, Chlorine in light green, Phosphorous in purple, Metal atoms in light grey or with their coordination polyhedra

Table S12 | 2D material candidates. Entries are listed with both their CCDC reference code and the original reference.

No.	CCDC Refcode	Compound	Structure	Reference
1	AFONAK	$[C_6H_5CH(CH_3)NH_3]_2[Fe_2(C_2O_4)_3(H_2O)_4]$	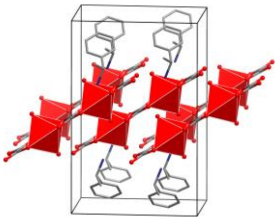	[17]
2	AVUKOR	$(C_8H_{12}N)_2[PdCl_4]$	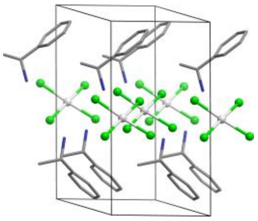	[18]
3	BUCDAG	[*R*-$(C_8H_{12}N)_2$][$CuCl_4$]	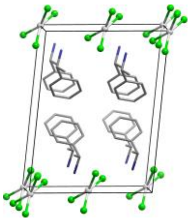	[19]
4	BUCDOU	[*rac*-$(C_8H_{12}N)_2$][$CuCl_4$]	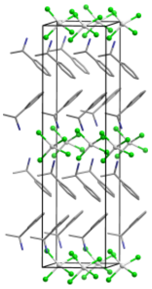	[19]

No.	CCDC Refcode	Compound	Structure	Reference
5	CUXZIF	[S-$(C_8H_{12}N)_2$][$Cu(C_3H_2O_4)_2(H_2O)_2$]	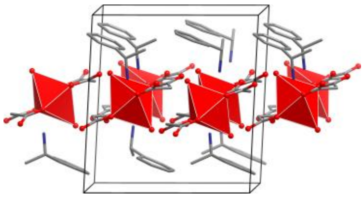	[20]
6	CUYBAA	[$(C_8H_9F_3N)_2$][$Cu(C_3H_2O_4)_2(H_2O)_2$]	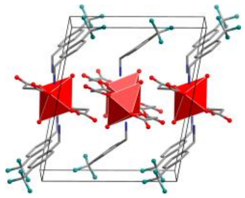	[20]
7	DENSOF	[*rac*-$(C_8H_{12}N)_3$][$PbCl_5$]·H_2O	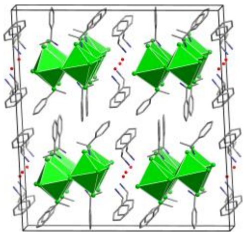	[21]
8	DENSUL	[*rac*-$(C_8H_{12}N)_3$][$PbBr_5$]·H_2O	Isostructural with DENSOF	[21]
9	DUPPUB	[*rac*-$(C_8H_{11}FN)_2$][$CoCl_4$]	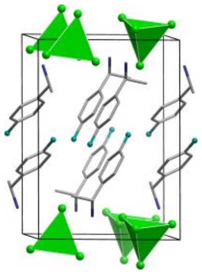	[22]
10	DUPQAI	[R-$(C_8H_{12}N)_3$][$CoCl_4$]Cl	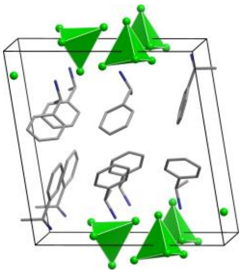	[22]
11	DUPQEM	[S-$(C_8H_{11}ClN)_3$][$CoCl_4$]Cl	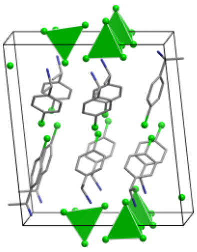	[22]

No.	CCDC Refcode	Compound	Structure	Reference
12	KIBLOX	[*R*-$(C_8H_{12}N)_2$][MoS_4]	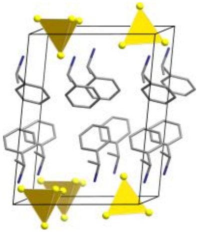	[23]
13	KIBLUD	[*R*-$(C_8H_{12}N)_2$][WS_4]	Isostructural with KIBLOX	[23]
14	PEYJOT	[*rac*-$(C_8H_{12}N)_2$][$SnCl_6$]	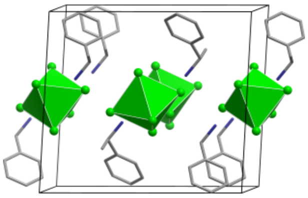	[24]
15	ROVYOS	[*R*-$(C_{12}H_{14}N)_2$][$CuCl_4$]	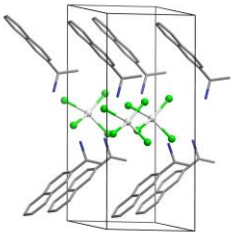	[25]
16	ROVYUY	[*R*-$(C_{12}H_{14}N)_2$][$CuCl_4$]	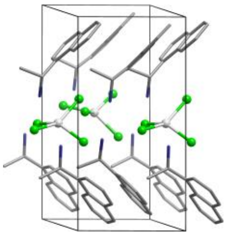	[25]
17	SUMRUP	[$(C_8H_{12}NO)_6$][$V_{10}O_{28}$]·$2H_2O$	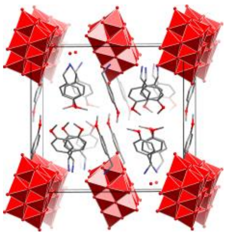	[26]
18	UGAFIT	[*rac*-$(C_8H_{12}N)_2$][$Zn(SO_4)_2(H_2O)_4$]	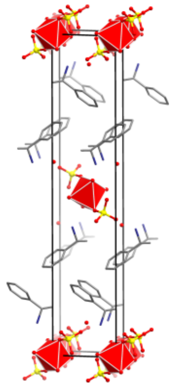	[27]

No.	CCDC Refcode	Compound	Structure	Reference
19	WILWUK	$[(C_7H_{10}N)_6][V_{10}O_{28}]\cdot 2H_2O$	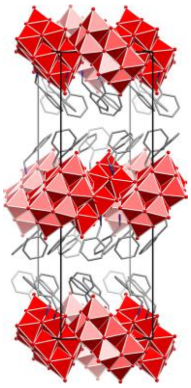	[28]
20	WIWPAV	[*rac*-$(C_8H_{12}N)_2][Co(SO_4)_2(H_2O)_4]$	Isostructural with UGAFIT	[29]
21	WIWPID	[*rac*-$(C_8H_{12}N)_2][Fe(SO_4)_2(H_2O)_4]$	Isostructural with UGAFIT	[29]
22	WIWPOJ	[*rac*-$(C_8H_{12}N)_2][Ni(SO_4)_2(H_2O)_4]$	Isostructural with UGAFIT	[29]
23	YADYUZ	$[(C_7H_9ClN)_4](Cd(P_6O_{18}))$	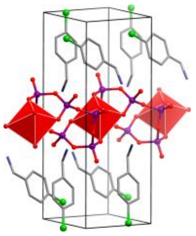	[30]
24	YIDHID	$[C_6H_5CH(CH_3)NH_3]_2[Co_2(C_2O_4)_3(H_2O)_4]$	Isostructural with AFONAK	[31]

References

[1] Kresse, G. & Joubert, D. From ultrasoft pseudopotentials to the projector augmented-wave method. *Phys. Rev. B* **59**, 1758 (1999).

[2] Kresse, G. & Hafner, J. Ab initio molecular dynamics for liquid metals. *Phys. Rev. B* **47**, 558 (1993).

[3] Kresse, G. & Hafner, J. Ab initio molecular-dynamics simulation of the liquid-metal–amorphous-semiconductor transition in germanium. *Phys. Rev. B* **49**, 14251 (1994).

[4] Perdew, J., Burke, K. & Ernzerhof, M. Generalized gradient approximation made simple. *Phys. Rev. Lett.* **77**, 3865 (1996)**.**

[5] Tkatchenko, A. & Scheffler, M. Accurate molecular van der Waals interactions from ground-state electron density and free-atom reference data. *Phys. Rev. Lett.* **102**, 073005 (2009).

[6] Bruker, APEX3. Bruker AXS Inc., Madison, Wisconsin, USA (2018).

[7] Sheldrick, G. M. A short history of SHELX. *Acta Cryst. A* **64**, 112-122 (2008);

[8] Sheldrick, G. M. SHELXT – Integrated Space-Group and Crystal-Structure Determination. *Acta Cryst. A* **71**, 3-8 (2015).

[9] Sheldrick, G. M. Crystal Structure Refinement with SHELXL. *Acta Cryst. C* **71**, 3-8 (2015).

[10] Dolomanov, O. V., Bourhis, L. J., Gildea, R. J., Howard, J. A. K., Puschmann, H. OLEX2: A Complete Structure Solution, Refinement and Analysis Program. *J. Appl. Crystallogr*. **42**, 339-341 (2009).

[11] Brandenburg, K. Diamond, Crystal Impact GbR: Bonn, Germany (2005).

[12] Mousdis, G. A., Papavassiliou, G. C., Terzis, A. & Raptopoulou, C. P. Preparation, Structures and Optical Properties of $[H_3N(CH_2)_6NH_3]BiX_5$(X=I, Cl) and $[H_3N(CH_2)_6NH_3]SbX_5$ (X=I, Br). *Z. Naturforsch.* **53b**, 927-931 (1998).

[13] Macrae, C. F., Edgington, P. R., McCabe, P., Pidcock, E., Shields, G. P., Taylor, R., Towler, M. & van de Streek, J. Mercury CSD 2.0 - new features for the visualization and investigation of crystal structures. *J. Appl. Cryst.* **39**, 453-457 (2006).

[14] Wagner, J. Optical characterization of heavily doped silicon. *Solid State Electron.* **30**, 1117-1120 (1987).

[15] Brittain, H. G. Vibrational Spectroscopic Studies of Cocrystals and Salts. 4. Cocrystal Products formed by Benzylamine, α-Methylbenzylamine, and their Chloride Salts. Crystal G. & Des. **116**, 2500-2509, (2011).

[16] Groom, C. R., Bruno, I. J., Lightfoot M. P. & Ward, S. C. The Cambridge Structural Database. *Acta Cryst.* **B72**, 171-179 (2016).

[17] Shan, Y. & Huang, S. D. Crystal structure of bis(R-(+)-1-phenylethylammonium) tetraaquatrioxolatodiferrate, $[C_6H_5CH(CH_3)NH_3]_2[Fe_2(C_2O_4)_3(H_2O)_4]$. *Z. Kristallogr. NCS* **216**, 373-374 (2001).

[18] Cruz-Cruz, S.; Rodríguez-Pastrana, M.; Bernès S. & Gutiérrez-Pérez, R. Bis-[(S)-(–)-1-phenylethylammonium]tetrachloropalladate(II). *Acta Cryst. E* **60**, m342-m344 (2004).

[19] Salah, A. M. B., Sayari, N., Naïli, H. & Norquist, A. J. Chiral and achiral copper(II) complexes: structure, bonding and biological activities. *RSC Adv.* **6**, 59055-59065 (2016).

[20] Keene, T. D., Zimmermann, I., Neels, A., Sereda, O., Hauser, J.; Liu, S.-X. & Decurtins, S. Crystal Engineering of a Series of Arylammonium Copper(II) Malonates. *Crystal Growth & Design* **10**, 1854-1859 (2010).

[21] Billing, D. G. & Lemmerer, A. Synthesis and crystal structures of inorganic–organic hybrids incorporating an aromatic amine with a chiral functional group. *CrystEngComm* **8**, 686-695 (2006).

[22] Mande, H. M., Ghalsasi, P. S. & Arulsamy, N. Racemic and conglomerate 1-(4-haloaryl)ethylammonium tetrachlorocobaltate salts: formation of helical structures. *RSC Adv.* **5**, 62719-62723 (2015).

[23] Srinivasan, B. R., Naik, A. R., Näther, C. & Bensch, W. Synthesis, Spectroscopy and Crystal Structures of Chiral Organic Ammonium Tetrathiometalates Showing N-H···S and C-H···S Interactions. *Z. allg. anorg. Chem.* **633**, 582-588 (2007).

[24] Billing, D. G., Lemmerer, A. & Rademeyer, M. Bis(1-phenylethylammonium) hexachloridostannate(IV) and bis(2-phenylethylammonium)hexachloridostannate(IV). *Acta Cryst. C* **63**, m101-m104 (2007).

[25] Mande, H. M., Ghalsasi, P. S. & Navamoney, A. Synthesis, structural and spectroscopic characterization of the thermochromic compounds A_2CuCl_4: $[(Naphthylethylammonium)_2CuCl_4]$. *Polyhedron* **91**, 141-149, (2015).

[26] Toumi, S., Ratel-Ramond, N. & Akriche, S. Decavanadate Cage-like Cluster Templated by Organic Counter Cation: Synthesis, Characterization and Its Antimicrobial Effect Against Gram Positive E. Feacium. *J. Cluster Sci.* **26**, 1821–1831 (2015).

[27] Kammoun, O., Rekik, W., Bataille, T., Mahmudov, K. T., Kopylovich, M. N. & Naili, H. Inorganic–organic hybrid double sulfates as catalysts of the diastereoselective nitroaldol reaction. *J. Organomet. Chem.* **741**, 136-140 (2013).

[28] Yraola, F., García-Vicente, S., Marti, L., Albericio, F., Zorzano, A. & Royo, M. Understanding the Mechanism of Action of the Novel SSAO Substrate $(C_7NH_{10})_6(V_{10}O_{28})\cdot 2H_2O$, a Prodrug of Peroxovanadate Insulin Mimetics. *Chem. Biol. Drug Des.* **69**, 423-428 (2007).

[29] Kammoun, O., Bataille, T., Lucas, A., Dorcet, V., Marlart, I., Rekik, W., Naïli, H. & Mhiri, T. A Supramolecular Double Sulfate Salt with a Lamellar Type: Crystal Structure and Thermal Behavior. *Inorg. Chem.* **53**, 2619-2627 (2014).

[30] Abid, S., Al-Deyab, S. S. & Rzaigui, M. The one-dimensional coordination polymer poly[tetrakis-[(4-chlorophenyl)methanaminium][cadmate-μ-cyclo-hexaphosphorato]]. *Acta Cryst. E* **67**, m1549-m1550 (2011).

[31] Yang, X., Li, J., Wang, H.-W., Zhao, X.-H. & Shan, Y.-K. Bis[(*R*)-1-phenyl-ethyl-aminium] μ-oxalato-κ^4O,O':O''O'''-bis-[diaqua-(oxalato-κ^2O,O')cobaltate(II)]. *Acta Cryst. E* **63**, m1554, (2007).

D.6. Band-Gap Tunable, Chiral Hybrid Metal Halides Displaying Second Harmonic Generation

Supporting Information on

Band-Gap Tunable, Chiral Hybrid Metal Halides Displaying Second-Harmonic Generation

Natalie Dehnhardt[†], Marleen Axt[‡], Jonas Zimmermann[‡], Meng Yang[†], Gerson Mette[‡,*], Johanna Heine[†,*].

†Department of Chemistry and Material Sciences Center, Philipps-Universität Marburg, Hans-Meerwein-Straße, 35043 Marburg, Germany.

‡ Department of Physics and Material Sciences Center, Philipps-Universität Marburg, Renthof 5, 35032 Marburg, Germany.

*Corresponding author E-mail address: gerson.mette@physik.uni-marburg.de; johanna.heine@chemie.uni-marburg.de

Table of Content

1. Additional Synthetic Details

Table S1: Individual amounts of reagents in the synthesis of **1**-**6**. An excess of amine is used for optimized crystallization.

Compound	**E_2O_3**	**(*R*)-1-(4-fluoro) phenylethylamine**	**HX solution, concentrated**	**Yield**
[(*R*)-1-(4-F)PEA]$_4$[Sb_2Cl_{10}] (**1**)	125 mg, 0.4 mmol	424 µL, 3.1 mmol	5 mL	121 mg, 24 %
[(*R*)-1-(4-F)PEA]$_4$[Sb_2Br_{10}] (**2**)	62 mg, 0.2 mmol	202 µL, 1.5 mmol	10 mL	74 mg, 23 %
[(*R*)-1-(4-F)PEA]$_4$[Sb_2I_{10}] (**3**)	62 mg, 0.2 mmol	202 µL, 1.5 mmol	10 mL	116 mg, 28 %
[(*R*)-1-(4-F)PEA]$_4$[Bi_2Cl_{10}] (**4**)	234 mg, 0.5 mmol	424 µL, 3.1 mmol	5 mL	266 mg, 40 %
[(*R*)-1-(4-F)PEA]$_4$[Bi_2Br_{10}] (**5**)	116 mg, 0.25 mmol	202 µL, 1.5 mmol	10 mL	260 mg, 58 %
[(*R*)-1-(4-F)PEA]$_4$[Bi_2I_{10}] (**6**)	116 mg, 0.25 mmol	202 µL, 1.5 mmol	10 mL	70 mg, 12 %

2. Additional Crystallographic Details

Table S2: Crystallographic data for **1**.

	1 (CCDC 1995573)
Empirical formula	$C_{32}H_{44}Cl_{10}F_4N_4Sb_2$
Formula weight /g·mol^{-1}	1158.71
Crystal color and shape	colorless plank
Crystal size	0.35 × 0.136 × 0.08
Crystal system	monoclinic
Space group	$P2_1$
a /Å	11.8394(7)
b /Å	12.8214(7)
c /Å	14.8843(9)
α /°	90
β /°	95.0706(19)
γ /°	90
V /Å^3	2250.6(2)
Z	2
ρ_{calc} /g·cm^{-3}	1.710
μ(Mo$_{K\alpha}$) /mm^{-1}	1.840
measurement temp. /K	100
Absorption correction type	multi-scan
Min/max transmission	0.565/0.867
2Θ range /°	4.218-50.664
No. of measured reflections	53239
No. of independent reflections	7915
R(int)	0.0488
No. of indep. reflections ($I > 2\sigma(I)$)	7460
No. of parameters	477
R_1 ($I > 2\sigma(I)$)	0.0195
wR_2 (all data)	0.0374
S (all data)	1.046
$\Delta\rho_{max}$, $\Delta\rho_{min}$ /e· Å^{-3}	0.36/-0.29
Flack parameter	-0.027(9)

Details of crystal structure measurement and refinement: Single crystal X-ray determination was performed at 100 K on a Bruker Quest D8 diffractometer with microfocus MoKα radiation and a Photon 100 (CMOS) detector.

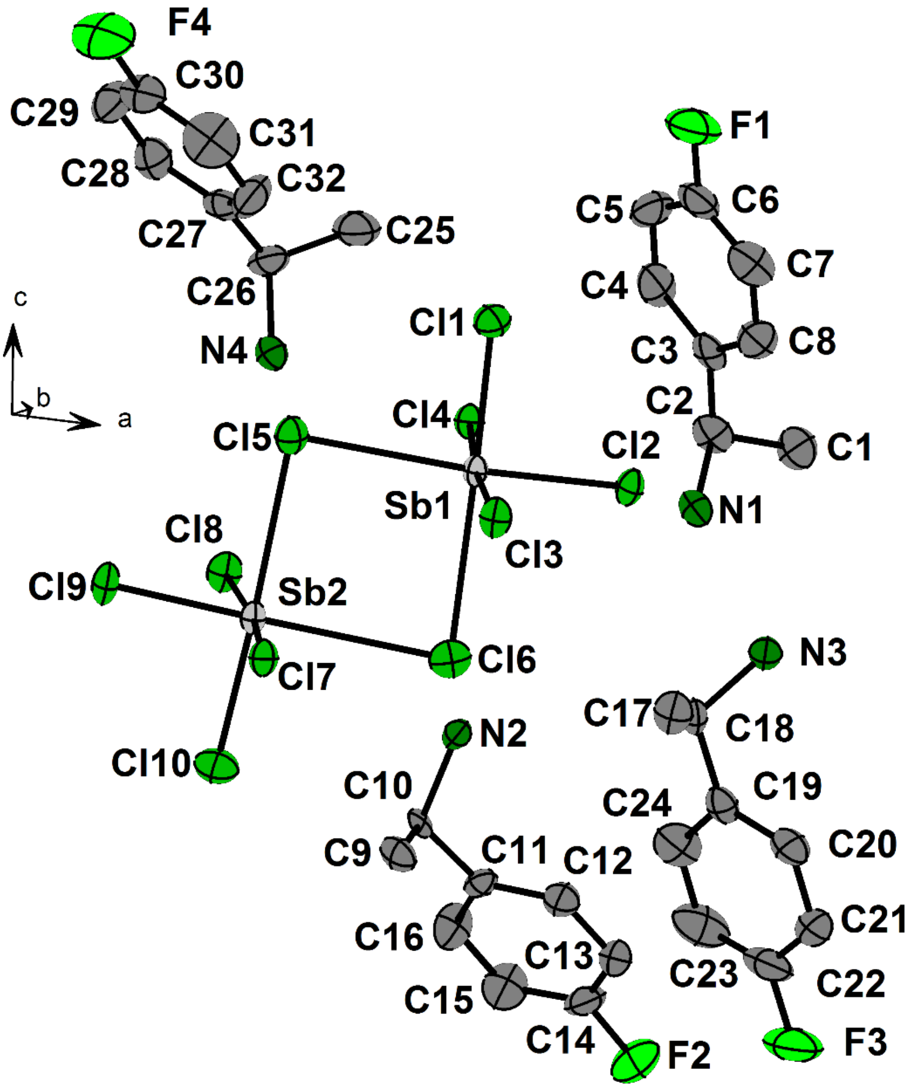

Figure S1: Asymmetric unit of **1**, ellipsoids at 80% probability.

Table S3: Crystallographic data for **2**.

	2 (CCDC 1995570)
Empirical formula	$C_{32}H_{44}Br_{10}F_4N_4Sb_2$
Formula weight /g·mol^{-1}	1603.31
Crystal color and shape	Colorless block
Crystal size	0.26 × 0.156 × 0.11
Crystal system	monoclinic
Space group	$P2_1$
a /Å	12.3557(5)
b /Å	13.4134(6)
c /Å	14.4815(6)
α /°	90
β /°	95.5638(13)
γ /°	90
V /Å^3	2388.74(17)
Z	2
ρ_{calc} /g·cm^{-3}	2.229
μ(Mo$_{K\alpha}$) /mm^{-1}	9.538
measurement temp. /K	100
Absorption correction type	multi-scan
Min/max transmission	0.4956/0.7452
2Θ range /°	4.494 to 50.652
No. of measured reflections	26419
No. of independent reflections	8554
R(int)	0.0352
No. of indep. reflections ($I > 2\sigma(I)$)	7881
No. of parameters	477
R_1 ($I > 2\sigma(I)$)	0.0200
wR_2 (all data)	0.0383
S (all data)	0.972
$\Delta\rho_{max}$, $\Delta\rho_{min}$ /e· Å^{-3}	0.39/-0.62
Flack parameter	0.004(5)

Details of crystal structure measurement and refinement: Single crystal X-ray determination was performed at 100 K on a Bruker Quest D8 diffractometer with microfocus MoKα radiation and a Photon 100 (CMOS) detector.

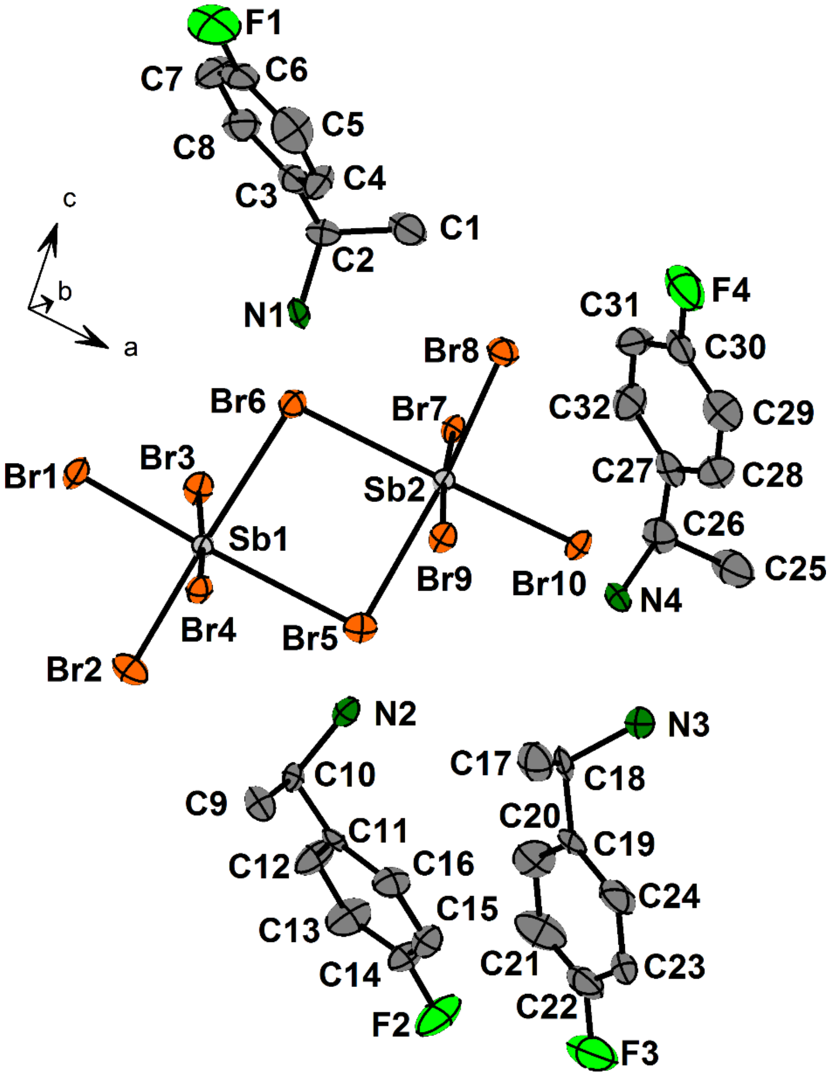

Figure S2: Asymmetric unit of **2**, ellipsoids at 80% probability.

Table S4: Crystallographic data for **3**.

	3 (CCDC 1995572)
Empirical formula	$C_{32}H_{44}F_4I_{10}N_4Sb_2$
Formula weight /g·mol^{-1}	2073.21
Crystal color and shape	orange block
Crystal size	0.252 × 0.205 × 0.194
Crystal system	monoclinic
Space group	$P2_1$
a /Å	12.9520(7)
b /Å	14.3430(7)
c /Å	14.3389(7)
α /°	90
β /°	94.966(2)
γ /°	90
V /Å^3	2653.7(2)
Z	2
ρ_{calc} /g·cm^{-3}	2.595
μ(Mo$_{K\alpha}$) /mm^{-1}	6.875
measurement temp. /K	100
Absorption correction type	multi-scan
Min/max transmission	0.5430/0.7452
2Θ range /°	4.246-50.618
No. of measured reflections	43870
No. of independent reflections	9664
R(int)	0.0338
No. of indep. reflections ($I > 2\sigma(I)$)	9284
No. of parameters	460
R_1 ($I > 2\sigma(I)$)	0.0172
wR_2 (all data)	0.0385
S (all data)	1.199
$\Delta\rho_{max}$, $\Delta\rho_{min}$ /e· Å^{-3}	0.60/-0.98
Flack parameter	0.009(15)

Details of crystal structure measurement and refinement: Single crystal X-ray determination was performed at 100 K on a Bruker Quest D8 diffractometer with microfocus MoKα radiation and a Photon 100 (CMOS) detector. Five atoms in the 4-fluoro-phenyl group in one of the ammonium moieties are disordered over two positions with 0.5 occupancy. Disordered atoms were refined isotropically. The AFIX 66 command was used to obtain reasonable C-C distances and C-C-C angles in the disordered moieties. SADI restraints were used on C-C distances in the phenyl rings of non-disordered units.

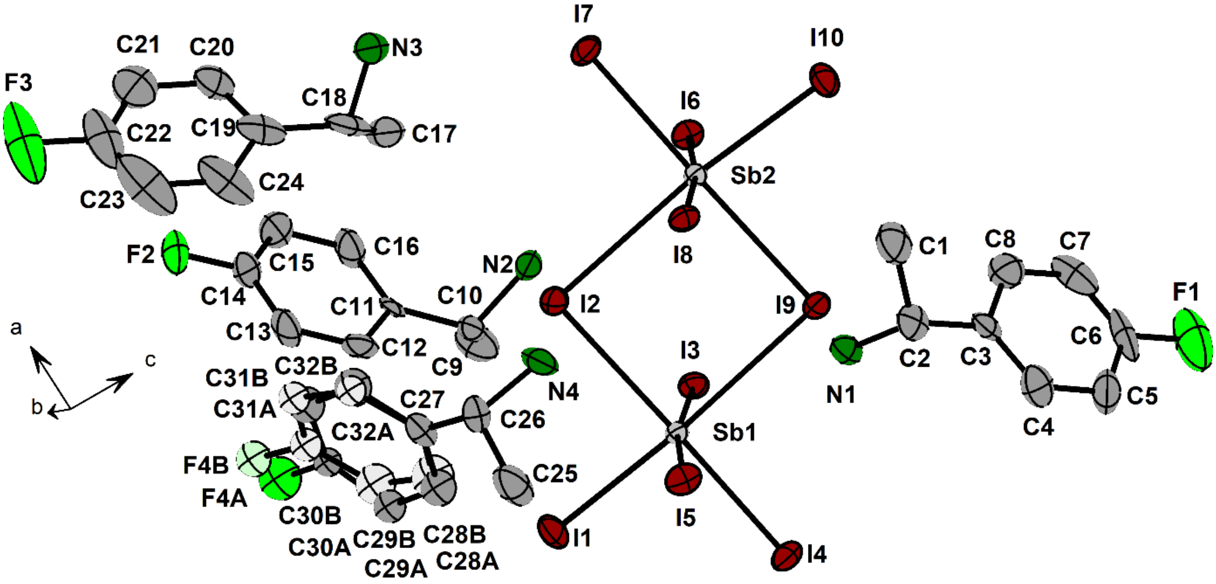

Figure S3: Asymmetric unit of **3**, ellipsoids at 80% probability.

Table S5: Crystallographic data for **4**.

	4 (CCDC 1995575)
Empirical formula	$C_{32}H_{44}Bi_2Cl_{10}F_4N_4$
Formula weight /g·mol^{-1}	1333.17
Crystal color and shape	colorless block
Crystal size	0.392 × 0.282 × 0.17
Crystal system	monoclinic
Space group	$P2_1$
a /Å	11.7357(5)
b /Å	13.9008(6)
c /Å	13.9806(6)
α /°	90
β /°	95.5476(14)
γ /°	90
V /Å^3	2270.05(17)
Z	2
ρ_{calc} /g·cm^{-3}	1.950
μ(Mo$_{K\alpha}$) /mm^{-1}	8.375
measurement temp. /K	100
Absorption correction type	multi-scan
Min/max transmission	0.4565/0.7452
2Θ range /°	4.33-50.614
No. of measured reflections	36302
No. of independent reflections	8204
R(int)	0.0558
No. of indep. reflections ($I > 2\sigma(I)$)	7435
No. of parameters	439
R_1 ($I > 2\sigma(I)$)	0.0272
wR_2 (all data)	0.0643
S (all data)	1.108
$\Delta\rho_{max}$, $\Delta\rho_{min}$ /e· Å^{-3}	1.44/-1.25
Flack parameter	0.013(5)

Details of crystal structure measurement and refinement: Single crystal X-ray determination was performed at 100 K on a Bruker Quest D8 diffractometer with microfocus MoKα radiation and a Photon 100 (CMOS) detector. Six atoms of the 4-fluoro-phenyl group in one of the ammonium moieties are disordered over two positions with 0.5 occupancy. A second moiety is disordered in its entirety over two positions with 0.5 occupancy. Disordered atoms were refined isotropically. In both cases, occupancies were first refined freely, resulting in values close to 0.5. Subsequently, occupancies were fixed to 0.5 to provide a more stable refinement. In the disordered moieties, AFIX 66 commands were used, in the non-disordered phenyl rings, SADI restraints were employed to obtain more reasonable C-C bond distances.

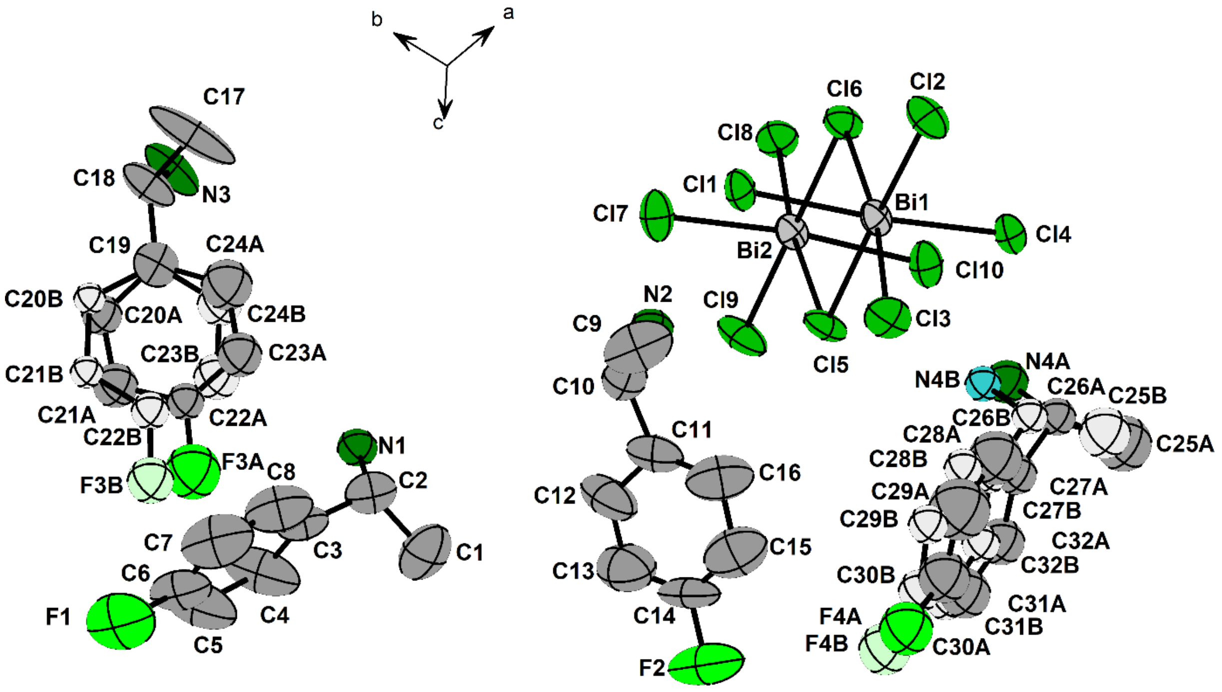

Figure S4: Asymmetric unit of **4**, ellipsoids at 80% probability.

Table S6: Crystallographic data for **5**.

	5 (CCDC 1995571)
Empirical formula	$C_{32}H_{44}Bi_2Br_{10}F_4N_4$
Formula weight /g·mol^{-1}	1777.77
Crystal color and shape	yellow plate
Crystal size	0.351 × 0.298 × 0.116
Crystal system	monoclinic
Space group	$P2_1$
a /Å	12.2017(6)
b /Å	14.1185(7)
c /Å	14.0742(7)
α /°	90
β /°	95.2271(17)
γ /°	90
V /Å^3	2414.5(2)
Z	2
ρ_{calc} /g·cm^{-3}	2.445
μ(Mo$_{K\alpha}$) /mm^{-1}	15.596
measurement temp. /K	100
Absorption correction type	multi-scan
Min/max transmission	0.073/0.265
2Θ range /°	4.232-50.658
No. of measured reflections	35531
No. of independent reflections	8688
R(int)	0.0583
No. of indep. reflections ($I > 2\sigma(I)$)	7657
No. of parameters	423
R_1 ($I > 2\sigma(I)$)	0.0447
wR_2 (all data)	0.1365
S (all data)	1.050
$\Delta\rho_{max}$, $\Delta\rho_{min}$ /e· Å^{-3}	2.64/-3.24
Flack parameter	0.022(9)

Details of crystal structure measurement and refinement: Single crystal X-ray determination was performed at 100 K on a Bruker Quest D8 diffractometer with microfocus MoKα radiation and a Photon 100 (CMOS) detector. Six atoms in the 4-fluoro-phenyl group in one of the ammonium moieties are disordered over two positions with 0.5 occupancy. Disordered atoms were refined isotropically. Occupancies were first refined freely, resulting in values close to 0.5. Subsequently, occupancies were fixed to 0.5 to provide a more stable refinement. ISOR restraints had to be used on a number of atoms in the ammonium moieties to obtain reasonable displacement parameters. AFIX 66 commands were used on all phenyl rings and SADI restraints on all other C-C distances.

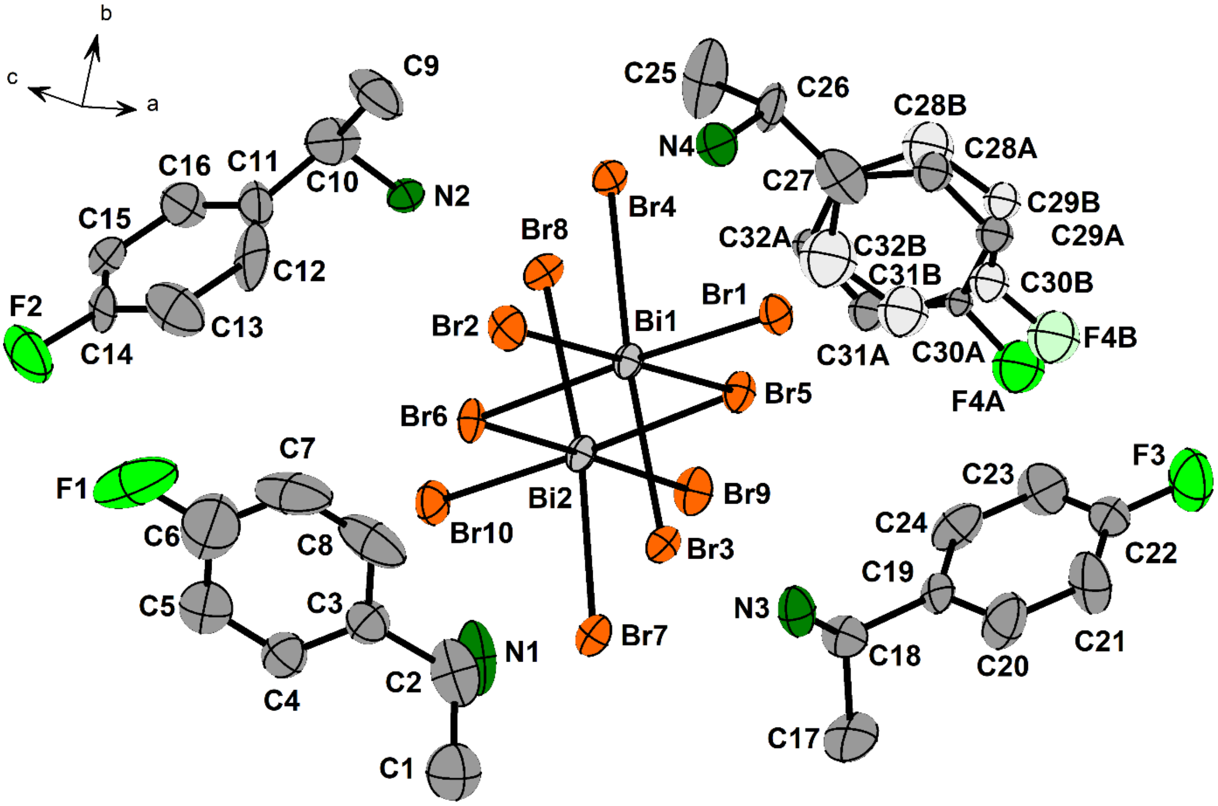

Figure S5: Asymmetric unit of **5**, ellipsoids at 80% probability.

Table S7: Crystallographic data for **6**.

	6 (CCDC 1995574)
Empirical formula	$C_{32}H_{44}Bi_2F_4I_{10}N_4$
Formula weight /g·mol^{-1}	2247.67
Crystal color and shape	orange plank
Crystal size	0.296 × 0.187 × 0.086
Crystal system	monoclinic
Space group	$P2_1$
a /Å	12.9207(5)
b /Å	14.6156(5)
c /Å	14.2779(5)
α /°	90
β /°	94.3351(14)
γ /°	90
V /Å^3	2688.58(17)
Z	2
ρ_{calc} /g·cm^{-3}	2.776
μ(Mo$_{K\alpha}$) /mm^{-1}	12.317
measurement temp. /K	100
Absorption correction type	multi-scan
Min/max transmission	0.5440/0.7452
2Θ range /°	4.214-50.592
No. of measured reflections	45033
No. of independent reflections	9798
R(int)	0.0611
No. of indep. reflections ($I > 2\sigma(I)$)	8286
No. of parameters	465
R_1 ($I > 2\sigma(I)$)	0.0268
wR_2 (all data)	0.0429
S (all data)	0.953
$\Delta\rho_{max}$, $\Delta\rho_{min}$ /e· Å^{-3}	0.73/-0.72
Flack parameter	0.013(8)

Details of crystal structure measurement and refinement: Single crystal X-ray determination was performed at 100 K on a Bruker Quest D8 diffractometer with microfocus MoKα radiation and a Photon 100 (CMOS) detector. ISOR restraints had to be used on a number of carbon and nitrogen atoms to obtain reasonable displacement parameters.

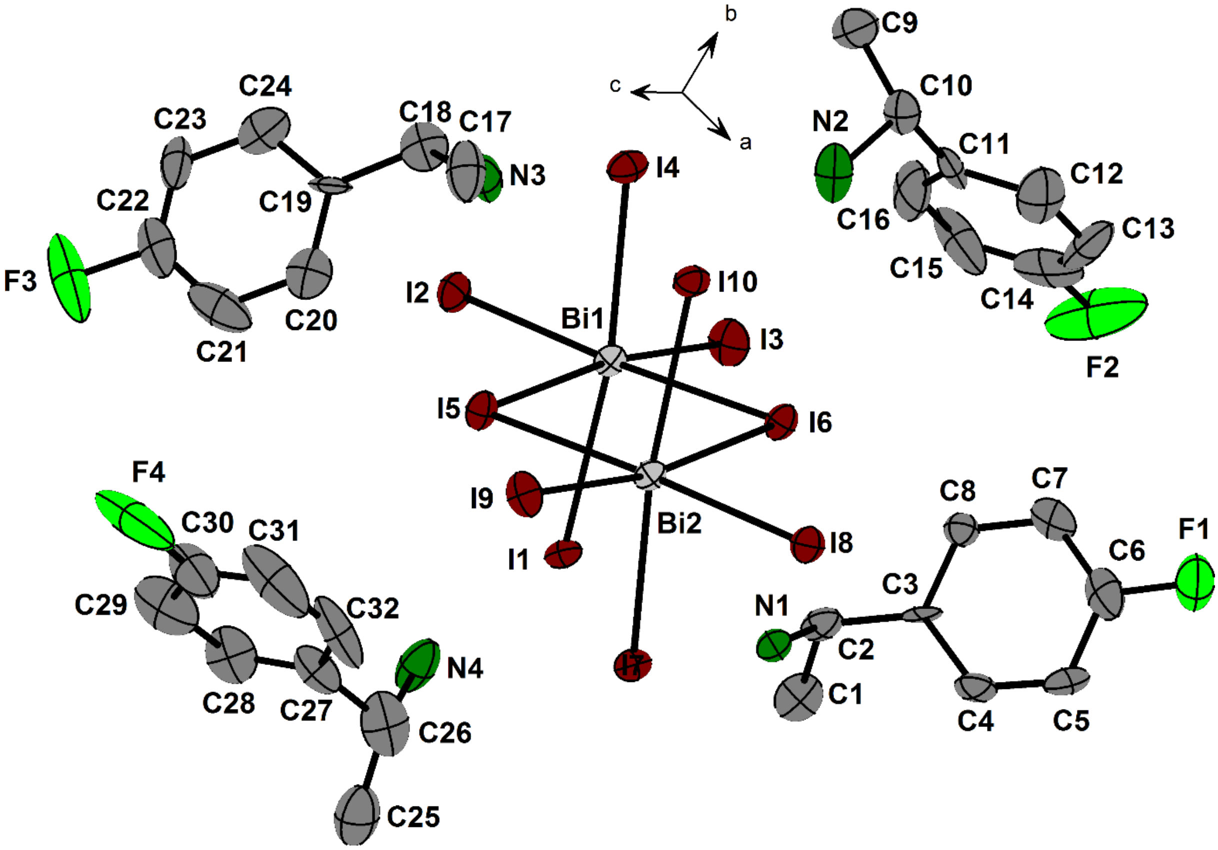

Figure S6: Asymmetric unit of **6**, ellipsoids at 80% probability.

Table S8: Comparison of selected crystallographic data and E-X bond lengths for **1**-**6**.

Compound	**1** (Sb/Cl)	**2** (Sb/Br)	**3** (Sb/I)	**4** (Bi/Cl)	**5** (Bi/Br)	**6** (Bi/I)
a / Å	11.8394(7)	12.3557(5)	12.9520(7)	11.7357(5)	12.2017(6)	12.9207(5)
b / Å	12.8214(7)	13.4134(6)	14.3430(7)	13.9008(6)	14.1185(7)	14.6156(5)
c / Å	14.8843(9)	14.4815(6)	14.3389(7)	13.9806(6)	14.0742(7)	14.2779(5)
β / °	95.0706(19)	95.5638(13)	94.966(2)	95.5476(14)	95.2271(17)	94.3351(14)
V / Å^3	2250.6(2)	2388.74(17)	2653.7(2)	2270.05(17)	2414.5(2)	2688.58(17)
E-X_{terminal} / Å	2.399-2.850	2.590-2.945	2.835-3.069	2.519-2.726	2.681-2.864	2.912-3.082
E-X_{mu} / Å	2.988-3.228	3.041-3.186	3.157-3.312	2.798-3.025	2.973-3.139	3.190-3.325

The comparison of cell parameters across **1**-**6** shows little difference between antimony and bismuth compounds with the same halogen and the expected progression towards larger cell volumes when going from chlorides to bromides and iodides. E-X bond lengths are within typical ranges, with antimonates and chlorides showing larger ranges than the heavier homologues.

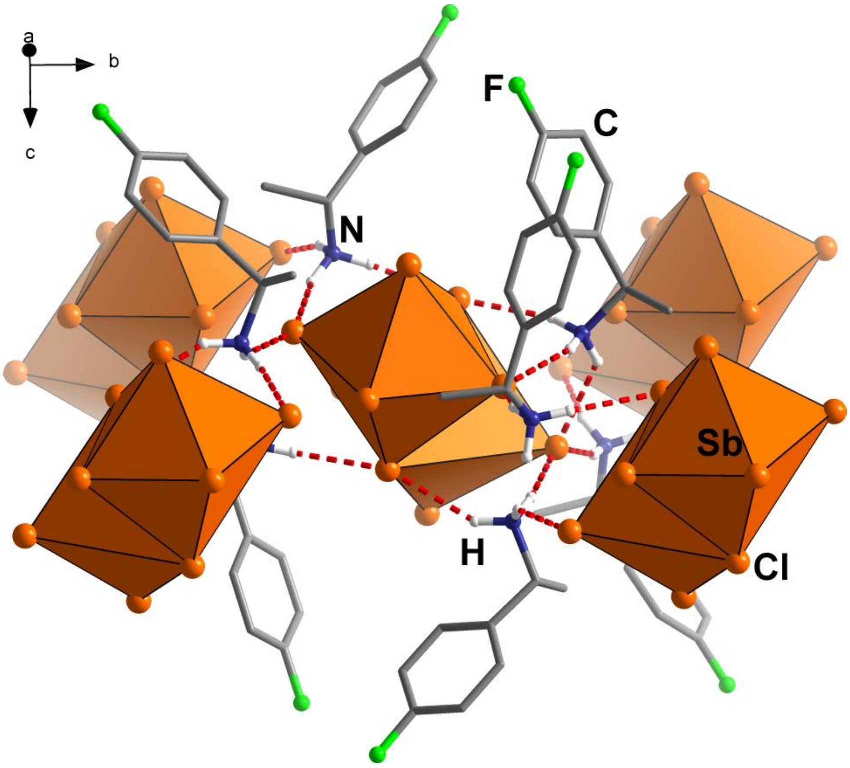

Figure S7: Excerpt of the crystal structure of **1** with short N-H···Cl contacts (between 2.2 and 2.6 Å) around a central $[Sb_2Cl_{10}]^{4-}$ anion drawn as fragmented red lines, showing an interconnection of individual anions through N-H···Cl-bridges in the *ab*-plane.

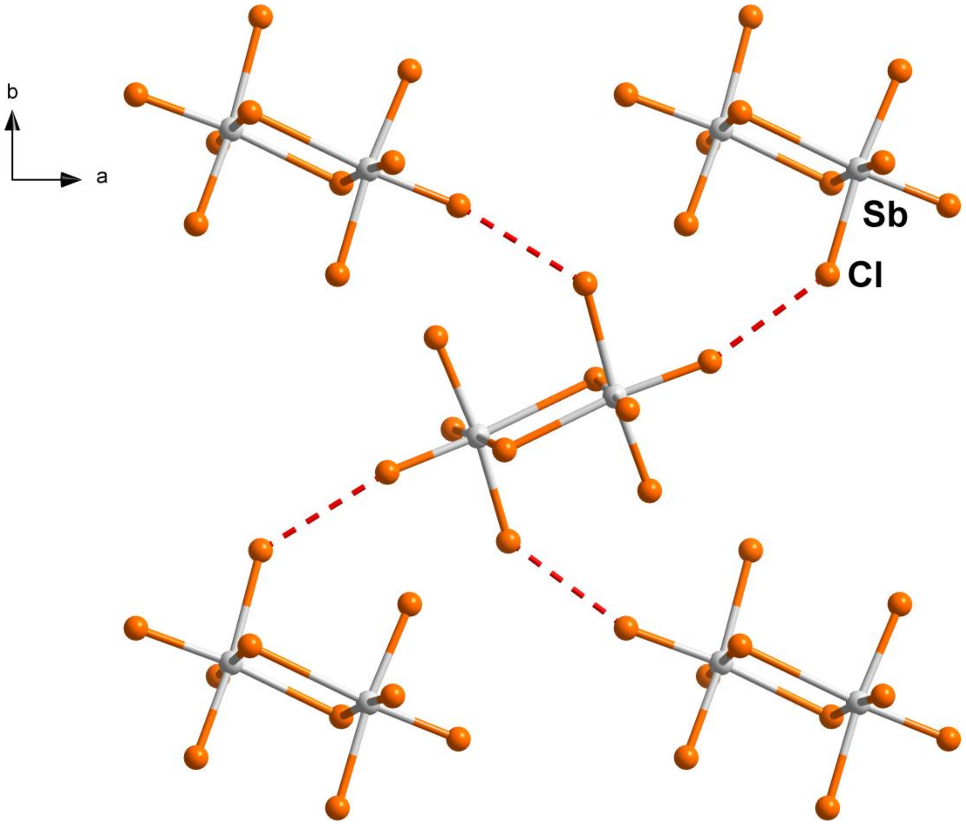

Figure S8: Excerpt of the crystal structure of **1** with short intermolecular Cl···Cl contacts (below 3.64 Å) around a central $[Sb_2Cl_{10}]^{4-}$ anion drawn as fragmented red lines, showing an interconnection of individual anions in the *ab*-plane.

3. Powder Diffraction

Powder patterns were recorded on a *STADI MP* (*STOE* Darmstadt) powder diffractometer, with CuK$_{\alpha 1}$ radiation with λ= 1.54056 Å at room temperature in transmission mode from 3 to 80° in 2θ, although in the patterns shown below no major reflections are found beyond 50° in 2θ. The patterns confirm the presence of the phase determined by SCXRD measurement and the absence of any major crystalline by-products.

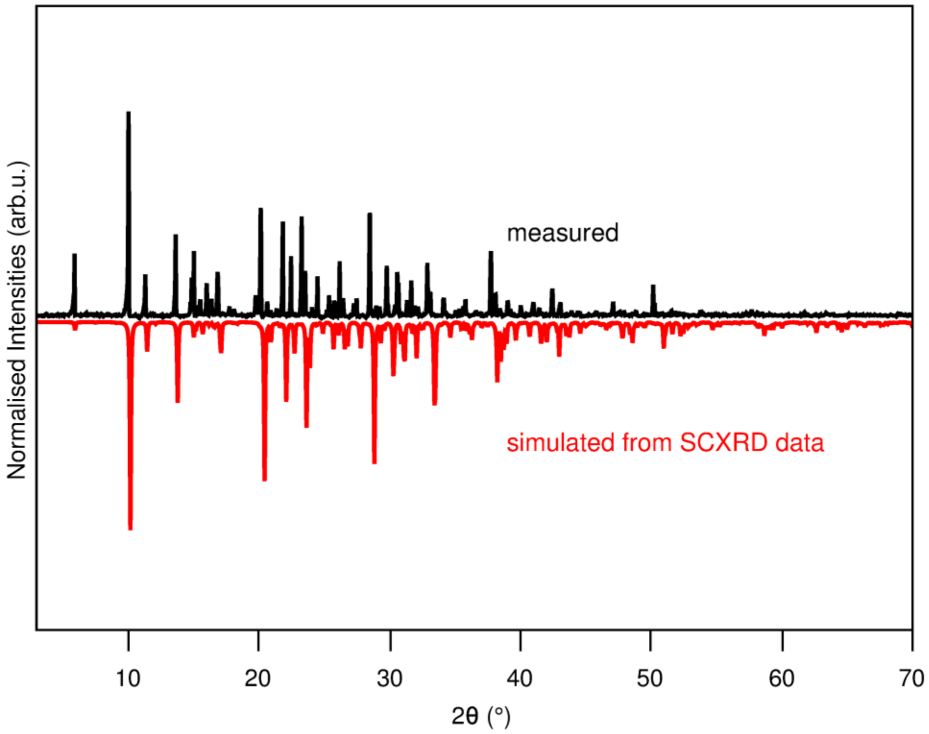

Figure S7: Powder diffraction pattern of **1**.

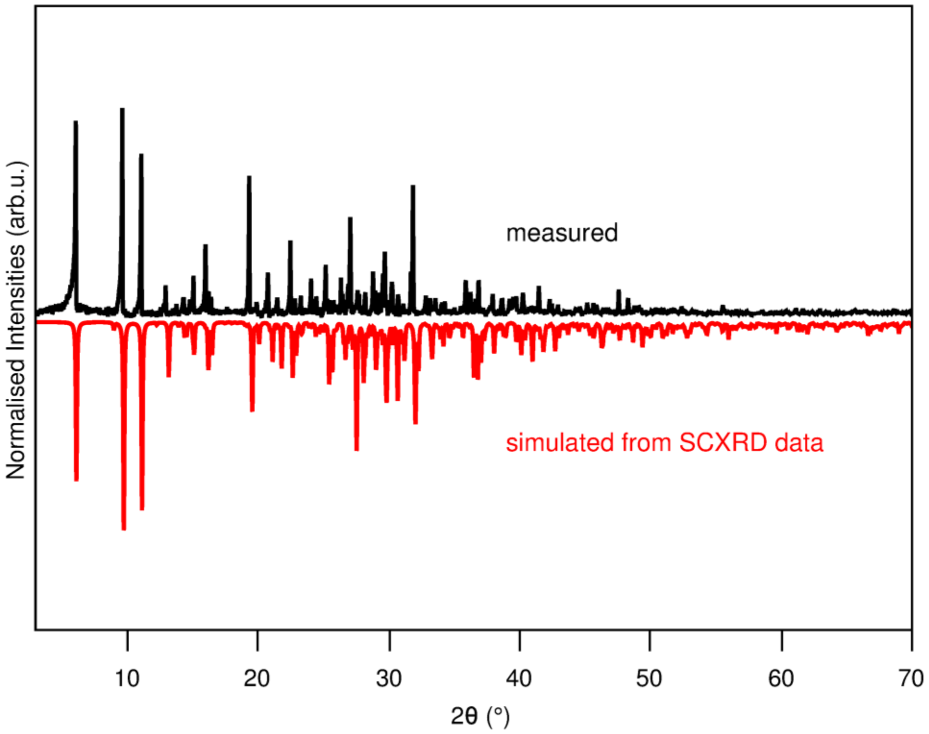

Figure S8: Powder diffraction pattern of **2**.

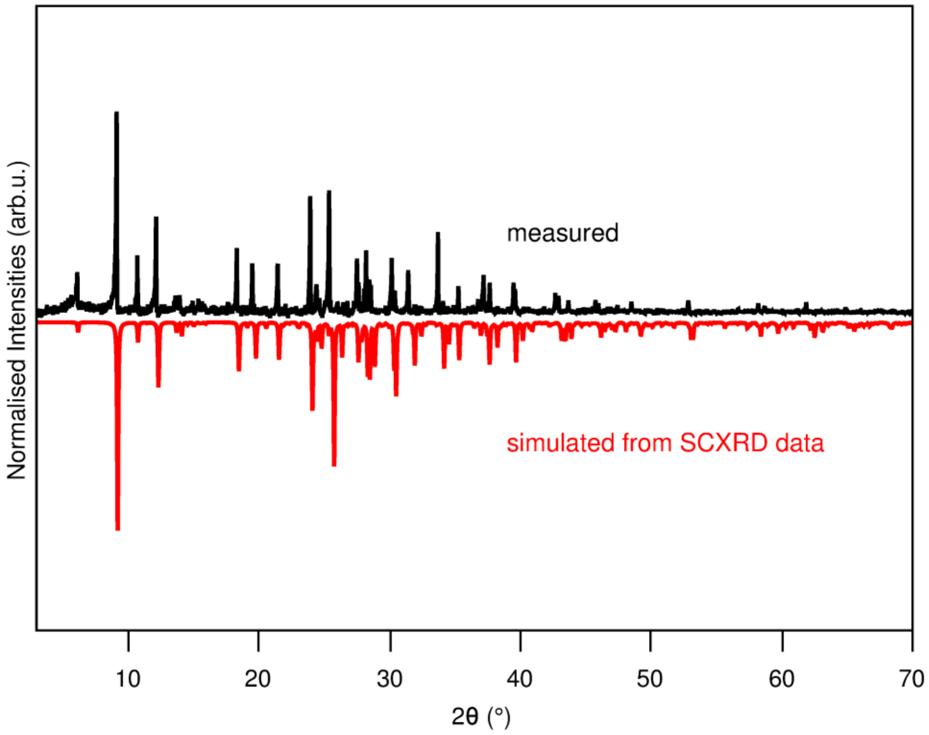

Figure S9: Powder diffraction pattern of **3.**

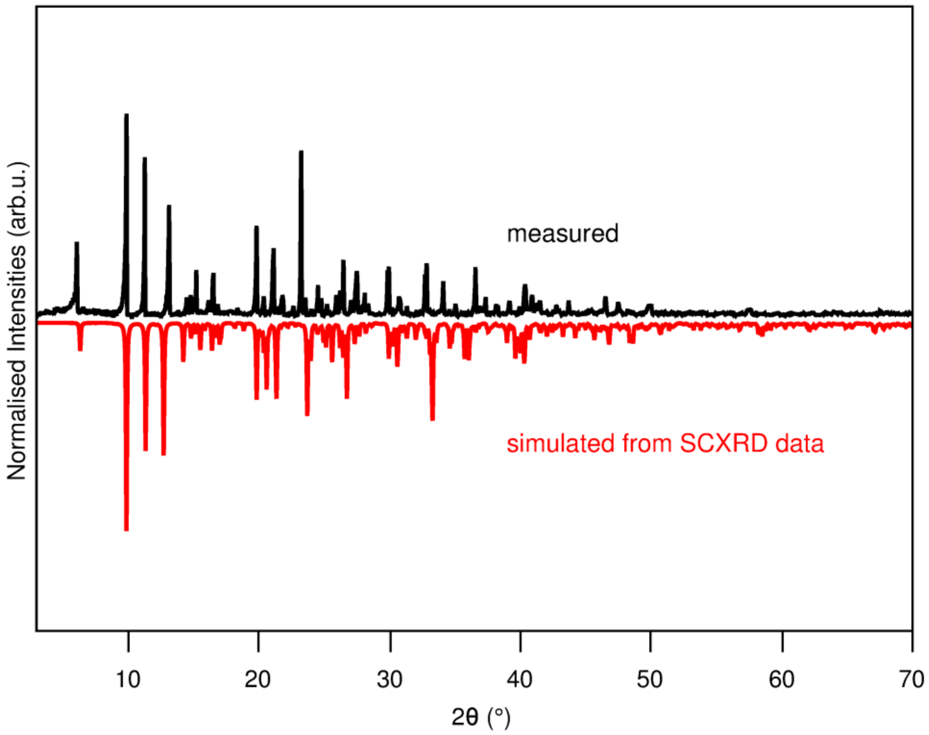

Figure S10: Powder diffraction pattern of **4**.

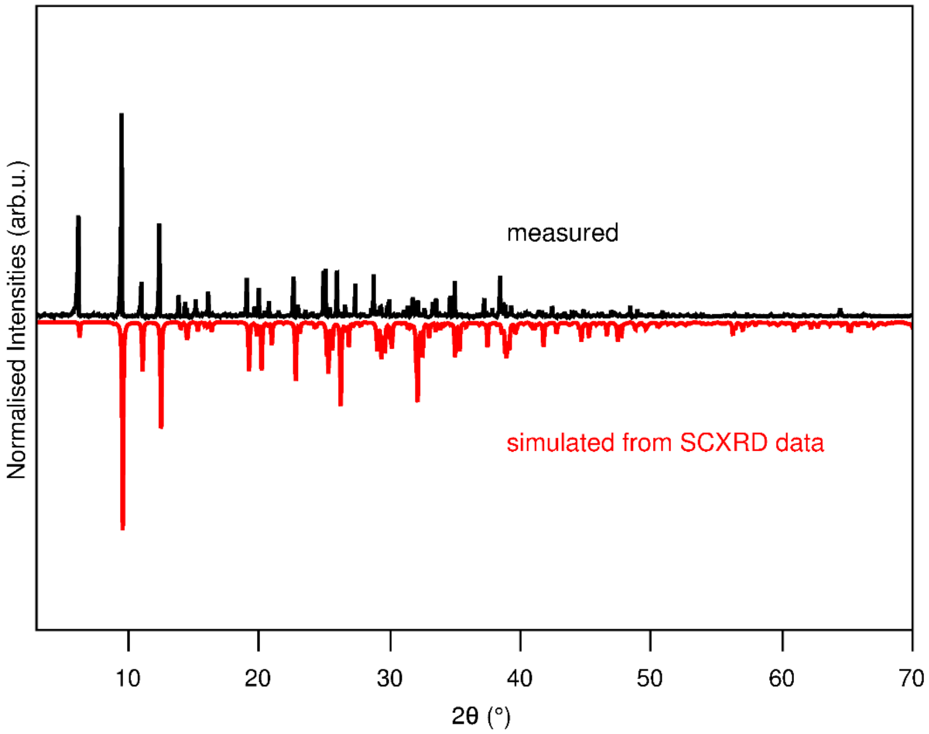

Figure S11: Powder diffraction pattern of **5**.

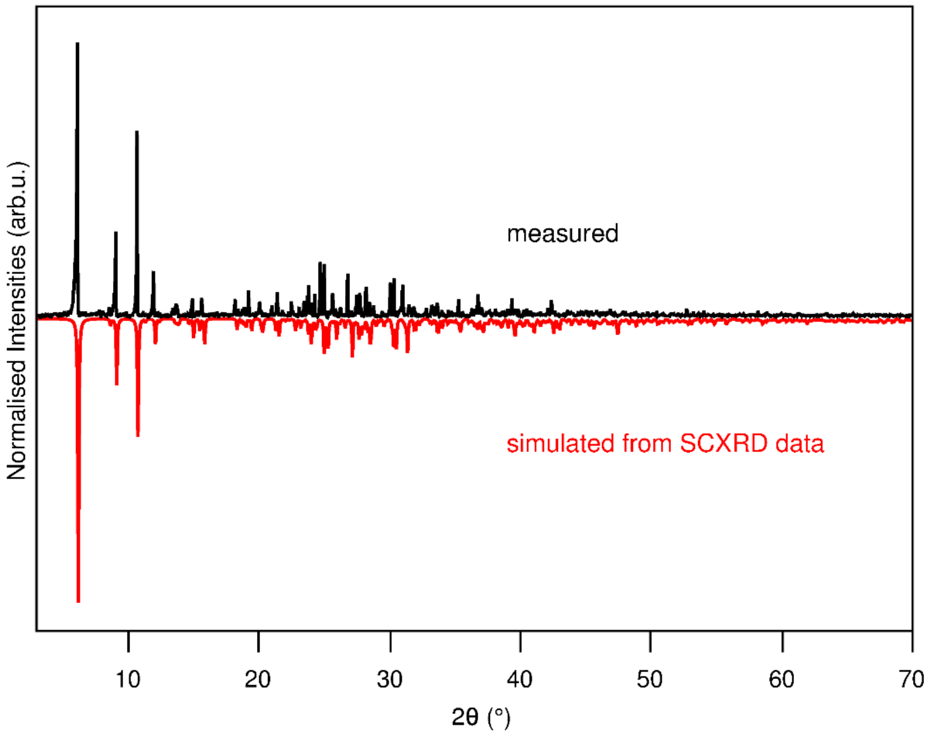

Figure S12: Powder diffraction pattern of **6**.

4. IR Spectroscopy

IR spectra were recorded on a *Bruker Tensor 37* FT-IR spectrometer equipped with an ATR-Platinum measuring unit.

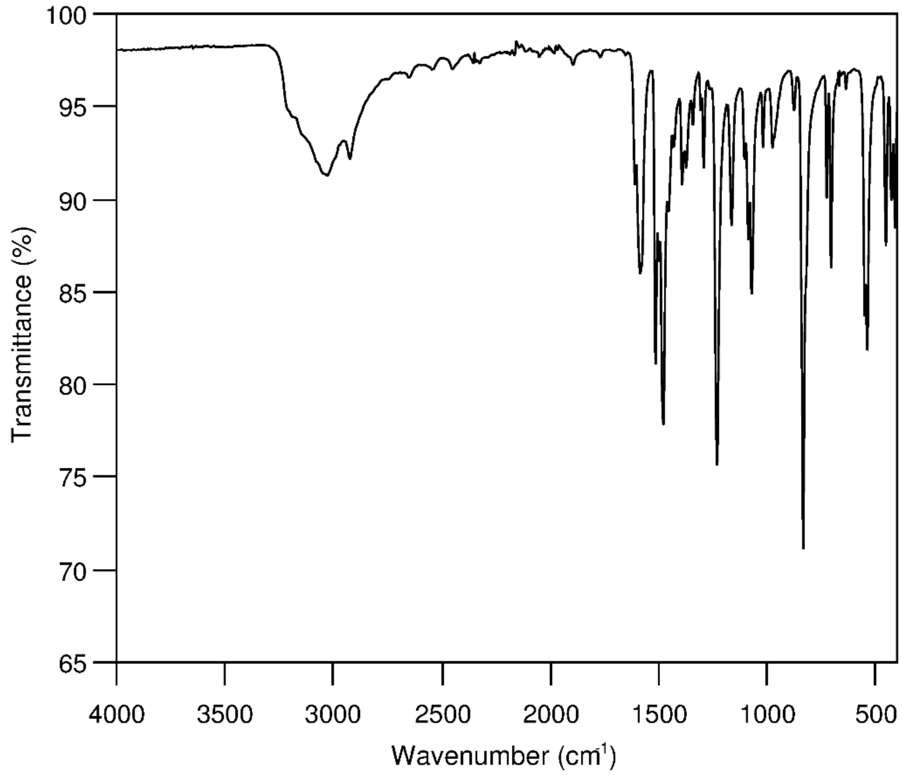

Figure S13. IR spectra of compound **1**. Spectra are dominated by bands of aromatic C-H stretching (3200 – 2800 cm^{-1}) and the aromatic benzene ring in the fingerprint region.[1]

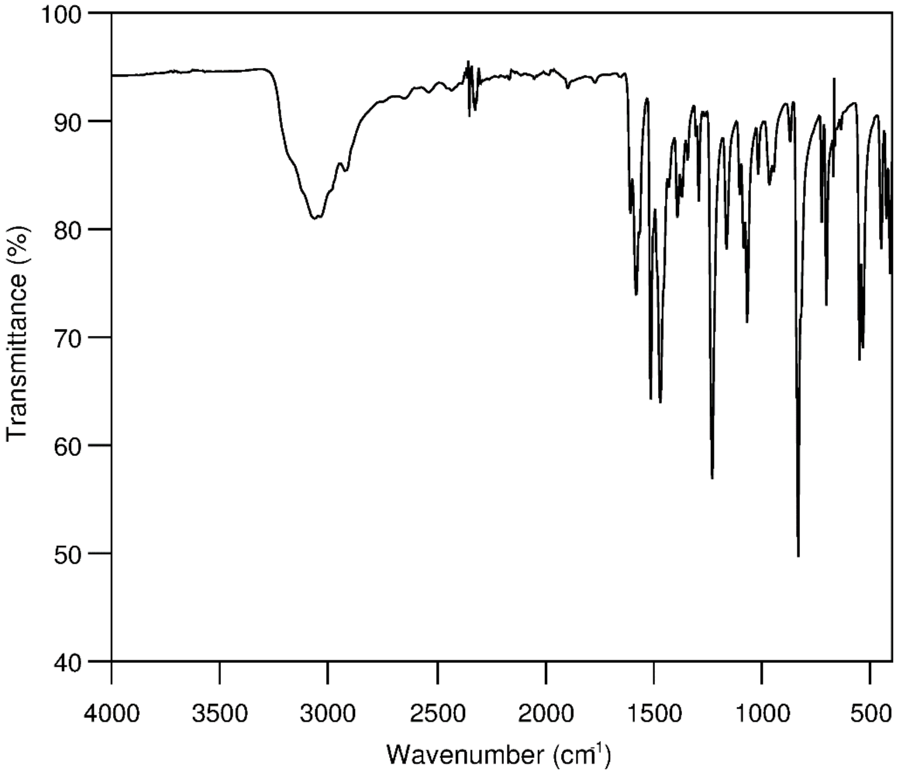

Figure S14. IR spectra of compound **2**. Spectra are dominated by bands of aromatic C-H stretching (3200 – 2800 cm^{-1}) and the aromatic benzene ring in the fingerprint region.[1]

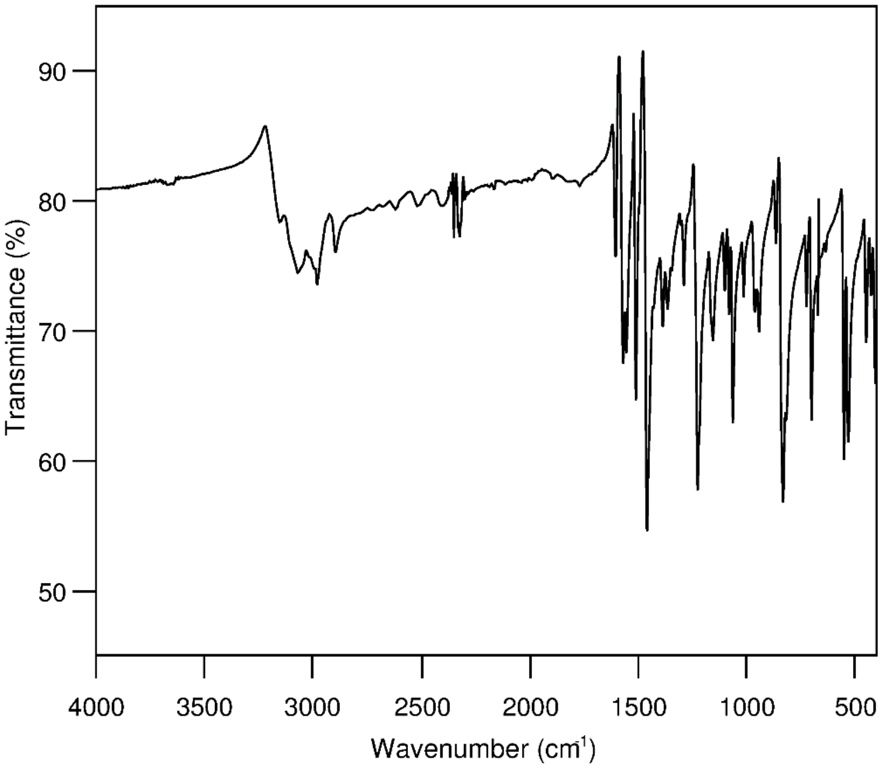

Figure S15. IR spectra of compound **3**. Spectra are dominated by bands of aromatic C-H stretching (3200 – 2800 cm^{-1}) and the aromatic benzene ring in the fingerprint region.[1]

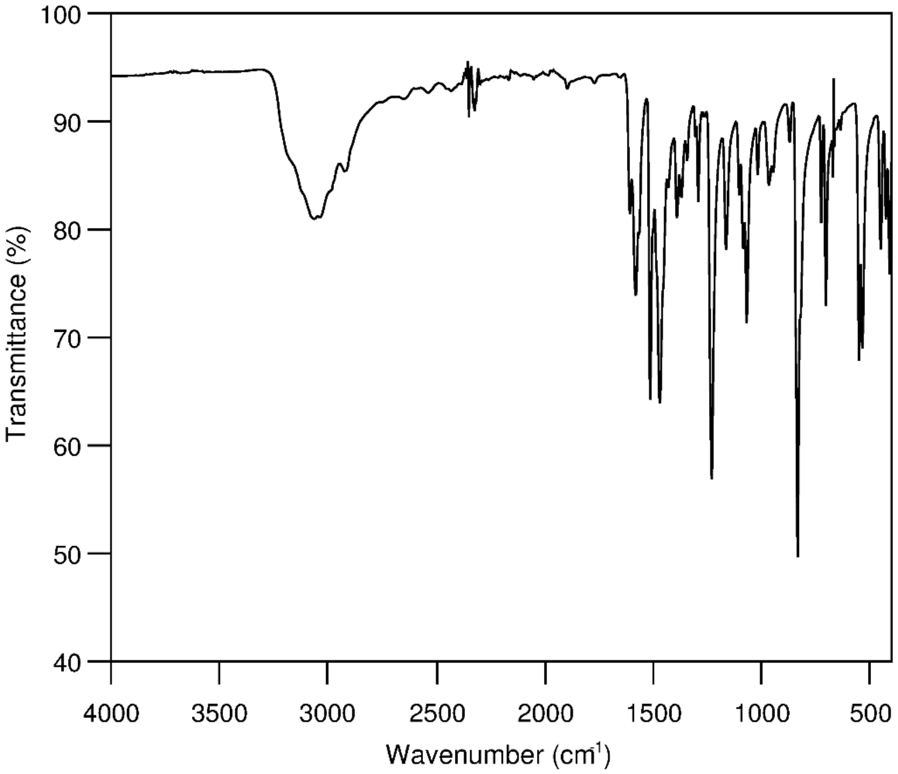

Figure S16. IR spectra of compound **4**. Spectra are dominated by bands of aromatic C-H stretching (3200 – 2800 cm^{-1}) and the aromatic benzene ring in the fingerprint region.[1]

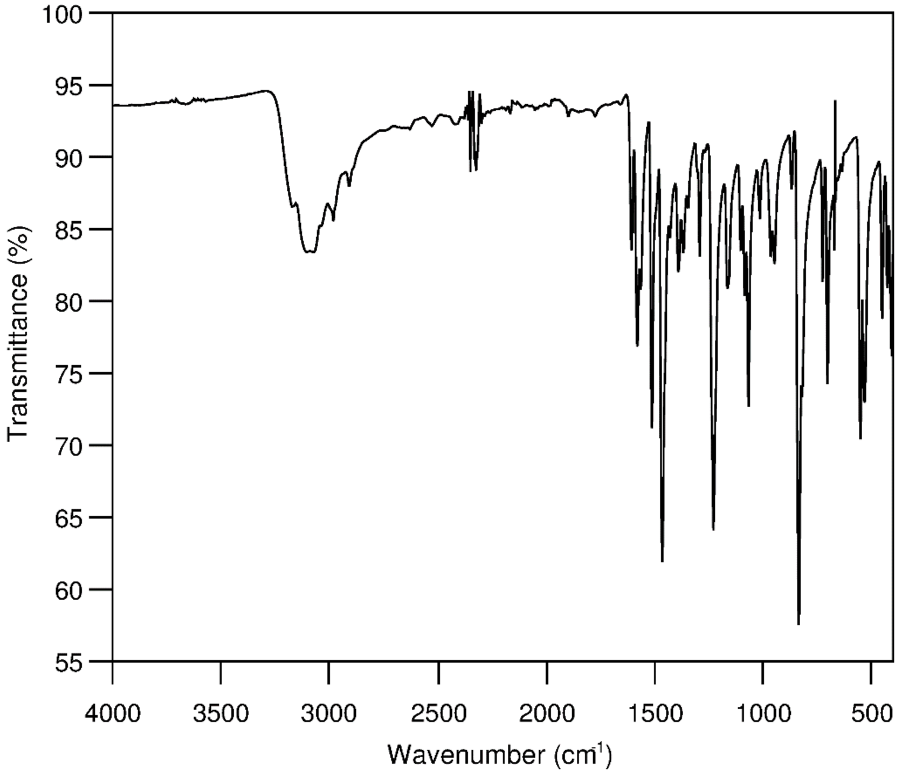

Figure S17. IR spectra of compound **5**. Spectra are dominated by bands of aromatic C-H stretching (3200 – 2800 cm^{-1}) and the aromatic benzene ring in the fingerprint region.[1]

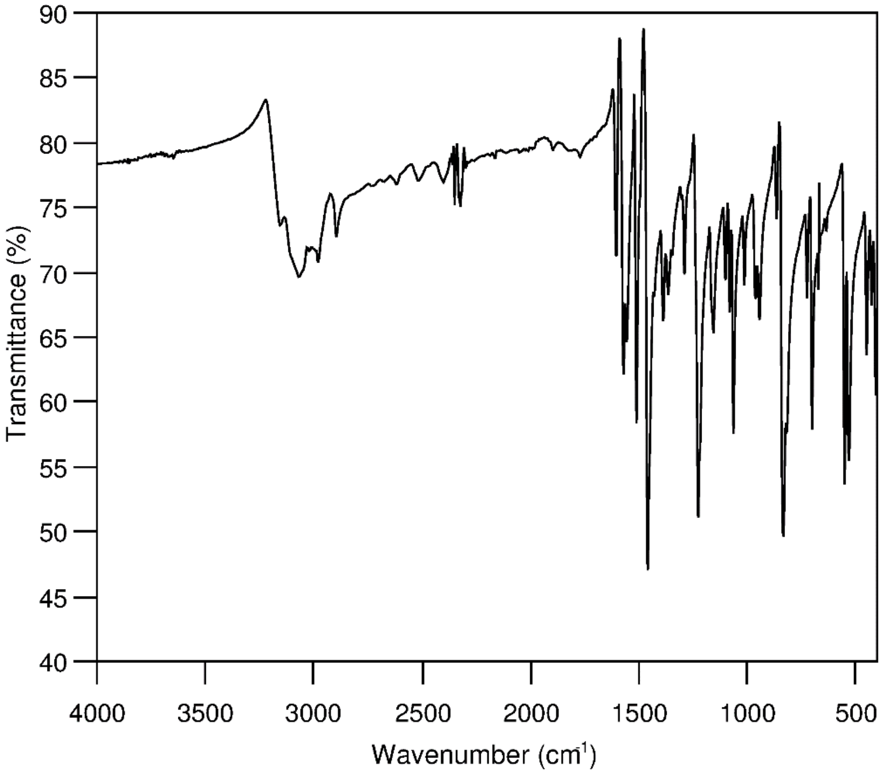

Figure S18. IR spectra of compound **6**. Spectra are dominated by bands of aromatic C-H stretching (3200 – 2800 cm^{-1}) and the aromatic benzene ring in the fingerprint region.[1]

5. Thermal Analysis

The thermal behavior of **1**-**6**, was studied on a Netzsch STA 409 CD from 25 to 1200 °C with a heating rate of 10 °C min^{-1} in a constant flow of 150 mL min^{-1} N_2.

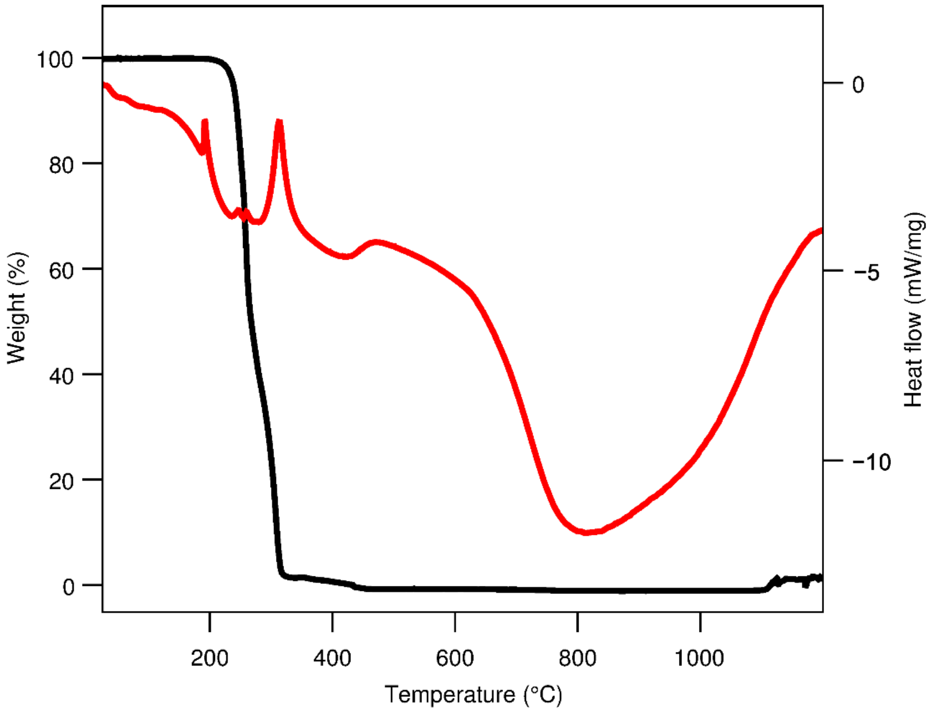

Figure S19. TGA and DSC of compound **1** with a mass loss of 99 % observed starting at 191 °C.

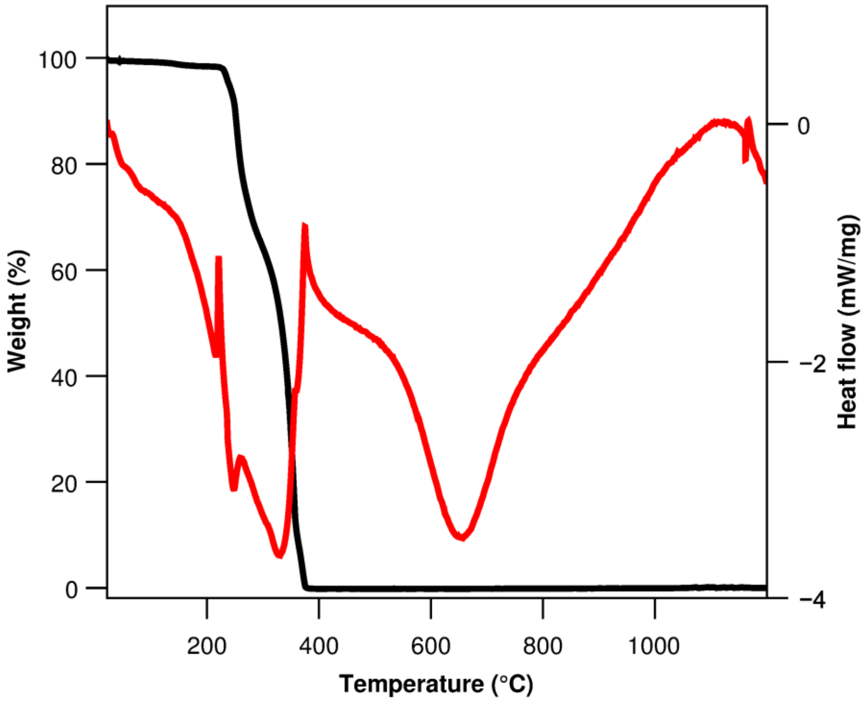

Figure S20. TGA and DSC of compound **2** with a mass loss of 99 % observed starting at 220 °C.

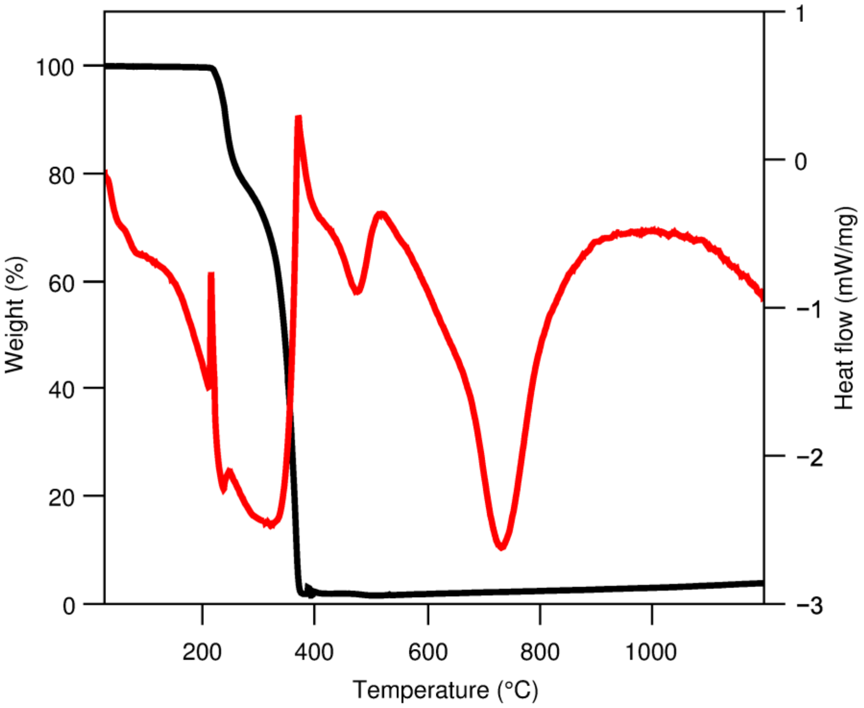

Figure S21. TGA and DSC of compound **3** with a mass loss of 98% observed starting at 215 °C.

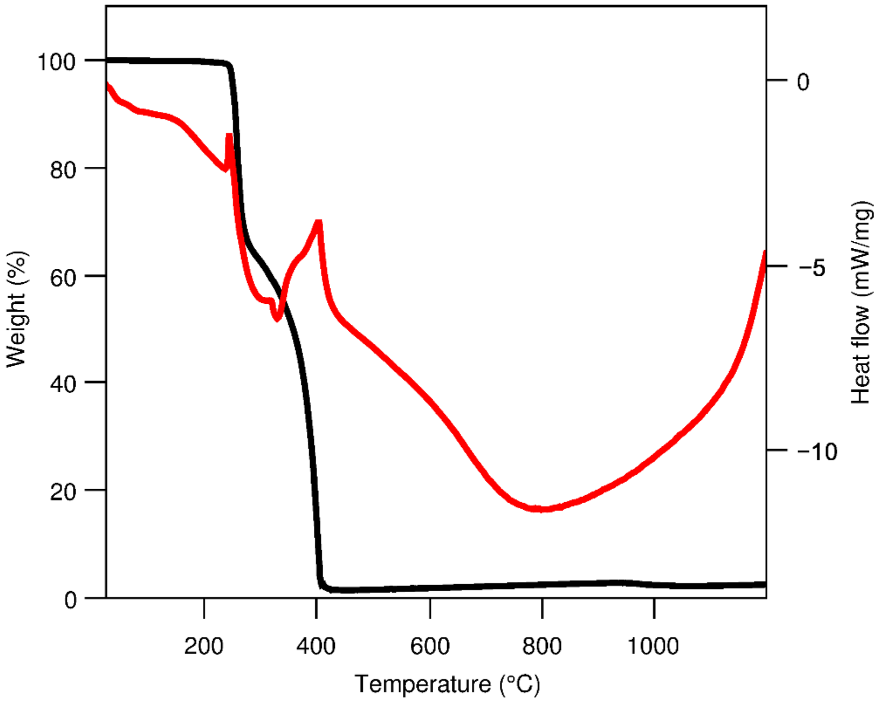

Figure S22. TGA and DSC of compound **4** with a mass loss of 98 % observed starting at 240 °C.

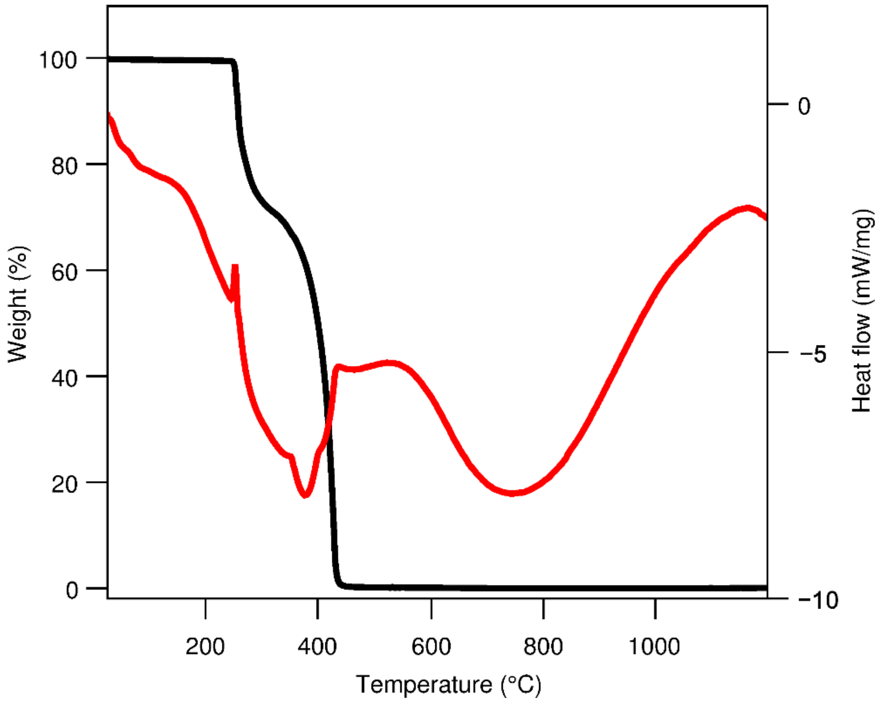

Figure S23. TGA and DSC of compound **5** with a mass loss of 100 % can be observed starting at 251 °C.

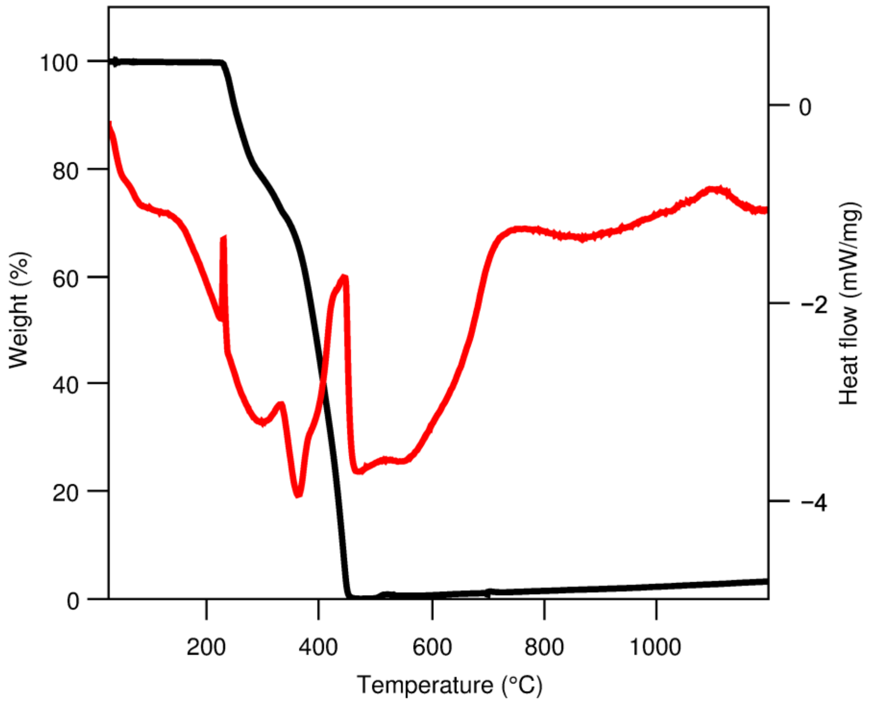

Figure S24. TGA and DSC of compound **6** with a mass loss of 100 % observed starting at 230 °C.

6. Optical Properties

Optical absorption spectra were recorded on a *Varian Cary 5000* UV/Vis/NIR spectrometer in the range of 300-800 nm in diffuse reflectance mode employing a Praying Mantis accessory (*Harrick*). For ease of viewing, raw data was transformed from %Reflectance R to Absorbance A according to A = log (1/R).[2] Onsets of absorptions are listed in Table S9.

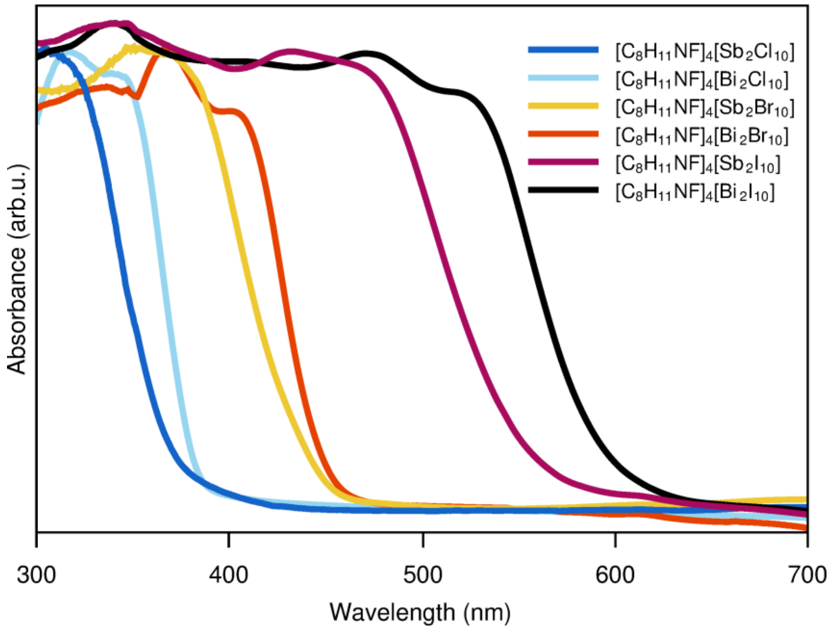

Figure S25. Optical absorption spectra of **1**-**6**, measured in diffuse reflectance.

Table S9. Onset of absorption for **1**-**6**.

Compound	Onset of absorption (nm)	Onset of absorption (eV)
$[C_8H_{11}NF]_4[Sb_2Cl_{10}]$ (**1**)	370	3.35
$[C_8H_{11}NF]_4[Sb_2Br_{10}]$ (**2**)	442	2.81
$[C_8H_{11}NF]_4[Sb_2I_{10}]$ (**3**)	548	2.26
$[C_8H_{11}NF]_4[Bi_2Cl_{10}]$ (**4**)	382	3.25
$[C_8H_{11}NF]_4[Bi_2Br_{10}]$ (**5**)	447	2.77
$[C_8H_{11}NF]_4[Bi_2I_{10}]$ (**6**)	592	2.09

7. Nonlinear optical properties

SHG setup

The SHG experiments were performed under ambient conditions using 10-fs laser pulses generated by a femtosecond Ti:Sapphire oscillator operating at 800 nm at a repetition rate of 82 MHz. The linear polarized laser beam at fundamental frequency ω was focused onto the sample as illustrated in Fig. S26. The generated second-harmonic (SH) light at frequency 2ω was observed in transmission for a chosen combination of input and output polarization, e.g. p-polarized incident fundamental light and s-polarized 2ω light (abbreviated by pS). The SH intensity is detected by a photomultiplier tube using a lock-in amplifier and an optical chopper.

All samples are measured in transmission after optimizing the polar angle of the crystals to realize phase-matching conditions. The second-harmonic signals are normalized with respect to a reference that was generated in a z-cut quartz crystal in pP configuration. The used quartz crystal has a wedge shape with a minimal thickness of 1.2 mm and an angle of 0.8°.

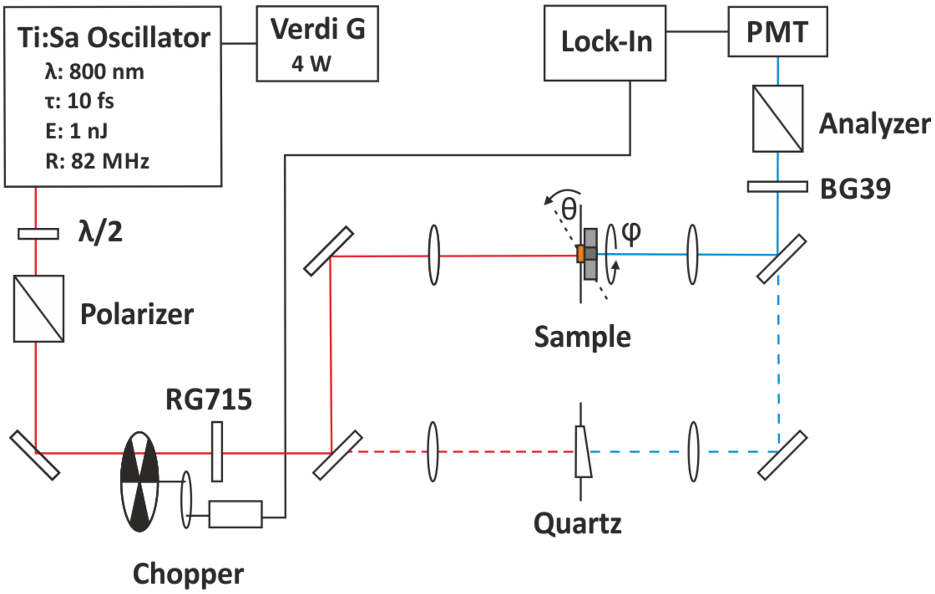

Figure S26. Experimental setup for SHG measurements. The home-built Ti:Sa oscillator is pumped by a Coherent Verdi G laser. The 800-nm output is focused (f=150mm) unto the sample and the 400-nm light of a certain polarization is detected after collimation (f=50mm) by a photomultiplier and a lock-in amplifier. The sample can be rotated around its polar angle (θ) to realize phase-matching conditions and around its azimuth angle (φ) for rotational anisotropy measurements. For comparison a SH reference generated in a z-cut quartz crystal in pP configuration is measured.

Structural symmetry and nonlinear susceptibility

Non-centrosymmetric materials like the compounds 1-6 can show strong nonlinear optical properties such as second-harmonic generation quantified by a non-vanishing second order polarization in dipole approximation.

$$\boldsymbol{P}^{(2)}(2\omega) = \epsilon_0\, \chi^{(2)}\colon \boldsymbol{E}(\omega)\boldsymbol{E}(\omega)$$

The nonlinear polarization $\boldsymbol{P}^{(2)}(2\omega)$ of the frequency doubled light depends on the electric field of the incoming fundamental laser $\boldsymbol{E}(\omega)$ and the second order nonlinear susceptibility $\chi^{(2)}$ which is represented by a third rank tensor with 27 elements. Our materials share a monoclinic space group ($P2_1$) which reduces $\chi^{(2)}$ to only 13 non-vanishing and independent elements[3]. For second-harmonic generation the two photons of the incoming laser are indistinguishable and we can describe $\chi^{(2)}$ by a reduced 3x6 matrix.

$$\begin{pmatrix} P_x \\ P_y \\ P_z \end{pmatrix} = \epsilon_0 \begin{pmatrix} 0 & 0 & 0 & \chi_{xzy} & 0 & \boldsymbol{\chi_{xxy}} \\ \boldsymbol{\chi_{yxx}} & \boldsymbol{\chi_{yyy}} & \chi_{yzz} & 0 & \chi_{yzx} & 0 \\ 0 & 0 & 0 & \chi_{zzy} & 0 & \chi_{zxy} \end{pmatrix} \begin{pmatrix} E_x^2 \\ E_y^2 \\ E_z^2 \\ 2E_yE_z \\ 2E_xE_z \\ 2E_xE_y \end{pmatrix}$$

Measurements are performed at normal incidence ($E_z = 0$) and therefore three elements (black) contribute to the generated second-harmonic polarization. Rotation of the crystal leads to the rotational anisotropy data shown in Fig. S27. Accordingly, we can transform $\chi^{(2)}$ by applying a rotation around the z-axis:

$$\chi'^{(2)}_{ijk} = \sum\nolimits_{lmn} R_{il} R_{jm} R_{kn} \chi^{(2)}_{lmn}$$

$$\text{with } \boldsymbol{R} = \begin{pmatrix} \cos(\Psi) & \sin(\Psi) & 0 \\ -\sin(\Psi) & \cos(\Psi) & 0 \\ 0 & 0 & 1 \end{pmatrix}$$

transforming $\chi^{(2)}$ from crystal coordinates (lmn) to lab coordinates (ijk).

Rotational anisotropy of the different compounds

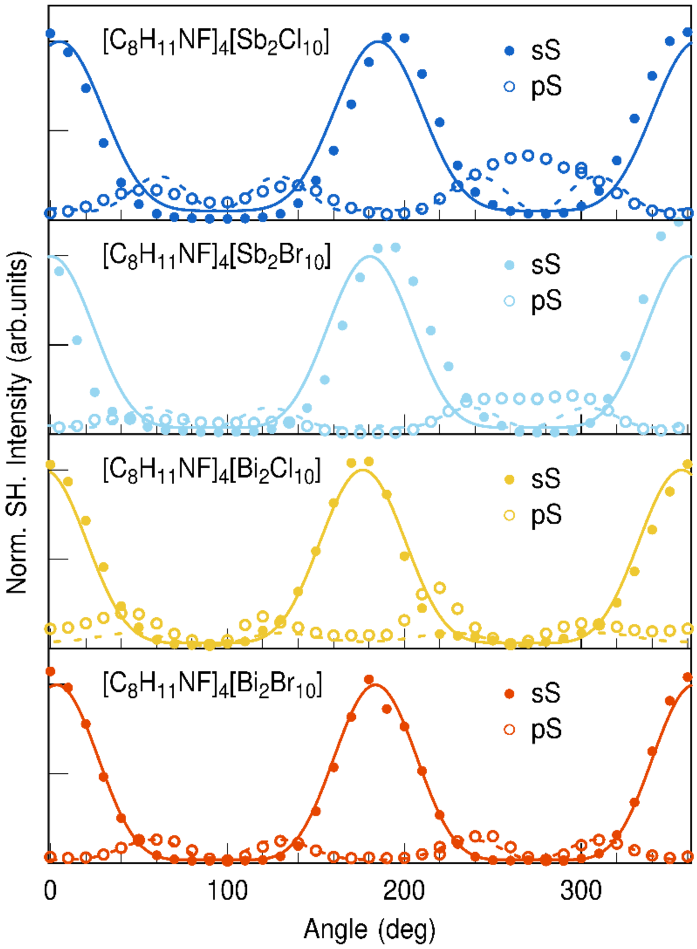

Figure S27. Measured rotational anisotropy of the compounds **1**, **2**, **4** and **5** for parallel (sS) and perpendicular (pS) input and output polarizations in comparison with the corresponding theoretical fits.

8. References

(1) Brittain, H. G. Vibrational Spectroscopic Studies of Cocrystals and Salts. 4. Cocrystal Products formed by Benzylamine, α-Methylbenzylamine, and their Chloride Salts. *Crystal G. & Des.* **2011**, *116*, 2500-2509.

(2) Boldish, S. I.; White, W. B. Optical band gaps of selected ternary sulfide minerals. *Am. Mineral.* **1998**, *83*, 865-871.

(3) Shen, Y. R.; The principles of nonlinear optics. Wiley & Sons, New Jersey, 2003.